



Digital pulse interval modulation for indoor optical wireless communication systems

HAYES, Andrew Robert

Available from the Sheffield Hallam University Research Archive (SHURA) at:

<http://shura.shu.ac.uk/7263/>

A Sheffield Hallam University thesis

This thesis is protected by copyright which belongs to the author.

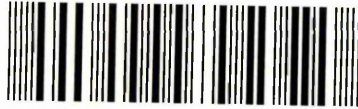
The content must not be changed in any way or sold commercially in any format or medium without the formal permission of the author.

When referring to this work, full bibliographic details including the author, title, awarding institution and date of the thesis must be given.

Please visit <http://shura.shu.ac.uk/7263/> and <http://shura.shu.ac.uk/information.html> for further details about copyright and re-use permissions.

LEARNING CENTRE
CITY CAMPUS, HOWARD STREET
SHEFFIELD S1 1WB

101 624 184 4



Fines are charged at 50p per hour

- 7 NOV 2003

3:58pm

07 NOV 2003

6pm

11 NOV 2003

9pm

12 NOV 2003

9pm

- 5 OCT 2004

REFERENCE

ProQuest Number: 10697076

All rights reserved

INFORMATION TO ALL USERS

The quality of this reproduction is dependent upon the quality of the copy submitted.

In the unlikely event that the author did not send a complete manuscript and there are missing pages, these will be noted. Also, if material had to be removed, a note will indicate the deletion.



ProQuest 10697076

Published by ProQuest LLC (2017). Copyright of the Dissertation is held by the Author.

All rights reserved.

This work is protected against unauthorized copying under Title 17, United States Code
Microform Edition © ProQuest LLC.

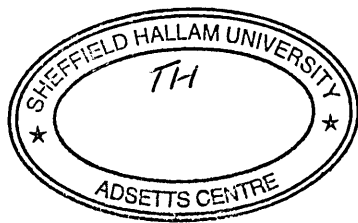
ProQuest LLC.
789 East Eisenhower Parkway
P.O. Box 1346
Ann Arbor, MI 48106 – 1346

Digital Pulse Interval Modulation for Indoor Optical Wireless Communication Systems

Andrew Robert Hayes

A thesis submitted in partial fulfilment of the requirements of
Sheffield Hallam University
for the degree of Doctor of Philosophy

February 2002



Abstract

Over the past decade, infrared has attracted a considerable amount of interest as an alternative medium to radio for short-range indoor wireless local area networks. Infrared offers a number of significant advantages over its radio frequency counterpart, such as the abundance of bandwidth that is currently unregulated worldwide, the availability of low cost emitters and detectors, inherent security and resistance to multipath fading. The work presented in this thesis focuses on modulation techniques, the fundamental aim being to assess the suitability of digital pulse interval modulation (DPIM) for use in indoor optical wireless communication systems.

Infrared transceivers are subject to eye safety regulations, and consequently power efficiency is an important criterion when evaluating modulation techniques. From the error probability analysis carried out on the non-distorting additive white Gaussian noise channel, it is shown that DPIM is able to trade off power efficiency against bandwidth efficiency by increasing the number of bits per symbol. Furthermore, by encoding an additional bit per symbol, DPIM can outperform pulse position modulation (PPM) both in terms of power efficiency and bandwidth efficiency when simple threshold detection is employed.

Indoor optical wireless systems generally operate in the presence of intense ambient light, emanating from both natural and artificial sources. Along with contributing to the generation of shot noise, artificial ambient light sources also introduce a periodic interference signal which can have a detrimental effect on link performance. Original analysis is presented which examines the error performance of DPIM in the presence of interference from a fluorescent lamp driven by a high-frequency electronic ballast, which is potentially the most degrading source of ambient light. It is found that such interference results in an average optical power requirement that is almost independent of the bit rate. The analysis then goes on to consider the effectiveness of electrical high-pass filtering as a simple means of mitigating the effect of the interference, taking into account the baseline wander introduced by the high-pass filter. DPIM was found to be more susceptible to the effects of baseline wander compared with PPM, a finding which is supported by the original analysis carried out on the power spectral density of the scheme. Consequently, whilst electrical high-pass filtering was found to be very effective at high bit rates, significant power penalties are still incurred at low to medium bit rates.

In non-directed line of sight and diffuse link configurations, multipath propagation gives rise to intersymbol interference (ISI), which must be taken into account for data rates above 10 Mbit/s. Original analysis is presented which examines the unequalized performance of DPIM in the presence of ISI. From this analysis, it is found that on any given channel, the improved bandwidth efficiency of DPIM results in lower average optical power penalties, compared with PPM. One novel technique which can be used to make DPIM more resistant to the effects of ISI is to add a guard band to each symbol, immediately following the pulse. Original contributions are presented which evaluate the effectiveness of this technique. To quantify the results obtained, analysis is also carried out on DPIM using a zero-forcing decision feedback equalizer (ZF-DFE), which represents a more traditional approach to mitigating the effects of ISI. It is shown that the guard band technique offers a similar level of performance to the ZF-DFE on all but the most severe channels, and has the advantage of reduced cost and complexity compared with implementing a ZF-DFE.

To support the theoretical and simulated performance of DPIM carried out in this thesis, details are given of a prototype 2.5 Mbit/s diffuse infrared link employing 16-DPIM which has been designed and constructed. The error performance of the link is measured under a variety of ambient light conditions, and the effectiveness of electrical high-pass filtering in mitigating the resulting interference is assessed. It is shown that whilst a fluorescent lamp driven by a high-frequency electronic ballast has the potential to significantly degrade link performance, the power penalty introduced by this source can be made manageable by careful selection of the high-pass filter cut-on frequency.

Acknowledgements

The work presented in this thesis was carried out in the Electronics Research Group within the School of Engineering at Sheffield Hallam University. The work was funded by a University of Sheffield - Sheffield Hallam University joint studentship award, which is gratefully acknowledged.

I would like to thank my director of studies, Professor Z. Ghassemlooy, for his advice, guidance, support and constant enthusiasm throughout this work. I would also like to thank him for proof reading this thesis, and for giving me the opportunity to undertake my studies in the first place.

Sincere thanks also goes to my second supervisor, Dr. N. L. Seed from the University of Sheffield, for providing invaluable help and advice throughout this work. In addition, a word of thanks must also go to Dr. R. Saatchi and Dr. R. McLaughlin for helping me out from time to time.

I would also like to thank my colleagues in the Electronics Research Group, both past and present, for sharing a few laughs with me and generally making my time in Sheffield a very enjoyable experience. Also, a word of thanks goes to the technical and secretarial staff within the School of Engineering who assisted me during my studies.

Finally, I would like to say a special thank you to my wife, Clair, for her constant support, patience, understanding and encouragement throughout the duration of this work.

Declaration

No portion of the work referred to in this thesis has been submitted in support of an application for another degree or qualification to this, or any other university, other institute of learning, or industrial organisation.

Andrew Robert Hayes

February 2002

Glossary of Abbreviations

1GS	One guard slot
2GS	Two guard slots
AC	Alternating current
APD	Avalanche photodiode
AWGN	Additive white Gaussian noise
BER	Bit error rate
BPSK	Binary phase-shift keying
DC	Direct current
DFE	Decision feedback equaliser
DPIM	Digital pulse interval modulation
DPIM(1GS)	DPIM with a guard band consisting of one slot
DPIM(2GS)	DPIM with a guard band consisting of two slots
DPIM(NGB)	DPIM with no guard band
DPPM	Differential pulse position modulation
DSSS	Direct sequence spread spectrum
ERP	Emitter radiation pattern
FHSS	Frequency-hopping spread spectrum
FIFO	First-in first-out
FOV	Field of view
FPGA	Field programmable gate array
FSF	Frequency scaling factor
GBP	Gain bandwidth product
HDL	Hardware description language
HPF	High pass filter
IEC	International Electrotechnical Commission
IEEE	Institute of Electrical and Electronics Engineers
IID	Independent, identically distributed
IM/DD	Intensity modulation with direct detection
IrDA	Infrared Data Association
ISI	Intersymbol interference
ISM	Industrial, scientific and medical
LAN	Local area network
LD	Laser diode
LE	Linear equaliser
LED	Light-emitting diode

LOS	Line of sight
MAP	Maximum <i>a posteriori</i>
ML	Maximum likelihood
MLSD	Maximum likelihood sequence detector
MPPM	Multiple pulse position modulation
MSE	Mean square error
NGB	No guard band
NPV	Nearest preferred value
NRZ	Non return to zero
OOK	On-off keying
OOK-NRZ	On-off keying using non return to zero signalling
OOK-RZ	On-off keying using return to zero signalling
PC	Personal computer
PDA	Personal digital assistant
PER	Packet error rate
PIM	Pulse interval modulation
PIN	Positive-intrinsic-negative
PPM	Pulse position modulation
PPM(MAP)	PPM using a maximum <i>a posteriori</i> detector
PPM(TH)	PPM using a threshold detector
PSD	Power spectral density
PWM	Pulse width modulation
QAM	Quadrature amplitude modulation
QPSK	Quadrature phase-shift keying
RAM	Random access memory
RC	Resistor capacitor
RMS	Root mean square
RZ	Return to zero
RZI	Return to zero inverted
SER	Slot error rate
SNR	Signal to noise ratio
TH	Threshold
WMF	Whitened matched filter
ZF	Zero forcing

Glossary of Symbols

A	Pulse amplitude
a	Constant related to RMS delay spread
A_1	Constant which relates low-frequency interference amplitude with I_B
A_2	Constants which relates high-frequency interference amplitude with I_B
\mathbf{a}_i	OOK bit sequence
a_i	Value of the penultimate bit in sequence \mathbf{a}_i
$a_{i,J}$	Value of the J^{th} bit in sequence \mathbf{a}_i
$A_{i,J}$	Matched filter output for bit sequence \mathbf{a}_i , sampled at end of J^{th} bit period
\mathbf{a}_n	DPIM(1GS) slot sequence
\mathbf{b}	PPM slot sequence containing n symbols
\mathbf{b}_i	PPM/DPIM slot sequence
b_i	Value of the penultimate slot in sequence \mathbf{b}_i
$b_{i,J}$	Value of the J^{th} slot in sequence \mathbf{b}_i
$B_{i,J}$	Matched filter output for slot sequence \mathbf{b}_i , sampled at end of J^{th} slot period
\mathbf{b}_k	DPIM(NGB) slot sequence
$\hat{\mathbf{b}}_k$	Estimate of \mathbf{b}_k
b_{m-1}	Value of $(m-1)^{\text{th}}$ slot in a DPIM sequence
b_m	Value of m^{th} slot in a DPIM sequence
b_{m+1}	Value of $(m+1)^{\text{th}}$ slot in a DPIM sequence
\hat{b}_{m-1}	Estimate of b_{m-1}
\hat{b}_m	Estimate of b_m
\hat{b}_{m+1}	Estimate of b_{m+1}
$C(z)$	Two-sided z transform of c_k
c_0	Zero tap of c_k
c_j	Discrete-time equivalent impulse response of cascaded transmitter filter, high-pass filter and receiver filter
c_k	Discrete-time equivalent impulse response of cascaded transmitter filter, channel and receiver filter
D	Number of bits in a packet
D_{mean}	Mean delay of channel
D_{RMS}	Channel RMS delay spread
D_T	Normalised delay spread
E	Energy of a pulse (and of a symbol in PPM and DPIM)
E_b	Average energy per bit

f	Frequency
f_c	High-pass filter cut-on frequency
$f_{c,off}$	Predetection filter cut-off frequency
f_{high}	Electronic ballast switching frequency
$g(t)$	Impulse response of high-pass filter
G_0	Optical gain of channel
g_0	Zero tap of g_k
g_k	Discrete-time equivalent impulse response of transmitter filter, channel and WMF
$g_{out}(t)$	Output of high-pass filter
$H(\omega)$	Transfer function of predetection filter
$H(s)$	Transfer function of Bessel filter
$h(t)$	Impulse response of channel
H_{avg}	Average received irradiance
I	Number of possible values for the product $a_n a_{n+k}$
I_B	DC photocurrent generated by background radiation
I_{pk-pk}	Peak-to-peak interference signal photocurrent
J	Length of truncated system impulse response
K	Number of distinct sequences
L	Order of PPM and DPIM
L_{avg}	Average DPIM symbol length
M	Total number of bits over a 20 ms interval
m	Number of bits/slots in sequence
$m_f(t)$	Interference photocurrent from fluorescent lamp
$m_{high}(t)$	High-frequency component of $m_f(t)$
m_k	Fluorescent light interference signal sample
$m_{low}(t)$	Low-frequency component of $m_f(t)$
N	Number of slots under consideration
$n(t)$	Shot noise
n_k	Noise sample
N_0	Noise power spectral density (single-sided)
$P(error one)$	Probability of error given that a one was sent
$P(error zero)$	Probability of error given that a zero was sent
$P(error)$	Overall probability of error
$P(f)$	Fourier transform of pulse shape
$P(one)$	Probability of a one
$P(s_0 one)$	Probability of s_0 given that a one was sent

$P(s_0 zero)$	Probability of s_0 given that a zero was sent
$p(t)$	Impulse response of transmitter filter
$P(zero)$	Probability of a zero
P_{avg}	Average optical power
$P_{e,bit,OOK}$	Probability of bit error for OOK
$P_{e,bit,PPM}$	Probability of bit error for PPM(TH and MAP)
$P_{e,slot,DPIM}$	Probability of slot error for DPIM
$P_{e,slot,DPIM(1GS)}$	Probability of slot error for DPIM(1GS)
$P_{e,slot,DPIM(NGB)}$	Probability of slot error for DPIM(NGB)
$P_{e,slot,PPM(TH)}$	Probability of slot error for PPM(TH)
$P_{e,slot,ZF-DFE}$	Probability of slot error for DPIM(NGB) using a ZF-DFE
$P_{e,symb,PPM(MAP)}$	Probability of symbol error for PPM(MAP)
$P_{e,symb,PPM(TH)}$	Probability of symbol error for PPM(TH)
$P(\mathbf{b}_i)$	Probability of occurrence for slot sequence \mathbf{b}_i
P_i	Probability of getting the i^{th} $a_n a_{n+k}$ product
P_{max}	Maximum optical transmit power
P_{RX}	Average received optical signal power
P_{TX}	Average transmitted optical signal power
q	Electron charge
$Q(\cdot)$	Marcum's Q -function
R	Photodetector responsivity
$r(t)$	Impulse response of receiver filter
R_b	Bit rate
RC	Filter time constant
R_k	Slot autocorrelation function
s	Laplace variable
$\tilde{S}(\omega)$	Fourier transform of signal
s_0	Sample value at output of receiver filter
$S_a(f)$	PSD of DPIM slot sequence
$S_c(f)$	Continuous component of $S_a(f)$
$S_{c,PPM}(f)$	Continuous component of electrical PSD of PPM
$S_d(f)$	Discrete component of $S_a(f)$
$S_{d,PPM}(f)$	Discrete component of electrical PSD of PPM
$S_{DPIM}(f)$	Electrical PSD of DPIM
$s_{DPIM}(t)$	DPIM slot sequence
SNR_{max}	Maximum SNR at output of predetection filter
SNR_{out}	SNR at output of predetection filter at sampling time t_0
$S_{OOK-NRZ}(f)$	Electrical PSD of OOK-NRZ

$S_{OOK-RZ(\gamma=0.5)}(f)$	Electrical PSD of OOK-RZ with $\gamma = 0.5$
$S_{PPM}(f)$	Electrical PSD of PPM
t	Time
T	Pulse duration
t_0	Sampling time
T_b	Bit duration
T_s	Slot duration
T_{symp}	Symbol duration
$u(t)$	Unit step function
$W(z)$	Factor of $C(z)$
$W^*(1/z^*)$	Factor of $C(z)$ {complex conjugate of $W(z)$ }
w_k	Tap coefficients of $1/W^*(1/z^*)$
$x(t)$	Intensity or power of optical source
$y(t)$	Photocurrent
y_i	Receiver filter output corresponding to penultimate bit/slot in sequence $\mathbf{a_i/b_i}$
y_j	Receiver filter output corresponding to sequence \mathbf{b}
y_{m-1}	Sampled output of receiver filter corresponding to the $(m-1)^{th}$ slot
y_m	Sampled output of receiver filter corresponding to the m^{th} slot
y_{m+1}	Sampled output of receiver filter corresponding to the $(m+1)^{th}$ slot
α	Threshold level
α_1	Suboptimal threshold level 1
α_2	Suboptimal threshold level 2
α_{opt}	Optimum threshold level
$\delta(t)$	Impulse response of ideal channel
$\delta()$	Dirac delta function
ϵ_i	Probability of bit/slot error for the penultimate bit/slot in sequence $\mathbf{a_i/b_i}$
$\epsilon_{i,k}$	Probability of bit/slot error for sequence $\mathbf{a_i/b_i}$ and interference signal sample m_k
ϵ_m	Probability of slot error for the m^{th} slot
ϵ_{m+1}	Probability of slot error for the $(m+1)^{th}$ slot
γ	Pulse duty cycle
ρ	Root of $C(z)$
ρ^*	Complex conjugate of ρ
φ_i	Phase of odd harmonics of 50 Hz
ϕ_i	Phase of even harmonics of 50 Hz
θ_j	Phase of switching frequency harmonics

σ_n	Standard deviation of noise at output of receiver filter
σ_n^2	Variance of noise at output of receiver filter
Φ_i	Amplitude of odd harmonics of 50 Hz
Ψ_i	Amplitude of even harmonics of 50 Hz
Γ_j	Amplitude of switching frequency harmonics

List of Figures

- 2.1 Equivalent baseband model of an optical wireless system using IM/DD
- 2.2(a)-(d) Link configurations: (a) directed LOS, (b) nondirected LOS, (c) diffuse, and (d) tracked
- 2.3 Optical power spectra of common ambient light sources
- 2.4(a)-(b) Incandescent bulb: (a) time domain waveform, and (b) detected electrical spectrum
- 2.5(a)-(b) Low-frequency fluorescent lamp: (a) time domain waveform, and (b) detected electrical spectrum
- 2.6(a)-(d) HF fluorescent lamp: time domain waveform: (a) low frequency component, (b) high frequency component and detected electrical spectrum: (c) low frequency component, (d) high frequency component
- 3.1 Basic implementation of multiple-subcarrier modulation
- 3.2(a)-(b) Transmitted waveforms for OOK: (a) NRZ, and (b) RZ ($\gamma = 0.5$)
- 3.3 PSD of OOK-NRZ and OOK-RZ ($\gamma = 0.5$)
- 3.4 Receiver for baseband OOK
- 3.5 Matched filter output for detected OOK-NRZ pulse
- 3.6 Maximum-likelihood sequence detector
- 3.7 Transmitted waveforms for 4-PPM
- 3.8 PSD of PPM for $L = 4, 8$ and 16
- 3.9(a)-(b) PPM receiver: (a) hard-decision, and (b) soft decision
- 3.10 Matched filter output for detected PPM pulse
- 3.11 Valid symbols for $\binom{4}{2}$ -MPPM
- 3.12 4-DPPM symbol set
- 4.1 Mapping of source data to transmitted symbols for 4-DPIM(NGB) and 4-DPIM(1GS)
- 4.2 Normalized bandwidth requirement versus number of bits per symbol for DPIM(NGB), DPIM(1GS) and PPM
- 4.3 PSD of DPIM(NGB) for $L = 4, 8, 16$ and 32
- 4.4 PSD of DPIM(1GS) for $L = 4, 8, 16$ and 32
- 4.5(a)-(d) Types of error in DPIM: (a) Transmitted 8-DPIM(1GS) signal, (b) erasure error, (c) false alarm error, and (d) wrong slot error
- 4.6 PER versus probability of slot error for 16-DPIM(NGB) using various packet lengths
- 4.7 Hard-decision DPIM receiver

- 4.8 Block diagram of a DPIM demodulator
- 4.9 Using DPIM in a fixed throughput system
- 4.10 Matched filter output for detected DPIM pulse
- 4.11 Conditional probability density functions of s_0 in the presence of signal independent AWGN
- 4.12 Scaled conditional probability density function of s_0 for $P(\text{zero}) > P(\text{one})$
- 4.13(a)-(b) Normalized optimum threshold level versus PER: (a) DPIM(NGB), and (b) DPIM(1GS)
- 4.14 Average optical power penalty incurred when using a midway threshold level versus number of bits per symbol for DPIM(NGB) and DPIM(1GS)
- 4.15 Normalized average optical power requirement versus normalized bandwidth requirement for various modulation techniques operating on a nondistorting AWGN channel
- 5.1(a)-(b) Photocurrent generated by the interference signal: (a) low frequency component, and (b) high frequency component
- 5.2 Block diagram of the OOK system
- 5.3 Normalized average optical power requirement versus bit rate for OOK with and without fluorescent light interference
- 5.4 Block diagram of the PPM system
- 5.5 Normalized average optical power requirement versus bit rate for PPM(TH) with and without fluorescent light interference
- 5.6 Normalized average optical power requirement versus bit rate for PPM(MAP) with and without fluorescent light interference
- 5.7 Block diagram of the DPIM system
- 5.8 Normalized average optical power requirement versus bit rate for DPIM(NGB) with and without fluorescent light interference
- 5.9 Normalized average optical power requirement versus bit rate for DPIM(1GS) with and without fluorescent light interference
- 5.10(a)-(c) 8-DPIM(1GS) sequence: (a) HPF input, (b) HPF output, and (c) matched filter output
- 5.11(a)-(b) Histogram of matched filter output for OOK with: (a) $f_c/R_b = 10^{-3}$, and (b) $f_c/R_b = 10^{-2}$
- 5.12 Normalized optical power requirement versus f_c/R_b for OOK
- 5.13 Histogram of matched filter output for 8-PPM with $f_c/R_b = 5 \times 10^{-2}$
- 5.14 Normalized average optical power requirement versus f_c/R_b for PPM(TH)
- 5.15 Normalized average optical power requirement versus f_c/R_b for PPM(MAP)

- 5.16(a)-(b) Histogram of matched filter output for 8-DPIM with $f_c/R_b = 10^{-2}$ for:
(a) NGB, and (b) 1GS
- 5.17 Normalized average optical power requirement versus f_c/R_b for DPIM(NGB)
- 5.18 Normalized average optical power requirement versus f_c/R_b for DPIM(1GS)
- 5.19 Normalized average optical power requirement versus normalized HPF cut-on frequency for OOK at various bit rates
- 5.20 Normalized average optical power requirement versus bit rate for OOK with fluorescent light interference and optimized high-pass filtering
- 5.21(a)-(d) Normalized average optical power requirement vs. normalized HPF cut-on frequency for PPM(TH) at various bit rates with: (a) $L = 4$, (b) $L = 8$,
(c) $L = 16$, and (d) $L = 32$
- 5.22(a)-(d) Normalized average optical power requirement vs. normalized HPF cut-on frequency for PPM(MAP) at various bit rates with: (a) $L = 4$, (b) $L = 8$,
(c) $L = 16$, and (d) $L = 32$
- 5.23 Normalized average optical power requirement versus bit rate for PPM(TH) with fluorescent light interference and optimized high-pass filtering
- 5.24 Normalized average optical power requirement versus bit rate for PPM(MAP) with fluorescent light interference and optimized high-pass filtering
- 5.25(a)-(d) Normalized average optical power requirement vs. normalized HPF cut-on frequency for DPIM(NGB) at various bit rates with:(a) $L = 4$, (b) $L = 8$,
(c) $L = 16$, and (d) $L = 32$
- 5.26(a)-(d) Normalized average optical power requirement vs. normalized HPF cut-on frequency for DPIM(1GS) at various bit rates with: (a) $L = 4$, (b) $L = 8$,
(c) $L = 16$, and (d) $L = 32$
- 5.27 Normalized average optical power requirement versus bit rate for DPIM(NGB) with fluorescent light interference and optimized high-pass filtering
- 5.28 Normalized average optical power requirement versus bit rate for DPIM(1GS) with fluorescent light interference and optimized high-pass filtering
- 6.1 Block diagram of the unequalized OOK system
- 6.2 Response of c_k to a single one in various bit positions
- 6.3 Normalized average optical power requirement vs. normalized delay spread for OOK
- 6.4(a)-(b) Simulated eye diagrams at the receiver filter output for: (a) $D_T = 0.02$, and
(b) $D_T = 0.2$
- 6.5 Block diagram of the unequalized PPM system
- 6.6 Normalized average optical power requirement versus normalized delay spread for OOK, PPM(TH) and PPM(MAP)

- 6.7 Average optical power penalty versus normalized delay spread for OOK, PPM(TH) and PPM(MAP)
- 6.8 Block diagram of the unequalized DPIM(NGB) system
- 6.9 Normalized average optical power requirement versus normalized delay spread for DPIM(NGB)
- 6.10 Average optical power penalty versus RMS delay spread normalized to slot duration for DPIM(NGB)
- 6.11 Normalized average optical power requirement versus normalized delay spread for DPIM(NGB) with $L = 4$ and $L = 32$ using various threshold levels
- 6.12 Mapping of source data to transmitted symbols for 4-DPIM(NGB), 4-DPIM(1GS) and 4-DPIM(2GS)
- 6.13(a)-(d) Normalized average optical power requirement versus normalized delay spread for DPIM(NGB), DPIM(1GS) and DPIM(2GS) with: (a) $L = 4$, (b) $L = 8$, (c) $L = 16$, and (d) $L = 32$
- 6.14 Average optical power penalty versus normalized delay spread for DPIM(NGB), DPIM(1GS) and DPIM(2GS) with $L = 4$ and $L = 32$
- 6.15(a)-(b) (a) Block diagram of DPIM system with DFE, and (b) Equivalent discrete-time block diagram of DPIM system with DFE
- 6.16 Normalized average optical power requirement versus normalized delay spread for DPIM(NGB) with a ZF-DFE
- 6.17 Normalized average optical power requirement versus normalized delay spread for DPIM(NGB), DPIM(1GS), DPIM(2GS) and DPIM(NGB) with a ZF-DFE for $L = 4$ and $L = 32$
- 7.1 System block diagram
- 7.2 Position of transmitter and receiver
- 7.3 Position of artificial ambient light sources
- 7.4 SER versus average received irradiance in the presence of natural light with $f_c \approx 48$ kHz
- 7.5 SER versus average received irradiance in the presence of various artificial ambient light sources with $f_c \approx 48$ kHz
- 7.6(a)-(b) Eye diagram at predetection filter output for two ambient light cases: (a) darkness, and (b) incandescent bulb without optical filter
- 7.7 Transmitted and received signal with $f_c = 100$ kHz
- 7.8 Normalized average optical power requirement versus normalized HPF cut-on frequency (simulated)
- 7.9 SER versus normalized HPF cut-on frequency (measured)
- 7.10 SER versus average received irradiance in the presence of natural light with $f_c \approx 884$ kHz

- 7.11 SER versus average received irradiance in the presence of various artificial ambient light sources with $f_c \approx 884$ kHz
- 7.12(a)-(b) Eye diagram at predetection filter output for two ambient light cases: (a) darkness, and (b) incandescent bulb without optical filter
- A.1 Possible DPIM(1GS) slot sequences resulting in a product of 1 when $k = 4$
- A.2(a)-(d) ACF of DPIM(1GS) for: (a) $L = 4$, (b) $L = 8$, (c) $L = 16$, and (d) $L = 32$
- B.1 Transmitter block diagram
- B.2 Block diagram of 'wr_mem' module
- B.3 Block diagram of 'rd_mem' module
- B.4 Schematic diagram of DPIM Modulator
- B.5 Optical transmitter
- B.6 Receiver block diagram
- B.7 Optical front end
- B.8 Post amplifier
- B.9 Peak SNR of 4th order Bessel low-pass filter (relative to matched filter case) versus normalized cut-off frequency for two different pulse shapes
- B.10 4th order Bessel low-pass filter
- B.11 Threshold detector
- B.12 Threshold detector operation
- B.13 Guard slot circuit
- B.14 Error counter
- B.15 Error counter operation

List of Tables

- 2.1 Artificial ambient light sources
- 2.2 I_B and I_{pk-pk} for incandescent bulb with and without optical filtering
- 2.3 I_B and I_{pk-pk} for low-frequency fluorescent lamp with and without optical filtering
- 2.4 I_B and I_{pk-pk} for high-frequency fluorescent lamp with and without optical filtering
- 5.1 Low frequency component phase values
- 5.2 High frequency component amplitude and phase values
- 7.1 Average background photocurrent from various ambient light sources
- B.1 Normalized component values for 4th order Bessel low-pass filter
- B.2 Calculated and nearest preferred component values for $f_{c,off} = 3.6$ MHz

Contents

Abstract	ii
Acknowledgements	iii
Declaration	iv
Glossary of Abbreviations	v
Glossary of Symbols	vii
List of Figures	xii
List of Tables	xvii
1. Introduction	1
1.1 Research Objectives	5
1.2 Organisation of Thesis	6
1.3 Original Contributions	8
1.4 List of Publications	10
2. Review of Indoor Optical Wireless Links	11
2.1 Introduction	11
2.2 Properties of Indoor Optical Wireless Links	12
2.3 Link Configuration	15
2.4 Review of Channel Characterisation	19
2.5 Optical Component Selection	21
2.6 Ambient Light Sources	24
2.6.1 Incandescent lamp	26
2.6.2 Fluorescent lamp driven by conventional ballast	27
2.6.3 Fluorescent lamp driven by electronic ballast	28
2.7 Summary	30
3. Review of Modulation Techniques	32
3.1 Introduction	32
3.2 On-Off Keying	36
3.2.1 Code properties	36
3.2.2 Power spectral density	37
3.2.3 Error performance on nondistorting channels	39
3.2.4 Review of error performance on multipath channels	42
3.3 Pulse Position Modulation	45
3.3.1 Code properties	45

3.3.2 Power spectral density	46
3.3.3 Error performance on nondistorting channels	47
3.3.4 Review of error performance on multipath channels	51
3.3.5 Trellis-coded PPM	53
3.3.6 PPM variants	54
3.4 Summary	56
4. DPIM Code Properties	58
4.1 Introduction	58
4.2 DPIM Code Properties	59
4.3 DPIM Spectral Properties	62
4.4 Measuring the Error Performance of DPIM	66
4.5 DPIM Receiver Structure	69
4.6 Error Performance on Nondistorting Channels	72
4.6.1 DPIM with no guard band	72
4.6.2 DPIM with one guard slot	74
4.6.3 Optimum threshold level	77
4.6.4 Performance comparison	83
4.7 Summary	86
5. The Effect of Ambient Light Sources on Link Performance	88
5.1 Introduction	88
5.2 Fluorescent Lamp Model	91
5.3 The Effect of Fluorescent Light Interference Without Electrical High-Pass Filtering	93
5.3.1 OOK	93
5.3.2 PPM	97
5.3.3 DPIM	103
5.4 The Effect of Baseline Wander Without Fluorescent Light Interference	108
5.4.1 OOK	110
5.4.2 PPM	114
5.4.3 DPIM	118
5.5 The Effect of Fluorescent Light Interference With Electrical High-Pass Filtering	124
5.5.1 OOK	124
5.5.2 PPM	128
5.5.3 DPIM	134
5.6 Summary	141

6. The Effect of Multipath Propagation on Link Performance	144
6.1 Introduction	144
6.2. Channel Model	145
6.3 Unequalized Performance of Various Modulation Techniques	148
6.3.1 OOK	148
6.3.2 PPM	153
6.3.3 DPIM	159
6.4 DPIM With a Guard Band	164
6.5 DPIM With Equalization	172
6.6 Summary	178
 7. System Implementation	 181
7.1 Introduction	181
7.2 System Overview	182
7.3 Link Setup	184
7.4 Performance of Experimental Link	186
7.4.1 Receiver not optimized for high-frequency fluorescent lamp	186
7.4.2 Receiver optimized for high-frequency fluorescent lamp	190
7.5 Summary	196
 8. Conclusions	 198
 9. Future Work	 205
 Appendix A: Derivation of Slot Autocorrelation Function of DPIM(1GS)	 207
 Appendix B: Details of Experimental System	 213
B.1 Transmitter	213
B.1.1 Modulator	214
B.1.2 Optical transmitter	218
B.2 Receiver	219
B.2.1 Optical front end	219
B.2.2 Post amplifier	222
B.2.3 Predetection filter	223
B.2.4 Threshold detector	227
B.2.5 Guard slot circuit	229
B.2.6 Error counter	229

B.3 ABEL HDL and C Source Code	231
B.3.1 ABEL HDL for 'wr_mem' module	231
B.3.2 C source code used to fill RAM with random data	232
B.3.3 ABEL HDL for 'rd_mem' module	233
References	234

Chapter 1

Introduction

The emergence of portable computing devices such as laptops, palmtops and personal digital assistants (PDAs) has fuelled the demand for mobile connectivity and hence, led to the development of wireless local area networks (LANs). Wireless LANs offer users increased mobility and flexibility compared with traditional wired networks, and may be classified as either infrastructure wireless or ad hoc wireless networks [1]. Untethered from conventional network connections, infrastructure wireless LANs allow users to maintain network connectivity whilst roaming anywhere within the coverage area of the network. This configuration requires the use of access points, or base stations, which are connected to the wired LAN and act as interfaces to the wireless devices. Each access point may accommodate multiple clients. Examples of practical applications for wireless infrastructure LANs which are often cited include medical professionals accessing patient records, real-time vital signs and other reference data at the patient bedside, and factory floor workers accessing part specifications and process information as and when required. In contrast, ad hoc wireless LANs are simple peer-to-peer networks in which each client only has access to the resources of the other clients on the network and not a central server. Ad hoc wireless LANs require no

administration or preconfiguration, and are created on demand only for as long as the network is needed. Examples of practical applications for wireless ad hoc LANs include employees sharing information during a meeting, and colleagues electronically swapping business cards.

The term wireless is synonymous with radio, and there are numerous radio LAN products on the market today. The majority of these products operate in the industrial, scientific and medical (ISM) band located at 2.4 GHz, which has the advantage of being licence free in most countries. However, the available bandwidth is limited to 83.5 MHz, and must be shared with numerous other products on the market such as cordless telephones and baby monitors. Consequently, robust spread spectrum modulation techniques are required, which result in low data rates. As an example, the IEEE 802.11-1997 standard for wireless LANs specifies two radio physical layers for operation in the 2.4 GHz ISM band. These two physical layers use frequency-hopping spread spectrum (FHSS) and direct sequence spread spectrum (DSSS), and offer maximum user data rates of just 2 Mbit/s [2]. This was improved upon in 1999 with the ratification of IEEE 802.11b, which adds two higher data rates of 5.5 Mbit/s and 11 Mbit/s to the DSSS standard [3]. Many of the products currently on the market today are either based on this standard, or the HomeRF standard, which also operates in the 2.4 GHz ISM band, and achieves a maximum data rate of 10 Mbit/s using FHSS [4]. The next generation of radio LAN products, which are just starting to emerge, operate in the so-called 5 GHz band, which has been allocated solely for use by wireless LAN products. Consequently, this allows systems to be optimised in terms of data rate and efficiency, free from the constraints associated with coexisting with other products. There are currently two competing standards in this band, these being IEEE 802.11a and HiperLAN2, both of which specify maximum data rates of 54 Mbit/s [5, 6]. One final radio LAN standard worthy of a mention is Bluetooth, which is a short range, point-to-multipoint standard for voice and data transfer, which again operates in the 2.4 GHz ISM band [7]. Whilst standard class 2 devices have an expected operating range of just 10 metres, and a maximum asymmetric data rate of a mere 723.2 kbit/s, the rationale behind bluetooth is low cost, allowing it to be integrated into a variety of portable electronic devices which may then communicate

with each other via ad hoc wireless networks termed piconets. Products equipped with Bluetooth are just starting to appear on the market.

Along with radio, the term wireless is also applicable to systems which utilise other regions of the electromagnetic spectrum, such as infrared. First proposed as a medium for short-range wireless communication more than two decades ago [8, 9], infrared offers a number of advantages over its radio frequency counterpart, the primary one being the abundance of bandwidth which is currently unregulated world-wide [10]. To an extent, radio and infrared may be viewed as complementary rather than competitive media. For example, if a wireless LAN is required to cover a large area, where users can roam freely and remain connected to the network at all times, then radio is the only cost-effective medium which can achieve this. If, however, a wireless LAN is required to cover a more modest area, but deliver advanced bandwidth-hungry multimedia network services such as video conferencing and video on demand, then infrared is the only medium which truly has the bandwidth available to deliver this.

There are a variety of configurations which an infrared link may take, the simplest of which is the directed line of sight (LOS) point-to-point link, as used in the home for the remote control of electrical appliances such as televisions and audio equipment. This is the chosen configuration for Infrared Data Association (IrDA) serial ports, which offer simple peer-to-peer networking between portable electronic devices such as laptops, palmtops, PDAs and digital cameras. These devices are specified to operate over a maximum range of 1 metre, and offer data rates from 9.6 kbit/s to 4 Mbit/s [11]. Whilst IrDA transceivers offer wireless connectivity at very low cost, and have found their way into many of the portable electronic devices on the market over the past 5 years or so, they are not widely used. One of the main reason for their lack of uptake is convenience of use, since before products equipped with IrDA serial ports can communicate with one another they must be in close proximity, have line of sight and be roughly aligned. In their current form, IrDA links look destined to loose out to the Bluetooth, which is more convenient to use and offers a similar data rate.

Exhibiting a similar behaviour to that of visible light, infrared signals are absorbed by dark objects, diffusely reflected by light-coloured objects and directionally reflected from shiny surfaces [12]. Such characteristics have given rise to another link configuration referred to as diffuse, in which reflections from room boundaries are relied upon to provide coverage. This is the chosen link configuration for the infrared physical layer of the IEEE 802.11-1997 standard, which specifies a peak wavelength range of 850 - 950 nm, and supports data rates of 1 Mbit/s and 2 Mbit/s [2]. Diffuse infrared links offer convenience on a par with radio, and the fact that transmissions are confined to the room in which they originate also makes them inherently secure. Furthermore, signal confinement also permits a potentially huge capacity per unit volume, since the same optical carrier can be reused in adjacent rooms without the risk of interference [10]. However, despite such offerings, diffuse infrared systems have had a very limited impact in the market place to date, since they do not offer any improvement in data rate over radio based products.

Although, to date, commercially available optical wireless systems have not come close to delivering the high data rates which are potentially available from the infrared medium, the reasons for this are more to do with cost constraints rather than any fundamental limitations of the core technology. This is proven by the existence of experimental solid state tracked systems which have been demonstrated operating at 155 Mbit/s [13, 14], which is significantly faster than the latest radio LAN products that are currently emerging. Nevertheless, infrared is a challenging medium and there are numerous considerations which must be taken into account when designing high speed indoor infrared links. Nondirected LOS and diffuse links incur a high optical path loss and must also contend with multipath propagation. Whilst multipath propagation does not result in multipath fading in indoor infrared systems, since detector sizes are huge in comparison with the wavelength, it does give rise to intersymbol interference, which is one of the primary impairments to achieving high speed communication. In addition to this, infrared links must be capable of operating in environments where intense ambient light levels exist, which degrades link performance in two ways. Firstly, the average power of the background radiation generates shot noise in the receiver, which is independent of the

transmitted signal, and secondly, artificial sources of ambient light generate a periodic interference signal, which can contain harmonics into the MHz region for fluorescent lamps driven by electronic ballasts [15, 16]. Finally, all these factors must be overcome without breaching eye safety regulations, which place limitations on the maximum optical transmit power which can be used.

Within the field of indoor optical wireless communications, a considerable amount of research has been carried out on the evaluation of modulation techniques. Whilst numerous schemes have been proposed, each having their own advantages and disadvantages, the two modulation techniques which have received by far the greatest attention, to date, are on-off keying (OOK) and pulse position modulation (PPM). In this thesis another modulation technique is considered, namely digital pulse interval modulation (DPIM). Whilst DPIM has been shown to be well suited to optical fibre communication applications, it possesses certain characteristics which suggest that it may also be an attractive choice for use in optical wireless communication systems. Thus, it is the use of DPIM on indoor optical wireless links which is the main focus of this work.

1.1 Research Objectives

The fundamental aim of the work presented in this thesis is to assess the suitability of digital pulse interval modulation as a candidate modulation scheme for indoor optical wireless communication systems. In order to achieve this, a number of research objectives have been identified, as outlined below:

- Review the fundamental properties of indoor optical wireless communication systems, understand the characteristics of the indoor infrared channel, and identify the constraints which the channel imposes on the rest of the system.

- Review the modulation schemes which have been proposed to date and identify the important criteria. Examine OOK and PPM in detail, and understand what advantages these schemes have over other techniques.
- Review the fundamental properties of DPIM. Investigate the spectral properties of the scheme, and examine the effect of parameters such as the choice of threshold level and the use of guard bands. In addition, identify any possible limitations of the scheme which may result from its nonuniform symbol structure.
- Examine the performance of DPIM in the presence of interference from artificial sources of ambient light. Investigate possible methods of improving the performance of the scheme, and compare with OOK and PPM.
- Examine the performance of DPIM in the presence of intersymbol interference resulting from multipath dispersion. Investigate the effectiveness of adding a guard band, and compare this with more traditional equalization methods. Also compare with the performance of OOK and PPM.
- Construct prototype diffuse optical wireless system using DPIM. Measure the error performance of the link under various ambient light conditions, and compare with the simulated results.

1.2 Organisation of Thesis

This thesis is divided into nine chapters. Following the introduction, chapter 2 provides a general introduction to indoor optical wireless links. In this chapter, the unique properties of the

indoor infrared channel are described, and the work done, to date, on the characterisation and modelling of this channel is reviewed. The chapter also describes the various configurations which indoor infrared links may take, and discusses the advantages and disadvantages of each. The chapter ends with an examination of ambient light sources, which are a source of degradation in indoor optical wireless communication systems.

Chapter 3 presents a review of the modulation techniques which have been considered for use in indoor optical wireless communication systems. The chapter begins by identifying the criteria which are important when evaluating modulation techniques for use in indoor infrared links, and gives a brief overview of the types of schemes considered. The chapter then goes on to focus on OOK and PPM, which are the two most widely adopted schemes to date. For each scheme the code properties, spectral properties and error performance are reviewed. In the case of PPM, coding schemes and variants of the technique which have also been considered for use in indoor optical wireless communication systems are discussed.

Chapter 4 provides an introduction to DPIM. In this chapter, the basic code properties of DPIM are described in detail, and a spectral analysis of DPIM is presented, which is based on a new expression for the slot autocorrelation function. The chapter goes on to discuss measures of performance for DPIM, and considers possible methods of detection. Finally, the chapter ends with an analysis of the error performance of DPIM on nondistorting channels limited by additive white Gaussian noise. In this analysis, the effect of adding a guard band and optimising the threshold level are also examined. Performance comparisons are made with OOK and PPM.

In chapter 5, the error performance of DPIM is examined in the presence of interference arising from artificial sources of ambient light. Since fluorescent lamps driven by electronic ballasts generate interference which is potentially the most degrading, consideration is limited to this type of source. The chapter also analyses the effectiveness of electrical high-pass filtering in mitigating the effect of this interference. This analysis includes the effect of baseline wander,

which is introduced by the high-pass filter. Throughout the chapter, analysis is also carried out for OOK and PPM, and the various modulation techniques are compared.

In chapter 6, the error performance of DPIM is analysed in the presence of intersymbol interference (ISI) arising from multipath propagation. After considering the unequalized performance of DPIM, the chapter goes on to investigate the effectiveness of adding a guard band to each DPIM symbol in order to mitigate the effect of the ISI. In order to quantify the effectiveness of the guard band, the performance of DPIM using a zero forcing decision feedback equalizer is then analysed, which is a more conventional approach to combating the effects of ISI. Again, similar analysis is also carried out in the chapter for OOK and PPM, and the various schemes are compared.

Chapter 7 describes the design of a prototype diffuse infrared link employing DPIM. The error performance of the prototype link was measured under a variety of ambient light conditions, and these results are also presented in the chapter.

In chapter 8, concluding remarks are made, and the major contributions of this thesis are outlined.

Finally, chapter 9 discusses possible areas where this work may be continued.

1.3 Original Contributions

During the course of this work, the author has:

1. Analysed the performance of DPIM on nondistorting AWGN channels. In chapter 4, using the packet error rate as a measure of error performance, it was shown that by encoding an additional bit per symbol, DPIM can outperform PPM in terms of both power efficiency and

bandwidth when a simple threshold-detection based receiver is used. Additionally, the effect of adding a guard band to each symbol and adjusting the threshold level were also investigated.

2. Derived a new expression for the slot autocorrelation function of DPIM using a single guard slot, and used this to determine the power spectral density of the scheme. From the analysis presented in chapter 4, it is apparent that DPIM has a nonzero DC component, and the addition of a guard band to each symbol was found to have little effect on the overall spectral profile of the scheme.
3. Investigated the performance of DPIM in the presence of interference from a fluorescent lamp driven by a high frequency ballast. The effectiveness of electrical high-pass filtering as a means of mitigating the interference was also investigated in chapter 5, which included an analysis of DPIM in the presence of baseline wander which is introduced by the high-pass filter. Optimum high-pass filter cut-on frequencies were also determined.
4. Investigated the unequalized performance of DPIM on multipath channels. In chapter 6, the effectiveness of adding a guard band consisting of one and two guard slots in order to mitigate the intersymbol interference was also investigated. Additionally, in order to quantify the findings, the performance of DPIM using a ZF-DFE was analysed.
5. Developed a low bit rate prototype diffuse infrared system employing DPIM, which is described in chapter 7. The error performance of the system was measured in the presence of various artificial ambient light sources, and effect of electrical high-pass filtering in mitigating the resulting interference was also assessed.

1.4 List of Publications

The work presented in this thesis has resulted in the following publications, which are listed in reverse chronological order.

1. Z. Ghassemlooy, A. R. Hayes and N. L. Seed, "The Effect of Multipath Propagation on the Performance of DPIM in Diffuse Optical Wireless Communications," in *Proceedings of IASTED International Conference on Wireless and Optical Communications*, Banff, Canada, 27-29 June 2001, pp. 166-172.
2. A. R. Hayes, Z. Ghassemlooy, N. L. Seed and R. McLaughlin, "Baseline-wander effects on systems employing digital pulse interval modulation," *IEE Proceedings - Optoelectronics*, vol. 147, no. 4, pp. 295-300, August 2000.
3. A. R. Hayes, Z. Ghassemlooy and N. L. Seed, "The performance of digital pulse interval modulation in the presence of multipath propagation," in *Proceedings of 2nd International Symposium on Communication Systems Networks and Digital Signal Processing*, Bournemouth University, U.K., 18-20 July 2000, pp. 141-146.
4. Z. Ghassemlooy and A. R. Hayes, "Digital pulse interval modulation for IR communication systems - a review," *International Journal of Communication Systems*, vol. 13, no. 7 & 8, pp. 519-536, November-December 2000.
5. A. R. Hayes, Z. Ghassemlooy and N. L. Seed, "The effect of baseline wander on the performance of digital pulse interval modulation," in *Proceedings of IEE Colloquium on Optical Wireless Communications*, London, U.K., 22 June 1999, pp. 13/1-13/5.
6. A. R. Hayes, Z. Ghassemlooy and N L Seed, "Indoor optical wireless communication using digital pulse interval modulation," poster presented at SET'99, House of Commons, London, U.K., 15 March 1999.
7. Z. Ghassemlooy, A. R. Hayes, N. L. Seed and E. D. Kaluarachchi, "Digital pulse interval modulation for optical communications," *IEEE Communications Magazine*, vol. 36, no. 12, pp. 95-99, December 1998.
8. A. R. Hayes, Z. Ghassemlooy and N. L. Seed, "Optical wireless communication using digital pulse interval modulation," in *Proceedings of SPIE Conference on Optical Wireless Communications*, Boston, U.S.A., 5 November 1998, vol. 3532, pp. 61-69.
9. Z. Ghassemlooy, A. R. Hayes, N. L. Seed and E. D. Kaluarachchi, "Digital pulse interval modulation for optical wireless communications," in *Proceedings of 3rd Iranian Academic Association Annual Conference on Computers and Communications*, New York, U.S.A., 19-20 September 1998, pp. 198-202.

Chapter 2

Review of Indoor Optical Wireless Links

2.1 Introduction

This chapter aims to provide a general introduction to indoor optical wireless links. In section 2.2, the unique properties of indoor optical wireless links are reviewed, and the constraints imposed on system design are highlighted. Indoor optical wireless links can be configured in a variety of ways, each suitable for different applications. In section 2.3, the various configurations are described, and their advantages and disadvantages discussed. In order to achieve efficient link design, it is imperative that the characteristics of the channel are well understood. A considerable amount of work has been published on channel characterisation, covering both experimental measurement and computer modelling. This work is reviewed in section 2.4. There are a number of considerations which must be taken into account when selecting the optical components of a system. These considerations are discussed in section 2.5. Infrared links usually operate in the presence of intense ambient light emanating from both

natural and artificial sources. These ambient light sources are discussed in section 2.6, and measurements taken of various sources are presented. Finally, the chapter is summarised in section 2.7.

2.2 Properties of Indoor Optical Wireless Links

For low-cost optical wireless communication systems, intensity modulation with direct detection (IM/DD) is the only feasible method of communication [10]. In this mode of operation, the intensity or power of the optical source $x(t)$ is directly modulated by varying the drive current. At the receiver, a photodetector is used to generate a photocurrent $y(t)$, which is proportional to the instantaneous optical power incident upon it. An optical wireless system using IM/DD has an equivalent baseband model which hides the high-frequency nature of the optical carrier [12]. This model is illustrated in Fig. 2.1 [10], in which R is the photodetector responsivity and $h(t)$ is the linear baseband channel impulse response.

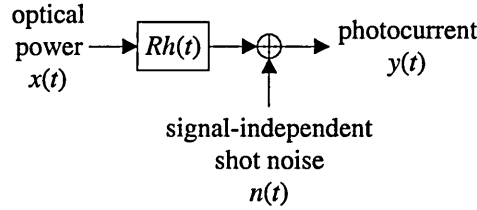


Fig. 2.1: Equivalent baseband model of an optical wireless system using IM/DD

As with radio systems, indoor optical wireless links are subject to multipath propagation, which is most pronounced in links using nondirectional transmitters and receivers. For both systems, multipath propagation causes the received electric field to undergo severe amplitude fades on the scale of a wavelength, and consequently, a detector smaller than one wavelength would experience multipath fading. However, infrared wireless receivers have detector areas which are typically millions of square wavelengths, and since the total photocurrent generated is proportional to the integral of the optical power over the entire photodetector surface, this

provides an inherent spatial diversity, thus preventing multipath fading [10]. Whilst indoor infrared links are not susceptible to multipath fading, multipath propagation does lead to dispersion, which is modelled as a linear baseband channel impulse response $h(t)$. Linearity follows from the fact that the received signal is comprised of multiple spatial modes [10]. The channel is fixed for a given position of the transmitter, receiver and intervening reflectors, and changes significantly only when any of these are moved by distances in the order of centimetres. Due to the high bit rates under consideration and the relatively slow movement of people and objects within a room, the channel will vary significantly only on the time scale of many bit periods, and therefore may be considered to be time invariant.

Infrared wireless transceivers will usually operate in environments containing an intense amount of ambient light, emanating from both natural (solar) and artificial sources. The average combined power of this background radiation generates a DC photocurrent I_B in the photodetector, giving rise to shot noise $n(t)$, which has a single-sided power spectral density N_o , given as [17]:

$$N_o = 2qI_B, \quad (2.1)$$

where q is the electron charge. Even when optical filtering is used to reject out of band light sources, the received signal power is much lower than the power from ambient light sources (typically 25 dB lower [10]). Consequently, I_B is much larger than the maximum photocurrent generated by the signal, and hence, the shot noise may be regarded as white, Gaussian and independent of the received signal [18]. In the presence of intense ambient light, which is usually the case, shot noise is the dominant noise source in a typical diffuse receiver [10]. Note that, if little or no ambient light is present, the dominant noise source is receiver preamplifier noise, which is also signal independent and Gaussian [12]. In addition to contributing to the generation of shot noise, artificial ambient light sources also generate a periodic interference signal, which must be added to $n(t)$. Ambient light sources are discussed in more detail in section 2.5.

The equivalent baseband model of an optical wireless link, as illustrated in Fig. 2.1, can be summarised by [12]:

$$y(t) = Rx(t) \otimes h(t) + n(t), \quad (2.2)$$

where R is the photodetector responsivity and the symbol “ \otimes ” denotes convolution. Simply stated, the received photocurrent $y(t)$ is the convolution of the transmitted optical power $x(t)$ with the channel impulse response $h(t)$, scaled by the photodetector responsivity R , plus an additive noise $n(t)$. Whilst (2.2) is simply a linear filter channel with additive noise, optical wireless systems differ from conventional electrical or radio systems since $x(t)$ represents power rather than amplitude. This places two constraints on the transmitted signal. Firstly, $x(t)$ must be non-negative, i.e.

$$x(t) \geq 0. \quad (2.3)$$

Secondly, eye safety requirements limit the maximum optical transmit power which may be employed. Generally, it is the average power requirement which is the most restrictive and hence, the average value of $x(t)$ must not exceed a specified value P_{\max} , i.e. [10]:

$$P_{\max} \geq \lim_{T \rightarrow \infty} \frac{1}{2T} \int_{-T}^T x(t) dt. \quad (2.4)$$

This is in contrast to the time averaged value of $|x(t)|^2$, which is the case on conventional channels when $x(t)$ represents amplitude.

These differences have a profound effect on system design. On conventional channels, the signal to noise ratio (SNR) is proportional to the average received power, whereas on optical wireless links, it is proportional to the square of the average received optical signal power; thus

implying that relatively high optical transmit powers are required, and only a limited path loss can be tolerated. The fact that the average optical transmit power is limited, suggests that modulation techniques possessing a high peak-to-mean power ratio are favourable. This is generally achieved by trading off power efficiency against bandwidth efficiency. When shot noise is dominant, the SNR is also proportional to the photodetector area. Thus, single element receivers favour the use of large area detectors. However, as the detector area increases so does its capacitance, which has a limiting effect on receiver bandwidth. This is in direct conflict with the increased bandwidth requirement associated with power efficient modulation techniques, and hence, a trade off exists between these two factors.

2.3 Link Configuration

Indoor optical wireless links may be configured in a variety of ways to support a multitude of applications. Street et. al. [19] grouped these into four generic system configurations, these being: directed LOS, nondirected LOS, diffuse and tracked, as illustrated in Fig. 2.2.

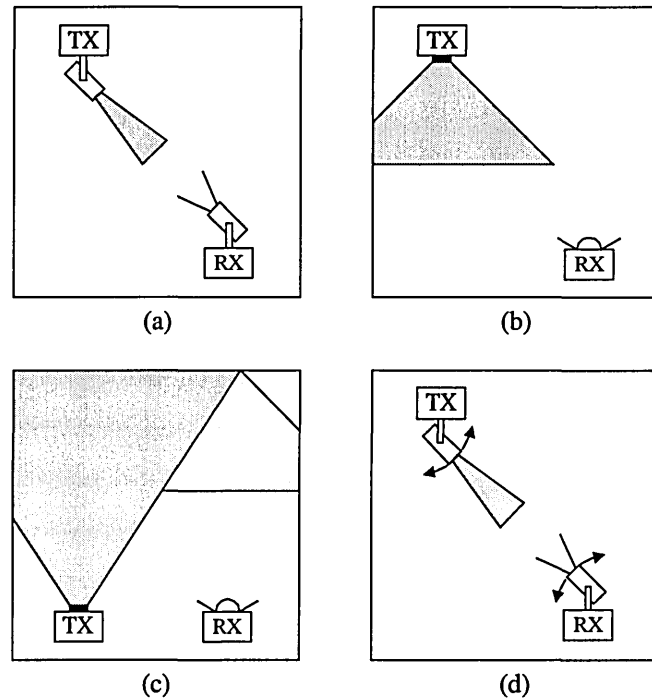


Fig. 2.2: Link configurations: (a) directed LOS, (b) nondirected LOS, (c) diffuse, and (d) tracked

The directed LOS configuration, illustrated in Fig. 2.2(a), achieves a high power efficiency by utilising narrow beam transmitters and narrow field of view (FOV) receivers. The use of narrow FOV receivers allows optical concentrators to be employed along with thin film optical filters, since the angular dependence of the filter response does not pose a problem. Furthermore, directed LOS systems do not suffer from multipath propagation, and ambient background light is largely rejected. Thus, the potential data rate is limited only by the available power budget rather than multipath dispersion [20]. However, directed LOS links must be pointed prior to use, and require an uninterrupted line of sight path between the transmitter and receiver, thus making them susceptible to blocking. In addition to this, by their very nature, they are more suited to point-to-point links rather than point-to-multipoint broadcast type links, thus reducing their flexibility. Directed LOS is the most well known link topology, and has been used for many years in low bit rate, simplex remote control applications for domestic electrical equipment, such as televisions and audio equipment. Additionally, directed LOS is the chosen configuration for IrDA links [11]. A number of experimental links using the directed LOS configuration have been reported [21-23], along with a demonstration of an IEEE 1394 multimedia home network [24].

The nondirected LOS configuration, illustrated in Fig. 2.2(b), uses wide beam transmitters and wide FOV receivers to achieve an increased coverage area and alleviate the need for pointing. Compared with the directed LOS configuration, these benefits are achieved at the expense of a reduced irradiance, for a given range and transmit power. The use of wide angle transmitters and receivers means that a portion of the received signal may have undergone one or more reflections from walls and room objects, thus giving rise to multipath propagation. Additionally, since the majority of power incident on the photodetector is due to the LOS path, nondirected LOS links are still prone to blocking. Nondirected LOS links are well suited to point-to-multipoint broadcast type applications. A typical scenario for this link topology would be an infrared access point located on the ceiling of a room, providing connectivity to the portable devices within its coverage area. Computer generated holograms have been proposed as a means

of accurately defining the coverage area of nondirected LOS links [25]. By controlling the coverage area, large rooms may be divided into ‘optical cells’, each serviced by a different infrared access port. Such an architecture has been used in experimental systems [26, 27] and proposed for a number of practical applications including telepoints [28], trading desks [29] and desk area networks [30]. An example of a commercial nondirected LOS system is VIPSLAN-10 manufactured by JVC [31]. The system generates a cell radius of up to 10 m, and offers a data rate of 10 Mbit/s, which is shared between the users operating within the cell.

The diffuse configuration, illustrated in Fig. 2.2(c), was first proposed in 1978 by Gfeller and Bapst [8, 9]. Typically, a diffuse transmitter points vertically upwards towards the ceiling, emitting a wide beam of infrared energy. The receiver has a wide FOV, and collects the signal after it has undergone one or more reflections from the ceiling, walls and room objects. Measurements to determine the reflection coefficient for a variety of materials commonly used in indoor environments were carried out by Gfeller and Bapst [9]. Reflection coefficients were found to range from 0.4 to 0.9, with white plaster walls varying between 0.7 and 0.85 depending on surface texture and angle of incidence. From a users point of view, the diffuse link topology is the most convenient since it does not require any pointing of the transmitter or receiver, nor does it require a LOS path to be maintained. In addition to this, the configuration is also extremely flexible, and can be used for both infrastructure and ad hoc networks [19]. However, along with nondirected LOS links, diffuse links incur a high optical path loss, which is typically 50 - 70 dB for a horizontal separation distance of up to 5 m [32]. The path loss is increased further if a person is standing next to the receiver such that the main signal path is obstructed, a situation referred to as shadowing. In addition to this, diffuse links must also contend with severe multipath propagation. Intersymbol interference limits the maximum unequalized bit rate to ~260 Mbit/s [9]. Thus, for a coverage volume of 10 x 10 x 3 m, the unequalized bit rate would be limited to ~16 Mbit/s [25]. Nevertheless, to date, the diffuse configuration has received the greatest interest from the research community, and a number of experimental diffuse links have been reported covering bit rates up to 50 Mbit/s [33-41]. Diffuse is also the chosen link configuration for the IEEE 802.11 infrared physical layer standard [2], and diffuse

systems are now commercially available. An example of a commercial diffuse system is the wireless network manufactured by Spectrix Corporation [42]. The system is specified to work over a coverage area of 1000 square feet, and achieves a data rate of 4 Mbit/s, which is shared between all the users within the cell.

For nondirected LOS and diffuse links, rather than using a single element detector, significant performance improvements can be achieved using an angle-diversity receiver, which may be implemented in one of two ways. A non-imaging angle-diversity implementation consists of multiple receiving elements that are oriented in different directions, each element having its own nonimaging concentrator. The main drawback of this approach is that it can lead to an excessively bulky and costly receiver. A more elegant implementation is the imaging angle-diversity receiver, the so called ‘fly-eye receiver’ first proposed by Yun and Kavehrad [43], which consists of an imaging optical concentrator (e.g. a lens) with a segmented photodetector array placed at its focal plane. Regardless of the implementation method, the photocurrent generated by each element is amplified separately and may then be processed in a variety of ways, which vary in terms of performance and complexity. Angle-diversity receivers can simultaneously achieve a high optical gain and a wide field of view. By exploiting the fact that unwanted signals are generally received from different directions to that of the desired signal, they can significantly reduce the effects of ambient light noise, co-channel interference and multipath distortion [44]. The performance gains achieved by angle-diversity receivers have been analysed in [45-51]. A further improvement in the power efficiency of diffuse links can be achieved by replacing the single wide-beam diffuse transmitter with a multi-beam transmitter, sometimes referred to as a quasi-diffuse transmitter, which consists of multiple narrow beams pointing in different directions [43]. The performance of diffuse links using multi-beam transmitters and angle-diversity receivers is presented in [43, 44, 52-56]. Details of an experimental 70 Mbit/s link using a multi-beam transmitter and an angle-diversity receiver are given in [54].

The final configuration is the tracked system, illustrated in Fig. 2.2(d), which offers the high power efficiency and potentially high bit rates of directed LOS links, with the increased coverage enjoyed by nondirected LOS systems. In an early experimental tracked system developed by B.T. Labs, which achieved a bit rate of 1 Gbit/s, the tracking was performed using mechanical steerable optics [57]. However, mechanical steerable optics are prohibitively expensive and difficult to miniaturise. Consequently, in the same paper, Wisely et. al. proposed a solid state tracked system, using multi-element transmitter and receiver arrays along with a lens arrangement. Using this arrangement, steering is merely a matter of selecting the appropriate array element. Conceptually, this is similar to the angle-diversity receiver discussed earlier. Solid state tracked systems are analysed in [58, 59], and experimental systems achieving data rates of 34 Mbit/s [60], 100 Mbit/s [61] and 155Mbit/s [13, 14] have been demonstrated. Note that, along with diffuse links using multi-beam transmitters and angle-diversity receivers, tracked systems offer the potential to implement space-division multiplexing, whereby multiple users can communicate without suffering a loss of per-user capacity, since each user is located in a different cell.

2.4 Review of Channel Characterisation

Detailed characterisation of the indoor optical wireless channel is essential for effective link design. The power penalties directly associated with the channel may be separated into two factors, these being optical path loss and multipath dispersion [62, 63]. For directed LOS and tracked configurations, reflections do not need to be taken into consideration, and consequently the path loss is easily calculated from knowledge of the transmitter beam divergence, receiver size and separation distance. For nondirected LOS and diffuse links, the optical path loss is more complex to predict, since it is dependent on a multitude of factors, such as room dimensions, the reflectivity of the ceiling, walls and objects within the room, and the position and orientation of the transmitter and receiver, to name but a few. In order to predict the path

loss for nondirected LOS and diffuse links, it is necessary to analyse the distribution of optical power for a given setup.

Gfeller and Bapst [8] studied the power distribution for diffuse links, basing their model on single reflections only. The authors showed that by using an optical source consisting of multiple elements oriented in different directions, a more uniform coverage can be obtained over a larger area, compared with a single wide-beam optical source. Lomba et. al. [64] addressed the optimization of the optical power distribution for diffuse and nondirected LOS links. Based on this work, the authors proposed a specification for the emitter radiation pattern (ERP) of the IEEE 802.11 infrared physical layer standard [2, 65]. Pakravan and Kavehrad [66] also analysed the optical power distribution for a typical conference room using various link configurations. For nondirected LOS links, as an alternative to adjusting the ERP, several researches have considered using a grid of ceiling mounted transmitters [67-69] in order to reduce the dynamic range of signal power.

Whilst determining the distribution of optical power throughout a room is adequate for basic power budget calculations, it does not allow the power penalty due to multipath propagation to be accurately predicted, since multiple reflections are not taken into consideration. Although the optical power associated with two or more reflections is relatively small, the signal arrives at the receiver much later than that undergoing only one reflection, and hence, cannot be ignored when considering high speed nondirected LOS and diffuse links. In order to generate an impulse response which includes higher order reflections, Barry et. al. [70, 71] developed a ray tracing algorithm in which the path loss and time delay for every path containing a given number of reflections are calculated. The algorithm then sums together all contributions to give an overall impulse response. The authors considered empty rectangular rooms and assumed the optical receiver was pointing vertically toward the ceiling. Abtahi et. al. [72] modified this work to consider the effects of furniture and people within the room, and also rooms of irregular shape. Pakravan [66] used a neural network to speed up the algorithm developed by Barry, whereby only a fraction of the total number of points need to be calculated, from which the neural

network learns the rest. Lomba et. al. [73] developed a computationally efficient ray tracing algorithm which uses look up tables and progressively decreased resolution to speed up the simulation. Hernandez et. al. also developed a computationally efficient algorithm based on Monte Carlo analysis [74, 75]. A different approach was taken by Carruthers and Kahn [62, 63], who developed the ceiling bounce model based on the claim that realistic multipath infrared channels can be characterised by only two parameters, these being optical path loss and root mean square (RMS) delay spread. The authors adopt a two stage modelling approach: first assuming an infinitely large room, i.e. considering only a single reflection from the ceiling, and then making a correction which takes into account the position of the transmitter and receiver within the room.

Practical channel characterisation was carried out by Kahn et al. [32], who measured channel frequency responses over the range 2-300 MHz using a swept frequency technique. From these measurements the authors computed impulse responses, path losses and RMS delay spreads. Both line of sight and diffuse link configurations were considered, using different receiver locations in 5 different rooms, giving a total of ~100 different channels. Hashemi et. al. [76], measured 8 rooms at various positions and also took measurements for different orientations and rotations of the photodetector, giving a total of 160 frequency response profiles. The authors show that the channel response is not only sensitive to the position of the photodetector, but also its orientation and rotation. Based on this knowledge, the authors proposed the angle-diversity receiver structure described in section 2.3.

2.5 Optical Component Selection

From a commercial point of view, the wavelength band between 780 and 950 nm is currently the best choice for most infrared applications due to the availability of low cost light-emitting diodes (LEDs) and laser diodes (LDs), and because it coincides with the peak responsivity of inexpensive silicon photodetectors [12]. However, electromagnetic radiation in this band can

cause damage to the human eye, and is therefore subject to eye safety regulations. The latest version of the most widely adopted standard on laser safety is IEC 825-1 (1993), published by the International Electrotechnical Commission [77]. In European member countries, this standard has been adopted as EN 60825-1 (1993) [78]. The standard contains a number of classifications, the lowest power of which is Class 1, implying that a device is safe under all foreseeable circumstances of use. Class 1 products require no warning labels, and only need to declare the classification in the product literature. The classification limits are dependent on a number of parameters, these being wavelength, apparent source size, pulse duty factor and exposure duration. The standard treats LD and LED sources equally, the only difference being that LDs are generally categorised as point sources, which can be focussed to a small area on the retina, whilst LEDs usually fall under the extended source category, and form a larger image on the retina. Note that products compliant with or merely interoperable under IrDA specifications must be classified as eye safe [79]. In contrast, compliance with the IEEE 802.11 standard does not ensure conformance with eye safety standards [25].

From a power budget point of view, the wavelength band around $1.5\text{ }\mu\text{m}$ would be a much better choice, since the safety standard permits larger optical transmit powers to be used, and as shown in Fig. 2.3, ambient light sources emit less power at these wavelengths. However, the major drawback to operating at such wavelengths is the lack of low cost optoelectronic devices available at present.

The choice of optical source is largely dependent on cost and performance. LEDs benefit from low cost and simple drive circuitry, but suffer from poor electrical-to-optical conversion efficiency, limited bandwidth and broad spectral width (typically 40 nm), which prevents the use of narrow-band optical filtering at the receiver. Consequently, LEDs are generally used in low speed, cost sensitive applications such as IrDA serial ports. In contrast, laser diodes are more expensive than LEDs and require more complicated drive circuitry, but offer a number of advantages such as improved conversion efficiency, wide modulation bandwidth and narrow spectral width, thus making them the obvious choice for high speed links. In terms of eye safety,

LEDs are generally supplied in a lensed package and do not require any additional components to make them eye safe. Laser diodes, on the other hand, are essentially point source devices and must be diffused in some way in order to be classified as eye safe. There are a number of methods of achieving this, including the use of computer generated holograms [80, 81] and integrating sphere diffusers [82, 83].

There are two options for the photodetector, these being the positive-intrinsic-negative (PIN) photodiode and the avalanche photodiode (APD). APDs use the avalanche effect to achieve low noise gain, and are well suited to applications where the background radiation is negligible. However, in optical wireless systems where shot noise due to intense ambient light is generally the dominant noise source, the gain of an APD is actually detrimental to performance. Consequently, PIN photodiodes are generally used in optical wireless receivers. Throughout the remainder of this thesis, it is assumed that a PIN photodiode is used.

Optical wireless receivers generally employ some form of optical concentrator in order to increase the effective area of the detector. High gains can be achieved using compound parabolic concentrators, but these devices have a narrow FOV and are therefore limited to use in directed links. Nondirected links generally make use of a hemispherical lens, which achieves a wide FOV and an omnidirectional gain. Optical filtering is also generally used to attenuate the out of band background radiation. Two basic types of optical filter exist, these being long pass and band pass filters. Long pass filters are generally constructed of coloured glass, and pass all wavelengths longer than a specified cut-on wavelength. In conjunction with a silicon PIN photodiode, which typically have a sensitivity range from 400 nm to 1.1 μm , high pass optical filters result in a bandpass response with a spectral width in the order of several hundred nm. In contrast, band pass filters, also referred to as interference filters, are constructed of multiple layers, and can achieve extremely narrow bandwidths. Such filters can be extremely effective when used in conjunction with laser diode sources. However, one of the characteristics of band pass optical filters is that the pass band shifts as the angle of incidence changes. This can therefore result in a narrowing of the FOV, which may be unacceptable in nondirected links. In

the experimental systems developed by Kahn et. al., the authors alleviated this problem by bonding the band pass filter to the curved surface of a hemispherical lens [34-36, 41].

2.6 Ambient Light Sources

Artificial sources of ambient light introduce a periodic interference signal in optical wireless receivers which, if ignored, has the potential to degrade link performance. Consequently, knowledge of ambient light sources, both in terms of their optical power spectra and detected electrical spectra, is necessary in order to develop effective methods of mitigating the interference they produce. Moreira et. al carried out extensive measurements of a variety of ambient light sources, and from these measurements, produced a model to describe the interference signal [84, 85]. Boucouvalas also carried out similar measurements, which included a number of consumer products which use infrared transmission [86]. Along with experimental characterisation of ambient light sources, a significant amount of work has been done on analysing the effect of ambient light interference on link performance [15-17, 87-92]. This is subject is covered in detail in chapter 5.

The three main sources of ambient light are sunlight, incandescent lamps and fluorescent lamps. The optical power spectra of these sources are shown in Fig. 2.3 [12]. Note that the spectra have been scaled to have equal maximum value, and the longer wavelength region of the fluorescent lamp spectrum has been amplified by a factor of 10 in order to make it clearly visible. When present, direct sunlight is typically much stronger than the other two sources, and represents an unmodulated source of ambient light with a very wide spectral width and a maximum power spectral density located at ~500 nm.

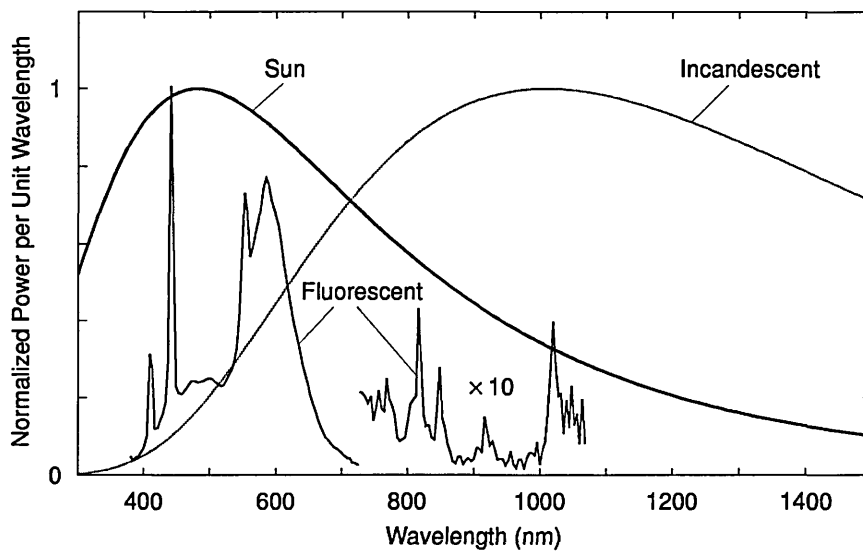


Fig. 2.3: Optical power spectra of common ambient light sources [12]

All artificial ambient light sources are modulated, either by the mains frequency or, in the case of some fluorescent lamps, by a high frequency switching signal. Measurements have been carried out to determine the time-domain waveforms and detected electrical spectra for the ambient light sources listed in Table 2.1. Note that it is these sources which are used when evaluating the link performance of the experimental system described in chapter 7.

Source	Details
Incandescent lamp	Bulb: Osram 60W
Low frequency fluorescent lamp	Ballast: Crompton C237 1 × 75W Tube: Osram L 70W/23
High frequency fluorescent lamp	Ballast: Thorn G81016.4 1 × 70W or 1 × 75W (specified frequency = 35 kHz) Tube: Osram L 70W/23

Table 2.1: Artificial ambient light sources

The measurements were taken using a Thorlabs PDA55 amplified silicon detector, with a transimpedance of 15 k Ω and a 3 dB bandwidth ranging from 25 Hz to 7.9 MHz. For each measurement, the distance between the source and the detector was set such that the average received photocurrent was 100 μ A. For the fluorescent lamps, all measurements were taken at the centre of the tube. Additionally, the effects of an RG780 optical long-pass filter were also

investigated. The filter passes all wavelengths longer than 780 nm and when combined with the spectral response of the PDA55, results in an optical bandpass response ranging from 780 nm to $\sim 1.1 \mu\text{m}$.

2.6.1 Incandescent lamp

Incandescent lamps have a maximum power spectral density around $1 \mu\text{m}$, and produce an interference signal which is a near perfect sinusoid with a frequency of 100 Hz. The slow response time of the filament means few harmonics are present. Fig. 2.4. shows the time domain waveform and detected electrical spectrum for the incandescent bulb listed in Table 2.1. No optical filtering was used.

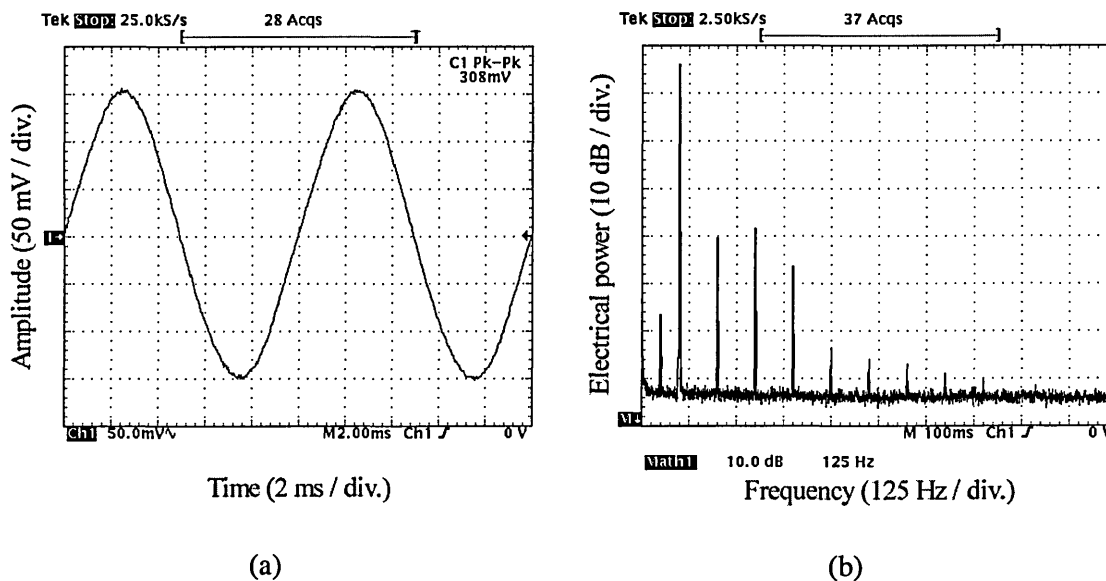


Fig. 2.4: Incandescent bulb: (a) time domain waveform, and (b) detected electrical spectrum

Only harmonics up to 400 Hz carry a significant amount of power, and beyond that, all harmonics are more than 60 dB below the fundamental. The average received photocurrent I_B and peak-to-peak interference signal photocurrent I_{pk-pk} are given in Table 2.2, with and without optical filtering.

	Without optical filter	With optical filter	Reduction
I_B	100 μA	20.5 μA	79.5 %
I_{pk-pk}	65.2 μA	12 μA	81.6 %
I_B/I_{pk-pk}	1.53	1.71	

Table 2.2: I_B and I_{pk-pk} for incandescent bulb with and without optical filtering

When optical filtering is used, I_B is reduced by 79.5 %, and the peak-to-peak amplitude of the interference signal is reduced by 81.6 %. The ratio of I_B/I_{pk-pk} is fairly similar both with and without optical filtering.

2.6.2 Fluorescent lamp driven by conventional ballast

Low frequency fluorescent lamps are driven by the mains frequency. The interference signal is a distorted 100 Hz sinusoid, and the electrical spectrum contains harmonics into the tens of kHz. Figure 2.5 shows the time domain waveform and detected electrical spectrum for the low-frequency fluorescent lamp listed in Table 2.1. No optical filtering was used.

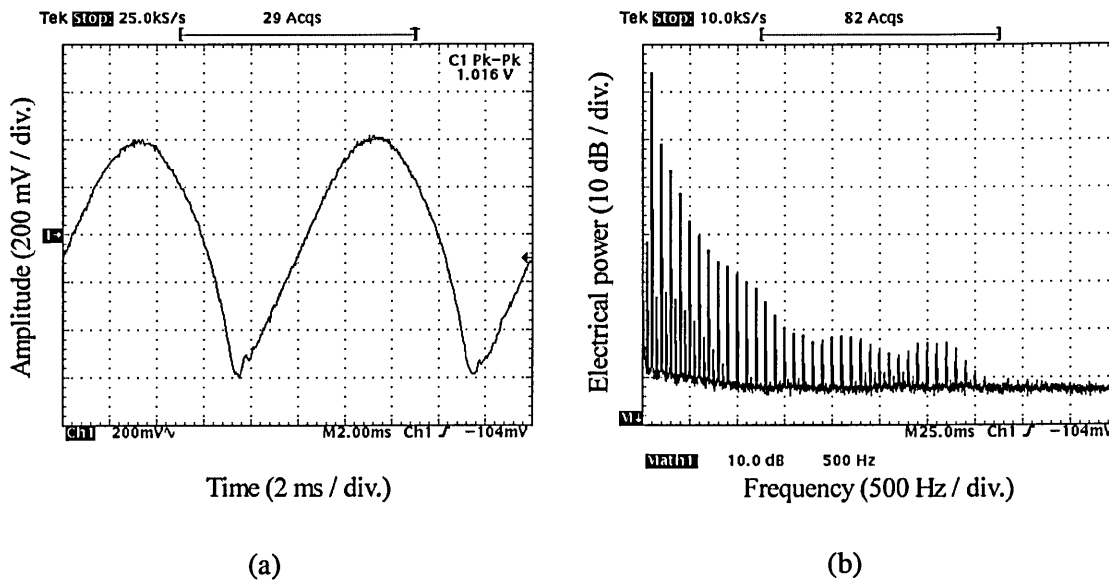


Fig. 2.5: Low-frequency fluorescent lamp:

(a) time domain waveform, and (b) detected electrical spectrum

The average received photocurrent and peak-to-peak interference signal photocurrent, with and without optical filtering, are given in Table 2.3.

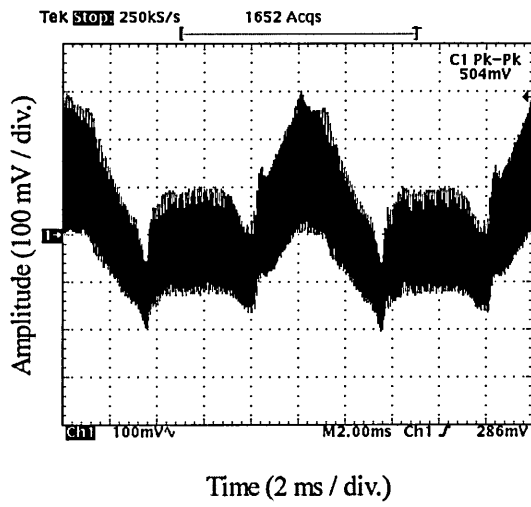
	Without optical filter	With optical filter	Reduction
I_B	100 μA	5.4 μA	94.6 %
I_{pk-pk}	67.7 μA	9.6 μA	85.8 %
I_B/I_{pk-pk}	1.48	0.56	

Table 2.3: I_B and I_{pk-pk} for low-frequency fluorescent lamp with and without optical filtering

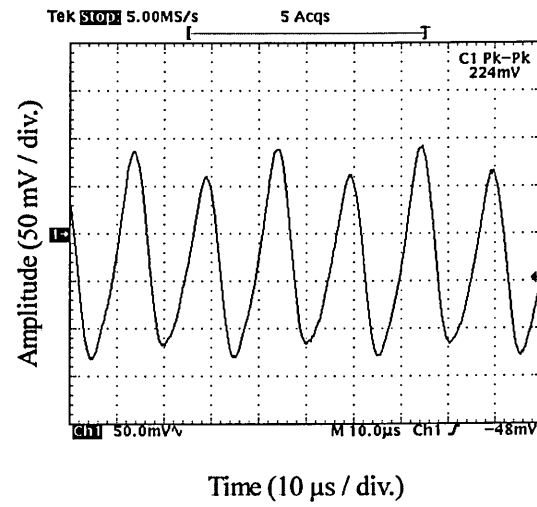
Optical filtering gives a significant reduction in both the average background photocurrent and the peak-to-peak interference amplitude. Since the reduction in I_B is greater than the reduction in I_{pk-pk} , with the optical filter in place, the peak-to-peak variation of the photocurrent is actually greater than the average background photocurrent.

2.6.3 Fluorescent lamp driven by electronic ballast

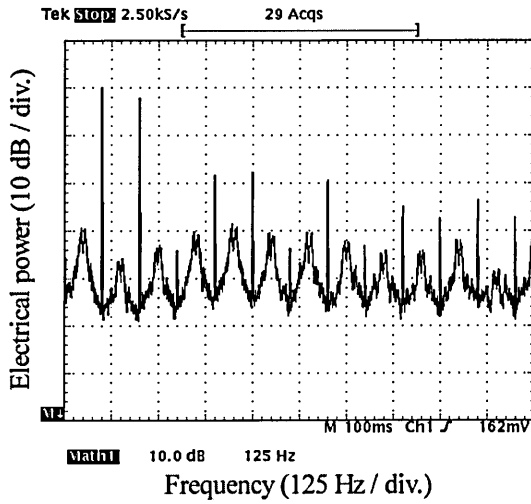
In recent years, fluorescent lamps have been introduced which are driven by high frequency electronic ballasts. This type of lamp has a number of advantages over its low frequency counterpart, such as a reduced electrical power consumption for a given level of illumination and increased life-expectancy of the tubes. The actual switching frequency used varies from one manufacturer to another, but is typically in the range 20 - 40 kHz. The detected electrical spectrum contains harmonics of the switching frequency and also harmonics of the mains frequency, similar to low frequency fluorescent lamps. Harmonics of the switching frequency can extend into the MHz range, and therefore present a much more serious impairment to optical wireless receivers [15]. Figure 2.6 shows the time-domain waveform and detected electrical spectrum for the high frequency fluorescent lamp listed in Table 2.1.



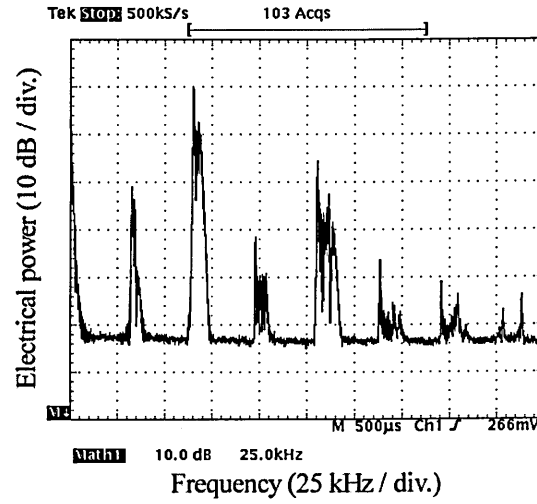
(a)



(b)



(c)



(d)

Fig. 2.6: HF fluorescent lamp:

time domain waveform: (a) low frequency component, (b) high frequency component and
detected electrical spectrum: (c) low frequency component, (d) high frequency component

The average received photocurrent and peak-to-peak interference signal photocurrent, with and without optical filtering, are given in Table 2.4.

	Without optical filter	With optical filter	Reduction
I_B	100 μ A	3.9 μ A	96.1 %
I_{pk-pk}	33.6 μ A	4.9 μ A	85.4 %
I_B/I_{pk-pk}	2.98	0.80	

Table 2.4: I_B and I_{pk-pk} for high-frequency fluorescent lamp with and without optical filtering

Without optical filtering, for a given background photocurrent, the interference amplitude produced by the high frequency fluorescent lamp is only about half that produced by the low frequency fluorescent lamp. Optical filtering gives a similar reduction in I_B and I_{pk-pk} as it did for the low frequency fluorescent lamp.

2.7 Summary

There are a variety of ways in which indoor optical wireless links may be configured, each offering suitability for different applications. In terms of system design, the limitations directly imposed by the channel, such as path loss and dispersion, are largely dependent on the chosen link configuration. For example, directed links have a small path loss and do not suffer from multipath propagation. However, in order to achieve a degree of mobility, it is necessary to use a tracked configuration, which greatly increases the cost and complexity of the system. In contrast, nondirected links offer some mobility without increasing system complexity, but must overcome high path loss and multipath propagation.

When deployed in a typical indoor environment, optical wireless links are required to operate in the presence of intense ambient light. Along with contributing to the generation of shot noise, artificial sources of ambient light also introduce a periodic interference signal in optical wireless receivers. Of all the artificial ambient light sources, fluorescent lamps driven by electronic ballasts are potentially the most detrimental to system performance, since their detected electrical spectrum can contain harmonics into the MHz region. The extent to which ambient light sources affect link performance is also dependent, to a degree, on the chosen link configuration. Due to the directional nature of their transmitters and receivers, directed links can reject much of the background radiation, whilst nondirected links are more susceptible.

Irrespective of the chosen link configuration, the indoor optical wireless channel is unique, combining the filtered Gaussian noise characteristics of conventional wire based channels with the IM/DD constraints of fibre-optic systems [10]. From a system design point of view, the diffuse configuration suffers the most severe channel parameters and consequently presents the greatest challenge to achieving robust, high speed communication. The remainder of this thesis focuses solely on the diffuse channel.

Chapter 3

Review of Modulation Techniques

3.1 Introduction

Selecting a modulation technique is one of the key technical decisions in the design of any communication system. Before selection can take place, it is necessary to define the criteria on which the various modulation techniques are to be assessed. For the indoor optical wireless channel, these criteria are listed below in order of decreasing importance.

(i) *Power Efficiency*: In order to comply with eye safety regulations, the average optical power emitted by an optical wireless transceiver is limited, as expressed in (2.4). Furthermore, in portable battery powered equipment it is desirable to keep the electrical power consumption to a minimum, which also places limitations on the optical transmit power. Consequently, the most important criterion when evaluating modulation techniques suitable for indoor optical wireless communication systems is power efficiency. Thus, different schemes are usually compared in terms of the average optical power required to achieve a desired bit error rate (BER) at a given data rate.

(ii) *Bandwidth Efficiency*: When shot noise is dominant, the received SNR is proportional to the photodetector area. Consequently, single element receivers favour the use of large area photodetectors. However, the high capacitance associated with large area photodetectors has a limiting effect on receiver bandwidth. In addition to this, for nondirected LOS and diffuse link configurations, the channel bandwidth is limited by multipath propagation. Therefore, it follows that modulation schemes which have a high bandwidth requirement are more susceptible to intersymbol interference, and consequently incur a greater power penalty. Thus, the second most important criterion when evaluating modulation techniques is bandwidth efficiency.

(iii) *Other Considerations*: Optical wireless transceivers intended for mass-market applications are likely to have tight cost constraints imposed upon them. Consequently, it is desirable that the chosen modulation technique is simple to implement. Achieving excellent power efficiency and/or bandwidth efficiency is of little use if the scheme is so complex to implement that cost renders it unfeasible. Another consideration when evaluating modulation techniques is the ability to reject the interference emanating from artificial sources of ambient light. As discussed in chapter 5, the simplest method to achieve this for baseband schemes is to use electrical high-pass filtering. Consequently, it is desirable that the chosen modulation technique does not have a significant amount of its power located at DC and low frequencies, thereby reducing the effect of baseline wander and thus permitting the use of higher cut-on frequencies. In addition to this, if the chosen modulation technique is required to operate at medium to high data rates over non directed LOS or diffuse links, then multipath dispersion becomes an issue. Consequently, it is also desirable that the scheme be resistant to ISI resulting from multipath propagation.

For the IM/DD indoor optical wireless channel discussed in chapter 2, candidate modulation techniques can be grouped into two general categories, these being baseband and subcarrier schemes. Note that throughout this thesis, the information source is assumed to be digital, and consequently, consideration is limited to digital modulation techniques.

Baseband modulation techniques are so-called because the spectrum of the modulated data is in the vicinity of DC. Baseband schemes include, amongst others, OOK and the family of pulse time modulation techniques. OOK is the simplest technique, in which the intensity of an optical source is directly modulated by the information sequence. In contrast, pulse time modulation techniques use the information sequence to vary some time-dependent property of a pulse train. Popular examples of such schemes include pulse width modulation (PWM), in which the width of the pulses convey the information, and PPM, in which the information is represented by the position of the pulses within fixed time frames [93-95]. The modulated pulse train is then used to intensity modulate an optical source.

Subcarrier modulation techniques operate by varying the amplitude, phase, or frequency (or combinations of these) of a sinusoidal subcarrier, in accordance with the information sequence being transmitted [96]. The modulated subcarrier is then used to intensity modulate an optical source. Since the subcarrier has both positive and negative values, a DC offset must be added in order to satisfy the requirement that $x(t)$ cannot be negative, as expressed in (2.3). Consequently, subcarrier modulation schemes are less power efficient than pulse modulation techniques. As an example, on nondistorting channels with IM/DD and AWGN, binary phase-shift keying (BPSK) and quadrature phase-shift keying (QPSK) both require 1.5 dB more optical power than OOK [10]. Along with single-subcarrier schemes, multiple-subcarrier modulation techniques also exist, allowing multiple users to communicate simultaneously using frequency division multiplexing [97]. As illustrated in the block diagram of Fig. 3.1, each user modulates data onto a different subcarrier frequency, and the frequency division multiplexed sum of all the modulated subcarriers is then used to intensity modulate an optical source. At the receiver, multiple bandpass demodulators are used to recover the individual data streams.

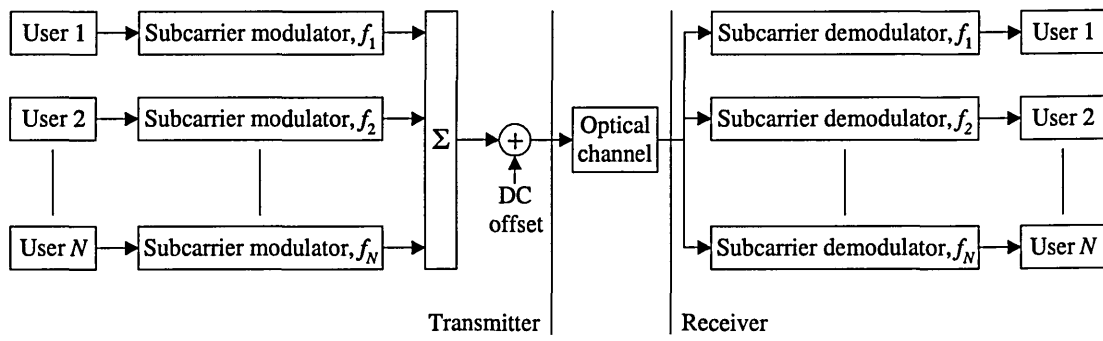


Fig. 3.1: Basic implementation of multiple-subcarrier modulation

Through simultaneous transmission of several narrowband subcarriers, multiple-subcarrier modulation techniques can achieve high aggregate bit rates and improved bandwidth efficiency [12]. However, multiple-subcarrier techniques are less power efficient than single-subcarrier schemes, and the power efficiency worsens as the number of subcarriers is increased. One of the reasons for this reduction in power efficiency is the fact that increasing the number of subcarriers also increases the DC offset required to avoid clipping. By allowing clipping to occur, the power efficiency can be improved slightly, despite the fact that this induces nonlinear distortion [97]. Taking quadrature amplitude modulation (QAM) as an example, for a given number of subcarriers, clipped 4-QAM (with zero DC offset) requires 0.46 dB less average optical power than 4-QAM with a DC offset applied [97]. Nevertheless, due to their poor power efficiency, subcarrier modulation techniques are not considered any further in this thesis.

The remainder of this chapter focuses on OOK and PPM, which are studied in detail in sections 3.2 and 3.3, respectively. For each technique, the code properties, spectral properties and error performance are reviewed. In the case of PPM, coding schemes and variants of the technique which have also been considered for use in indoor optical wireless communication systems are discussed. Finally, the chapter is summarised in section 3.4.

3.2 On-Off Keying

3.2.1 Code properties

Of all the modulation techniques suitable for IM/DD, OOK is the simplest to implement. In OOK, a one is represented by transmitting a pulse of constant power for a duration of up to one bit and a zero is represented by not transmitting anything during the bit duration. OOK can use either non-return-to-zero (NRZ) or return-to-zero (RZ) signalling. OOK-NRZ employs pulses which span the whole bit duration T_b , whilst OOK-RZ uses pulses with a duration less than T_b . Assuming an average optical power P_{avg} , the transmitted waveforms for OOK using NRZ pulses and RZ pulses with a pulse duty cycle γ of 0.5 are shown in Figs. 3.2(a) and (b), respectively.

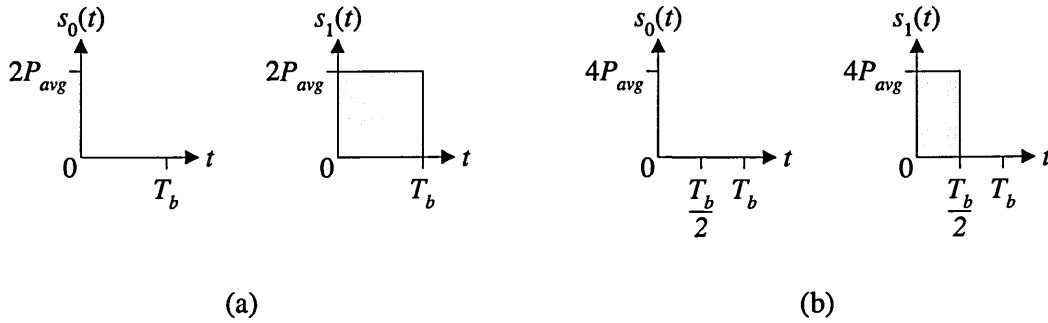


Fig. 3.2: Transmitted waveforms for OOK: (a) NRZ, and (b) RZ ($\gamma = 0.5$)

The simplicity of OOK has led to its use in commercial optical wireless systems such as IrDA links operating below 4 Mbit/s [11]. In these links, return-to-zero-inverted (RZI) signalling is used, in which a pulse represents a zero rather than a one. At bit rates up to and including 115.2 kbit/s, the pulse duration is nominally 3/16 of the bit duration. For data rates of 0.576 Mbit/s and 1.152 Mbit/s, the pulse duration is nominally 1/4 of the bit duration.

3.2.2 Power spectral density

For the OOK-NRZ waveforms shown in Fig. 3.2(a), assuming ones and zeros are equally likely, the electrical power spectral density (PSD) is given by [95]:

$$S_{OOK-NRZ}(f) = (P_{avg} R)^2 T_b \left(\frac{\sin \pi f T_b}{\pi f T_b} \right)^2 \left[1 + \frac{1}{T_b} \delta(f) \right], \quad (3.1)$$

where R is the photodetector responsivity and $\delta(\cdot)$ is the Dirac delta function.

Similarly, for the OOK-RZ ($\gamma = 0.5$) waveforms shown in Fig. 3.2(b), the PSD is given by [95]:

$$S_{OOK-RZ(\gamma=0.5)}(f) = (P_{avg} R)^2 T_b \left(\frac{\sin(\pi f T_b / 2)}{\pi f T_b / 2} \right)^2 \left[1 + \frac{1}{T_b} \sum_{n=-\infty}^{\infty} \delta\left(f - \frac{n}{T_b}\right) \right]. \quad (3.2)$$

The PSDs of OOK-NRZ and OOK-RZ ($\gamma = 0.5$) are plotted in Fig. 3.3. The power axis is normalized to the average electrical power multiplied by the bit duration, and the frequency axis is normalized to the bit rate, $R_b (=1/T_b)$. Both curves were plotted using the same average optical power, P_{avg} .

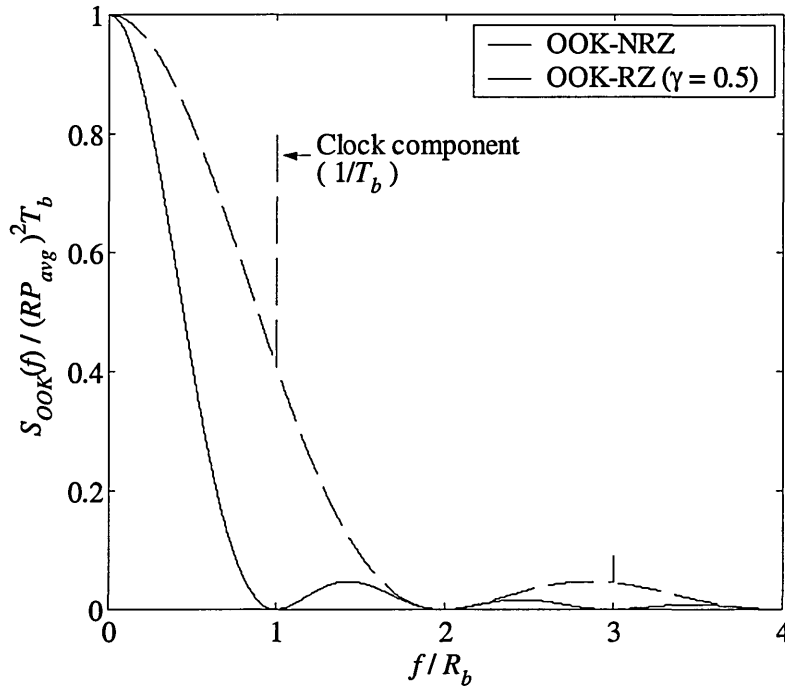


Fig. 3.3: PSD of OOK-NRZ and OOK-RZ ($\gamma = 0.5$)

For baseband modulation techniques, the bandwidth requirement is generally defined as the span from DC to the first null in the PSD of the transmitted signal. As expected, OOK-RZ ($\gamma = 0.5$) has twice the bandwidth requirement of OOK-NRZ, since the pulses are only half as wide. Both OOK-NRZ and OOK-RZ ($\gamma = 0.5$) have discrete (impulse) terms at DC, with a weight P_{avg}^2 . These are not shown in the plot. OOK-RZ ($\gamma = 0.5$) also has discrete terms at odd multiples of the bit rate. The impulse at $f = R_b$ can be used to recover the clock signal at the receiver. OOK-NRZ, on the other hand, has spectral nulls at multiples of the bit rate, and consequently requires the introduction of some non-linearity in order to achieve clock recovery [98]. Both OOK-NRZ and OOK-RZ have a significant power content at DC and low frequencies. As discussed in detail in chapter 5, this characteristic means that electrical high-pass filtering is not effective in reducing the interference produced by artificial sources of ambient light, since high cut-on frequencies cannot be used without introducing significant baseline wander. Comparing the areas under the two curves it is evident that, for a given average optical transmit power, OOK-RZ ($\gamma = 0.5$) has twice the average electrical power of OOK-NRZ.

3.2.3 Error performance on nondistorting channels

In the absence of channel distortion, the ideal maximum likelihood (ML) receiver for OOK in the presence of AWGN consists of a continuous-time filter with an impulse response $r(t)$, which is matched to the transmitted pulse shape $p(t)$, followed by a sampler and threshold detector set midway between expected one and zero levels [12], as illustrated in Fig. 3.4. The output of the matched filter is sampled at the end of each bit period, where the SNR is at its maximum, and a one or zero is assigned to each slot depending on whether the sample is above or below the threshold level.

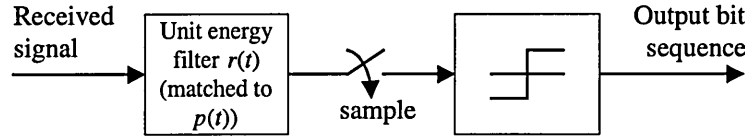


Fig. 3.4: Receiver for baseband OOK

For the OOK-NRZ waveforms shown in Fig. 3.2(a), neglecting any bandwidth limitations imposed by the transmitter or receiver, a unit-energy matched filter has a rectangular impulse response $r(t)$ with amplitude $1/\sqrt{T_b}$ and duration T_b . As illustrated in Fig. 3.5, in the absence of noise, the peak output of this filter when a one is transmitted is $\sqrt{E} = 2RP_{avg}\sqrt{T_b}$, where R is the photodetector responsivity and P_{avg} is the average received optical signal power. When a zero is transmitted, the peak output of the matched filter is 0.

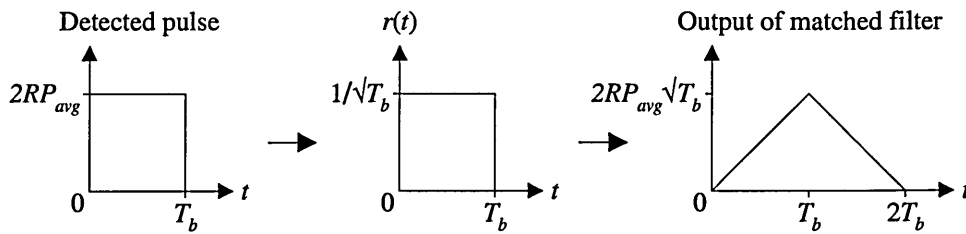


Fig. 3.5: Matched filter output for detected OOK-NRZ pulse

For a matched filter, the variance of the noise samples at the output of the filter is dependent only on the PSD of the noise input and the energy in the impulse response of the matched filter. Thus, if the input is AWGN with double-sided PSD $N_0/2$, the variance of the noise at the output of the matched filter is given by [99]:

$$\sigma_n^2 = \frac{N_0}{2} \int_{t=0}^{T_b} r^2(t) dt. \quad (3.3)$$

Consequently, for a unit-energy matched filter, the variance of the noise samples at the output of the matched filter is $N_0/2$. Assuming independent, identically distributed (IID) binary data, the optimum threshold level α_{opt} , which minimises the probability of error, lies midway between expected one and zero levels. Thus,

$$\alpha_{opt} = RP_{avg} \sqrt{T_b}. \quad (3.4)$$

Therefore, the probability of bit error for OOK-NRZ may be derived from [95] as:

$$P_{e,bit,OOK} = P(one) \cdot Q\left(\frac{2RP_{avg} \sqrt{T_b} - \alpha_{opt}}{\sqrt{N_0/2}}\right) + P(zero) \cdot Q\left(\frac{\alpha_{opt}}{\sqrt{N_0/2}}\right), \quad (3.5)$$

where $P(one)$ and $P(zero)$ represent the probabilities of getting a one and zero, respectively, and $Q(\cdot)$ is Marcum's Q -function, which is the area under the Gaussian tail, given by [93]:

$$Q(x) = \frac{1}{\sqrt{2\pi}} \int_x^{\infty} e^{-\alpha^2/2} d\alpha. \quad (3.6)$$

When the data is IID, $P(one) = P(zero) = 0.5$, and (3.5) reduces to [17]:

$$P_{e,bit,OOK} = Q\left(\frac{RP_{avg}\sqrt{T_b}}{\sqrt{N_0/2}}\right). \quad (3.7)$$

This result may also be expressed in a more conventional form as [95]:

$$P_{e,bit,OOK} = Q\left(\sqrt{\frac{E_b}{N_0}}\right), \quad (3.8)$$

where E_b is the average energy per bit, which for OOK-NRZ is given as:

$$E_b = \frac{E}{2} = 2(RP_{avg})^2 T_b. \quad (3.9)$$

The ratio E_b/N_0 is usually referred to as the signal-to-noise ratio per bit [99].

For OOK-RZ, whilst reducing the pulse duty cycle increases the bandwidth requirement by a factor of $1/\gamma$, it also increases the average energy per bit, which is given as:

$$E_b = 2(RP_{avg})^2 T_b / \gamma. \quad (3.10)$$

Consequently, for a given value of P_{avg} , OOK-RZ ($\gamma = 0.5$) has twice the ratio E_b/N_0 compared with OOK-NRZ. Therefore, in order to achieve the same error performance, OOK-RZ ($\gamma = 0.5$) requires 3 dB less electrical power or 1.5 dB less average optical power compared with OOK-NRZ. However, this improvement in power efficiency is achieved at the expense of doubling the bandwidth requirement. Similarly, setting $\gamma = 0.25$ results in a 3 dB reduction in average optical power requirement compared with OOK-NRZ, but requires four times the bandwidth.

The average optical power requirements and bandwidth requirements of OOK-NRZ and OOK-RZ are plotted in Fig. 4.15, along with those of other modulation techniques. Note that in Fig. 4.15, the average optical power requirement is normalized to that required by OOK-NRZ to send 1 Kbyte packets at an average packet error rate of 10^{-6} , and the bandwidth requirement is normalized to OOK-NRZ. From Fig. 4.15, the reduction in average power requirement as the pulse duty cycle decreases is evident. This is due to the fact that the increased noise associated with the expanded bandwidth is outweighed by the $1/\gamma$ increase in peak optical power [12]. However, it is also evident from Fig. 4.15 that there comes a point where, rather than continuing to reduce the pulse duty cycle in order to improve the power efficiency, it is actually more efficient to switch to an alternative modulation technique, such as PPM or DPIM. To highlight this point, if OOK-RZ ($\gamma = 0.33$) is compared with 8-PPM, it is clear that 8-PPM using hard-decision decoding offers a 1.4 dB reduction in average optical power and actually requires 11 % less bandwidth. Using soft-decision decoding gives an additional 1.5 dB reduction in average optical power requirement.

3.2.4 Review of error performance on multipath channels

On channels which suffer from multipath dispersion, the performance of OOK without equalization is considered in [32, 71]. The authors found that significant power penalties are incurred for bit rates above 10 Mbit/s. The unequalized performance of OOK is also analysed in detail in chapter 6.

From a probability of error point of view, the optimum method of detecting signals in the presence of ISI is maximum-likelihood sequence detection [99]. In 1972, Forney [100] developed a maximum-likelihood sequence detector (MLSD) for a digital pulse amplitude modulated sequence in the presence of ISI and white Gaussian noise. As illustrated in Fig. 3.6, Forney's MLSD comprises of a whitened matched filter (WMF) and a recursive nonlinear

processor, known as the Viterbi algorithm. The WMF consists of a continuous-time filter matched to the received pulse shape, followed by a symbol rate sampler and a discrete-time noise whitening filter [18].

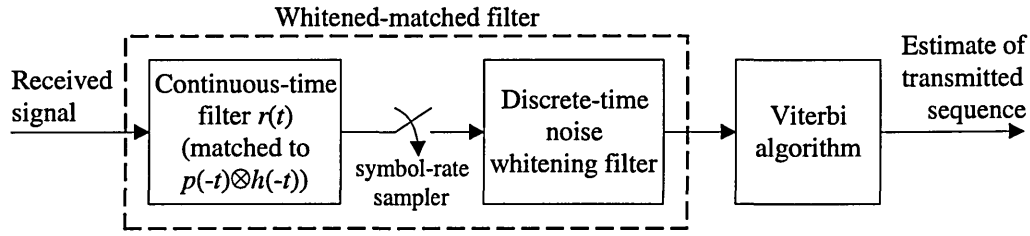


Fig. 3.6: Maximum-likelihood sequence detector

In addition to whitening the noise, which is not white at the output of the sampled matched filter, the whitening filter also turns the two-sided isolated pulse response at the output of the sampled matched filter into a causal response. In other words, the noise whitening filter equalizes the noncausal portion of the ISI, which is known as precursor ISI, and is defined as the interference from future data symbols [18]. MLSD is then performed by comparing the WMF output sequence against what the output sequence would be for each feasible sequence of input data symbols in the absence of noise; and choosing the data symbols that best match the WMF output according to a Euclidean distance measure [18]. This function may be carried out efficiently using the Viterbi algorithm, originally proposed in 1967 [101].

The performance of OOK using MLSD on measured indoor optical wireless channels is analysed in [102, 103]. MLSD is found to offer a significant improvement over unequalized systems, resulting in a slower rate of increase of power penalty as the severity of ISI increases. However, the major drawback of MLSD is the delay and complexity required for practical implementation, which may render it impractical for low cost systems such as infrared wireless receivers. This has led a number of researchers to consider equalization, which is the term used to describe any suboptimal, reduced complexity strategy for the detection of signals in the presence of ISI.

Equalization techniques can be subdivided into two general categories, these being linear and nonlinear equalization. In its simplest form, a linear equalizer (LE) employs a traversal filter structure, and has a computational complexity that is a linear function of the channel dispersion length [99]. Since the most meaningful measure of performance for a digital communication system is the average probability of error, it is desirable to choose the filter coefficients to minimise this performance index. However, the probability of error is a highly nonlinear function, and hence, using this criterion for optimizing the filter coefficient is impractical. Two criteria which have found widespread use are the zero forcing (ZF) criterion and the mean square error (MSE) criterion. As the name implies, the zero forcing criterion forces the ISI to be zero at the sampling instants. Thus, the ZF-LE has a frequency response which is the inverse of the channel frequency response. However, the main drawback of this is that it ignores the presence of additive noise. If, for example, the channel contains a range of frequencies where the attenuation is very high, the ZF-LE attempts to compensate for this by placing large gains at these frequencies. However, this compensates for the channel distortion at the expense of enhancing the additive noise. The MSE-LE improves on this by relaxing the zero ISI constraint and selecting the filter coefficients such that the combined power in the residual ISI and the additive noise at the output of the equalizer is minimised.

The main drawback of LEs is their inability to cope with severe ISI, and this has motivated research into nonlinear equalization techniques. One such nonlinear equalizer is the decision feedback equalizer (DFE), which offers a performance and complexity intermediate between the LE and the MLSD [18]. The same criteria for optimizing the filter coefficients in LEs also apply to DFEs. The performance of MSE-DFEs is generally superior to that of ZF-DFEs, but at high SNR their performance is virtually identical [104]. The performance of OOK using DFEs is analysed in [32, 105, 106], and results of an experimental OOK system employing a DFE are reported in [35, 36]. A more detailed discussion of the ZF-DFE is given in section 6.5.

3.3 Pulse Position Modulation

3.3.1 Code properties

PPM is an orthogonal modulation technique which improves on the power efficiency of OOK, at the expense of an increased bandwidth requirement and greater complexity. In PPM, each block of $\log_2 L$ data bits is mapped to one of L possible symbols. Generally, the notation L -PPM is used to indicate the order. Each symbol consists of a pulse of constant power occupying one slot, along with $L-1$ empty slots. Information is encoded by the position of the pulse within the symbol. The slot duration T_s is related to the bit duration by the following expression:

$$T_s = T_b \log_2 L / L. \quad (3.11)$$

Assuming an average optical power of P_{avg} , the transmitted waveforms for 4-PPM are shown in Fig. 3.7.

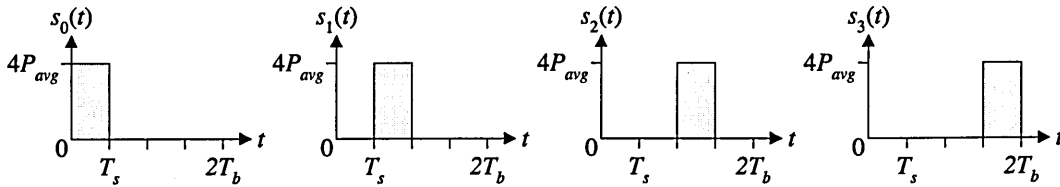


Fig. 3.7: Transmitted waveforms for 4-PPM

Compared with OOK, employing PPM results in increased system complexity, since the receiver requires both slot and symbol synchronisation in order to demodulate the signal. Nevertheless, primarily due to its power efficiency, PPM is an attractive modulation technique for optical wireless communication systems, and has been widely adopted [12]. The infrared physical layer section of the IEEE 802.11 standard on wireless LANs specifies 16-PPM for bit rates of 1 Mbit/s and 4-PPM for 2 Mbit/s (both schemes giving the same slot rate) [2]. In addition to this, IrDA serial data links operating at 4 Mbit/s specify 4-PPM [11].

3.3.2 Power spectral density

The detected electrical power spectrum of L -PPM is given as [107]:

$$S_{PPM}(f) = |P(f)|^2 [S_{c,PPM}(f) + S_{d,PPM}(f)], \quad (3.12)$$

where $S_{c,PPM}(f)$ and $S_{d,PPM}(f)$ are the continuous and discrete components, respectively, which are given as [107]:

$$S_{c,PPM}(f) = \frac{1}{T_{symp}} \left[\left(1 - \frac{1}{L}\right) + \frac{2}{L} \sum_{k=1}^{L-1} \left(\frac{k}{L} - 1\right) \cos\left(\frac{k 2\pi f T_{symp}}{L}\right) \right], \quad (3.13)$$

$$S_{d,PPM}(f) = \frac{2\pi}{T_{symp}^2} \sum_{k=-\infty}^{\infty} \delta\left(f - \frac{kL}{T_{symp}}\right). \quad (3.14)$$

$P(f)$ is the Fourier transform of the pulse shape and T_{symp} is the symbol duration, which is given as $T_{symp} = T_b \cdot \log_2 L$.

The PSD of PPM for $L = 4, 8$ and 16 is shown in Fig. 3.8. All three curves were plotted for the same average optical power, using rectangular shaped pulses occupying the full slot duration. Again, the power axis is normalized to the average electrical power multiplied by the bit duration and the frequency axis is normalized to the bit rate R_b . By choosing pulses which occupy the full slot duration, the nulls of $|P(f)|^2$ overlap the locations of all delta functions in (3.14), except at DC. These discrete terms are not shown in Fig. 3.8.

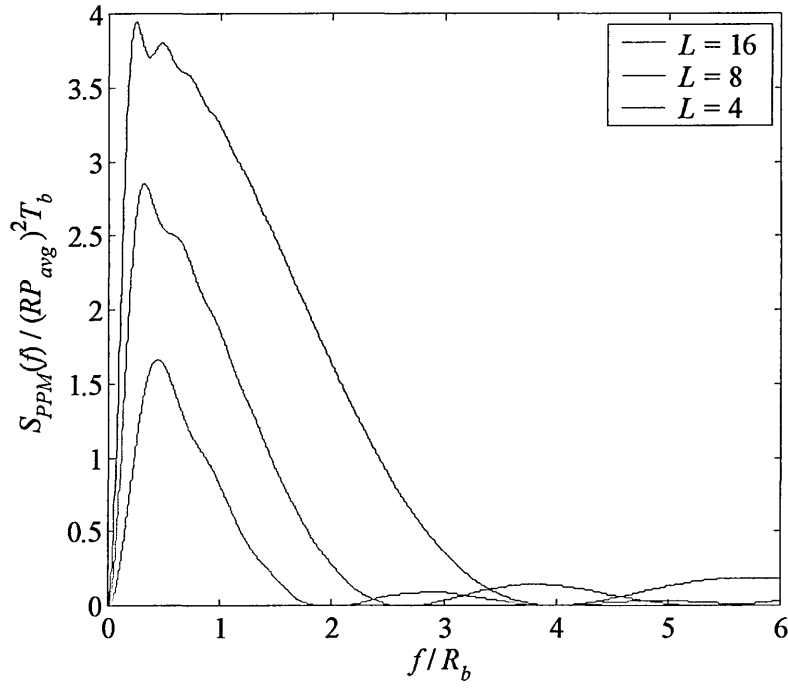


Fig. 3.8: PSD of PPM for $L = 4, 8$ and 16

From Fig. 3.8 it is clear that, unlike OOK, the PSD of PPM falls to zero at DC for all values of L . Consequently, PPM is more resistant to the effects of baseline wander compared with OOK, and therefore permits the use of higher cut-on frequencies when using high-pass filtering to reject the interference produced by artificial sources of ambient light. This topic is discussed in detail in chapter 5. As expected, by observing the positions of the first spectral nulls, it is clear that the bandwidth requirement increases as L increases. Furthermore, comparing the areas under the curves, it may also be observed that for a given average optical power, the detected electrical power increases as L increases.

3.3.3 Error performance on nondistorting channels

There are two methods of decoding PPM signals, these being hard-decision decoding using a threshold detector, which is abbreviated as PPM(TH), and soft-decision decoding using a maximum *a posteriori* (MAP) or maximum likelihood detector, which is abbreviated as

PPM(MAP). Hard decision decoding involves sampling the incoming signal at the slot rate, and assigning a one or zero to each slot depending on whether the sample is above or below the threshold level. The output is then determined by which of the L samples in the symbol is a one. If the block of L samples consists entirely of zeros, or two or more ones, then clearly an error has occurred and the receiver must mediate. Soft decision decoding compares the values of all L samples within a symbol, and assigns a one to the slot containing the sample with the highest value. The remaining $L-1$ slots are then assigned as zeros. In this method, it is not the actual values of the samples which are important, but rather, their value relative to each other. This method of decoding is optimal for systems in which AWGN is the dominant noise source and there is no channel distortion [99]. Block diagrams of PPM receivers using hard-decision and soft-decision decoding are shown in Figs. 3.9(a) and (b), respectively.

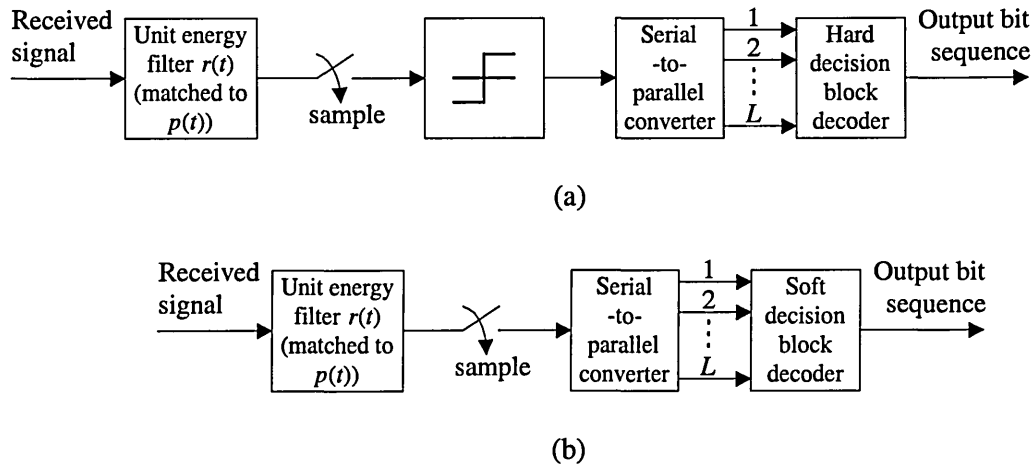


Fig. 3.9: PPM receiver: (a) hard-decision, and (b) soft decision

Since the duty cycle of PPM is fixed at $1/L$, each pulse must have an amplitude of LP_{avg} in order to maintain an average optical power of P_{avg} , assuming rectangular shaped pulses are used. A unit-energy filter matched to the transmitted pulse shape $p(t)$ has a rectangular impulse response $r(t)$ with amplitude $1/\sqrt{T_s}$ and duration T_s . As illustrated in Fig. 3.10, in the absence of noise, the peak output of this filter when a pulse is transmitted is $\sqrt{E} = LRP_{avg}\sqrt{T_s}$. When an empty slot is transmitted, the peak output of the matched filter is 0.

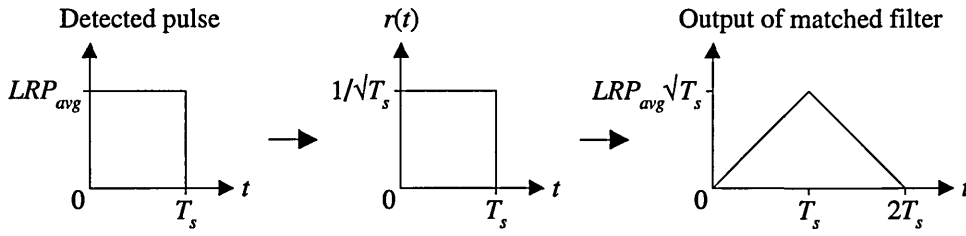


Fig. 3.10: Matched filter output for detected PPM pulse

For $L > 2$, the probability of receiving a zero is greater than the probability of receiving a one. Consequently, for hard decision decoding, the optimum threshold level does not lie midway between one and zero levels. It is a complicated function of the signal and noise powers, and the order L . Thus, in the presence of AWGN with double-sided PSD $N_0/2$, the probability of slot error for PPM(TH) may be derived from [95] as:

$$P_{e,slot,PPM(TH)} = P(one)Q\left(\frac{\sqrt{E}-\alpha}{\sqrt{N_0/2}}\right) + P(zero)Q\left(\frac{\alpha}{\sqrt{N_0/2}}\right), \quad (3.15)$$

where α is the threshold level, and $P(one)$ and $P(zero)$ represent the probabilities of getting a pulse and an empty slot, respectively, as given by:

$$P(one) = \frac{1}{L} \quad P(zero) = \frac{(L-1)}{L}. \quad (3.16)$$

When the probability of error is low, a threshold level set midway between expected one and zero levels is very close to the optimum value. Thus, when $\alpha = \sqrt{E}/2$, (3.15) reduces to [17]:

$$P_{e,slot,PPM(TH)} = Q\left(\sqrt{\frac{E}{2N_0}}\right). \quad (3.17)$$

Note that in the above expression, E is the energy of a symbol, which encodes $\log_2 L$ bits of data.

Hence, the average energy per bit, E_b , is given by [99]:

$$E_b = \frac{E}{\log_2 L}. \quad (3.18)$$

Thus, (3.17) may be expressed in terms of E_b/N_0 by substituting for E . Note that, since

$\sqrt{E} = LRP_{avg}\sqrt{T_s}$, substituting for T_s from (3.11), E_b may be expressed simply as:

$$E_b = \frac{E}{\log_2 L} = \frac{(LRP_{avg})^2 T_s}{\log_2 L} = L(RP_{avg})^2 T_b. \quad (3.19)$$

Since each symbol contains L slots, the probability of slot error may be converted into a corresponding symbol error probability using the expression derived from [18] as:

$$P_{e,symb,PPM(TH)} = 1 - (1 - P_{e,slot,PPM(TH)})^L. \quad (3.20)$$

Assuming the data is IID, each symbol is equally likely and the probability of symbol error may be converted into a corresponding bit error rate by the following [99]:

$$P_{e,bit,PPM} = \frac{L/2}{L-1} P_{e,symb,PPM}. \quad (3.21)$$

For PPM(MAP), in the presence of AWGN with double-sided PSD $N_0/2$, the probability of symbol error given as [99]:

$$P_{e, \text{symbol}, \text{PPM}(\text{MAP})} = \frac{1}{\sqrt{2\pi}} \int_{-\infty}^{\infty} \{1 - [1 - Q(y)]^{L-1}\} e^{-\frac{(y - \sqrt{2E/N_0})^2}{2}} dy, \quad (3.22)$$

where, as before, E represents the energy of a symbol. Again, this expression may be converted into a corresponding bit error rate using (3.21).

The average optical power requirements and bandwidth requirements of PPM(TH), with the threshold level optimized, and PPM(MAP) are plotted in Fig. 4.15, along with those of other modulation techniques. Again, note that in Fig. 4.15, the average optical power requirement is normalized to that required by OOK-NRZ to send 1 Kbyte packets at an average packet error rate of 10^{-6} , and the bandwidth requirement is normalized to OOK-NRZ. From Fig. 4.15 it may be observed that, in the absence of multipath distortion, PPM yields an average power requirement that decreases steadily as L increases. This is due to the fact that the increased noise associated with the $(L/\log_2 L)$ -fold increase in receiver bandwidth is outweighed by the L -fold increase in peak optical power [12]. Comparing the two methods of detection, it is clear that whilst hard-decision decoding is simpler to implement, it does incur a ~ 1.5 dB average optical power penalty compared with the more complex soft-decision decoding [17]. This power penalty is consistent for all orders of PPM.

3.3.4 Review of error performance on multipath channels

The performance of PPM on multipath channels without equalization is considered in [107]. The authors found that the power penalty due to ISI increases more rapidly for PPM than for OOK, and increases most rapidly for large L , due to the shorter slot duration. For small values of normalized delay spread D_T , which is defined as the channel RMS delay spread divided by the bit duration, PPM maintains its lower average power requirement over OOK, with higher values of L still giving the best power efficiency. However, as D_T increases, i.e. when the severity of ISI increases and/or the data rate increases, higher order PPM suffers a greater

increase in ISI power penalty and consequently lower values of L become more power efficient. Eventually, as D_T increases further, the ISI power penalty for PPM becomes too severe and OOK becomes the more efficient modulation technique. The unequalized performance of PPM on multipath channels is considered in some detail in chapter 6.

In the presence of multipath distortion, the optimum PPM receiver employs a whitened matched filter front end, followed by a MLSD which can be performed on a symbol by symbol basis using the Viterbi algorithm [10]. The performance of PPM using MLSD on multipath channels is analysed in [102, 103]. MLSD is found to offer a significant improvement over unequalized systems, resulting in a significantly slower rate of increase of power penalty as D_T increases. Additionally, when MLSD is used, higher values of L consistently maintain a higher power efficiency. However, even when MLSD is used, PPM is found to suffer larger ISI power penalties than OOK using MLSD. Consequently, as D_T increases, the advantage of any given PPM order over OOK diminishes.

Due to the complexity and delay associated with the implementation of MLSD, a number of suboptimal adaptive equalization techniques for PPM have been proposed. The performance of ZF-DFEs, operating at both the slot rate and symbol rate, was analysed by Barry [10, 108, 109]. For the slightly more complex symbol rate equalizers, which feedback symbol decisions rather than intermediate slot decisions, methods to cancel intrasymbol interference were also considered. Barry found that whilst the equalizers were effective at mitigating ISI, for some channels there remained a significant gap between their performance and that of the MLSD. Audeh et. al. analysed the performance of PPM using chip rate and symbol rate ZF-DFEs on a collection of 46 experimentally measured indoor infrared channels [110]. Compared with MLSD, the authors found that the performance of both equalizers is very close to that of MLSD on the channels considered, with the symbol rate ZF-DFE giving a small improvement in performance over the slot rate ZF-DFE.

3.3.5 Trellis-coded PPM

The performance of PPM on multipath channels may be improved by using trellis coding, which is designed to maximise the minimum Euclidean distance between allowed signal sequences [111]. The two key concepts of trellis coding are signal set expansion and set partitioning. Signal set expansion is used to provide the redundancy necessary for coding to take place. Note that this does not necessarily result in an increased bandwidth requirement or a reduced the data rate. For example, consider 16-PPM which encodes 4 bits of data per symbol. If each symbol is replaced by two 8-PPM symbols, encoding 6 bits of data, then a rate $2/3$ code can be accommodated whilst still maintaining the same slot and data rates [111]. In the presence of multipath dispersion, set partitioning increases the Euclidean distance between valid symbols compared with uncoded PPM. Consequently, the power requirements of trellis-coded PPM grow at a much slower rate compared with uncoded PPM as the severity of ISI increases. Using MLSD, Lee et. al. analysed the performance of rate- $2/3$ coded 8-PPM and rate- $3/4$ coded 16-PPM on multipath channels [111]. For a normalized delay spread of 0.06, the authors found that rate $3/4$ coded 16-PPM achieved the highest power efficiency of the schemes considered, with a gain of 6.3 dB (electrical) over uncoded 32-PPM, though it does have a slightly lower bandwidth requirement. The problem with using MLSD for the detection of trellis-coded PPM is that its high computational complexity excludes the use of high constraint length codes or prevents operation under severe channel conditions. This prompted Lee et. al. to consider the use of suboptimal, reduced complexity detection techniques for trellis-coded PPM, which allow better codes to be used at the expense of a power penalty resulting from the suboptimal detection [112, 113]. The fundamental idea behind this is that if the gain due to the use of better codes is greater than the penalty incurred due to suboptimal detection, then an overall net improvement in performance can be achieved. The authors considered the use of parallel decision-feedback decoding and symbol-rate DFE to mitigate the ISI, leaving the Viterbi algorithm to deal solely with the process of decoding. For the same level of complexity, the suboptimal detection techniques achieved net gains ranging from ~ 0.5 dB to ~ 2 dB (electrical) as the delay spread increased.

3.3.6 PPM variants

There are a number of variants of PPM which have also been considered for use in indoor optical wireless communication systems. Multiple PPM (MPPM) is one such variant, originally proposed for use in direct detection free-space laser communications to give an improvement in bandwidth efficiency over PPM [114, 115]. In MPPM, each symbol of duration $T_{\text{symp}} = T_b \log_2 L$ is divided into n slots, each with a duration of T_{symp}/n . A pulse is transmitted in w of these slots, thereby giving $\binom{n}{w}$ possible symbols and hence, the potential to encode $\log_2 \binom{n}{w}$ bits. As an example, $\binom{4}{2}$ -MPPM has 6 possible symbols, as illustrated in Fig. 3.11.

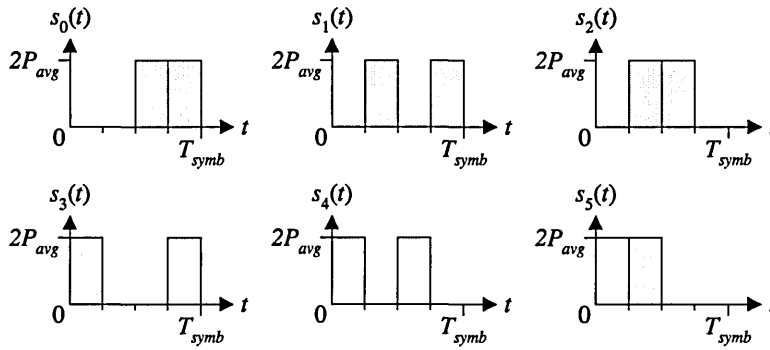


Fig. 3.11: Valid symbols for $\binom{4}{2}$ -MPPM

However, not all of the possible symbols are necessarily used. For example, a reduced symbol set may be chosen which has a large minimum Hamming distance. Park and Barry examined the performance of MPPM on the AWGN channel [116]. The authors found that with $w = 2$, MPPM outperforms PPM both in terms of bandwidth efficiency and power efficiency. Moving to $w = 8$ greatly increases the number of valid symbols, thereby giving an improvement in bandwidth efficiency at the expense of an increased power requirement. Park and Barry extended their analysis of MPPM by examining the effects of ISI [117, 118]. For both unequalized detection and MLSD, the authors found that the power requirements of MPPM increase at a similar rate to

those of PPM as the severity of ISI increases. As with PPM, the performance of MPPM in the presence of ISI may be improved through the use of trellis coding. Park and Barry compared the performance of trellis-coded $\binom{17}{2}$ -MPPM and trellis-coded 16-PPM over multipath channels, both using the same constraint length and MLSD [119]. The authors found that whilst PPM outperforms MPPM on channels which suffer only mildly from multipath dispersion, MPPM is the more power efficient technique when the ISI is more severe.

Another variant of PPM which has also been proposed for use in indoor optical wireless communication systems is differential PPM (DPPM) [120, 121]. DPPM symbols may be derived from PPM symbols simply by omitting the empty slots which follow the pulses, thus resulting in symbols of unequal duration and hence, a nonuniform data rate. As an example, the symbols for 4-DPPM are illustrated in Fig. 3.12.

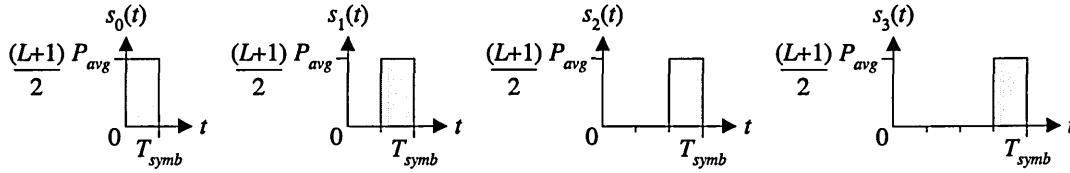


Fig. 3.12: 4-DPPM symbol set

Since symbol boundaries are not known prior to detection, soft decision decoding of DPPM requires the use of MLSD, even in the absence of coding or ISI. Consequently, hard-decision decoding is the most likely method of detection for practical systems employing DPPM, a process which is made simpler by the fact that DPPM does not require any symbol synchronisation. On the AWGN channel, for any given L , DPPM has a slightly higher power requirement but a much lower bandwidth requirement compared with PPM. In the presence of multipath dispersion, for both unequalized hard-decision detection and MLSD, the ISI power penalty for DPPM is lower than that of PPM for any given value of normalized delay spread. A number of suboptimal equalization techniques for DPPM have also been considered, these being slot-rate and multislot-rate ZF-DFEs. For a 3 dB average optical power penalty, systems using a

slot-rate DFE can tolerate a delay spread approximately three times higher than the unequalized system. At this delay spread, the multislot-rate DFE yields a 0.5 dB optical power gain over the slot-rate DFE.

3.4 Summary

In this chapter, the modulation techniques which have been considered for use in indoor optical wireless communication systems have been reviewed. Since power efficiency is the most important criterion when evaluating modulation techniques, this favours schemes which have a low duty cycle, thereby achieving a large peak-to-mean power ratio. Consequently, baseband modulation techniques are more power efficient than subcarrier based schemes, with PPM offering a better power efficiency than OOK. However, it is not simply a question of selecting a modulation technique which offers a low duty cycle, since this also influences how well the scheme satisfies the other selection criteria. Baseband schemes which offer a low duty cycle, such as PPM, also suffer from poor bandwidth efficiency, and are therefore more susceptible to intersymbol interference resulting from multipath dispersion. This is evident when comparing the unequalized performance of OOK and PPM. As the ratio of channel delay spread to bit duration increases, the power advantage of any given PPM order over OOK diminishes. This subject is covered in detail in chapter 6. In the presence of multipath dispersion, the performance of both modulation techniques may be improved using MLSD, suboptimal equalization and/or some form of coding scheme. However, all these techniques result in an increase in system cost and complexity, which cannot be ignored in mass-market optical wireless transceivers. In addition, there are other considerations which must also be taken into account when selecting a modulation technique. One such consideration is the ability of a scheme to mitigate interference from artificial sources of ambient light, which has the potential to induce severe power penalties if ignored. As examined in detail in chapter 5, due to its more sophisticated method of detection, PPM(MAP) is virtually immune to ambient light interference at medium to high data rates. For baseband modulation techniques which use threshold

detection, schemes which do not have a significant amount of their power located at DC and low frequencies are more favourable, thereby allowing electrical high-pass filtering to be used effectively without introducing significant baseline wander.

Thus, when selecting a modulation technique suitable for use in indoor optical wireless communication systems, there are numerous considerations which must be taken into account, and there is no one modulation scheme which is best in each of the selection criteria. Nevertheless, to date, PPM has generally been the preferred choice, primarily due to its power efficiency.

Chapter 4

DPIM Code Properties

4.1 Introduction

Pulse interval modulation (PIM) is a baseband scheme which belongs to the family of pulse time modulation techniques, and was first considered for use in analogue optical fibre communication systems more than two decades ago [122-125]. As the name implies, PIM operates by varying the interval between adjacent pulses in accordance with the modulating signal. More recently, Ghassemlooy *et. al.* introduced a discrete version of PIM for use on digital signals [126, 127], in which time is divided into discrete slots. In order to differentiate this from traditional analogue PIM, the authors referred to the new scheme as digital PIM (DPIM). Although PPM, as discussed in the previous chapter, refers to digital PPM as opposed to its analogue counterpart, the naming convention for DPIM is maintained throughout this thesis in order to avoid any confusion. DPIM has been investigated for use in transmitting analogue signals over optical fibre [126-130], and has also been briefly examined for transmitting analogue signals over short range free-space point-to-point links [131].

Unlike PPM, DPIM is classified as an anisochronous modulation technique, meaning that it does not have a fixed symbol structure. This characteristic yields benefits such as an improved bandwidth efficiency, but also has repercussions when considering such things as maximum likelihood detection and nonuniform throughput. These issues are addressed in the chapter when they arise.

This chapter provides a general introduction to DPIM, and discusses the characteristics which make it suited for use in indoor optical wireless communication systems, bearing in mind the selection criteria outlined in section 3.1. Where appropriate, the scheme is compared with the more established techniques of OOK and PPM. The remainder of this chapter is organised as follows. DPIM code properties are introduced in section 4.2, and a full spectral analysis is presented in section 4.3, which is based on a new expression for the slot autocorrelation function. Appropriate measures of performance for DPIM are discussed in section 4.4, and the receiver structure is examined in section 4.5. The error performance of DPIM on nondistorting channels limited by AWGN is studied in section 4.6, which includes the effects of adding a guard band and optimizing the threshold level. Finally, the chapter is summarized in section 4.7.

4.2 DPIM Code Properties

In DPIM, each block of $\log_2 L$ data bits is mapped to one of L possible symbols, each different in length. Every symbol begins with a pulse, followed by a series of empty slots, the number of which is dependent on the decimal value of the block of data bits being encoded. Consequently, the minimum and maximum symbol durations are T_s and LT_s , respectively, where T_s is the slot duration. In order to provide some immunity to the effects of ISI, a guard band consisting of one or more empty slots may be added to each symbol immediately following the pulse. Clearly, adding a single guard slot changes the minimum and maximum symbol durations to $2T_s$ and $(L+1)T_s$, respectively. The mapping of source data to transmitted symbols for 4-DPIM with no

guard band (NGB) and with a guard band consisting of one slot (1GS) is shown in Fig. 4.1 The shaded areas in the figure represent the guard slots.

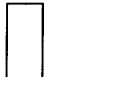

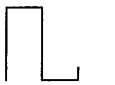





Source Data	4-DPIM Symbols	
	NGB	1GS
00		
01		
10		
11		

Fig. 4.1: Mapping of source data to transmitted symbols for 4-DPIM(NGB) and 4-DPIM(1GS)

In DPIM, since the symbol duration is variable, the overall data rate is also variable. Therefore, the slot duration is chosen such that the mean symbol duration is equal to the time taken to transmit the same number of bits using fixed data rate schemes such as OOK or PPM. This slot duration is given as:

$$T_s = \frac{T_b \log_2 L}{L_{avg}}, \quad (4.1)$$

where T_b is the bit duration and L_{avg} is the mean symbol length in slots. Assuming IID random data, each symbol is equally likely and consequently, L_{avg} is given as:

$$L_{avg} = \frac{(L+1)}{2} \quad \text{for DPIM(NGB)}, \quad (4.2)$$

$$L_{avg} = \frac{(L+3)}{2} \quad \text{for DPIM(1GS)}. \quad (4.3)$$

When the data is IID, for any given L , DPIM achieves the same average data rate as PPM, but has a longer slot duration, and consequently requires less bandwidth. The bandwidth requirement, normalized to the bit rate, versus number of bits per symbol is plotted in Fig. 4.2 for PPM, DPIM(NGB) and DPIM(1GS). As expected, the bandwidth requirement of DPIM approaches half that of PPM as L increases, since an average length DPIM symbol with contain only approximately half the number of slots of a PPM symbol.

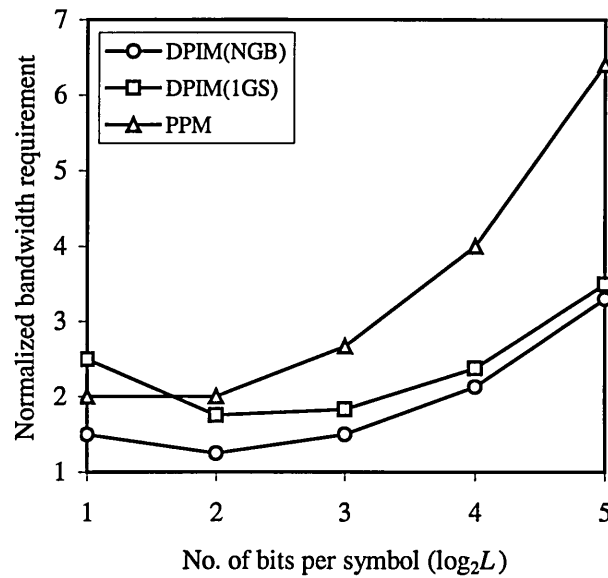


Fig. 4.2: Normalized bandwidth requirement versus number of bits per symbol for DPIM(NGB), DPIM(1GS) and PPM

A further advantage of DPIM is the fact that, since each symbol is initiated with a pulse, symbol synchronisation is not required in the receiver. This is in contrast to PPM, which requires a more complex receiver since both slot and symbol synchronisation are required.

4.3 DPIM Spectral Properties

A DPIM slot sequence may be expressed as [128]:

$$s_{DPIM}(t) = \sum_{n=-\infty}^{\infty} a_n p(t - nT_s), \quad (4.4)$$

where $p(t)$ is the pulse shape, T_s is the slot duration, and a_n is a random variable which represents the presence or absence of a pulse in the n^{th} time slot. The sequence $s_{DPIM}(t)$ is a cyclostationary process [132] and, following the method outlined in [120, 121], its PSD may be calculated using:

$$S_{DPIM}(f) = \frac{1}{T_s} |P(f)|^2 S_a(f), \quad (4.5)$$

where $P(f)$ is the Fourier transform of the pulse shape $p(t)$, and $S_a(f)$ is the PSD of the slot sequence. For unit amplitude rectangular shaped pulses with a duration of T_s , $P(f)$ is given by:

$$P(f) = T_s \frac{\sin(\pi f T_s)}{\pi f T_s}. \quad (4.6)$$

$S_a(f)$ is found by calculating the discrete-time Fourier transform of the slot autocorrelation function R_k . Since DPIM(NGB) symbols may be thought of as time reversed DPPM symbols, DPIM(NGB) has a slot autocorrelation function identical to that of DPPM, which is given by [121]:

$$R_k = \begin{cases} \frac{2}{(L+1)} & k=0 \\ \frac{2}{L^k} (L+1)^{k-2} & 1 \leq k \leq L. \\ \frac{1}{L} \sum_{i=1}^L R_{k-i} & k > L \end{cases} \quad (4.7)$$

For DPIM(1GS), the slot autocorrelation function is given by [133]:

$$R_k = \begin{cases} L_{avg}^{-1} & k=0 \\ 0 & k=1 \\ \left(\frac{L_{avg}^{-1} L^{-1}}{\sqrt{1+4L^{-1}}} \right) \left[\left(\frac{1+\sqrt{1+4L^{-1}}}{2} \right)^{k-1} - \left(\frac{1-\sqrt{1+4L^{-1}}}{2} \right)^{k-1} \right] & 2 \leq k \leq L+1, \\ \frac{1}{L} \sum_{i=1}^L R_{k-1-i} & k > L+1 \end{cases} \quad (4.8)$$

where L_{avg} is given in (4.3). For reference, a full derivation of this expression may be found in Appendix A. For both DPIM(NGB) and DPIM(1GS), R_k approaches L_{avg}^{-2} as k increases, which is intuitive since two pulses far away from each other appear uncorrelated. It is found that for $k > 5L$, R_k may be approximated as L_{avg}^{-2} with a good degree of accuracy. Since the mean value of the slot sequence is non-zero, $S_a(f)$ is composed of a continuous term, $S_c(f)$, and a discrete term, $S_d(f)$, i.e.:

$$S_a(f) = S_c(f) + S_d(f). \quad (4.9)$$

When consideration is limited to rectangular shaped pulses which occupy the full slot duration, the nulls of $|P(f)|^2$ cancel out the delta functions in $S_d(f)$, except at DC. Consequently, the discrete term is ignored in this analysis. The continuous component of $S_a(f)$ may be calculated from R_k using [120, 121]:

$$S_c(f) \cong \sum_{k=-5L}^{5L} (R_k - L_{avg})^{-2} e^{j2\pi k f T_s}. \quad (4.10)$$

By substituting the appropriate R_k into (4.10), and then substituting for $P(f)$ and $S_a(f)$ in (4.5), the PSD of DPIM(NGB) and DPIM(1GS) was plotted for $L = 4, 8, 16$ and 32 , as shown in Figs. 4.3 and 4.4, respectively. All curves were plotted for the same average optical power, using rectangular shaped pulses occupying the full slot duration. In both figures, the power axis is normalized to the average electrical power multiplied by the bit duration and the frequency axis is normalized to the bit rate R_b . The discrete terms at DC are not shown in either of the two figures.

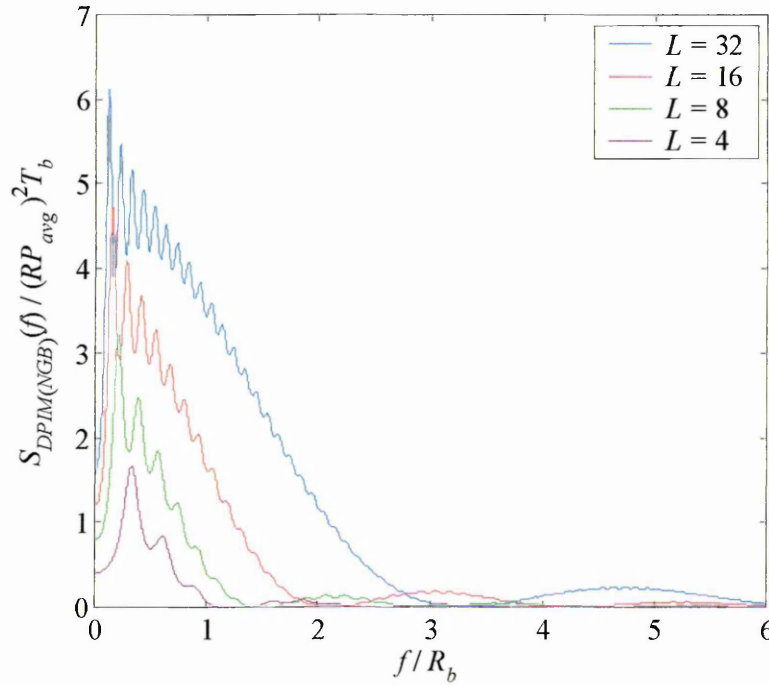


Fig. 4.3: PSD of DPIM(NGB) for $L = 4, 8, 16$ and 32

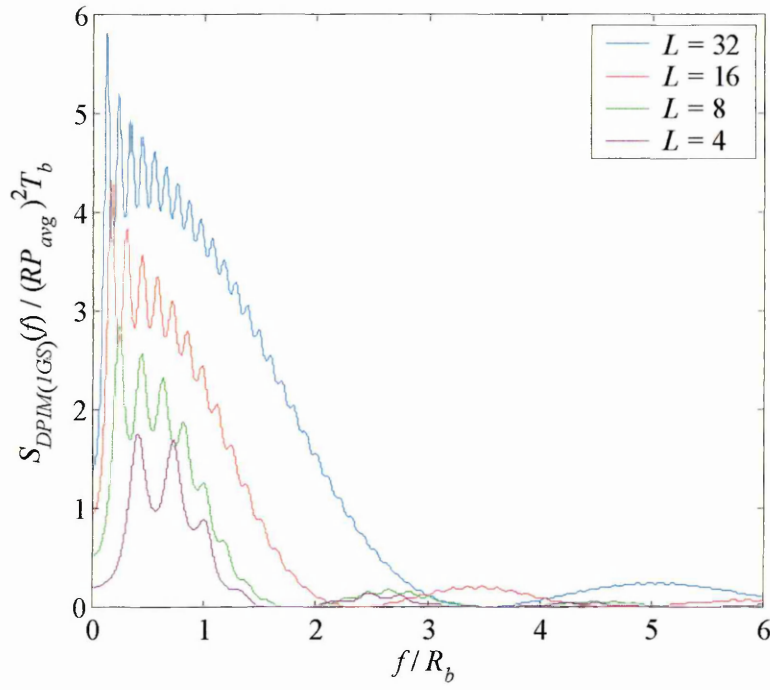


Fig. 4.4: PSD of DPIM(1GS) for $L = 4, 8, 16$ and 32

From Figs. 4.3 and 4.4 it is clear that, unlike PPM, the PSD of DPIM does not fall to zero at DC, though the power content at low frequencies is relatively small compared with OOK. Consequently, this implies that DPIM will be more susceptible to the effects of baseline wander compared with PPM, a subject which is investigated in detail in chapter 5. Comparing the two DPIM schemes, for any given L , DPIM(NGB) has a slightly higher DC power component compared with DPIM(1GS), again suggesting a greater susceptibility to baseline wander. By observing the null positions, the slightly higher bandwidth requirement of DPIM(1GS) compared with DPIM(NGB) is also evident. Furthermore, if the areas under the curves are compared, for a given average optical power, the increase in detected electrical power as L increases is easily observed.

4.4 Measuring the Error Performance of DPIM

In isochronous schemes such as PPM, an error is confined to the symbol in which it occurs. Consequently, a single slot error can affect a maximum of $\log_2 L$ bits. By calculating the average number of bit errors per symbol error, it is possible to convert the probability of symbol error into a corresponding BER using (3.21). In DPIM however, since the pulses actually define the symbol boundaries, errors are not confined to the symbols in which they occur. To explain this further, consider the transmitted 8-DPIM(1GS) sequence shown in Fig. 4.5(a).

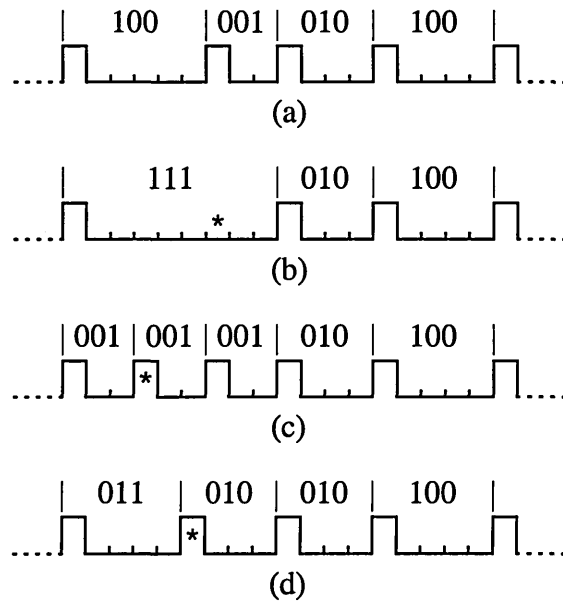


Fig. 4.5: Types of error in DPIM: (a) Transmitted 8-DPIM(1GS) signal, (b) erasure error, (c) false alarm error, and (d) wrong slot error

There are three types of error which need to be considered, as indicated by the asterisks in Figs. 4.5(b), (c) and (d). These errors are described as follows:

Erasure error: An erasure error occurs when a transmitted pulse is not detected, as depicted in Fig. 4.5(b). In DPIM, this type of error combines two symbols into one longer duration symbol. In the example given, data blocks 100 and 001 are combined into a single block 111. Only if the newly created symbol is longer than the maximum symbol duration will an error be detected. If

the new symbol length is valid, then the receiver will assume that this is the symbol which was transmitted and consequently, the remaining symbols in the packet will shift one position to the left with respect to the transmitted sequence. If no other errors occur in the packet, then the packet length will be short by $\log_2 L$ bits.

False alarm error: A false alarm error occurs when a transmitted zero is falsely detected as a one, as depicted in Fig. 4.5(c). In DPIM, this has the effect of splitting one symbol into two shorter length symbols. In the example given, data block 100 is received as two blocks of 001. The error is only detected if one or both of the newly created symbols are shorter than the minimum symbol duration. If both new symbols are valid, then the receiver will assume that these two symbols were transmitted and consequently, the remaining symbols in the packet will shift one position to the right with respect to the transmitted sequence. If no further errors occur in the packet, then the packet will contain $\log_2 L$ extra bits.

Wrong slot error: A wrong slot error occurs when a pulse is detected in a slot adjacent to the one in which it was transmitted, as depicted in Fig. 4.5(d). This type of error may be thought of as an erasure error combined with a false alarm error. In the example given, adjacent data blocks 100 and 001 are demodulated as 011 and 010. Unless the error results in at least one of the newly created symbols being either shorter than the minimum symbol length or longer than the maximum symbol length, it will not be detected. A pulse detected in the wrong slot affects both symbols either side of the pulse, but has no affect on the remaining symbols in the packet.

Thus, in the case of DPIM, since a single slot error has the potential to affect all the remaining bits in a packet, this makes the BER a meaningless measure of performance. Consequently, for the remainder of this thesis, the packet error rate (PER) is used when evaluating the error performance of modulation techniques. This is in accordance with the majority of network protocols, such as Ethernet and IEEE 802.11, which use packet based error detection and automatic repeat request [2, 134].

A packet is considered to be in error if one or more slots within the packet are in error. For a packet containing D bits of IID random data, the average number of slots contained within the packet is $L_{avg} D / \log_2 L$ and hence, the PER may be derived from [18] as:

$$PER = 1 - \left(1 - P_{e,slot,DPIM}\right)^{L_{avg} D / \log_2 L}, \quad (4.11)$$

where $P_{e,slot,DPIM}$ is the probability of slot error. When $P_{e,slot,DPIM} \ll 1$, this may be approximated as:

$$PER \approx \frac{L_{avg} D}{\log_2 L} P_{e,slot,DPIM}. \quad (4.12)$$

Packet lengths vary depending on the network protocol used. For example, the payload of an IEEE 802.11 packet may contain between 0 and 2500 bytes of data [2], whereas Ethernet packet payloads vary between 46 and 1500 bytes [134]. Figure 4.6 shows the relationship between PER and probability of slot error for 16-DPIM(NGB) using various packet lengths. Clearly, since longer packets contain more slots, they require a lower probability of slot error in order to achieve the same PER as shorter packets. Depending on the packet lengths in question, this reduction can be greater than an order of magnitude. Similarly, the probability of slot error required for a given PER decreases as L increases. Throughout this thesis, all analysis and results are based on a fixed packet length of 1 kByte, i.e. 1024 bits.

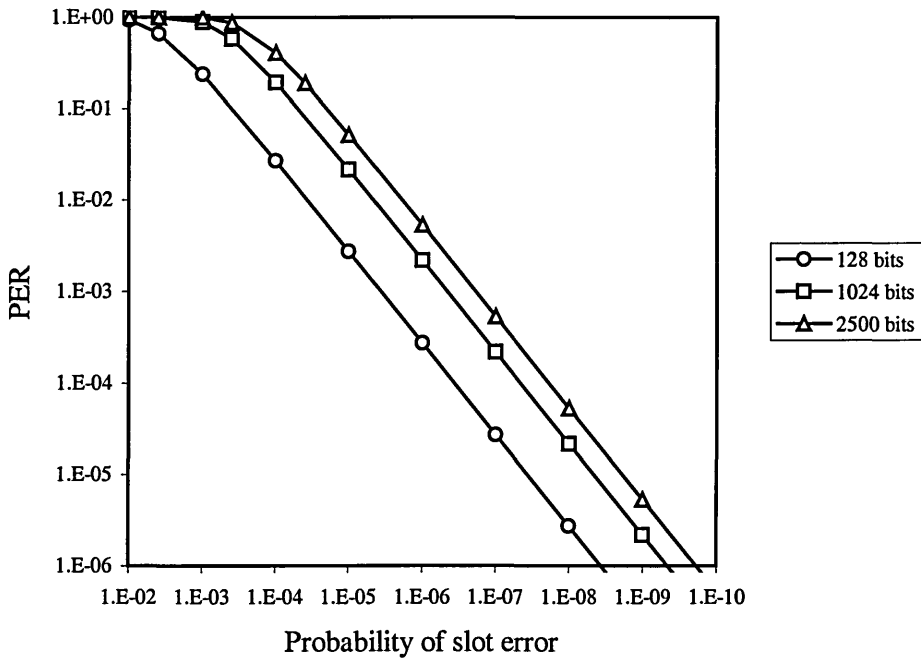


Fig 4.6: PER versus probability of slot error for 16-DPIM(NGB) using various packet lengths

4.5 DPIM Receiver Structure

As highlighted by Shiu and Kahn for DPPM, since symbol boundaries are not known prior to detection, the optimal soft-decision decoding of DPIM would require the use of MLSD, even in the absence of coding or ISI [120, 121]. In practise, this means that for a packet containing n slots and w pulses, the receiver would have to compare the received sequence with every possible combination of w pulses in n slots. Even for very short packet lengths of say 64 bits, a 16-DPIM(NGB) packet would contain on average 136 slots of which 16 would be ones. There are $\binom{136}{16} \approx 10^{20}$ possible combinations of 16 pulses in 136 slots, and clearly, comparing the received sequence against each of these is unfeasible. Thus, the most likely method of detection for DPIM is hard decision decoding using a threshold detector.

As illustrated in Fig. 4.7, a DPIM receiver employing hard-decision decoding is functionally identical to the hard-decision receivers already described in chapter 3 for OOK and PPM(TH). The receiver consists of a continuous-time filter with an impulse response $r(t)$, which is matched to the transmitted pulse shape $p(t)$. The filter output is sampled at the end of each slot period, and a one or zero is assigned depending on whether the sample is above or below the threshold level. A DPIM decoder is then used to convert the slot sequence back into a bit sequence.

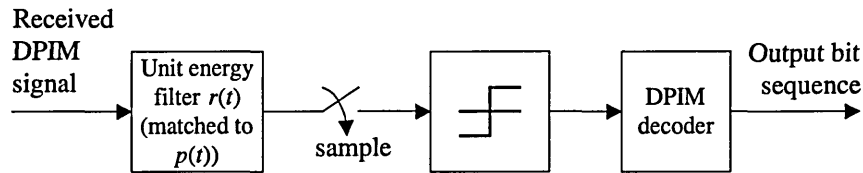


Fig. 4.7: Hard-decision DPIM receiver

As illustrated in Fig. 4.8, the functionality of a DPIM decoder is very simple, since it merely counts the number of empty slots between successive pulses. The falling edge of a detected pulse is used to initiate a counter, which operates at the slot rate. On the rising edge of the next detected pulse, the count value is equal to the $\log_2 L$ bits which have been encoded in that particular symbol. The count value is loaded into the data store and the counter is then reset, ready to begin counting again on the falling edge of the pulse. The data bits can then be read out serially from the data store as required, which could either be as soon as they are available or at the end of the current packet. If the DPIM symbols contain a guard band, this is handled simply by delaying the initiation of the counter by a predetermined number of slots. Due to its simple functionality, a DPIM decoder is also easily implemented in hardware, or expressed using a hardware description language such as VHDL.

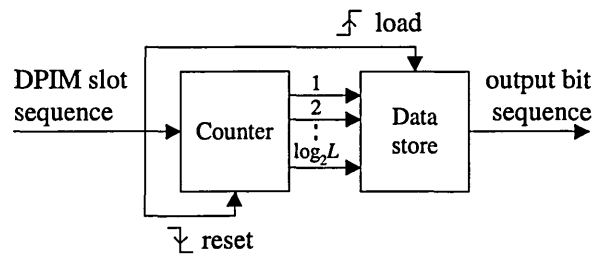


Fig. 4.8: Block diagram of a DPIM demodulator

Since DPIM symbol lengths are variable, the overall data rate is also variable. Within a network environment, packet buffers are generally used in both the transmitter and receiver, and hence, the variable data rate does not pose a problem. If a fixed throughput is required, then one solution is to employ a dual mapping technique, as suggested by Shiu and Kahn for DPPM [121], whereby source bits are mapped to symbols either normally or in reverse fashion, which ever yields the shorter number of slots. A flag slot is added at the beginning of the packet to indicate the choice of mapping used, and empty slots are appended to the end of the packet until the mean packet duration is reached.

If DPIM is required to operate in a non packet based real time fixed throughput application, one method of achieving this is to use a first-in first-out (FIFO) buffer in both the transmitter and receiver, as illustrated in Fig. 4.9.

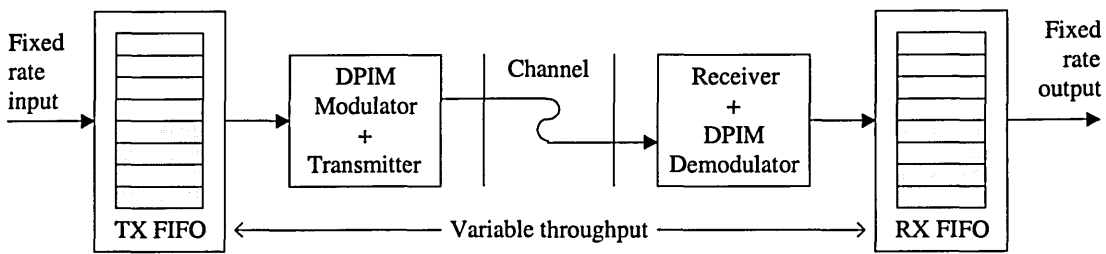


Fig. 4.9: Using DPIM in a fixed throughput system

By setting the slot rate such that DPIM yields the same average data rate as the fixed throughput required, and operating the FIFOs at nominally half full, the variable data rate of the DPIM sequence is effectively masked from the rest of the fixed rate system. The FIFOs must be

sufficiently large to avoid underflow and overflow errors, and the minimum required size may be determined from the source data statistics. If a succession of symbols are transmitted which are shorter than the average symbol length, the DPIM data rate will be momentarily faster than the fixed data rate, causing the transmitter FIFO to empty and the receiver FIFO to fill. Conversely, if a number of longer duration symbols are transmitted, the DPIM data rate will be momentarily slower than the fixed rate, causing the transmitter FIFO to fill and the receiver FIFO to empty.

4.6 Error Performance on Nondistorting Channels

4.6.1 DPIM with no guard band

Since the average duty cycle of a DPIM encoded packet is $1/L_{avg}$, it follows that each pulse must have an amplitude of $L_{avg}P_{avg}$ in order to maintain an average optical power of P_{avg} , assuming rectangular shaped pulses are used. A unit-energy filter matched to the transmitted pulse shape $p(t)$ has a rectangular impulse response $r(t)$ with amplitude $1/\sqrt{T_s}$ and duration T_s . As illustrated in Fig. 4.10, in the absence of noise, the peak output of this filter when a pulse is transmitted is $\sqrt{E} = L_{avg}RP_{avg}\sqrt{T_s}$. When an empty slot is transmitted, the peak output of the matched filter is 0.

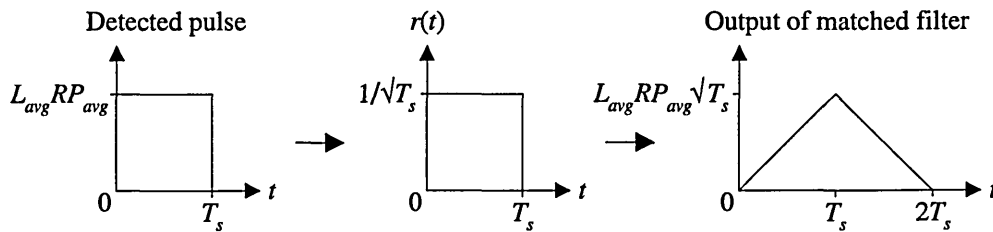


Fig. 4.10: Matched filter output for detected DPIM pulse

Thus, in the presence of AWGN with double-sided PSD $N_0/2$, the probability of slot error for DPIM(NGB) using hard decision decoding may be derived from [95] as:

$$P_{e,slot,DPIM(NGB)} = P(one)Q\left(\frac{\sqrt{E}-\alpha}{\sqrt{N_0/2}}\right) + P(zero)Q\left(\frac{\alpha}{\sqrt{N_0/2}}\right), \quad (4.13)$$

where $P(one)$ and $P(zero)$ are the *a priori* probabilities of getting a pulse and an empty slot, respectively, as given by:

$$P(one) = \frac{1}{L_{avg}} \quad \text{and} \quad P(zero) = \frac{(L_{avg} - 1)}{L_{avg}}. \quad (4.14)$$

As discussed in section 4.6.3, when the probability of error is low, a threshold level set midway between expected one and zero levels is very close to the optimum value. Thus, when $\alpha = \sqrt{E}/2$, (4.13) reduces to:

$$P_{e,slot,DPIM(NGB)} = Q\left(\sqrt{\frac{E}{2N_0}}\right). \quad (4.15)$$

Note that in the above expression, E is the energy of a symbol, which encodes $\log_2 L$ bits of data.

Hence, the average energy per bit, E_b , is given as:

$$E_b = \frac{E}{\log_2 L}. \quad (4.16)$$

Thus, (4.15) may be expressed in terms of E_b/N_0 by substituting for E . Note that, since

$\sqrt{E} = L_{avg} RP_{avg} \sqrt{T_s}$, substituting for T_s from (4.1), E_b may be expressed simply as:

$$E_b = \frac{E}{\log_2 L} = \frac{(L_{avg} RP_{avg})^2 T_s}{\log_2 L} = L_{avg} (RP_{avg})^2 T_b. \quad (4.17)$$

The average optical power requirements and bandwidth requirements of DPIM(NGB) are plotted in Fig. 4.15 for various L . In Fig. 4.15, the average optical power requirement is normalized to that required by OOK-NRZ to send 1 kByte packets at an average PER of 10^{-6} and the bandwidth requirement is also normalized to OOK-NRZ. Note that the power requirements assume that an optimum threshold level is used, as covered in detail in section 4.6.3. The performance of the scheme on nondistorting channels limited by AWGN is discussed in section 4.6.4.

4.6.2 DPIM with one guard slot

When a guard band is employed, upon detection of a pulse the following slot(s) contained within the guard band are automatically assigned as zeros, regardless of whether or not the sampled output of the receiver filter is above or below the threshold level. In the case of DPIM(1GS), the probability of slot error for any given slot is dependent on the decision made for the previous slot. Thus, there are four possible scenarios which need to be considered:

(i) *The previous slot was a one and was correctly detected*

If the previous slot was a one, the current slot is a guard slot and therefore must be a zero. Since the receiver detected the previous slot correctly, the current slot is automatically assigned a zero, and consequently it is not possible for an error to occur in the current slot. Thus,

$$P_{e,slot} = 0. \quad (4.18)$$

(ii) *The previous slot was a one but was falsely detected as a zero*

If the previous slot was a one, the current slot is a guard slot and must therefore be a zero. However, since the previous slot was incorrectly detected as a zero, the receiver will not automatically assign a zero to the current slot. Therefore, a wrong decision could be made should a false alarm error occur in the current slot. The probability of this occurring is given by:

$$P_{e,slot} = \frac{1}{L_{avg}} \cdot Q\left(\frac{\sqrt{E} - \alpha}{\sqrt{N_0/2}}\right) \cdot Q\left(\frac{\alpha}{\sqrt{N_0/2}}\right). \quad (4.19)$$

In this expression, the first term represents the probability that the previous slot was a one, the second term is the probability of that one being detected as a zero, and the third term is the probability that the current slot is falsely detected as a one. Clearly, when the probability of error is low, this scenario contributes very little to the overall average probability of slot error, since an erasure error and a false-alarm error must occur in adjacent slots.

(iii) *The previous slot was a zero and was correctly detected*

If the previous slot was a zero, the current slot could be either a one or a zero. Since the previous slot was correctly detected, the current slot is not automatically assigned a zero. Thus, the expression for the probability of error for the current slot is given as:

$$P_{e,slot} = \frac{(L_{avg} - 1)}{L_{avg}} \cdot \left[1 - Q\left(\frac{\alpha}{\sqrt{N_0/2}}\right)\right] \cdot \left[\frac{(L_{avg} - 1)}{L_{avg}} \cdot Q\left(\frac{\alpha}{\sqrt{N_0/2}}\right) + \frac{1}{L_{avg}} \cdot Q\left(\frac{\sqrt{E} - \alpha}{\sqrt{N_0/2}}\right)\right]. \quad (4.20)$$

In this expression, the first term represents the probability of a zero and the second term is the probability of that zero being correctly detected. The third term is simply the probability of error for the current slot, as given in (4.13) for DPIM(NGB).

(iv) *The previous slot was a zero but was falsely detected as a one.*

If the previous slot was falsely detected as a one, the current slot is incorrectly assumed to be a guard slot and the receiver automatically assigns a zero to it. If the current slot should be a one, then an error will occur. The probability of this occurring is given by:

$$P_{e,slot} = \frac{(L_{avg} - 1)}{L_{avg}} \cdot Q\left(\frac{\alpha}{\sqrt{N_0/2}}\right) \cdot \frac{1}{L_{avg}}. \quad (4.21)$$

The first term represents the probability of a zero, the second term is the probability of that zero being falsely detected as a one, and the third term is the probability that the following slot is a one.

Thus, putting these possible scenarios together in one expression, the probability of slot error for DPIM(1GS) is given by:

$$P_{e,slot,DPIM(1GS)} = \left[\frac{1}{L_{avg}} \cdot Q\left(\frac{\sqrt{E} - \alpha}{\sqrt{N_0/2}}\right) \cdot Q\left(\frac{\alpha}{\sqrt{N_0/2}}\right) \right] + \left[\frac{(L_{avg} - 1)}{L_{avg}} \cdot \left[1 - Q\left(\frac{\alpha}{\sqrt{N_0/2}}\right) \right] \cdot \left[\frac{(L_{avg} - 1)}{L_{avg}} \cdot Q\left(\frac{\alpha}{\sqrt{N_0/2}}\right) + \frac{1}{L_{avg}} \cdot Q\left(\frac{\sqrt{E} - \alpha}{\sqrt{N_0/2}}\right) \right] \right] + \left[\frac{(L_{avg} - 1)}{L_{avg}} \cdot Q\left(\frac{\alpha}{\sqrt{N_0/2}}\right) \cdot \frac{1}{L_{avg}} \right]. \quad (4.22)$$

Using the optimum threshold level, as discussed in section 4.6.3, the average optical power requirements and bandwidth requirements of DPIM(1GS) are plotted in Fig. 4.15 for various L . The performance of the scheme on nondistorting AWGN channels is discussed in section 4.6.4. As previously mentioned, the average optical power requirement in Fig. 4.15 is normalized to that required by OOK-NRZ to send 1 kByte packets at an average PER of 10^{-6} , and the bandwidth requirement is also normalized to OOK-NRZ.

4.6.3 Optimum threshold level

Assume OOK is used to transmit an information sequence comprising of IID random data, and the transmitted signal is corrupted by signal-independent AWGN. If the received signal is passed through a matched filter and sampled at the optimum point, let s_0 denote the sample value of any given bit in the sequence. There are two conditional probability density functions for s_0 , depending on whether a one or a zero was sent, as illustrated in Fig. 4.11.

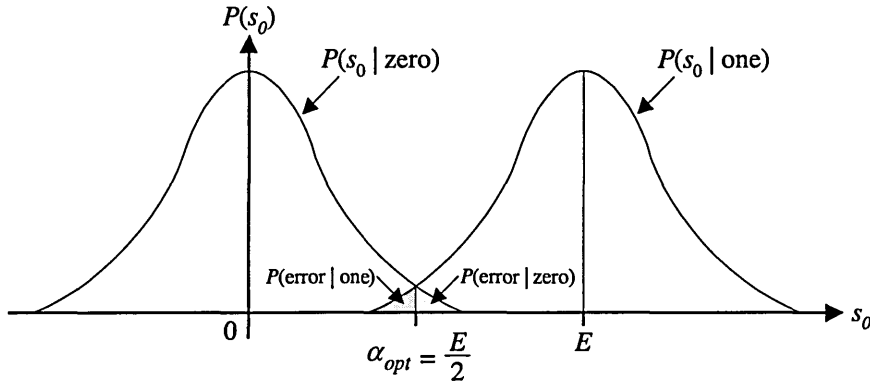


Fig. 4.11: Conditional probability density functions of s_0
in the presence of signal independent AWGN

Since the AWGN is independent of the signal, the probability density functions are symmetrical, and are given by [95]:

$$P(s_0 | zero) = \frac{1}{\sqrt{2\pi}\sigma} \cdot e^{-\frac{s_0^2}{2\sigma^2}}, \quad (4.23)$$

$$P(s_0 | one) = \frac{1}{\sqrt{2\pi}\sigma} \cdot e^{-\frac{(s_0 - E)^2}{2\sigma^2}}, \quad (4.24)$$

where $P(s_0 | zero)$ is the probability of s_0 given that a zero was sent, $P(s_0 | one)$ is the probability of s_0 given that a one was sent, and σ is the standard deviation of the AWGN. A decision is made by comparing s_0 with the threshold level α , and assigning a one if $s_0 > \alpha$ and

a zero otherwise. There are two possible ways in which errors can arise. If a one was sent and $s_0 < \alpha$, an erasure error occurs, as illustrated by the shaded area to the left of α in Fig. 4.11.

The probability of erasure error is given by [95]:

$$P(error | one) = \int_{-\infty}^{\alpha} P(s_0 | one) ds_0. \quad (4.25)$$

Similarly, if a zero was sent and $s_0 > \alpha$, a false alarm error occurs, as illustrated by the shaded area to the right of α in Fig. 4.11. The probability of false alarm error is given by [95]:

$$P(error | zero) = \int_{\alpha}^{\infty} P(s_0 | zero) ds_0. \quad (4.26)$$

Thus, the overall probability of error is given by [95]:

$$P(error) = P(one) \cdot \int_{-\infty}^{\alpha} P(s_0 | one) ds_0 + P(zero) \cdot \int_{\alpha}^{\infty} P(s_0 | zero) ds_0. \quad (4.27)$$

The optimum threshold level, i.e. that which minimises the probability of error, may be found by differentiating (4.27) with respect to α , and then solving for the threshold level that set the derivative equal to zero [95, 96]. In the case of OOK, since ones and zeros are equally likely and the probability distributions are identical, the optimum threshold level occurs at the point at which the two conditional probability density functions intersect, which is midway between expected one and zero levels [96, 135]. Thus, for OOK, $\alpha_{opt} = E/2$.

With the exception of 2-DPIM(NGB), for all orders of DPIM(NGB) and DPIM(1GS), the probability of receiving a zero is greater than the probability of receiving a one. Therefore, the

optimum threshold level does not lie midway between expected one and zero levels. Intuitively, since zeros are more likely, it is apparent that the probability of error can be improved by using a threshold level which is slightly higher than the midway value. This increases the probability of correctly detecting a zero, at the expense of increasing the probability of an erasure error. However, since zeros are more likely, an overall improvement in average error performance is achieved.

Generally, the cost of mistaking a zero for a one is the same as the cost of mistaking a one for a zero. In this case, if the probability densities are scaled by the *a priori* probabilities given in (4.14), then the optimum threshold level occurs where the probability densities intersect [135], as illustrated in Fig. 4.12.

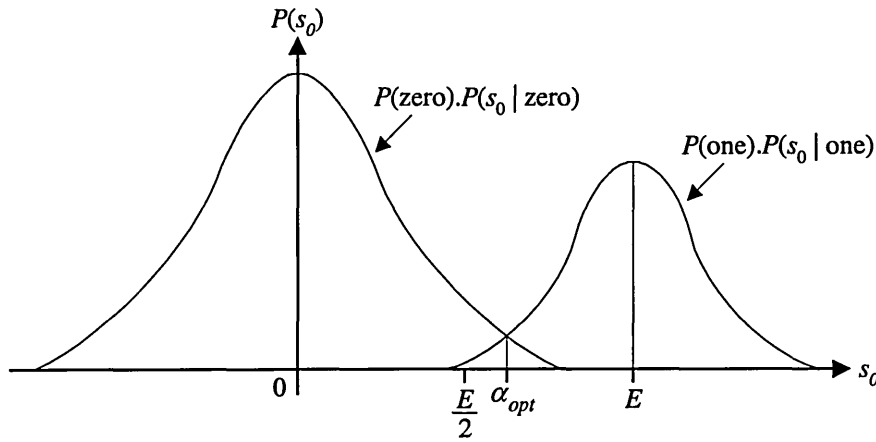


Fig. 4.12: Scaled conditional probability density function of s_0 for $P(\text{zero}) > P(\text{one})$

At the point of intersection,

$$P(\text{one}) \cdot \frac{1}{\sqrt{2\pi}\sigma} \cdot e^{-\frac{(s_0-E)^2}{2\sigma^2}} = P(\text{zero}) \cdot \frac{1}{\sqrt{2\pi}\sigma} \cdot e^{-\frac{s_0^2}{2\sigma^2}}. \quad (4.28)$$

Therefore, the optimum threshold level is equal to the value of s_0 which satisfies:

$$f(s_0) = P(one) \cdot \frac{1}{\sqrt{2\pi}\sigma} \cdot e^{-\frac{(s_0-E)^2}{2\sigma^2}} - P(zero) \cdot \frac{1}{\sqrt{2\pi}\sigma} \cdot e^{-\frac{s_0^2}{2\sigma^2}} = 0. \quad (4.29)$$

In order to find the optimum threshold level from (4.29), the Newton-Raphson procedure for solving nonlinear equations may be used. The Newton-Raphson iteration procedure for obtaining an approximation to the root of $f(x)$ is given by [136]:

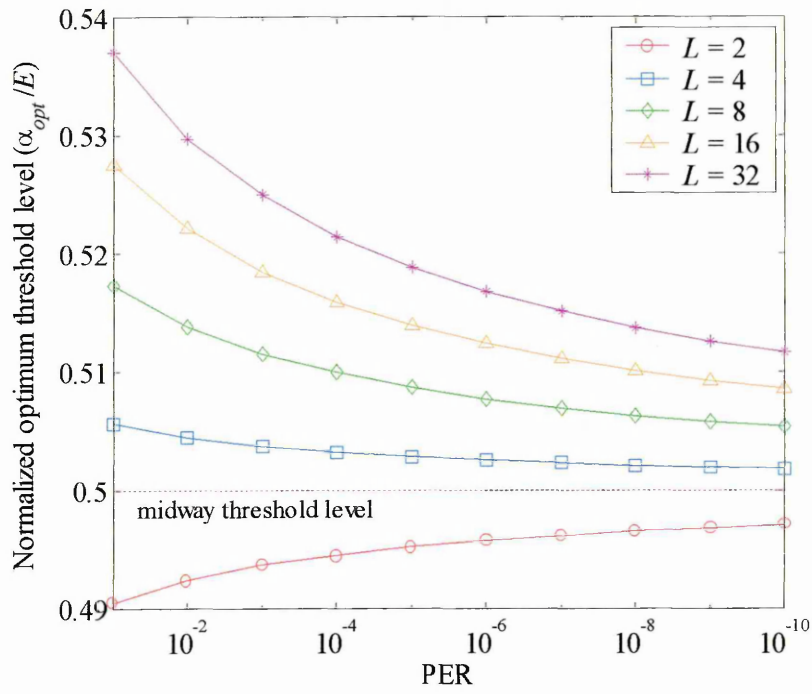
$$x_{n+1} = x_n - \frac{f(x_n)}{f'(x_n)} \quad (n = 0, 1, 2, \dots). \quad (4.30)$$

Thus, differentiating (4.29) with respect to s_0 :

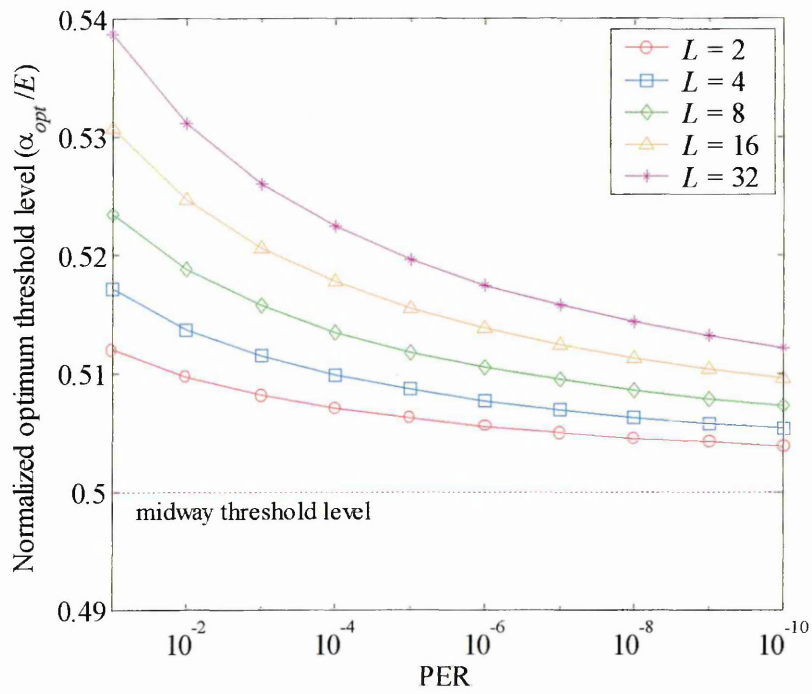
$$f'(s_0) = P(one) \cdot \frac{(s_0 - E)}{\sigma^2} \cdot e^{-\frac{(s_0-E)^2}{2\sigma^2}} - P(zero) \cdot \frac{s_0}{\sigma^2} \cdot e^{-\frac{s_0^2}{2\sigma^2}} = 0. \quad (4.31)$$

Starting with an initial guess of a midway threshold level, i.e. $\alpha = E/2$, the Newton-Raphson method finds the optimum threshold level to a good degree of accuracy after several iterations.

For various PERs, based on a packet length of 1 kByte, the optimum threshold level was determined iteratively for various orders of DPIM(NGB) and DPIM(1GS). The method used to achieve this involves making an initial guess for P_{avg} , and then iteratively determining the optimum threshold level and hence, the minimum PER. This value is then compared with the target PER and, if necessary, P_{avg} is adjusted and the whole process repeated until the target PER is reached. The optimum threshold level versus PER for DPIM(NGB) and DPIM(1GS) are plotted in Figs. 4.13(a) and 4.13(b), respectively. In both figures, the optimum threshold level is normalized to the expected matched filter output when a one is transmitted.



(a)



(b)

Fig. 4.13: Normalized optimum threshold level versus PER:

(a) DPIM(NGB), and (b) DPIM(IGS)

From Figs. 4.13(a) and (b) it is clear that as the probability of error falls, i.e. as the SNR increases, the optimum threshold level tends towards the midway value for both DPIM(NGB) and DPIM(1GS). With the exception of moving from 2-DPIM(NGB) to 4-DPIM(NGB), it is also evident that increasing L moves the optimum threshold level further away from the midway value. For example, at a PER of 10^{-6} , the optimum threshold level for 4-DPIM(NGB) is 0.5 % above the midway value, and this increases to ~3.3 % when 32-DPIM(NGB) is used. This is due to the fact that increasing the number of bits per symbol increases $P(\text{zero})$ and decreases $P(\text{one})$, thereby moving the point of intersection of the scaled conditional probability density functions further away from the midway value. 2-DPIM(NGB) is the one case where the probability of a one is greater than the probability of a zero. Consequently, the optimum threshold level lies below the midway value. Increasing the order from 2-DPIM(NGB) to 4-DPIM(NGB) actually brings the *a priori* probabilities closer together, and consequently results in an optimum threshold level which is closer to the midway value. Comparing DPIM(NGB) and DPIM(1GS), for any given L and PER, the normalized optimum threshold level is slightly higher for DPIM(1GS). This is due to the fact that the presence of the guard slot increases $P(\text{zero})$ and reduces $P(\text{one})$, which consequently increases the optimum threshold level slightly. The difference between the two schemes is more pronounced for small values of L , where adding a guard slot has a more significant effect on the *a priori* probabilities. As an example, for a PER of 10^{-6} , adding a guard slot increases the normalised optimum threshold level by ~1 % for $L = 4$, whilst the increase is just ~0.2 % for $L = 32$. Nevertheless, for an average PER of 10^{-6} , the optimum threshold level is within 3.5 % of the midway value for all orders of DPIM(NGB) and DPIM(1GS) considered.

In order to quantify the extent to which the choice of threshold level affects error performance, the average optical power penalty incurred when using a midway threshold level as oppose to the optimum level is plotted in Fig. 4.14 for both DPIM(NGB) and DPIM(1GS). The power penalties are based on a PER of 10^{-6} and a packet length of 1 kByte.

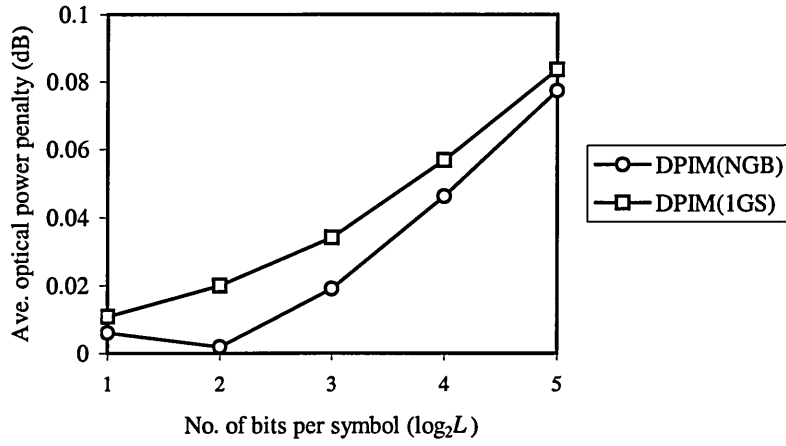


Fig. 4.14: Average optical power penalty incurred when using a midway threshold level versus number of bits per symbol for DPIM(NGB) and DPIM(1GS)

From Fig. 4.14 it is clear that, in terms of average optical transmit power, there is very little difference between using a midway threshold level and the optimum value. For both DPIM(NGB) and DPIM(1GS), the power penalty increases as the number of bits per symbol is increased, due to the fact that the *a priori* probabilities move further apart. The one exception to this is moving from 2-DPIM(NGB) to 4-DPIM(NGB), which lowers the power penalty due to the fact that, as previously stated, the *a priori* probabilities move closer together. The power penalties for DPIM(1GS) are slightly higher than they are for DPIM(NGB), again due to the *a priori* probabilities being further apart for any given L . Of the schemes considered, 32-DPIM(1GS) benefits the most from using an optimum threshold level, but this still only yields a mere ~ 0.08 dB reduction in average optical transmit power compared with a midway threshold level.

4.6.4 Performance comparison

In order to compare the performance of DPIM(NGB) and DPIM(1GS) on a nondistorting channel limited by AWGN, the average optical power requirement versus bandwidth requirement is plotted for both schemes in Fig. 4.15. To aid comparison, similar curves are also

plotted for OOK and PPM. Note that following [120, 121], the average optical power requirement is normalized to that required by OOK-NRZ to send 1 kByte packets at an average packet error rate of 10^{-6} . The bandwidth requirement is also normalized to OOK-NRZ.

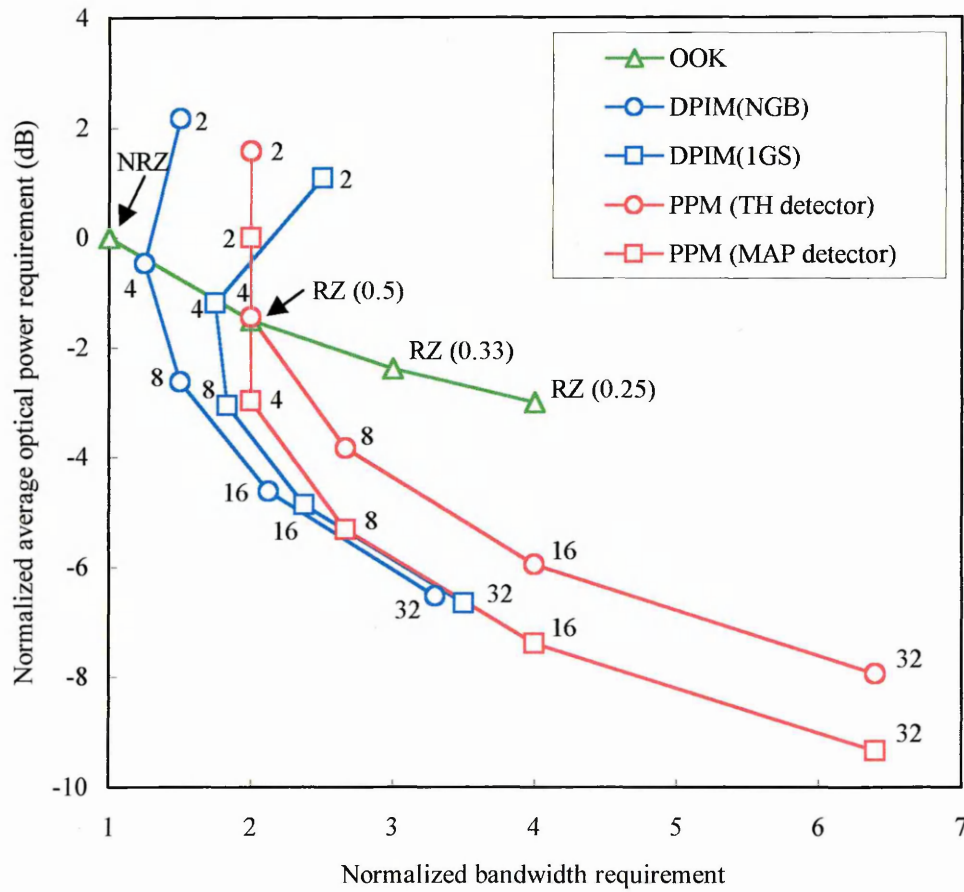


Fig. 4.15: Normalized average optical power requirement versus normalized bandwidth requirement for various modulation techniques operating on a nondistorting AWGN channel

In a similar manner to PPM, both DPIM(NGB) and DPIM(1GS) yield an average optical power requirement which decreases steadily as L increases. For any given L , due to the inclusion of a guard slot, DPIM(1GS) has a lower average duty cycle compared with DPIM(NGB), and consequently achieves a higher peak-to-mean power ratio. As a result, DPIM(1GS) has a slightly lower average optical power requirement compared with DPIM(NGB), which is achieved at the expense of a slightly higher bandwidth requirement. As L increases, the

difference in performance between the two DPIM schemes diminishes, since the inclusion of a guard slot has less effect on the average duty cycle for larger values of L .

Comparing the performance of the two DPIM schemes with OOK, it is evident that there is little point in using DPIM to encode a single bit per symbol, since OOK-NRZ outperforms 2-DPIM(NGB) and 2-DPIM(1GS) both in terms of power efficiency and bandwidth efficiency. For $L > 2$, both DPIM schemes yield a reduction in average optical power requirement compared with OOK-NRZ, at the expense of an increased bandwidth requirement.

Comparing the performance of both DPIM schemes with PPM using a threshold detector, it is clear that, for a given number of bits per symbol, PPM(TH) has a lower average power requirement compared with DPIM, all be it at the expense of an increased bandwidth requirement. This is due to the fact that each PPM symbol has a fixed duty cycle of $1/L$, whereas DPIM symbols have a variable duty cycle, the average of which is higher than $1/L$. Consequently, for any given L , PPM yields a higher peak-to-mean power ratio than both DPIM(NGB) and DPIM(1GS). However, for any given L , DPIM symbols contain, on average, only approximately half the number of slots of PPM symbols. By exploiting this fact, DPIM can encode an additional bit per symbol, thereby giving an improvement in both power efficiency and bandwidth efficiency over PPM(TH). To highlight this point, consider the performance of 32-DPIM(1GS) and 16-PPM(TH). 32-DPIM(1GS) has an average duty cycle of $1/17.5$ compared with $1/16$ for 16-PPM. Consequently, due to its higher peak-to-mean power ratio, 32-DPIM(1GS) requires ~ 0.7 dB less average optical power than 16-PPM(TH). In addition to this, since 32-DPIM(1GS) encodes 5 bits per symbol, it has a normalized bandwidth requirement of 3.5, compared with 4 for 16-PPM.

Compared with PPM using a MAP detector, encoding an additional bit per symbol allows 4-DPIM(NGB) and 4-DPIM(1GS) to offer an improvement in both power efficiency and bandwidth efficiency over 2-PPM(MAP). 8-DPIM(1GS) also yields a small improvement in power efficiency and bandwidth efficiency over 4-PPM(MAP), whilst 8-DPIM(NGB) is slightly

less power efficient. However, for $L \geq 8$, encoding an extra bit per symbol is not sufficient to make DPIM more power efficient than PPM(MAP). As an example, 32-DPIM(1GS) requires a ~ 0.7 dB increase in average optical power requirement in order to achieve the same level of performance as 16-PPM(MAP).

4.7 Summary

In this chapter, the basic properties of DPIM have been presented, and its performance on nondistorting AWGN channels has been analysed. DPIM has been shown to offer a number of advantages over OOK and PPM, making it a worthy contender for use in indoor optical wireless communication systems. The unique symbol structure of DPIM results in a simplified receiver design, since symbol synchronisation is not required. In addition to this, DPIM is a more bandwidth efficient modulation technique compared with PPM, since DPIM symbols contain, on average, fewer slots than PPM symbols, for any given L . As an example, 16-DPIM(NGB) requires just ~ 53 % of the bandwidth required by 16-PPM. Unfortunately, this fact also means that DPIM has an inferior peak-to-mean power ratio compared with PPM, which results in an increased average optical power requirement. Comparing the same two codes, 16-DPIM(NGB) has a ~ 1.3 dB higher average optical power requirement than 16-PPM(TH). However, by encoding an additional bit per symbol, DPIM can outperform PPM using a threshold detector both in terms of power efficiency and bandwidth efficiency. As an example of this, 32-DPIM(NGB) has a ~ 0.6 dB lower average optical power requirement than 16-PPM(TH), and requires 17.5 % less bandwidth. If MAP detection is used, then PPM offers a lower average optical power requirement than DPIM(NGB) and DPIM(1GS) for $L \geq 8$, though this is achieved at the expense of a more complex receiver structure.

Adding a guard band to each DPIM symbol increases the peak-to-mean power ratio of the scheme, and thus results in a lower average optical power requirement, which is achieved at the

expense of a slightly higher bandwidth requirement. For example, 16-DPIM(1GS) has a ~0.2 dB lower average optical power requirement than 16-DPIM(NGB), but requires ~12 % more bandwidth. However, the main objective of the guard band is to provide a simple means of making the scheme more resistant to ISI resulting from multipath propagation. This subject is discussed in detail in chapter 6.

Whilst DPIM is a more bandwidth efficient scheme compared with PPM, it does have a greater proportion of its power located in the vicinity of DC. Although small in comparison with OOK, this fact does suggest that DPIM will be more sensitive to the effects of baseline wander compared with PPM. Consequently, this will limit the maximum electrical high-pass filter cut-on frequency which can be used, thereby making it a less effective method for mitigating the interference emanating from artificial sources of ambient light. This subject is focussed on in chapter 5.

Thus, DPIM is a promising modulation technique for use in indoor optical wireless communication systems. However, in order to provide a better assessment of its suitability, the performance of the scheme must be evaluated in the presence of artificial light interference and multipath dispersion. This analysis is carried out in chapters 5 and 6, respectively.

Chapter 5

The Effect of Ambient Light Sources on Link Performance

5.1 Introduction

Infrared transceivers operating in typical indoor environments are subject to intense ambient light, emanating from both natural and artificial sources. The average power of this background radiation generates shot noise, which is accurately modelled as white, Gaussian and independent of the received signal [18]. In addition to this, artificial sources of ambient light also generate a periodic interference signal, which has the potential to significantly degrade link performance. Of all the artificial sources of ambient light, fluorescent lamps driven by electronic ballasts are potentially the most degrading, since the resulting interference signal contains harmonics of the switching frequency which can extend into the MHz range [15, 16]. Consequently, in this chapter, consideration is limited to this type of interference source.

The most widely adopted technique used to mitigate the effect of ambient light interference is electrical high-pass filtering, which may be achieved in practice by tuning the AC coupling between successive amplifier stages [15]. However, whilst electrical high-pass filtering may be effective in attenuating the interference signal, it also introduces a form of ISI known as baseline wander, which is more severe for baseband modulation techniques which contain a significant amount of power at DC and low frequencies. The higher the high-pass filter (HPF) cut-on frequency, the greater the attenuation of the interference signal, but also the more severe the baseline wander. Thus, a trade off exists between the extent of fluorescent light interference rejection and the severity of baseline wander [89, 137]. In this chapter, electrical high-pass filtering is investigated as a means of mitigating the effect of high frequency fluorescent light interference. This analysis includes the effect of baseline wander, and determines optimum HPF cut-on frequencies which minimize the overall power penalty.

In terms of operating environment, there are numerous factors which affect the performance of an indoor infrared wireless system, such as: the number, type and location of artificial light sources within a room; the location, orientation and directionality of the transmitter and receiver; the existence of natural ambient light, and if so, the size and location of windows, along with the weather conditions. Due to the existence of such a large number of factors, it is convenient to evaluate the performance by considering a typical indoor environment. To facilitate comparison with published research in this area, two cases of ambient light conditions first chosen by Moreira *et. al.* [15] in a similar study are used. These cases are as follows:

Case 1: No interference:

Natural (solar) ambient light, generating an average photocurrent I_B of 200 μA .

Case 2: Fluorescent light interference:

Natural ambient light as in case 1, plus electronic ballast driven fluorescent light, generating an average photocurrent of 2 μA , thus giving a total average background photocurrent of 202 μA .

The major differences between electronic ballast driven fluorescent lamps offered by different manufacturers are the switching frequency used, which are typically in the range 20 - 40 kHz, and the relative strengths of the high frequency and low frequency components [84, 85]. Unlike the case of lamps driven by the power line, emissions from lamps driven by different electronic ballasts are generally not synchronised. Hence, for a given time-averaged fluorescent-induced photocurrent, corresponding to a given level of illumination, the waveform from one or more tubes driven by a single ballast will generally have the greatest possible amplitude excursion and slope, and will thus represent the worst case [16]. In this analysis, the fluorescent light interference signal is generated using the model developed by Moreira *et. al.* [84, 85].

In this chapter, the performance of DPIM(NGB) and DPIM(1GS) operating at bit rates of 1, 10 and 100 Mbit/s is considered. For comparison, OOK-NRZ (hereafter referred to as OOK), PPM(TH) and PPM(MAP) are also evaluated. Throughout the chapter, all power requirements are normalized to the average optical power required by OOK to send 1 Kbyte packets at an average PER of 10^{-6} when operating at 1 Mbit/s in the absence of fluorescent light interference and electrical high-pass filtering. The remainder of this chapter is organised as follows. Section 5.2 describes the model used to generate the fluorescent light interference signal. In section 5.3, numerical analysis is used to evaluate the performance of the three schemes in the presence of fluorescent light interference without high-pass filtering. Section 5.4 examines the effect of the baseline wander introduced by the high-pass filter, in the absence of fluorescent light interference. In section 5.5, optimum high-pass filter cut-on frequencies are determined, and using these optimum values, power penalties are estimated in order to evaluate the effectiveness of high-pass filtering in mitigating the effect of fluorescent light interference. Finally, the main findings of the chapter are summarized in section 5.6.

5.2 Fluorescent Lamp Model

Based on extensive measurements of a variety of fluorescent lamps driven by electronic ballasts, Moreira *et. al.* produced a model to describe the interference signal [84, 85]. All measurements were taken using an optical long-pass filter, and consequently, the values used in the model reflect this particular case. The interference signal is comprised of a low frequency component, similar to that of a fluorescent lamp driven by a conventional ballast, and a high frequency component, which is generated by the switching circuit of the electronic ballast. Thus, the zero mean periodic component of the photocurrent $m_{\mu}(t)$ is given as [84, 85]:

$$m_{\mu}(t) = m_{low}(t) + m_{high}(t). \quad (5.1)$$

The low frequency component may be expressed as [84, 85]:

$$m_{low}(t) = \frac{I_B}{A_1} \sum_{i=1}^{20} [\Phi_i \cos(2\pi(100i - 50)t + \varphi_i) + \Psi_i \cos(2\pi \cdot 100it + \phi_i)], \quad (5.2)$$

where Φ_i and Ψ_i are the amplitudes of the odd and even harmonics of 50 Hz, respectively, given by [84, 85]:

$$\Phi_i = 10^{(-13.1 \cdot \ln(100i - 50) + 27.1)/20} \quad 1 \leq i \leq 20, \quad (5.3)$$

$$\Psi_i = 10^{(-20.8 \cdot \ln(100i) + 92.4)/20} \quad 1 \leq i \leq 20, \quad (5.4)$$

and φ_i and ϕ_i are the phase of the odd and even harmonics of 50 Hz, respectively, as given in Table 5.1. A_1 is the constant that relates the interference amplitude with I_B , taken to be 5.9 in this analysis, and I_B is the average photocurrent generated by the fluorescent lamp, taken to be 2 μA .

i	φ_i (rad)	ϕ_i (rad)	i	φ_i (rad)	ϕ_i (rad)
1	4.65	0	11	1.26	6.00
2	2.86	0.08	12	1.29	6.17
3	5.43	6.00	13	1.28	5.69
4	3.90	5.31	14	0.63	5.37
5	2.00	2.27	15	6.06	4.00
6	5.98	5.70	16	5.49	3.69
7	2.38	2.07	17	4.45	1.86
8	4.35	3.44	18	3.24	1.38
9	5.87	5.01	19	2.07	5.91
10	0.70	6.01	20	0.87	4.88

Table 5.1: Low frequency component phase values

The high frequency component may be expressed as [84, 85]:

$$m_{high}(t) = \frac{I_B}{A_2} \sum_{j=1}^{22} \Gamma_j \cos(2\pi f_{high} j t + \theta_j), \quad (5.5)$$

where Γ_j and θ_j are the amplitude and phase of the harmonics, f_{high} is the electronic ballast switching frequency, and A_2 is the constant that relates the interference amplitude to I_B , taken to be 2.1 in this analysis. The parameters f_{high} , Γ_j and θ_j depend on the type of electronic ballast, and vary from one manufacturer to the next. In this work, f_{high} is taken to be 37.5 kHz and the parameter values given in Table 5.2 represent a particular case with this switching frequency.

j	Γ_j (dB)	θ_j (rad)	j	Γ_j (dB)	θ_j (rad)
1	-22.2	5.09	12	-39.3	3.55
2	0	0	14	-42.7	4.15
4	-11.5	2.37	16	-46.4	1.64
6	-30.0	5.86	18	-48.1	4.51
8	-33.9	2.04	20	-53.1	3.55
10	-35.3	2.75	22	-54.9	1.78

Table 5.2: High frequency component amplitude and phase values

For the chosen switching frequency of 37.5 kHz, there are 750 cycles of the high frequency component per cycle of the low frequency component. With $I_B = 2 \mu\text{A}$, one complete cycle of

the low frequency component and three complete high frequency component cycles of the interference photocurrent are shown in Fig. 5.1.

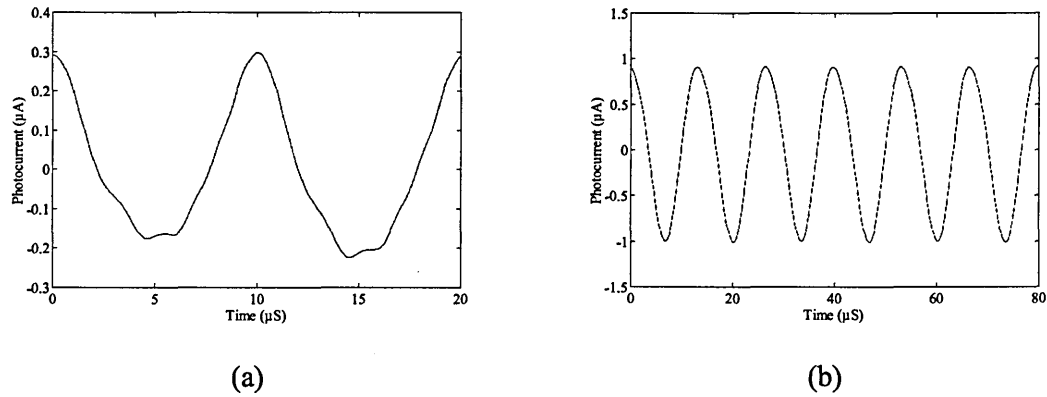


Fig. 5.1: Photocurrent generated by the interference signal:

(a) low frequency component, and (b) high frequency component

5.3 The Effect of Fluorescent Light Interference Without Electrical High-Pass Filtering

5.3.1 OOK

A block diagram of the OOK system under consideration is shown in Fig. 5.2.

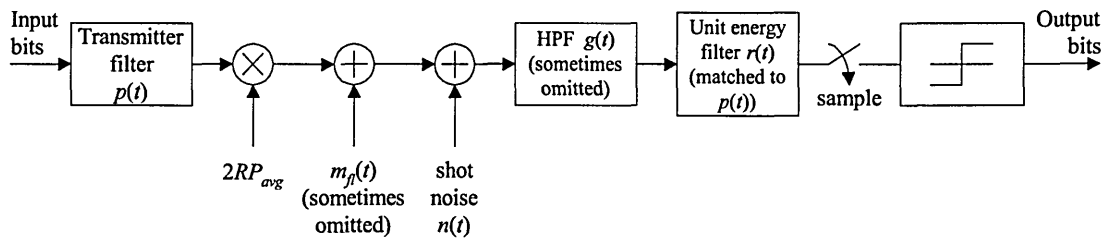


Fig. 5.2: Block diagram of the OOK system

The transmitter filter has a unit-amplitude rectangular impulse response $p(t)$, with a duration of one bit, T_b . The output of the transmitter filter is scaled by the peak detected signal photocurrent $2RP_{avg}$, where R is the photodetector responsivity and P_{avg} is the average received optical signal power. The fluorescent light induced photocurrent, $m_f(t)$, is then added to the signal, along with the signal independent shot noise, $n(t)$, which is modelled as white and Gaussian, with a double-sided power spectral density, $N_o/2$, given as [17]:

$$N_o/2 = qI_B, \quad (5.6)$$

where q is the electron charge and I_B is the average photocurrent generated by the background light, which is taken as 202 μ A. In this section, the HPF is omitted and the detected signal is passed directly to a unit energy filter with an impulse response $r(t)$, which is matched to $p(t)$. The filter output is sampled at the end of each bit period, and a one or zero is assigned depending on whether the signal is above or below the threshold level at the sampling instant. The threshold level is set to its optimum value of $\alpha_{opt} = RP_{avg}\sqrt{T_b}$, which is midway between expected one and zero levels.

The output of the matched filter due to the fluorescent light interference signal, sampled at the end of each bit period, is given as [16]:

$$m_k = m_f(t) \otimes r(t) \Big|_{t=kT_b}, \quad (5.7)$$

where the symbol \otimes denotes convolution. By considering every bit over a 20 ms interval (i.e. one complete cycle of $m_f(t)$) and averaging, the probability of bit error is given as [16]:

$$P_{e,bit,OOK} = \frac{1}{2M} \sum_{k=1}^M \left[Q \left(\frac{RP_{avg}\sqrt{T_b} + m_k}{\sqrt{N_o/2}} \right) + Q \left(\frac{RP_{avg}\sqrt{T_b} - m_k}{\sqrt{N_o/2}} \right) \right], \quad (5.8)$$

where M is the total number of bits over a 20 ms interval. For a given packet length, D , the probability of bit error may be converted into a corresponding PER using the expression derived from [18] as:

$$PER = 1 - (1 - P_{e,bit,OOK})^D. \quad (5.9)$$

In order to achieve viable simulation run times, a number of assumptions are required, as described below:

- i) When analysing OOK operating at 1 Mbit/s, a sampling interval of 200 ns is used when generating the interference signal, giving 5 samples per bit duration. Maintaining 5 samples per bit duration at 100 Mbit/s would result in 10^7 samples per cycle of the interference signal, which is unfeasible. Therefore, when analysing bit rates of 10 Mbit/s and 100 Mbit/s, the sampling interval is held at 200 ns and linear interpolation is used to approximate the values of the interference amplitude in between the actual sample points. Since a sample interval of 200 ns gives ~133 samples per high frequency component cycle, linear interpolation should provide reasonably good accuracy.
- ii) With a switching frequency of 37.5 kHz, there are 750 cycles of the high frequency component per cycle of the low frequency component, and hence, the low frequency component may be assumed to be an offset which is constant over the duration of one high frequency component cycle. Rather than evaluating all of the 750 offset values, a single offset is used, which is equal to the RMS value of the low frequency component of the interference signal, taken over one complete cycle, i.e. 20 ms. Thus, two new interference signals are generated, one being a single high frequency cycle plus the offset and the other being a single high frequency cycle minus the offset. For each bit interval, the error probability is calculated for both signals and the mean value is then taken. This gives a

significant reduction in computation time, since only one high frequency cycle needs to be considered in order to evaluate the error probability.

In order to verify the accuracy of this method, the optical power penalty resulting from the fluorescent light interference was calculated using both the exact method and the RMS offset method described above. It was found that for bit rates of 1, 10 and 100 Mbit/s the RMS offset method gives a power penalty which is just 0.23, 0.17 and 0.12 dB less than the exact method, respectively.

iii) For 10 Mbit/s and 100 Mbit/s analysis, only one bit period per sampling interval is evaluated.

Since there are ~133 samples per high frequency component cycle, the variation in amplitude of the interference signal between bit periods within the same sampling interval will be small, and therefore this assumption should not result in a large inaccuracy.

For each bit rate under consideration, the PER was calculated and the average received optical signal power varied until the target PER of 10^{-6} was achieved. The normalized average optical power requirements for OOK, with and without fluorescent light interference, are plotted in Fig. 5.3.

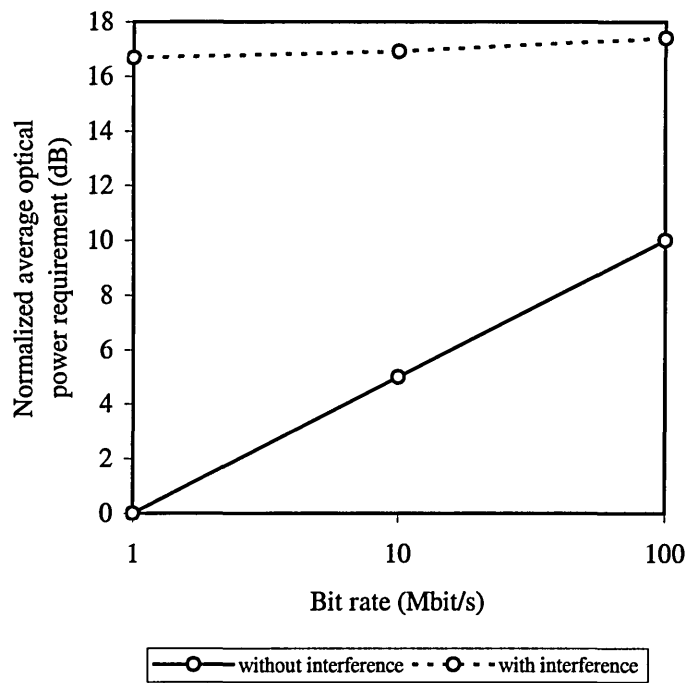


Fig. 5.3 : Normalized average optical power requirement versus bit rate for OOK
with and without fluorescent light interference

From Fig. 5.3 it can be observed that, in the presence of fluorescent light interference, the average optical power required to achieve a given PER is almost the same for all three bit rates under consideration. Relative to the power requirements without interference, power penalties decrease as the bit rate increases. For bit rates of 1, 10 and 100 Mbit/s fluorescent light interference results in significant power penalties of 16.7, 11.9 and 7.4 dB, respectively.

5.3.2 PPM

A block diagram of the PPM system, considering both threshold detection and MAP detection, is shown in Fig. 5.4.

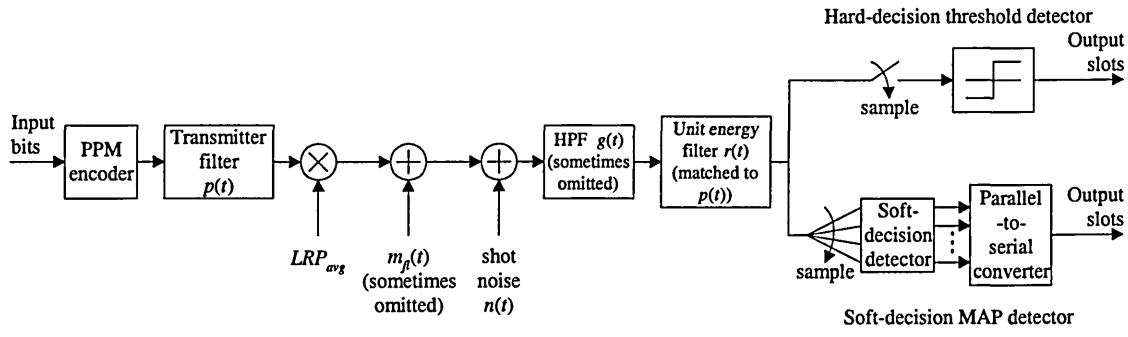


Fig. 5.4: Block diagram of the PPM system

The PPM encoder maps each block of $\log_2 L$ input bits to one of L possible symbols. The symbols are passed to a transmitter filter, which has a unit-amplitude rectangular impulse response $p(t)$, with a duration of one slot T_s , where $T_s = T_b \log_2 L / L$. The output of the transmitter filter is scaled by the peak detected signal photocurrent LRP_{avg} . The fluorescent light interference signal $m_f(t)$ is then added to the signal, along with the shot noise $n(t)$. In this section, the HPF is omitted and the detected signal is passed directly to a unit energy filter with an impulse response $r(t)$, which is matched to $p(t)$. For the threshold detection based receiver, the filter output is sampled at the end of each slot, and a one or zero is assigned depending on whether the signal is above or below the threshold level at the sampling instant. In cases where no sample or more than one sample is above the threshold level, mediation is required. The threshold level is set to $\alpha = R P_{avg} \sqrt{L T_b \log_2 L} / 2$, which is midway between expected one and zero levels. Note that unlike OOK, this represents a suboptimal threshold level. However, in order to overcome the interference, the peak signal power to shot noise ratio must be high, and therefore a midway threshold is actually very close to the optimum value. For the MAP detection based receiver, the filter is sampled at the end of each slot period and each block of L samples are then passed to a soft decision detector, which assigns a one to the slot which contains the largest sample and zeros to the remaining slots.

For the analysis of PPM(TH), a similar approach to that outlined for OOK is employed, but in this case every slot is considered over a 20 ms interval, rather than every bit. The output of the matched filter due to the fluorescent light interference signal, sampled at the end of each slot

period, is given by (5.7), with the sampling times replaced by $t = kT_b \log_2 L/L$. The same assumptions are made in order to keep the run-times manageable, and it is necessary to change the sampling interval slightly in order to ensure that it is a multiple of the slot duration. The probability of slot error for PPM(TH) is given as:

$$P_{e,slot,PPM(TH)} = \frac{1}{N} \sum_{k=1}^N \left[\frac{1}{L} Q \left(\frac{RP_{avg} \sqrt{LT_b \log_2 L/2 + m_k}}{\sqrt{N_o/2}} \right) + \frac{(L-1)}{L} Q \left(\frac{RP_{avg} \sqrt{LT_b \log_2 L/2 - m_k}}{\sqrt{N_o/2}} \right) \right], \quad (5.10)$$

where N is the total number of slots over a 20 ms interval.

For a given packet length, D , the probability of slot error may be converted into a corresponding PER using the expression derived from [18] as:

$$PER = 1 - \left(1 - P_{e,slot,PPM(TH)} \right)^{LD / \log_2 L}. \quad (5.11)$$

For each bit rate and order under consideration, the PER was calculated and the average received optical signal power varied until the target PER of 10^{-6} was achieved. The normalized average optical power requirements for PPM(TH), with and without fluorescent light interference, are shown in Fig. 5.5.

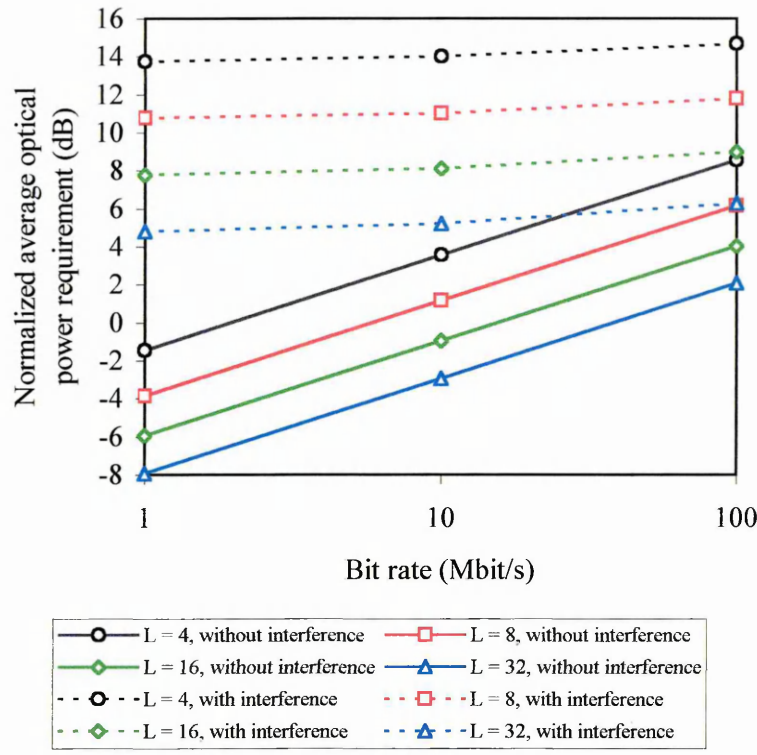


Fig. 5.5: Normalized average optical power requirement versus bit rate for PPM(TH)
with and without fluorescent light interference

Similar to OOK, it is evident from Fig. 5.5 that the average optical power required by PPM(TH) to achieve a given PER in the presence of fluorescent light interference is almost independent of the bit rate. Relative to the power requirements without interference, power penalties at 1 Mbit/s range from 12.8 - 15.2 dB, whilst at 100 Mbit/s the range is 4.2 - 6.1 dB. Whilst these power penalties are slightly lower than those of OOK, they are nevertheless significant.

For PPM(MAP), rather than considering each slot individually, each of the N/L symbols, consisting of L consecutive slots, must be considered together. Thus, for each symbol, a vector $[m_{iL+1} \ m_{iL+2} \ \dots \ m_{iL+L}]$ is defined, where $0 \leq i \leq (N/L)-1$, which represents the matched filter outputs due to the interference signal. A one is then assigned to each of the L slots in turn, and the corresponding probability of symbol error is calculated using the union bound. From these L probabilities, the mean probability of symbol error is then calculated. This process is repeated for the next interference signal vector, and so on until all the symbols have been considered. The

overall probability of symbol error is then found by averaging over all N/L symbols. Assumptions similar to those used in the analysis of OOK and PPM(TH) are made, but this time assumption (iii) is changed such that one symbol period per sampling interval is evaluated, rather than one bit period. Thus, the probability of symbol error for PPM(MAP) is given as [16]:

$$P_{e, \text{symp}, \text{PPM}(\text{MAP})} = \frac{1}{N} \sum_{i=0}^{(N/L)-1} \sum_{j=1}^L \sum_{\substack{k=1 \\ k \neq j}}^L Q \left(\frac{RP_{\text{avg}} \sqrt{L \log_2 L T_b} + m_{iL+j} - m_{iL+k}}{\sqrt{N_o}} \right). \quad (5.12)$$

For a given packet length of D bits, the probability of symbol error may be converted into a corresponding PER using the expression derived from [18] as:

$$\text{PER} = 1 - \left(1 - P_{e, \text{symp}, \text{PPM}(\text{MAP})} \right)^{D/\log_2 L}. \quad (5.13)$$

For each bit rate and order under consideration, the PER was calculated and the average received optical signal power varied until the target PER of 10^{-6} was achieved. The normalized average optical power requirements for PPM(MAP), with and without fluorescent light interference, are shown in Fig. 5.6.

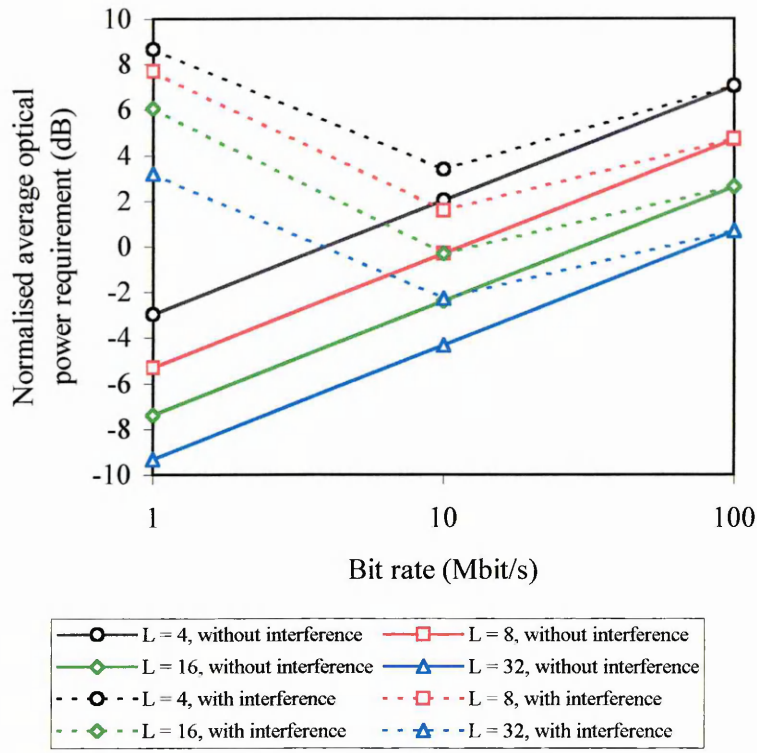


Fig. 5.6: Normalized average optical power requirement versus bit rate for PPM(MAP)
with and without fluorescent light interference

From Fig. 5.6 it is clear that for PPM(MAP), the average optical power required to achieve a given PER in the presence of fluorescent light interference is dependent on the bit rate. Interestingly, for any given L , bit rates of 10 and 100 Mbit/s actually require less average optical power than the 1 Mbit/s case, with 10 Mbit/s yielding the lowest average power requirements. At 1 Mbit/s, power penalties are marginally lower than those of PPM(TH), ranging from 11.6 - 13.5 dB. At 10 Mbit/s, power penalties are down to just 1.3 - 2.1 dB, whilst at 100 Mbit/s, fluorescent light interference does not result in a power penalty for any of the values of L considered. The reduction in power penalty as the bit rate increases is due to the reduced variation of the fluorescent light interference signal over the duration of one symbol. Since, in MAP detection, it is the values of the fluorescent light interference samples relative to other samples within the same symbol which is important, rather than the absolute values, this reduction lowers the probability of symbol error, thus reducing the power penalty.

5.3.3 DPIM

A block diagram of the DPIM system under consideration is shown in Fig. 5.7.

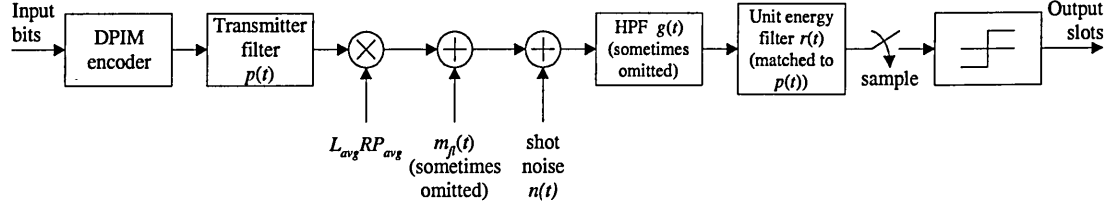


Fig. 5.7: Block diagram of the DPIM system

The DPIM encoder maps each block of $\log_2 L$ input bits to one of L possible symbols. The symbols are passed to a transmitter filter, which has a unit-amplitude rectangular impulse response $p(t)$, with a duration of one slot T_s , where $T_s = T_b \log_2 L / L_{avg}$ and L_{avg} is the average symbol length in slots. The output of the transmitter filter is scaled by the peak detected signal photocurrent $L_{avg} R P_{avg}$. The fluorescent light interference photocurrent $m_f(t)$, is then added to the signal, along with the shot noise $n(t)$. In this section, the high-pass filter is omitted and the detected signal is passed directly to a unit energy filter, which has an impulse response $r(t)$, which is matched to $p(t)$. The filter output is sampled at the end of each slot period, and a one or zero is assigned depending on whether the signal is above or below the threshold level at the sampling instant. The threshold level is set to $\alpha = R P_{avg} \sqrt{L_{avg} T_b \log_2 L} / 2$, which is midway between expected one and zero levels. Again, as with PPM(TH), note that this threshold level is suboptimal.

The output of the matched filter due to the fluorescent light interference signal, sampled at the end of each slot period, is given by (5.7), with the sampling times replaced by $t = k T_b \log_2 L / L_{avg}$.

Following a similar method used for the PPM(TH) analysis, again with the sampling interval changed slightly in order to ensure it is a multiple of the slot duration, the average probability of slot error for DPIM(NGB) is given as:

$$P_{e,slot,DPIM(NGB)} = \frac{1}{N} \sum_{k=1}^N \left[\frac{1}{L_{avg}} Q \left(\frac{RP_{avg} \sqrt{L_{avg} T_b \log_2 L / 2 + m_k}}{\sqrt{N_o / 2}} \right) + \frac{(L_{avg} - 1)}{L_{avg}} Q \left(\frac{RP_{avg} \sqrt{L_{avg} T_b \log_2 L / 2 - m_k}}{\sqrt{N_o / 2}} \right) \right], \quad (5.14)$$

where N is the total number of slots under consideration, and L_{avg} is the average number of slots per symbol, as given in (4.2). For a given packet length of D bits, the probability of slot error may be converted into a corresponding PER using (4.11), with the substitution $L_{avg} = (L + 1)/2$.

For each bit rate and order under consideration, the PER was calculated and the average received optical signal power varied until the target PER of 10^{-6} was achieved. The normalized average optical power requirements for DPIM(NGB), with and without fluorescent light interference, are plotted in Fig. 5.8.

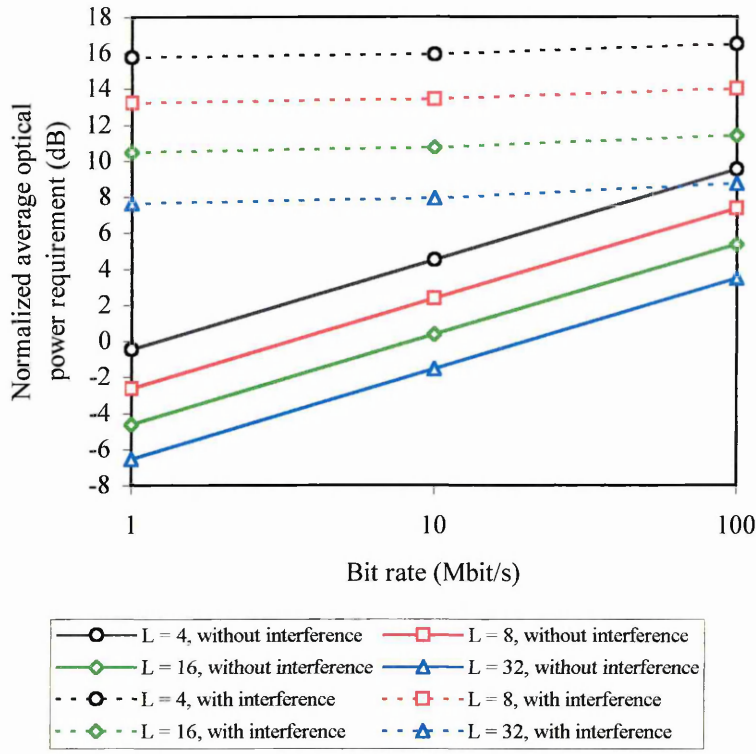


Fig. 5.8: Normalized average optical power requirement versus bit rate for DPIM(NGB)
with and without fluorescent light interference

As previously observed for OOK and PPM(TH), it is evident from Fig. 5.8 that DPIM(NGB) also has average optical power requirements which are very similar for all three bit rates under consideration, when operating in the presence of fluorescent light interference. Again, relative to the power requirements without interference, power penalties are seen to fall as the bit rate increases. DPIM(NGB) has power penalties which are slightly higher than those of PPM(TH), ranging from 14.2 - 16.2 dB at 1 Mbit/s to 5.3 - 7 dB at 100 Mbit/s.

For DPIM(1GS), when calculating the probability of slot error for any given slot, k , it is necessary to consider both m_k and m_{k-1} . The average probability of slot error is given as:

$$\begin{aligned}
P_{slot, DPIM(1GS)} = & \frac{1}{(N-1)} \sum_{k=2}^N \left[P(one) Q\left(\frac{\sqrt{E}/2 + m_{k-1}}{\sqrt{N_o}/2}\right) Q\left(\frac{\sqrt{E}/2 - m_k}{\sqrt{N_o}/2}\right) + \right. \\
& P(zero) \left(1 - Q\left(\frac{\sqrt{E}/2 - m_{k-1}}{\sqrt{N_o}/2}\right)\right) \left(P(one) Q\left(\frac{\sqrt{E}/2 + m_k}{\sqrt{N_o}/2}\right) + P(zero) Q\left(\frac{\sqrt{E}/2 - m_k}{\sqrt{N_o}/2}\right) \right) + \\
& \left. P(zero) Q\left(\frac{\sqrt{E}/2 - m_{k-1}}{\sqrt{N_o}/2}\right) P(one) \right], \quad (5.15)
\end{aligned}$$

where N is the total number of slots under consideration, $\sqrt{E} = RP_{avg} \sqrt{L_{avg} T_b \log_2 L}$ is the expected output of the matched filter due to a one, L_{avg} is the average number of slots per symbol, as given in (4.3), and $P(one)$ and $P(zero)$ are the *a priori* probabilities of getting a pulse and an empty slot, respectively, as given in (4.14). The first term is the probability of slot error for the case when the previous slot is falsely detected as a zero. The second term is the probability of slot error given that the previous slot is correctly detected as a zero, and the third term is the probability of slot error when the previous slot is falsely detected as a one. Again, the probability of slot error may be converted into a corresponding PER using (4.11), with the substitution $L_{avg} = (L+3)/2$.

For each bit rate and order under consideration, the PER was calculated and the average received optical signal power varied until the target PER of 10^{-6} was achieved. The normalized average optical power requirements for DPIM(1GS), with and without fluorescent light interference, are plotted in Fig. 5.9.

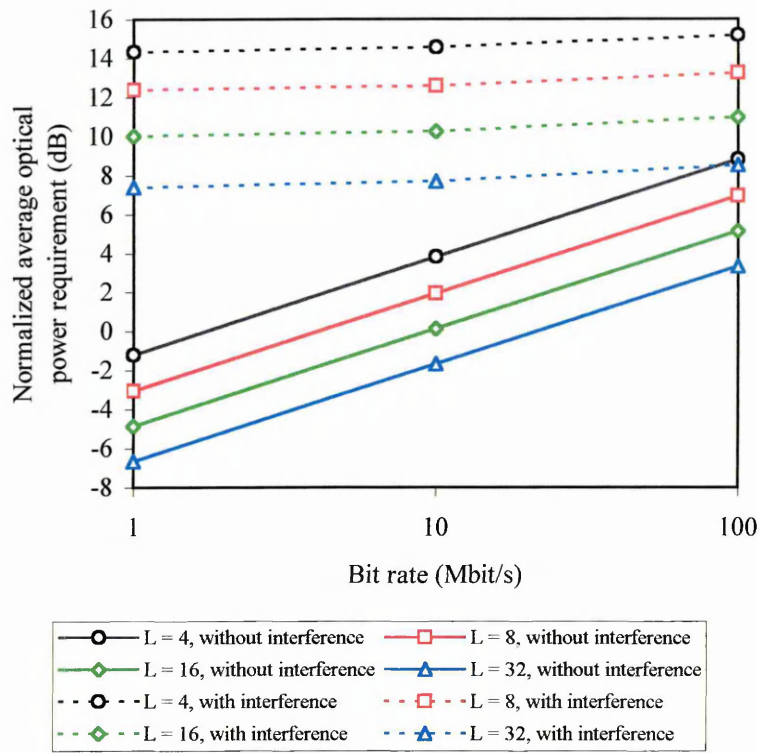


Fig. 5.9: Normalized average optical power requirement versus bit rate for DPIM(1GS)
with and without fluorescent light interference

From Fig. 5.9 it is again evident that when operating in the presence of fluorescent light interference, the power requirements are very similar for all three bit rates under consideration. Compared with DPIM(NGB), for any given L and bit rate, DPIM(1GS) has a marginally lower average optical power requirement. This is due to the fact that the inclusion of a guard band gives a slight improvement in power efficiency, as previously discussed in chapter 4. Again, relative to the power requirements without interference, power penalties are seen to fall as the bit rate increases. At 1 Mbit/s DPIM(1GS) has power penalties of 14.1 - 15.5 dB, which fall to 5.2 - 6.4 dB at 100 Mbit/s.

5.4 The Effect of Baseline Wander Without Fluorescent Light

Interference

A sequence of pulses which is passed through a HPF experiences a variation in the nominal zero level, which at any given time is offset by an amount that is determined by the past history of the pulses [138]. This variation in the nominal zero level is a form of ISI known as baseline wander, which has a detrimental effect on the performance of baseband modulation techniques. In this section, the optical power penalty required to overcome the effect of baseline wander is investigated.

For all the analysis involving high-pass filtering throughout this chapter, the HPF is modelled as a first-order RC filter with a 3 dB cut-on frequency of f_c , and an impulse response denoted as $g(t)$. The response of the HPF to a single rectangular pulse of amplitude A and duration T_b may be expressed as [139]:

$$g_{out}(t) = \begin{cases} Ae^{-t/RC} & 0 \leq t \leq T_b \\ -A(e^{T_b/RC} - 1)e^{-t/RC} & t > T_b \end{cases}, \quad (5.16)$$

where RC is the filter time constant, which is related to the cut-on frequency by $RC = 1/2\pi f_c$.

Due to the principle of superposition of linear systems, if a sequence of such pulses is passed through a HPF, the output is equal to the summation of the individual responses of the pulses within the sequence. Thus, for a bit sequence $A_1 A_2 \dots A_n$, where $A_{1\dots n} \in \{0,1\}$, the output of a first order RC HPF at the end of the n^{th} bit may be expressed as [89]:

$$g_{out}(t)|_{t=nT_b} = \sum_{i=1}^n A_i \left(e^{-2\pi f_c T_b} - 1 \right) \left(e^{-2\pi f_c T_b} \right)^{i-1}. \quad (5.17)$$

To illustrate the effect of baseline wander, consider 5 μs of an 8-DPIM(1GS) sequence, operating at 1 Mbit/s, which is passed through a high-pass filter and then a unit-energy rectangular impulse response filter. Assume the input to the HPF consists of rectangular shaped pulses with an amplitude of 1 V, as shown in Fig. 5.10(a). The output of the HPF for a cut-on frequency of 100 kHz, i.e. $f_c/R_b = 0.1$, is shown in Fig. 5.10(b). The output of the matched filter is shown in Fig. 5.10(c). Note the variation in the peak matched filter output as the pulse density varies, which has a detrimental effect on the error performance.

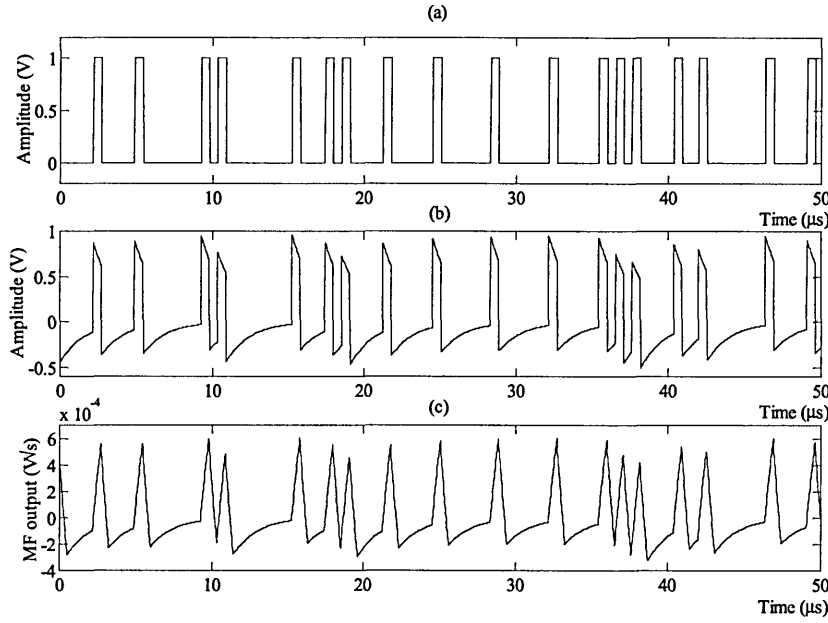


Fig. 5.10: 8-DPIM(1GS) sequence: (a) HPF input, (b) HPF output, and (c) matched filter output

For all the analysis involving high-pass filtering throughout this chapter, sequence lengths are carefully chosen to ensure that the output of the filter has reached a steady state, i.e. the signal has no DC component, prior to any analysis being carried out. Throughout the remainder of this chapter, HPF cut-on frequencies are generally normalized to the bit rate, denoted as f_c/R_b . Consequently, the power penalties calculated in this section (section 5.4) differ to those derived in the rest of this chapter since they are essentially independent of the bit rate.

5.4.1 OOK

The effect of baseline wander on the performance of OOK may be analysed using the system shown in Fig. 5.2, with the high-pass filter present and the fluorescent light interference signal absent.

In order to examine the probability distribution of the baseline wander, an OOK sequence containing 10^5 bits, with $P_{avg} = 1$ W and $R_b = 1$ Mbit/s, was passed through the system. If the DC component of the signal is removed, but the cut-on frequency is sufficiently small to ensure there is no baseline wander, the expected unit energy matched filter outputs for a one and a zero will be $RP_{avg}\sqrt{T_b}$ and $-RP_{avg}\sqrt{T_b}$, respectively. In the absence of noise, a histogram plot of the difference between the expected and actual matched filter output was generated for normalized cut-on frequencies of 10^{-3} and 10^{-2} , as shown in Fig. 5.11. For both histograms, the values are grouped into 51 classes, each having a width of 2×10^{-5} . The solid line in the centre of the middle class indicates a value of zero, i.e. no difference between expected and actual matched filter outputs, which would be the case in the absence of baseline wander.

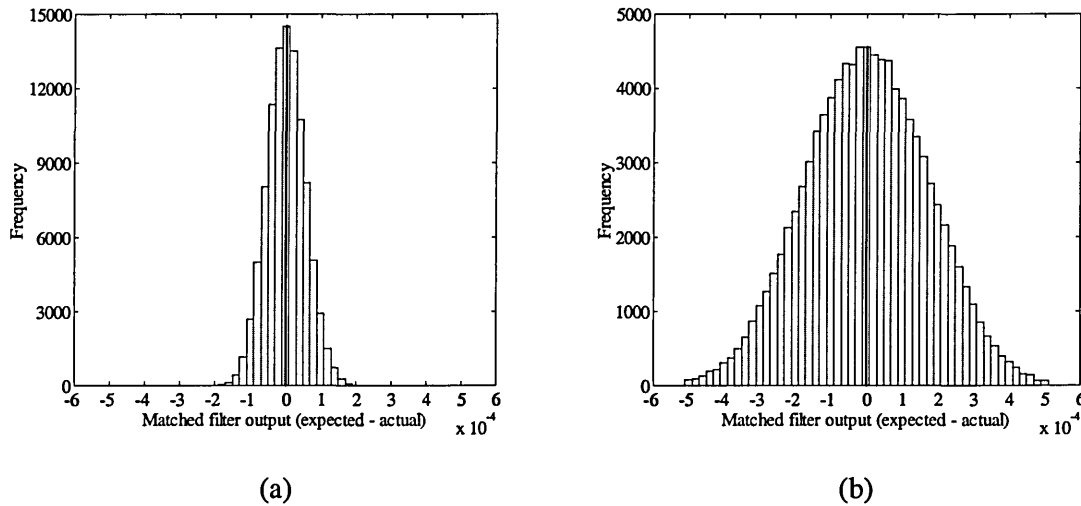


Fig. 5.11: Histogram of matched filter output for OOK with:

(a) $f_c/R_b = 10^{-3}$, and (b) $f_c/R_b = 10^{-2}$

The increase in the variance of the probability distribution as f_c/R_b increases from 10^{-3} to 10^{-2} is evident from the figure. For the relatively low values of f_c/R_b considered, the HPF impulse response spans many bit periods. Accordingly, the ISI introduced by the HPF is comprised of the weighted sum of many IID binary random variables. Therefore, as a result of the central limit theorem, the distribution can be approximated as Gaussian [16], as confirmed by the overall shape of the histograms. Street *et. al.* [140] used this Gaussian approximation to develop closed form expressions for the probability of error due to baseline wander and Gaussian noise for OOK and Manchester encoding. Samaras *et. al.* [89, 137] extended this work, using nonclassical gauss quadrature rules to determine the probability of error, rather than assuming a Gaussian distribution.

The method used to analyse the effect of baseline wander on error performance is as follows: The discrete time equivalent impulse response of the cascaded transmitter filter, high-pass filter and receiver filter is calculated, denoted as c_j . The resulting impulse response has an infinite duration, but because it decays rapidly to zero with time, it can be truncated without significant loss of accuracy [16]. Let the length of the truncated impulse response be denoted as J . The exact method of calculating the BER would then be to generate every possible sequence of bits with a length equal to J , calculate the probability of error for the J^{th} bit in each sequence and then average over all possible sequences. However, in order to keep the computation time practical, this method is only viable for sequence lengths below 20. Simulation has shown that this is not sufficient to accurately quantify the BER for medium values of f_c/R_b . Therefore, rather than generate every possible sequence, K distinct sequences are generated and the probability of error is then found by averaging over K . Before the analysis can be carried out, it is necessary to determine suitable values for J and K , which will give reasonable run-times and yet still maintain a good degree of accuracy. For small values of f_c/R_b ($\sim 10^{-5}$) the HPF impulse response spans many bit periods and hence, long values of J are required. However, the baseline wander effect is almost negligible and hence there is little variation between sequences and consequently small values of K are sufficient. As f_c/R_b increases, the impulse response

decays much more rapidly and hence, shorter sequence lengths may be used. However, the effect of baseline wander is greater and therefore more sequences need to be averaged in order to obtain reliable results. By a process of trial and error, values of $J = 200$ and $K = 50\,000$ were found to give a good compromise between accuracy and computation time.

The discrete time equivalent impulse response, truncated to have a duration of J bit periods, is given as [16]:

$$c_j = \begin{cases} p(t) \otimes g(t) \otimes r(t) \Big|_{t=jT_b} & 1 \leq j \leq J \\ 0 & \text{otherwise} \end{cases}. \quad (5.18)$$

Considering K distinct bit sequences of length J , denoted as $\mathbf{a}_1, \mathbf{a}_2, \dots, \mathbf{a}_K$, let $a_{i,J}$ represent the value of the J^{th} bit in sequence \mathbf{a}_i , where $a_{i,J} \in \{0,1\}$. When \mathbf{a}_i is passed through the system, the matched filter output, sampled at the end of the J^{th} bit period, is given by:

$$A_{i,J} = 2RP_{avg} \mathbf{a}_i \otimes c_j \Big|_{j=J}. \quad (5.19)$$

The BER is then found by averaging over all K sequences:

$$P_{e,bit,OOK} = \frac{1}{K} \sum_{i=1}^K Q\left(\frac{|A_{i,J}|}{\sigma_n}\right), \quad (5.20)$$

where σ_n is the standard deviation of the zero-mean non-white Gaussian noise, given as [89, 137]:

$$\sigma_n = \sqrt{\frac{N_o}{2} \cdot \frac{(1 - e^{-2\pi f_c T_b})}{2\pi f_c} \cdot \frac{1}{T_b}}. \quad (5.21)$$

Note that the optimum threshold level is now zero since the HPF removes the DC component of the signal. A value of $I_B = 200 \mu\text{A}$ is used in (5.6) to generate $N_0/2$, since the fluorescent interference signal is not considered in this section.

For each value of f_c/R_b in the range 10^{-5} to 1, the PER was calculated and the average received optical signal power varied until the target PER of 10^{-6} was achieved. Fig. 5.12 shows a plot of normalized average optical power requirement versus f_c/R_b for OOK.

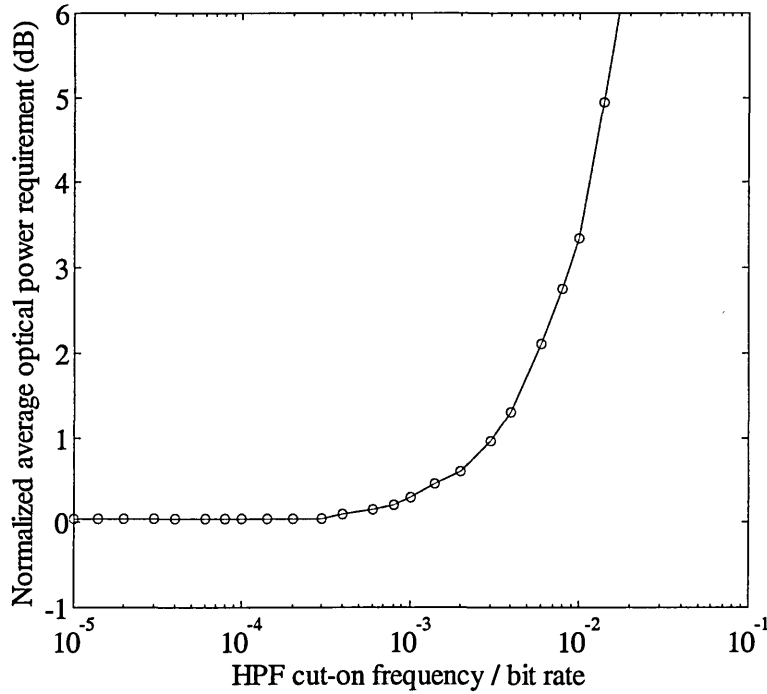


Fig. 5.12: Normalized optical power requirement versus f_c/R_b for OOK

From Fig. 5.12 it is evident that OOK is very susceptible to baseline wander. Power penalties are incurred for normalized cut-on frequencies above $\sim 10^{-3}$, and a 3 dB average optical power penalty is introduced when the HPF cut-on frequency is a mere $\sim 1\%$ of the bit rate.

5.4.2 PPM

The effect of baseline wander on the performance of PPM may be analysed using the system shown in Fig. 5.4, with the HPF present and the fluorescent light interference signal absent.

Again, the probability distribution of the baseline wander was examined, in the absence of noise, using an 8-PPM sequence containing 10^5 slots, with $P_{avg} = 1$ W and $R_b = 1$ Mbit/s. A histogram plot of the difference between the expected matched filter output (in the absence of baseline wander) and the actual matched filter output was generated for a normalized cut-on frequency of 5×10^{-2} , as shown in Fig. 5.11. The values are grouped into 51 classes, each class having a width of 2.5×10^{-5} . The solid line indicates a value of zero, i.e. no difference between expected and actual matched filter outputs, which would be the case in the absence of baseline wander.

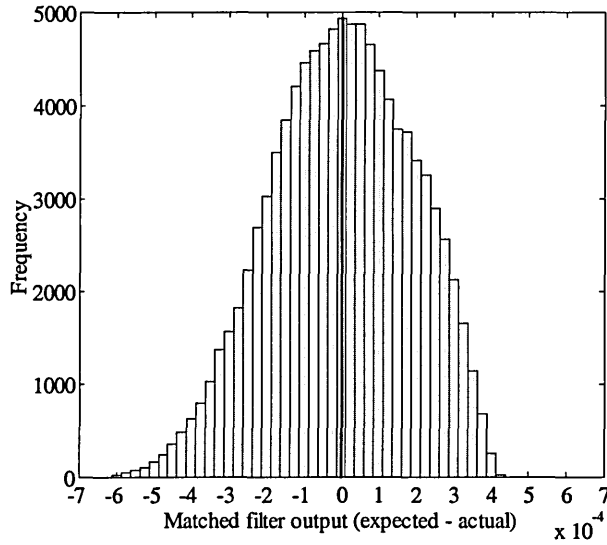


Fig. 5.13: Histogram of matched filter output for 8-PPM with $f_c/R_b = 5 \times 10^{-2}$

Since the PPM slot sequence is not IID and the HPF cut-on frequencies are not necessarily small compared to the bit rate, the probability distribution cannot be assumed to be Gaussian [16].

PPM(TH) may be evaluated in the same way as OOK. The discrete time impulse response given in (5.18) is used, with the sampling times replaced by $t = jT_b \log_2 L/L$. Considering K distinct PPM slot sequences of length J , denoted as $\mathbf{b}_1, \mathbf{b}_2, \dots, \mathbf{b}_K$, let $b_{i,J}$ represent the value of the J^{th} bit in sequence \mathbf{b}_i , where $b_{i,J} \in \{0,1\}$. When \mathbf{b}_i is passed through the system, the matched filter output, sampled at the end of the J^{th} slot period, is given by:

$$B_{i,J} = LRP_{avg} \mathbf{b}_i \otimes \mathbf{c}_J \Big|_{j=J}. \quad (5.22)$$

The probability of slot error is then found by averaging over all K sequences:

$$P_{e,slot,PPM(TH)} = \frac{1}{K} \sum_{i=1}^K Q\left(\frac{|B_{i,J} - \alpha|}{\sigma_n}\right), \quad (5.23)$$

where α is the threshold level, set midway between one and zero levels in the absence of any baseline wander, given as:

$$\alpha = RP_{avg} \sqrt{LT_b \log_2 L} \left(\frac{1}{2} - \frac{1}{L}\right), \quad (5.24)$$

and σ_n is the standard deviation of the zero-mean non-white Gaussian noise, given as:

$$\sigma_n = \sqrt{\frac{N_o}{2} \cdot \frac{(1 - e^{-2\pi f_c T_s})}{2\pi f_c} \cdot \frac{1}{T_s}}, \quad (5.25)$$

where $T_s = T_b \log_2 L/L$. The probability of slot error may then be converted into a PER using (5.11).

For PPM(MAP), the method is similar, but rather than just considering the J^{th} slot in each sequence, the next whole symbol after the J^{th} slot is considered. Therefore, slightly longer sequences must be generated. For sequence k , let the next whole symbol after the J^{th} slot be denoted as $b_{i,p} b_{i,p+1} \dots b_{i,p+L}$, where $p \geq J$. The corresponding outputs of the system are given by (5.22) with the sampling times replaced by $j = p, p+1, \dots p+L$. Assuming that, for the final symbol of each sequence under consideration, the ‘one’ was transmitted in slot $(p + w)$, where $1 \leq w \leq L$, the probability of symbol error for PPM(MAP) is given as:

$$P_{e,\text{symb},\text{PPM}(\text{MAP})} = \frac{1}{K} \sum_{i=1}^K \sum_{\substack{j=1 \\ j \neq p+w}}^L Q\left(\frac{B_{i,p+w} - B_{i,p+j}}{\sigma_n}\right), \quad (5.26)$$

where,

$$\sigma_n = \sqrt{N_o \cdot \frac{(1 - e^{-2\pi f_c T_s})}{2\pi f_c} \cdot \frac{1}{T_s}}. \quad (5.27)$$

Again, this may be converted into a corresponding PER using (5.13).

For each value of f_c/R_b in the range 10^{-5} to 1, and each order under consideration, the PER was calculated and the average received optical signal power varied until the target PER of 10^{-6} was achieved. Figures 5.14 and 5.15 show plots of normalized average optical power requirement versus f_c/R_b for PPM(TH) and PPM(MAP), respectively.

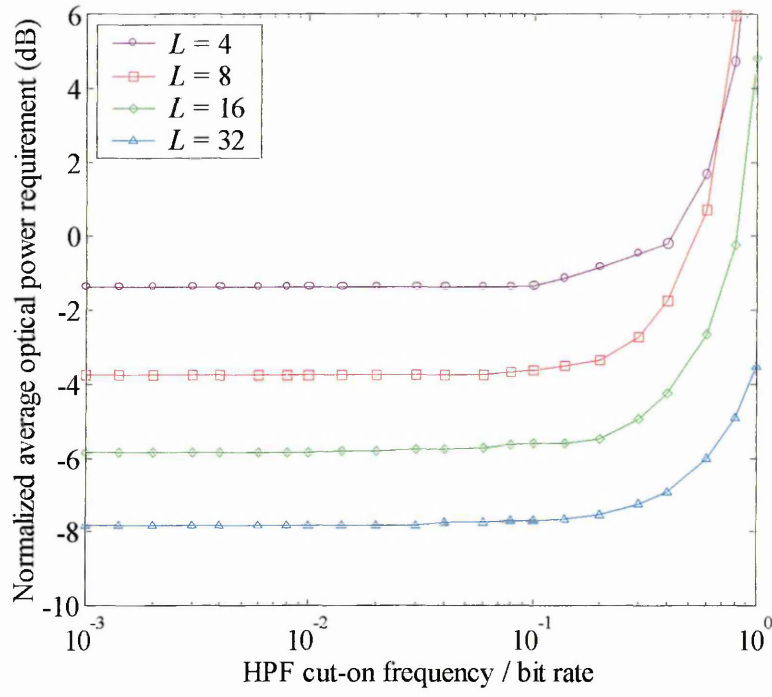


Fig. 5.14: Normalized average optical power requirement versus f_c/R_b for PPM(TH)

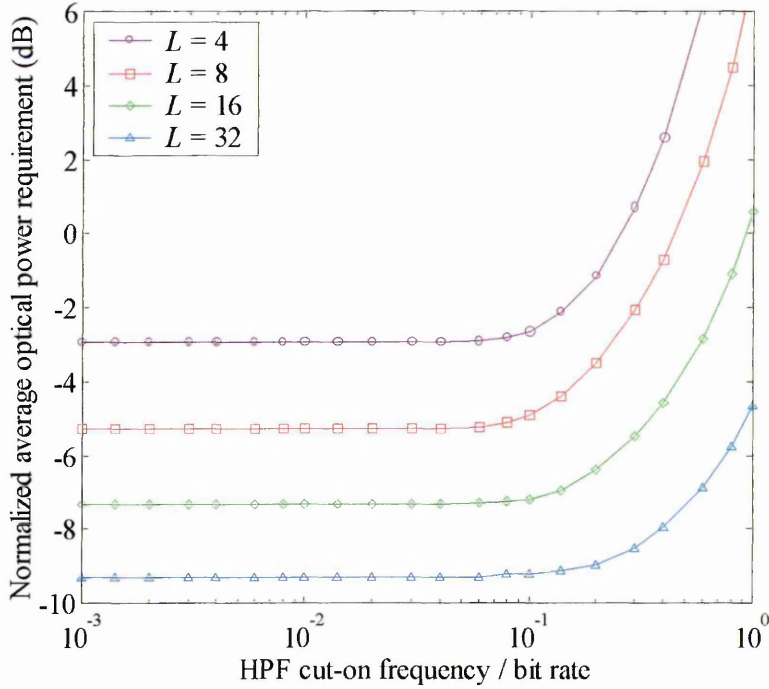


Fig. 5.15: Normalized average optical power requirement versus f_c/R_b for PPM(MAP)

From Figs. 5.14 and 5.15 it is evident that PPM is much more resistant to the effects baseline wander compared with OOK. For both methods of detection, power penalties are not incurred

until the HPF cut-on frequency reaches $\sim 10\%$ of the bit rate, which is several orders of magnitude higher than OOK. Other than the ~ 1.5 dB reduction in optical power penalty which MAP detection offers over threshold detection, there is little difference between the two sets of curves. As expected, higher orders are slightly more resistant to baseline wander since the bandwidth requirement is greater and consequently, there is less power below the cut-on frequency as a fraction of the total power.

5.4.3 DPIM

The effect of baseline wander on the performance of DPIM may be analysed using the system shown in Fig. 5.7, with the HPF present and the fluorescent light interference signal absent.

The probability distribution of the baseline wander was investigated, in the absence of noise, using an 8-DPIM sequence containing 10^5 slots, again with $P_{avg} = 1$ W and $R_b = 1$ Mbit/s. Histograms of the difference between the expected matched filter output (in the absence of baseline wander) and the actual matched filter output were generated for both 8-DPIM(NGB) and 8-DPIM(1GS), with a normalized cut-on frequency of 10^{-2} , as shown in Fig. 5.16. Both histograms use 51 classes, with a class width of 2×10^{-5} . The solid line indicates a value of zero, i.e. no difference between expected and actual matched filter outputs, which would be the case in the absence of baseline wander.

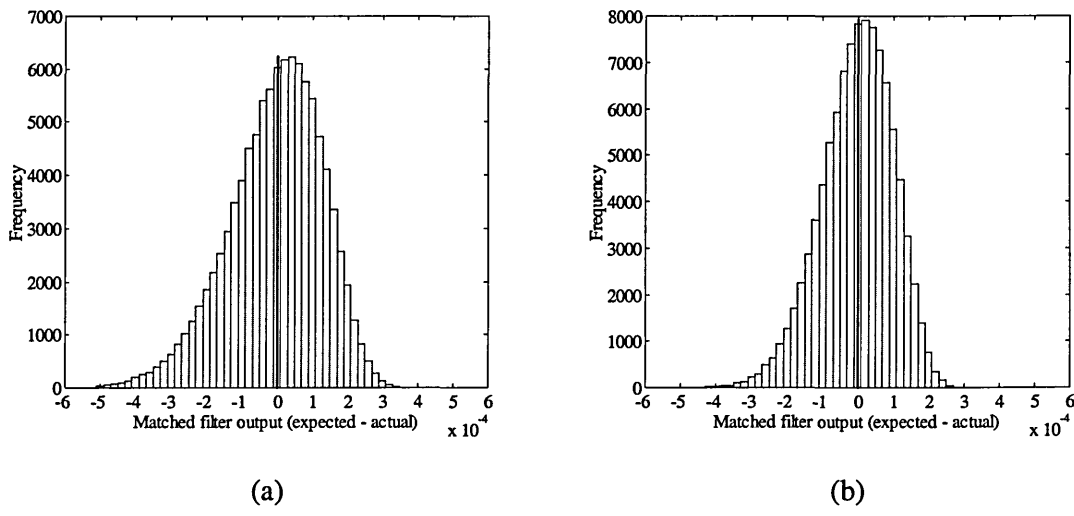


Fig. 5.16: Histogram of matched filter output for 8-DPIM with $f_c/R_b = 10^{-2}$
for: (a) NGB, and (b) 1GS

Again, for the same reason given for PPM, the probability distribution of baseline wander in systems employing DPIM is clearly non-Gaussian. Comparing the two histograms, it is evident that the presence of a guard slot gives a slight reduction in the variance of the distribution. This is due to the fact that, whilst the spectra of the two schemes are very similar, adding a guard slot results in a small increase in bandwidth requirement, thus making the scheme slightly more resistant to baseline wander. This is analogous to the slight improvement noticed with higher order values.

The method used to evaluate OOK and PPM(TH) may also be used to analyse the effect of baseline wander on the performance of DPIM. The discrete time impulse response given in (5.18) is used, with the sampling times replaced by $t = jT_b \log_2 L/L_{avg}$. Considering K distinct DPIM slot sequences of length J , denoted as $\mathbf{b}_1, \mathbf{b}_2, \dots, \mathbf{b}_K$, let $b_{i,J}$ represent the value of the J^{th} bit in sequence \mathbf{b}_i . When \mathbf{b}_i is passed through the system, the matched filter output, sampled at the end of the J^{th} slot period, is given by:

$$B_{i,J} = L_{avg} R P_{avg} \mathbf{b}_i \otimes c_j \Big|_{j=J}. \quad (5.28)$$

The probability of slot error is then found by averaging over all K sequences:

$$P_{e,slot,DPIM(NGB)} = \frac{1}{K} \sum_{i=1}^K Q\left(\frac{|B_{i,J} - \alpha|}{\sigma_n}\right), \quad (5.29)$$

where α is the threshold level, set midway between expected one and zero levels in the absence of any baseline wander, given as [141]:

$$\alpha = RP_{avg} \sqrt{L_{avg} T_b \log_2 L} \left(\frac{1}{2} - \frac{1}{L_{avg}} \right), \quad (5.30)$$

and σ_n is the standard deviation of the zero-mean non-white Gaussian noise, given by (5.25) with the substitution $T_s = T_b \log_2 L / L_{avg}$.

For DPIM(1GS), the expression for the probability of slot error would be unwieldy in the same format as (5.29). Therefore it is more convenient to express the probability of slot error as pseudo code. Let $b_{i,J}$ and $b_{i,J-1}$ represent the values of the J^{th} and $(J-1)^{\text{th}}$ slots in sequence \mathbf{b}_i , where $b_{i,J}$ and $b_{i,J-1} \in \{0,1\}$. Also, let $B_{i,J}$ and $B_{i,J-1}$ represent the corresponding matched filter outputs, after passing through the system, where:

$$B_{i,J} = L_{avg} RP_{avg} \mathbf{b}_i \otimes c_j \Big|_{j=J}, \quad (5.31)$$

$$B_{i,J-1} = L_{avg} RP_{avg} \mathbf{b}_i \otimes c_j \Big|_{j=J-1}. \quad (5.32)$$

Therefore, the probability of slot error for the J^{th} slot of sequence \mathbf{b}_i , is calculated using the following pseudo code:

if $\{b_{i,J-1} = 1 \ \& \ B_{i,J-1} \geq \alpha\}$

$$P_{e,slot,DPIM(1GS)} = 0$$

elseif $\{b_{i,J-1} = 1 \ \& \ B_{i,J-1} < \alpha\}$

$$P_{e,slot,DPIM(1GS)} = Q\left(\frac{\alpha - B_{i,J}}{\sigma_n}\right)$$

elseif $\{b_{i,J-1} = 0 \ \& \ B_{i,J-1} < \alpha\}$

if $\{b_{i,J} = 1\}$

$$P_{e,slot,DPIM(1GS)} = Q\left(\frac{B_{i,J} - \alpha}{\sigma_n}\right)$$

else

$$P_{e,slot,DPIM(1GS)} = Q\left(\frac{\alpha - B_{i,J}}{\sigma_n}\right)$$

end

elseif $\{b_{i,J-1} = 0 \ \& \ B_{i,J-1} \geq \alpha\}$

if $\{b_{i,J} = 1\}$

$$P_{e,slot,DPIM(1GS)} = 1$$

else

$$P_{e,slot,DPIM(1GS)} = 0$$

end

end

The probability of slot error is then found by averaging over K sequences.

For each value of f_c/R_b in the range 10^{-5} to 1, and each order under consideration, the PER was calculated and the average received optical signal power varied until the target PER of 10^{-6} was achieved. Figures 5.17 and 5.18 show plots of normalized average optical power requirement versus f_c/R_b for DPIM(NGB) and DPIM(1GS), respectively.

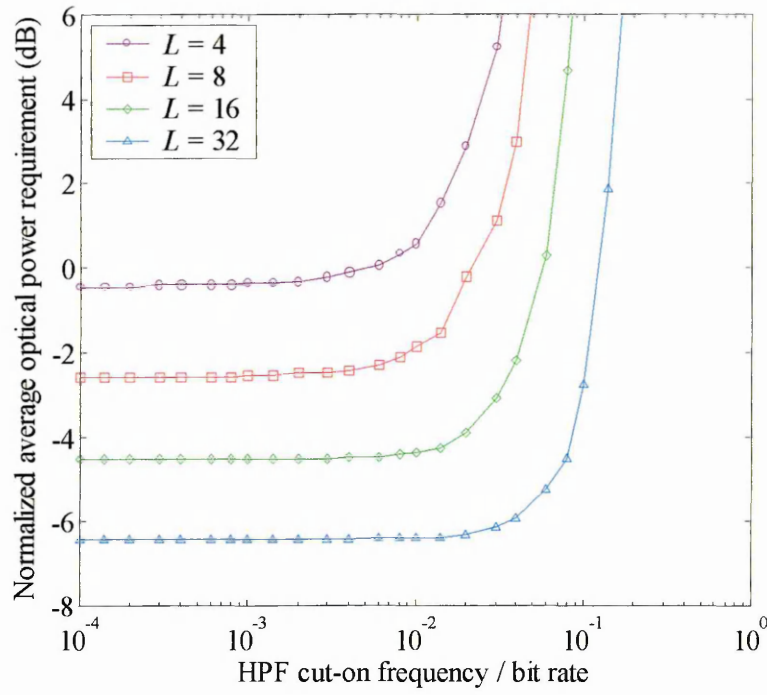


Fig. 5.17: Normalized average optical power requirement versus f_c/R_b for DPIM(NGB)

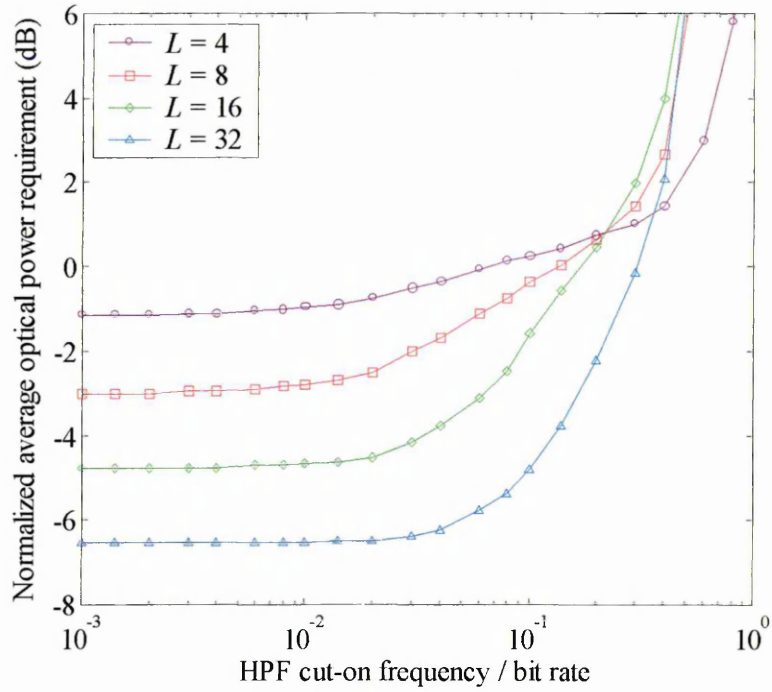


Fig. 5.18: Normalized average optical power requirement versus f_c/R_b for DPIM(1GS)

Comparing Fig. 5.17 with the OOK curve plotted in Fig. 5.12, it is evident that DPIM(NGB) is more resistant to baseline wander than OOK, with higher orders achieving the greatest

robustness, which is again due to the increased bandwidth requirement. For lower orders, power penalties start to become apparent at normalized cut-on frequencies of ~ 0.01 , which is an order of magnitude higher than OOK, whilst 32-DPIM(NGB) does not incur a 3 dB average optical power penalty until the cut-on frequency reaches $\sim 9\%$ of the bit rate. Compared with the performance of PPM, plotted in Figs. 5.14 and 5.15, DPIM(NGB) is more susceptible to baseline wander. As an example, 16-PPM(TH), which has a similar bandwidth requirement to 32-DPIM(NGB), does not incur a 3 dB power penalty until the cut-on frequency reaches $\sim 60\%$ of the bit rate. As discussed in chapters 3 and 4, this inferiority is due to the fact that the PSD of DPIM contains a larger proportion of its power around DC compared with PPM.

From Fig. 5.18 it is clear that the curves for DPIM(1GS) do not follow the same general trend as the other modulation techniques considered. Initially, the rate of increase of average optical power requirement is relatively slow, and then increases around $f_c/R_b = 0.4$. This effect is more pronounced on lower order curves. The reason for this is that at low values of f_c/R_b , the impulse response of the HPF spans many slots and therefore a guard band consisting of just one slot has only a limited effect. Consequently, cut-on frequencies at which the power requirements start to increase are similar to those for DPIM(NGB). As f_c/R_b increases, the HPF impulse response decays much more rapidly, Consequently, in DPIM(NGB), the probability of error is dominated by sequences containing consecutive ones [133]. However, consecutive ones cannot occur in DPIM(1GS) due to the presence of the guard slot in each symbol, and therefore the rate of increase of optical power requirement is lower. As the HPF cut-on frequency approaches the bit rate, the large power penalties are primarily due to the fact that the HPF has removed the majority of the energy in the pulses.

5.5 The Effect of Fluorescent Light Interference With Electrical

High-Pass Filtering

As mentioned previously in section 5.1, the choice of cut-on frequency is a trade-off between the extent of fluorescent light interference rejection and the severity of the baseline wander introduced by the HPF. In this section, the optimum HPF cut-on frequency, i.e. that which minimises the overall power penalty, is estimated using a method which combines the analysis carried out in the previous two sections. Then, using the optimum cut-on frequencies, optical power requirements are calculated, and compared with those obtained in section 5.3 in order to assess the effectiveness of high-pass filtering as a means of mitigating the effect of fluorescent light interference. Again, all power requirements in this section are normalized to the average optical power required by OOK to send 1 Kbyte packets at an average PER of 10^{-6} when operating at 1 Mbit/s in the absence of fluorescent light interference and electrical high-pass filtering.

5.5.1 OOK

In order to determine the optimum cut-on frequency for OOK, the system shown in the block diagram of Fig. 5.2 is used, with both the fluorescent light interference signal and the HPF included.

After passing through the HPF and matched filter, the fluorescent light interference signal is sampled at the end of each bit period. The value of these samples is given by [16]:

$$m_k = m(t) \otimes g(t) \otimes r(t) \Big|_{t=kT_b} . \quad (5.33)$$

Using the same notation as section 5.4.1, when sequence \mathbf{a}_i is passed through the system, the matched filter output, sampled at the end of the J^{th} bit period, $A_{i,J}$, is given by (5.19). Thus, the probability of bit error for any given m_k and $A_{i,J}$ is:

$$\epsilon_{i,k} = \begin{cases} Q\left(\frac{A_{i,J} + m_k}{\sigma_n}\right) & \text{if } a_{i,J} = 1 \\ Q\left(\frac{-A_{i,J} - m_k}{\sigma_n}\right) & \text{if } a_{i,J} = 0 \end{cases}, \quad (5.34)$$

where σ_n is standard deviation of the noise, given in (5.21). The overall probability of bit error is found by averaging over N bits and K sequences:

$$P_{e,bit,OOK} = \frac{1}{NK} \sum_{k=1}^N \sum_{i=1}^K \epsilon_{i,k}. \quad (5.35)$$

The probability of bit error may then be converted into a corresponding PER using (5.9).

For each normalized cut-on frequency in the range 10^{-5} to 1, the PER was calculated using the method described, and the average optical signal power was adjusted until the target PER of 10^{-6} was achieved. For the analysis, a value of $K = 2000$ was used, in order to keep the run times manageable. Whilst 2000 sequences is not enough to obtain reliable results in terms of the effect of baseline wander, it is sufficient to identify the approximate optimum cut-on frequency of the high-pass filter. Figure 5.19 shows a plot of normalized average optical power requirement versus f_c/R_b , for bit rates of 1, 10 and 100 Mbit/s.

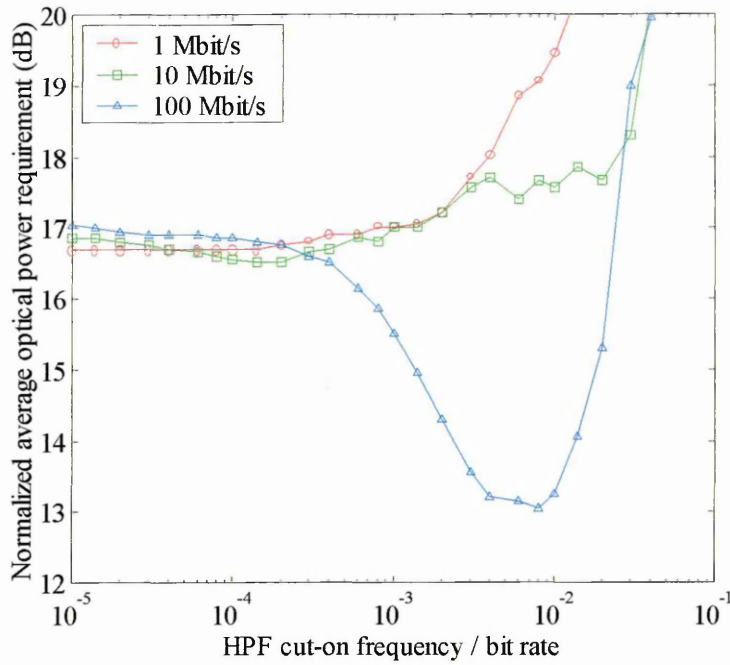


Fig. 5.19: Normalized average optical power requirement versus normalized HPF cut-on frequency for OOK at various bit rates

From Fig 5.19 it is evident that high-pass filtering gives virtually no reduction in the average optical power requirement for bit rates of 1 and 10 Mbit/s. For the purpose of calculating power requirements, optimum normalized cut-on frequencies of 1.4×10^{-4} and 2×10^{-4} were identified for 1 and 10 Mbit/s, respectively. These cut-on frequencies represent the maximum values which can be used without introducing power penalties due to baseline wander. At a bit rate of 100 Mbit/s, by using a normalized cut-on frequency of around 7×10^{-3} , it is clear that high-pass filtering can yield a reduction in the average optical power requirement.

Using these optimum normalized cut-on frequencies, with $K = 5 \times 10^4$, the average optical power requirements were calculated for bit rates of 1, 10 and 100 Mbit/s, as shown in Fig. 5.20. Also shown in the figure are the power requirements for OOK with no interference or high-pass filtering.

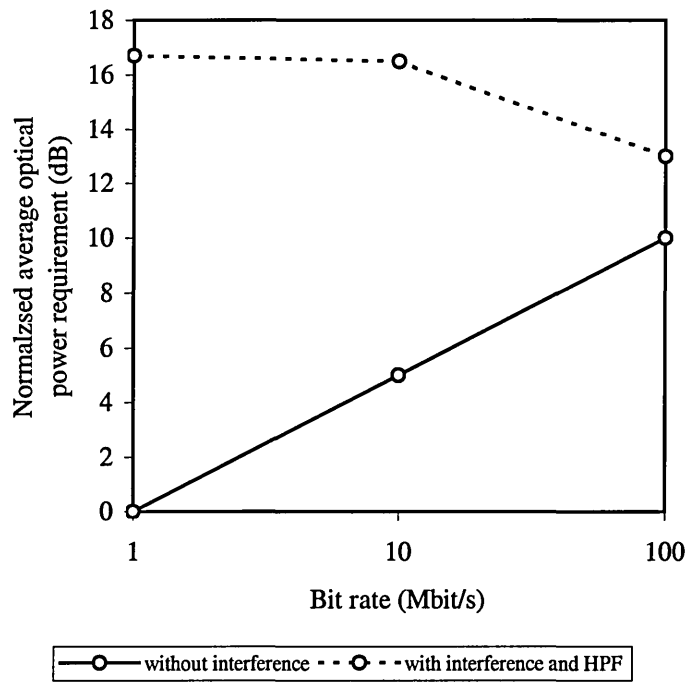


Fig. 5.20: Normalized average optical power requirement versus bit rate for OOK with fluorescent light interference and optimized high-pass filtering

By comparing Fig. 5.20 with Fig. 5.3, it is clear that for bit rates of 1 and 10 Mbit/s, high-pass filtering is not effective in reducing the power penalty caused by fluorescent light interference. This is due to the fact that OOK is very susceptible to baseline wander and consequently, only low normalized cut-on frequencies are possible, which at low to medium bit rates, are not effective in attenuating the interference signal. At a bit rate of 100 Mbit/s, high-pass filtering is more effective, giving a ~4.4 dB reduction in the average optical power requirement. However, this still leaves a power penalty of ~3 dB compared with the same bit rate without interference. The use of line coding has been suggested to permit an increase in HPF cut-on frequency [106], though this would be at the expense of a reduced throughput. Active baseline restoration has also been suggested [35], allowing the use of higher cut-on frequencies without reducing the throughput. It is also possible that higher-order HPFs may be more suitable for OOK [16].

5.5.2 PPM

Using the system shown in Fig. 5.4, with both the fluorescent light interference signal and the HPF included, optimum HPF cut-on frequencies may be determined for PPM(TH) and PPM(MAP) operating with various orders and bit rates.

The fluorescent light interference signal, after passing through the HPF and matched filter, is sampled at the end of each slot period. The value of these samples is given by (5.33), with the sampling times replaced by $t = kT_b \log_2 L/L$. Using the same notation as section 5.4.2, when sequence \mathbf{b}_i is passed through the system, the matched filter output, sampled at the end of the J^{th} bit period, $B_{i,J}$, is given by (5.22). Thus, the probability of slot error for any given m_k and $B_{i,J}$ is:

$$\epsilon_{i,k} = \begin{cases} Q\left(\frac{B_{i,J} + m_k - \alpha}{\sigma_n}\right) & \text{if } b_{i,J} = 1 \\ Q\left(\frac{\alpha - B_{i,J} - m_k}{\sigma_n}\right) & \text{if } b_{i,J} = 0 \end{cases}, \quad (5.36)$$

where α is the threshold level, given in (5.24), and σ_n is standard deviation of the noise, given in (5.25). The overall probability of slot error is then found by averaging over N slots and K sequences:

$$P_{e,\text{slot},\text{PPM(TH)}} = \frac{1}{NK} \sum_{k=1}^N \sum_{i=1}^K \epsilon_{i,k}. \quad (5.37)$$

The probability of slot error may then be converted into a corresponding PER using (5.11).

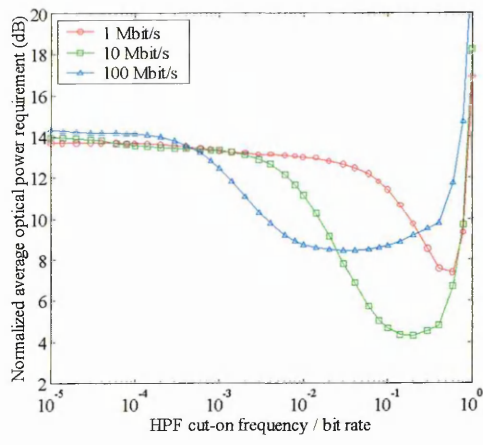
For PPM(MAP), using the same notation as section 5.4.2, let $B_{i,p}, B_{i,p+1}, \dots, B_{i,p+L}$ represent the output of the system corresponding to the last symbol in sequence \mathbf{b}_i , which is given by (5.22), with the sampling time replaced by $j = p, p+1, \dots, p+L$. Assume that, for the final symbol of each

sequence under consideration, the ‘one’ was transmitted in slot $(p + w)$, where $1 \leq w \leq L$. Again, N/L interference signal vectors are defined, denoted as $m_{nL+1} \ m_{nL+2} \ \dots \ m_{nL+L}$, where $0 \leq n \leq (N/L)-1$. For each of the interference signal vectors under consideration, the probability of symbol error is calculated for all K sequences, and the overall probability of symbol error is then obtained by averaging:

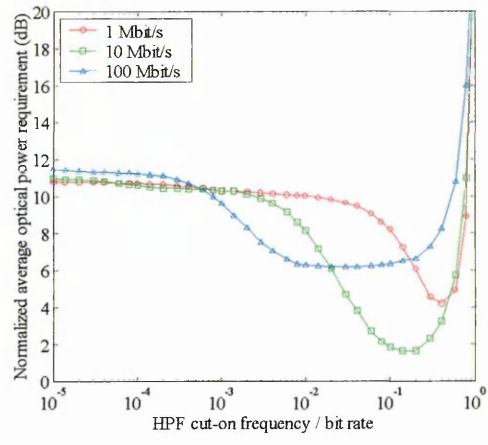
$$P_{e, \text{symbol}, \text{PPM}(\text{MAP})} = \frac{1}{N/L} \cdot \frac{1}{K} \sum_{n=0}^{(N/L)-1} \sum_{i=1}^K \sum_{\substack{j=1 \\ j \neq w}}^L Q\left(\frac{B_{i,p+w} + m_{nL+w} - (B_{i,p+j} + m_{nL+j})}{\sigma_n}\right), \quad (5.38)$$

where σ_n is given in (5.27). Again, the probability of symbol error may be converted into a corresponding PER using (5.13).

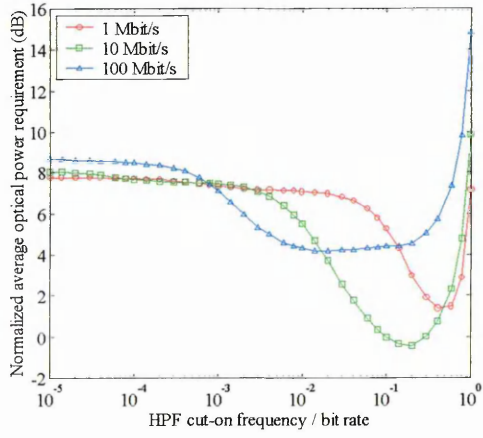
For each value of f_c/R_b , the PER was calculated and the average optical signal power adjusted until the target PER of 10^{-6} was reached. Again, a value of $K = 2000$ was used in the analysis. Figs. 5.21 and 5.22 show plots of normalized average optical power requirement versus f_c/R_b for PPM(TH) and PPM(MAP), respectively, for various orders and bit rates.



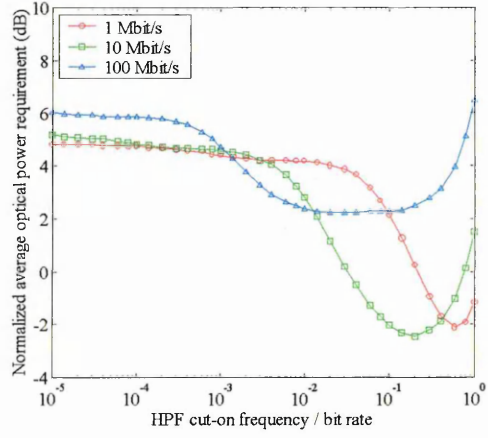
(a)



(b)

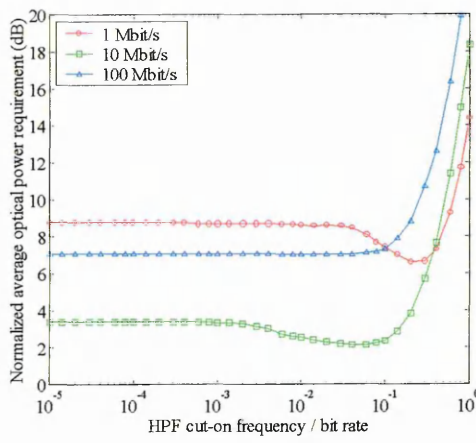


(c)

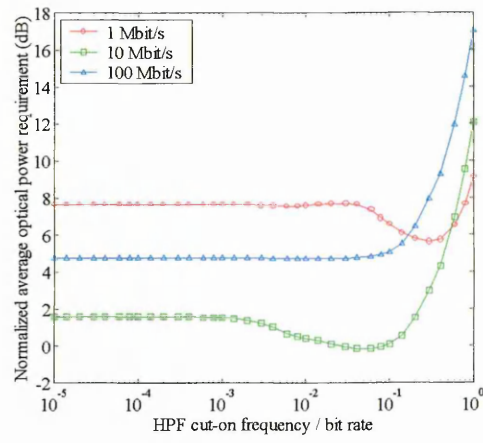


(d)

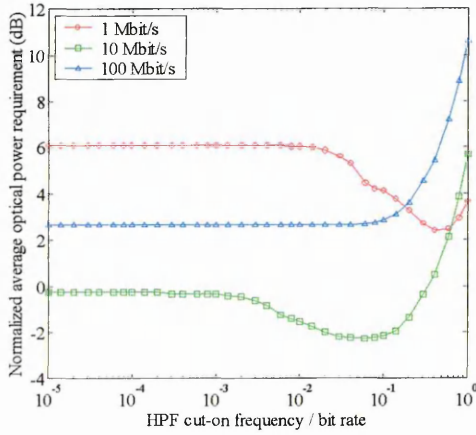
Fig. 5.21: Normalized average optical power requirement vs. normalized HPF cut-on frequency for PPM(TH) at various bit rates with: (a) $L = 4$, (b) $L = 8$, (c) $L = 16$, and (d) $L = 32$



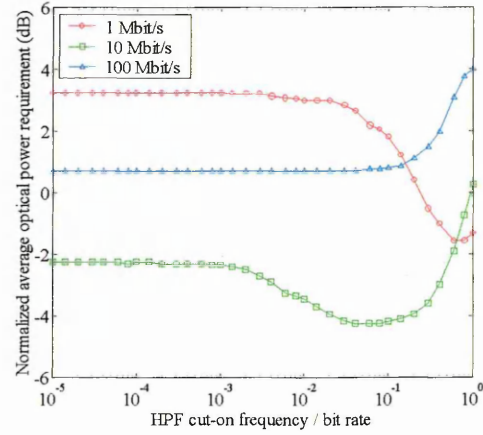
(a)



(b)



(c)



(d)

Fig. 5.22: Normalized average optical power requirement vs. normalized HPF cut-on frequency for PPM(MAP) at various bit rates with: (a) $L = 4$, (b) $L = 8$, (c) $L = 16$, and (d) $L = 32$

With reference to Fig. 5.21, it is evident that electrical high-pass filtering yields reductions in the average optical power requirements of PPM(TH), even when operating at just 1 Mbit/s. The narrowness of the troughs in the 1 Mbit/s curves of Fig. 5.21 suggest that little variation can be tolerated in the HPF cut-on frequency if optimum performance is to be achieved. At 10 Mbit/s the troughs are broader, making the actual choice of f_c/R_b not quite so critical. At 100 Mbit/s there is a floor in the power requirement curves of Fig. 5.21, indicating that there is a region in which the cut-on frequency is high enough to attenuate the interference signal sufficiently such that it has no effect, but is not high enough for baseline wander to affect performance. Within this region, the fluorescent light induced power penalty is due to the additional shot noise only,

and selecting a HPF cut-on frequency anywhere within this region will give approximately the same level of performance.

With reference to Fig. 5.22, it is clear that electrical high-pass filtering yields reductions in the average optical power requirements of PPM(MAP) when operating at 1 Mbit/s. At 10 Mbit/s, from the analysis carried out in section 5.3.2, PPM(MAP) was found to suffer only small power penalties without the use of electrical high-pass filtering. Consequently, the reduction in the average optical power requirements of Fig. 5.22 appear modest, and the broad troughs suggest that the HPF cut-on frequency does not have to be very precise in order to minimize the average optical power requirements. At 100 Mbit/s, PPM(MAP) was found to be immune to fluorescent light interference without the use of electrical high-pass filtering, and consequently there is no reduction in the average optical power requirement curves of Fig. 5.22.

Using optimum HPF cut-on frequencies, with $K = 5 \times 10^4$ sequences, the average optical power requirements were calculated for PPM(TH) and PPM(MAP), for various orders and bit rates, as plotted in Figs. 5.23 and 5.24, respectively. Also shown in the figures is the performance with no interference or high-pass filtering.

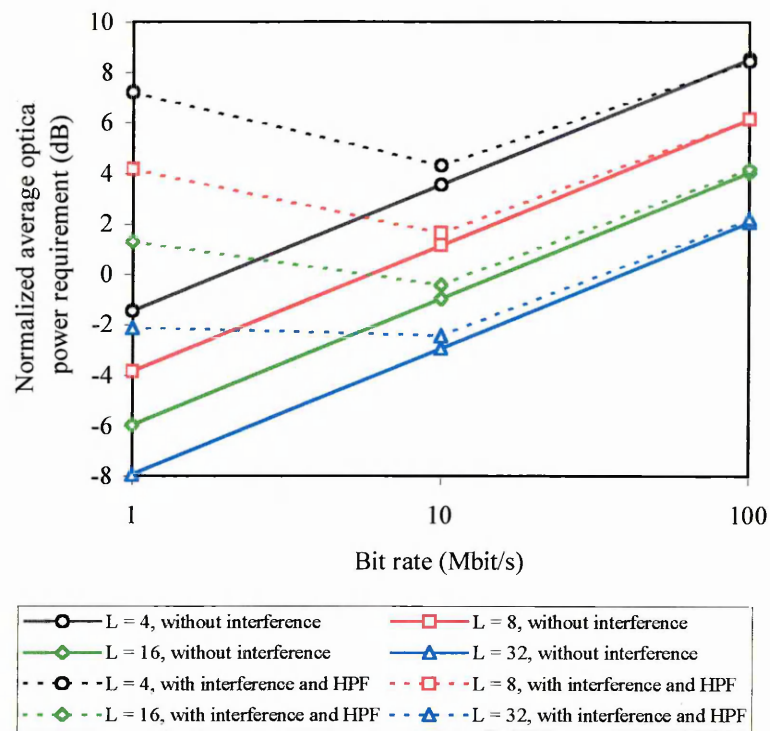


Fig. 5.23: Normalized average optical power requirement versus bit rate for PPM(TH) with fluorescent light interference and optimized high-pass filtering

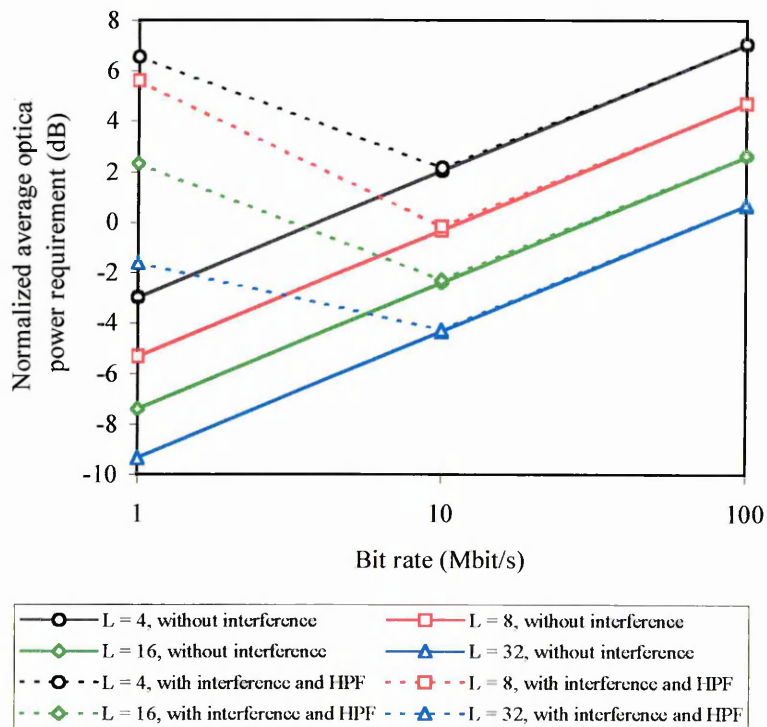


Fig. 5.24: Normalized average optical power requirement versus bit rate for PPM(MAP) with fluorescent light interference and optimized high-pass filtering

Comparing Fig. 5.23 with Fig. 5.5, for PPM(TH) operating at 1 Mbit/s, high-pass filtering is found to offer a 6.5 – 6.9 dB reduction in average optical power requirement, although power penalties of 5.8 - 8.7 dB still exist. At 10 Mbit/s, high-pass filtering is more effective, resulting in optical power penalties of less than 1 dB, compared with the same bit rate without interference. At 100 Mbit/s, high-pass filtering is very effective, completely eliminating the power penalties due to fluorescent light interference.

With reference to Fig. 5.24 and Fig. 5.6, PPM(MAP) operating at 100 Mbit/s is immune to fluorescent light interference and hence, high-pass filtering gives no improvement. At 10 Mbit/s without high-pass filtering, fluorescent light interference results in power penalties ranging from 1.3 - 2.1 dB, compared with the same bit rate with no interference. These power penalties are eliminated when electrical high-pass filtering is employed. At 1 Mbit/s, high-pass filtering gives a modest 2.1 - 4.8 dB reduction in optical power requirement, leaving power penalties of 7.7 - 10.9 dB compared with the same bit rate without interference, which are actually higher than the remaining power penalties for PPM(TH) at 1 Mbit/s.

5.5.3 DPIM

Using the system shown in Fig. 5.7, with both the fluorescent light interference signal and the HPF included, optimum HPF cut-on frequencies may be determined for DPIM(NGB) and DPIM(1GS) operating with various orders and bit rates.

The fluorescent light interference signal, after passing through the HPF and matched filter, is sampled at the end of each slot period. The value of these samples is given by (5.33), with the sampling times replaced by $t = kT_b \log_2 L/L_{avg}$. Using the same notation as used in section 5.4.3, when sequence \mathbf{b}_i is passed through the system, the matched filter output, sampled at the

end of the J^{th} bit period, $B_{i,J}$, is given by (5.28). Thus, for DPIM(NGB), the probability of slot error for any given m_k and $B_{i,J}$ is given as:

$$\epsilon_{i,k} = \begin{cases} Q\left(\frac{B_{i,J} + m_k - \alpha}{\sigma_n}\right) & \text{if } b_{i,J} = 1 \\ Q\left(\frac{\alpha - B_{i,J} - m_k}{\sigma_n}\right) & \text{if } b_{i,J} = 0 \end{cases}, \quad (5.39)$$

where α is the threshold level, given in (5.30), and σ_n is standard deviation of the noise, given in (5.25) with the substitution $T_s = T_b \log_2 L / L_{\text{avg}}$. The overall probability of slot error is found by averaging over N slots and K sequences, as given by:

$$P_{e,\text{slot},\text{DPIM(NGB)}} = \frac{1}{NK} \sum_{k=1}^N \sum_{i=1}^K \epsilon_{i,k}. \quad (5.40)$$

The probability of slot error may then be converted into a corresponding PER using (4.11), with the substitution $L_{\text{avg}} = (L + 1)/2$.

For DPIM(1GS), using the same notation as used in section 5.4.3, the probability of slot error for the J^{th} slot of sequence \mathbf{b}_i , is expressed using the following pseudo code:

if $\{b_{i,J-1} = 1 \ \& \ (B_{i,J-1} + m_{k-1}) \geq \alpha\}$

$$\epsilon_{i,k} = 0$$

elseif $\{b_{i,J-1} = 1 \ \& \ (B_{i,J-1} + m_{k-1}) < \alpha\}$

$$\epsilon_{i,k} = Q\left(\frac{\alpha - B_{i,J} - m_k}{\sigma_n}\right)$$

elseif $\{b_{i,J-1} = 0 \ \& \ (B_{i,J-1} + m_{k-1}) < \alpha\}$

if $\{b_{i,J} = 1\}$

```

         $\varepsilon_{i,k} = Q\left(\frac{B_{i,J} + m_k - \alpha}{\sigma_n}\right)$ 
    else
         $\varepsilon_{i,k} = Q\left(\frac{\alpha - B_{i,J} - m_k}{\sigma_n}\right)$ 
    end

elseif {  $b_{i,J-1} = 0$  &  $(B_{i,J-1} + m_{k-1}) \geq \alpha$  }

    if {  $b_{i,J} = 1$  }
         $\varepsilon_{i,k} = 1$ 
    else
         $\varepsilon_{i,k} = 0$ 
    end

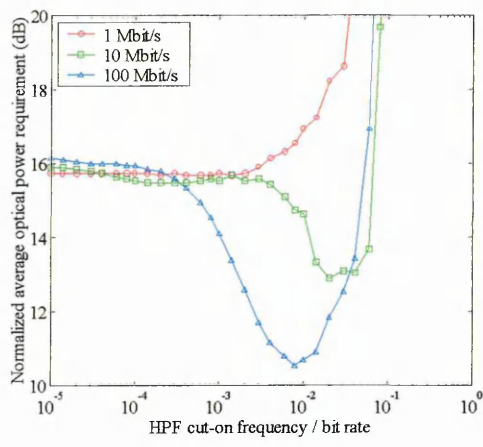
end

end

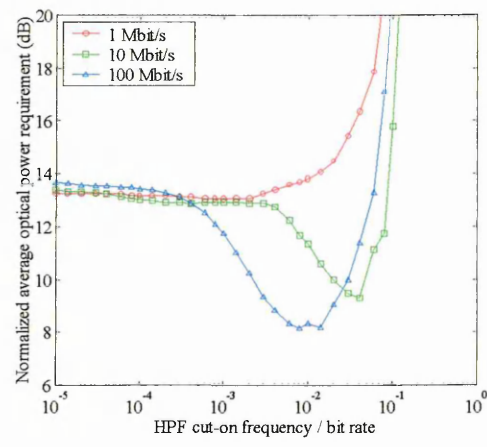
```

Again, the overall probability of slot error is found by averaging over N slots and K sequences, as expressed in (5.40) for DPIM(NGB), which may then be converted into a corresponding PER using (4.11), with the substitution $L_{avg} = (L+3)/2$.

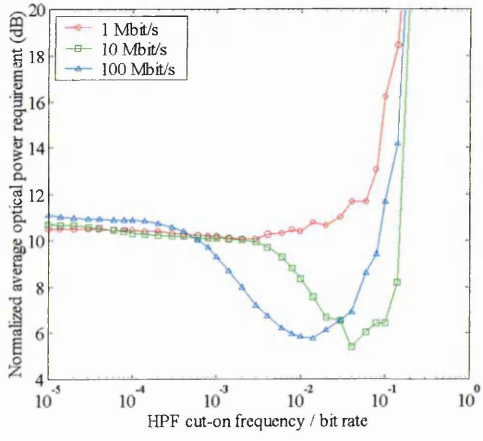
For each value of f_c/R_b , the PER was calculated and the average optical signal power adjusted until the target PER of 10^{-6} was reached. Again, a value of $K = 2000$ was used in the analysis. Figs. 5.25 and 5.26 show plots of normalized average optical power requirement versus f_c/R_b for DPIM(NGB) and DPIM(1GS), respectively, for various orders and bit rates.



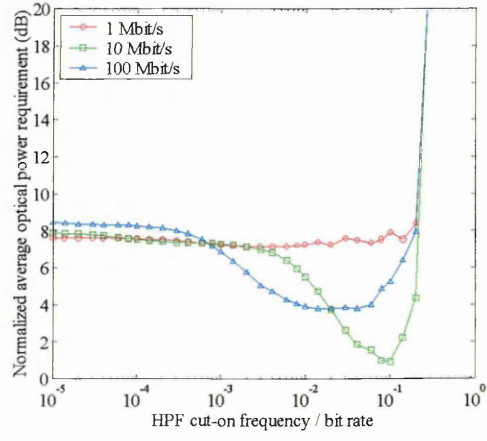
(a)



(b)

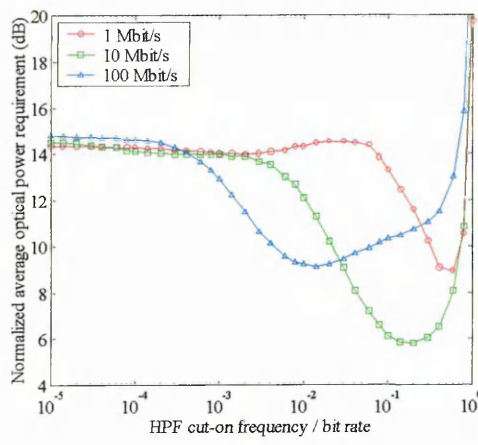


(c)

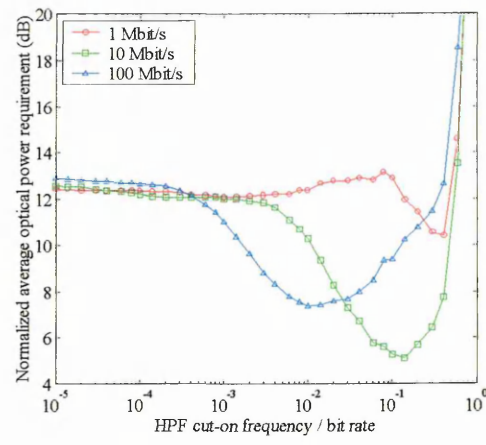


(d)

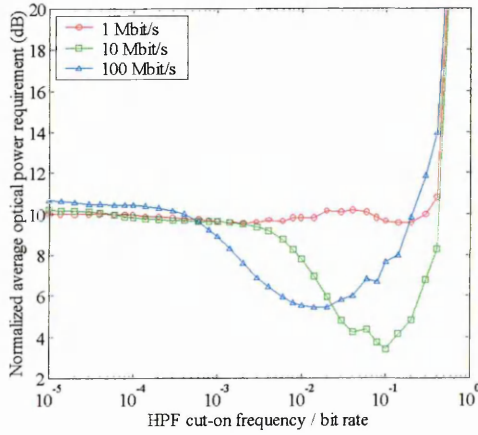
Fig. 5.25: Normalized average optical power requirement vs. normalized HPF cut-on frequency for DPIM(NGB) at various bit rates with:(a) $L = 4$, (b) $L = 8$, (c) $L = 16$, and (d) $L = 32$



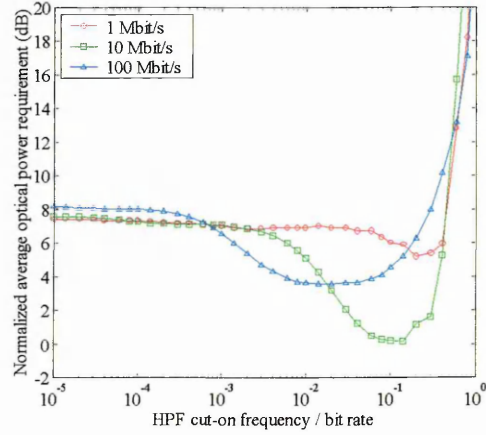
(a)



(b)



(c)



(d)

Fig. 5.26: Normalized average optical power requirement vs. normalized HPF cut-on frequency for DPIM(1GS) at various bit rates with: (a) $L = 4$, (b) $L = 8$, (c) $L = 16$, and (d) $L = 32$

From Fig. 5.25, it is evident that when operating at 1 Mbit/s in the presence of fluorescent light interference, electrical high-pass filtering gives no reduction in the average optical power requirements of DPIM(NGB). Moving to 10 Mbit/s, electrical high-pass filtering is more effective, yielding a reduction in the average optical power requirements. Compared with PPM(TH), DPIM(NGB) has lower optimum HPF cut-on frequencies, which is a result of its greater susceptibility to baseline wander. At 100 Mbit/s, electrical high-pass filtering again achieves a reduction in the average optical power requirements, and the broad troughs suggest that the HPF cut-on frequency does not have to be exact in order to achieve near maximum reductions.

In contrast to DPIM(NGB), from Fig. 5.26 it is evident that electrical high-pass filtering yields some reduction in the average optical power requirements of DPIM(1GS) when operating at 1 Mbit/s. This is due to the fact that the presence of the guard slot increases the schemes robustness to baseline wander and consequently, higher HPF cut-on frequencies can be supported. The troughs in the power requirement curves of Fig. 5.26 are relatively narrow, thus implying that fairly accurate HPF cut-on frequencies are required in order to achieve optimum performance. At 10 Mbit/s, electrical high-pass filtering again yields reductions in the average optical power requirements. Compared with DPIM(NGB) operating at 10 Mbit/s, the optimum HPF cut-on frequencies for DPIM(1GS) are higher, as can be observed by comparing Fig. 5.26 with Fig. 5.25. At 100 Mbit/s, power penalty reductions can again be achieved through electrical high-pass filtering, and optimum HPF cut-on frequencies appear to be similar for both DPIM(NGB) and DPIM(1GS). In addition, there is a floor in the power requirement curve for 32-DPIM(1GS), as previously observed for all orders of PPM(TH) operating at 100 Mbit/s.

Using optimum HPF cut-on frequencies, with $K = 5 \times 10^4$ sequences, the average optical power requirements were calculated for DPIM(NGB) and DPIM(1GS), for various orders and bit rates, as plotted in Figs. 5.27 and 5.28, respectively. Also shown in the figures is the performance with no interference or high-pass filtering.

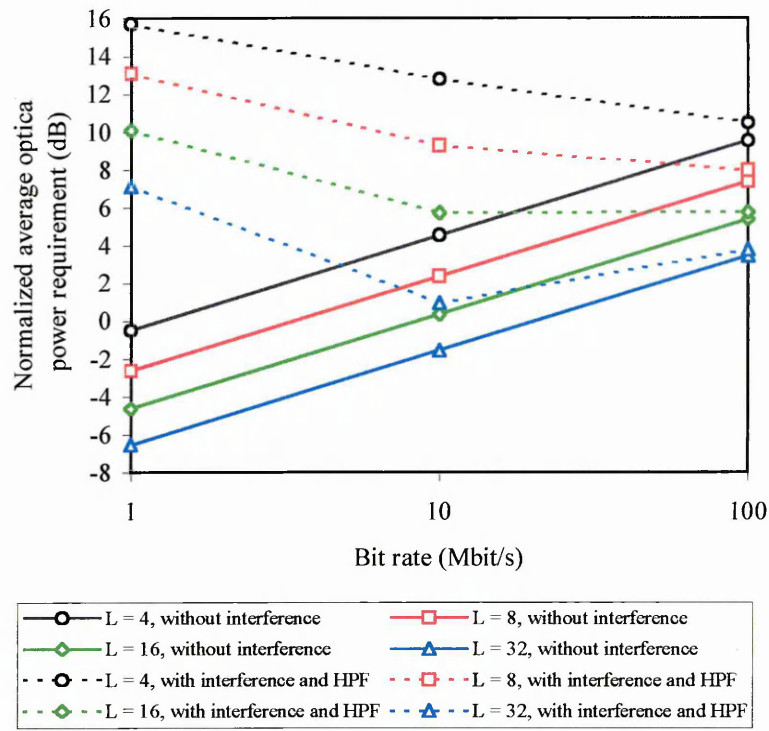


Fig. 5.27: Normalized average optical power requirement versus bit rate for DPIM(NGB) with fluorescent light interference and optimized high-pass filtering

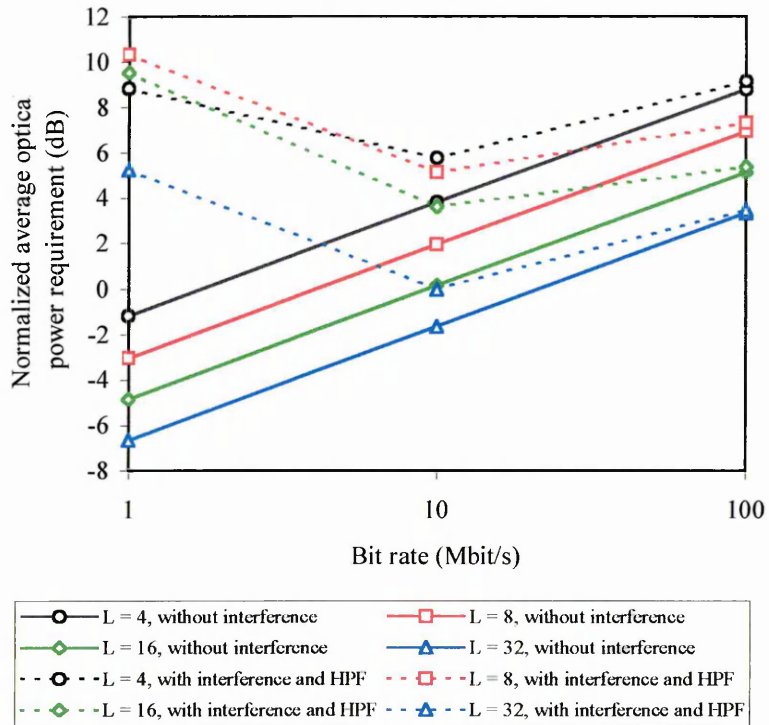


Fig. 5.28: Normalized average optical power requirement versus bit rate for DPIM(1GS) with fluorescent light interference and optimized high-pass filtering

Comparing Fig. 5.27 with Fig. 5.8, it is clear that for DPIM(NGB) operating at 1 Mbit/s, electrical high-pass filtering offers virtually no reduction in the average optical power requirement for any of the orders considered. Moving to a bit rate of 10 Mbit/s, electrical high-pass filtering yields reductions of 3.2 - 7 dB, leaving power penalties of 2.5 – 8.2 dB compared with the same bit rate without interference. At this bit rate, electrical high-pass filtering is significantly more effective for higher orders since, with reference to Fig. 5.17, higher normalized cut-on frequencies can be supported. At 100 Mbit/s, electrical high-pass filtering is very effective, resulting in average optical power penalties of less than 1 dB, compared with the same bit rate without interference.

Comparing Fig. 5.28 with Fig. 5.9, it is evident that for DPIM(1GS) operating at 1 Mbit/s, electrical high-pass filtering yields modest power penalty reductions of 0.5 - 5.5 dB. However, this still leaves power penalties in excess of 10 dB compared with the same bit rate without interference. Interestingly, larger reductions are achieved for lower orders. This is due to the fact that for a given baseline wander power penalty, lower orders can achieve higher normalized HPF cut-on frequencies, as can be observed in Fig. 5.18. Moving to 10 Mbit/s, electrical high-pass filtering achieves gives reductions of 6.6 – 8.8 dB, resulting in power penalties of 1.6 – 3.5 dB compared with the same bit rate without interference. At 100 Mbit/s, as was the case for DPIM(NGB), electrical high-pass filtering is very effective, virtually eliminating the average optical power penalty due to fluorescent light interference.

5.6 Summary

For all the modulation techniques considered in this chapter which use threshold detection, i.e. OOK, PPM(TH), DPIM(NGB) and DPIM(1GS), the average optical power requirements when operating in the presence of interference from a fluorescent lamp driven by a high frequency electronic ballast are almost independent of bit rate. Relative to the optical power requirements

without interference, low bit rate systems are found to suffer the largest power penalties. In contrast to this, the optical power requirements for PPM(MAP) are dependent on the bit rate, with 10 Mbit/s giving the lowest average optical power requirements of the three bit rates considered. As the bit rate increases, there is a significant decrease in the fluorescent light induced power penalty. At 100 Mbit/s the power penalty is zero, thus implying that the scheme is completely immune to the interference. This is due to the fact that, at higher bit rates, there is little variation in the interference signal over the duration of one symbol, and therefore, the effect of interference is very small. It is also worth noting that for the same reason, higher orders of PPM(MAP) are more resistant to fluorescent light interference than lower orders [16].

One of the simplest techniques which is often used to mitigate the interference from artificial sources of ambient light is electrical high-pass filtering. However, electrical high-pass filtering introduces baseline wander, which is more severe for modulation techniques which contain a significant amount of power located at DC and low frequencies. For this reason, of the three modulation techniques considered, OOK is the most susceptible to baseline wander. In contrast, PPM is the most resistant to baseline wander, since its PSD falls to zero at DC. From the PSD of DPIM carried out in chapter 4, it was postulated that DPIM would be more resistant to baseline wander compared with OOK, but would not perform as well as PPM. This was confirmed by the analysis carried out in section 5.4. As an example, for OOK, baseline wander was found to introduce a 3 dB average optical power penalty when the HPF cut-on frequency was $\sim 1\%$ of the bit rate. 16-PPM(TH) and 16-PPM(MAP) on the other hand, do not suffer 3 dB baseline wander power penalties until the HPF cut-on frequency reaches at least 30 % of the bit rate. In comparison, for 16-DPIM(NGB), the 3 dB power penalty cut-on frequency is $\sim 5\%$ of the bit rate. The addition of a single guard slot was found to increase the schemes resistance to baseline wander, thereby increasing the 3 dB power penalty cut-on frequency to $\sim 10\%$ of the bit rate for 16-DPIM(1GS).

For electrical high-pass filtering to be effective, the HPF must be capable of significantly attenuating the interference signal without introducing sizeable power penalties due to baseline

wander. At low bit rates, this is generally difficult to achieve, and consequently high-pass filtering is not very effective for any of the modulation techniques considered when operating at 1 Mbit/s. For OOK and DPIM(NGB), electrical high-pass filtering was found to offer virtually no reduction in average optical power requirements, and offers modest reductions of 0.5 - 5.5 dB for DPIM(1GS), which can support the use of higher cut-on frequencies. At 1 Mbit/s, electrical high-pass filtering was found to be most effective for PPM(TH), but even so, fluorescent light interference still results in power penalties of 5.8 - 8.7 dB. At a bit rate of 10 Mbit/s, electrical high-pass filtering is more effective for all the modulation techniques considered, with the exception of OOK which still experiences virtually no reduction in the average optical power requirement. Using electrical high-pass filtering, DPIM(NGB) incurs power penalties of 2.5 – 8.2 dB, the larger values occurring for lower orders, whilst for DPIM(1GS), power penalties are reduced to less than 3.5 dB for the orders considered. Again, PPM performs best of all, with PPM(TH) achieving power penalties below 1 dB when electrical high-pass filtering is used. For PPM(MAP), power penalties are eliminated when electrical high-pass filtering is used, though it must be pointed out that due to its more sophisticated method of detection, PPM(MAP) is virtually immune to high frequency fluorescent light interference without electrical high-pass filtering when operating at 10Mbps and above. At 100 Mbit/s, electrical high-pass filtering is very effective, virtually eliminating the fluorescent light induced power penalties for all the schemes considered, again with the exception of OOK which still incurs an average optical power penalty of ~3 dB.

Chapter 6

The Effect of Multipath Propagation on Link Performance

6.1 Introduction

In both diffuse and nondirected LOS infrared link configurations, the transmitted optical signal may undergo multiple reflections from the walls, ceiling, floor and objects within a room, before arriving at the surface of the photodetector. In the case of the diffuse configuration, where a LOS path does not exist, all the transmitted signal incident on the photodetector surface has experienced at least one reflection. This multipath propagation causes the transmitted pulses to spread in time, resulting in ISI. The effect of ISI is significant for bit rates above 10 Mbit/s [71].

In this chapter, the performance of DPIM is analysed in the presence of multipath propagation and AWGN, which is independent of the received signal. Again, for comparison, OOK, PPM(TH) and PPM(MAP) are also evaluated. Throughout the chapter, all power requirements

are normalized to the average optical power required by OOK, operating at a given bit rate, to send 1 Kbyte packets at an average PER of 10^{-6} over an ideal channel, i.e. with an impulse response $\delta(t)$, limited only by AWGN.

The remainder of this chapter is organised as follows: In section 6.2, the parameters used to quantify the severity of the ISI are defined, and the channel model used in the analysis is described. The unequalized performance of OOK, PPM and DPIM is evaluated in section 6.3. One method of improving the performance of DPIM in the presence of ISI involves placing a guard band in each symbol immediately following the pulse. In section 6.4 the effectiveness of this technique is analysed, and the results are compared with those obtained for DPIM without a guard band. The more common method of combating the effects of ISI is to employ some form of equalization technique. In section 6.5, the performance of DPIM using a zero forcing decision feedback equalizer is evaluated, and these results are compared with those obtained in the guard band analysis. Finally, the main findings of the chapter are summarized in section 6.6.

6.2. Channel Model

The multipath channel, which is completely characterised by its impulse response $h(t)$, is fixed for a given position of the transmitter, receiver and intervening reflectors, and changes significantly only when any of these are moved by distances in the order of centimetres [142]. Due to the high bit rates under consideration and the relatively slow movement of people and objects within a room, the channel will vary significantly only on the time scale of many bit periods, and hence, it is justifiable to model the channel as time invariant.

The power penalties associated with the channel may be separated into two factors: optical path loss and multipath dispersion [62, 63]. The optical gain for a channel with impulse response $h(t)$ is defined as:

$$G_0 = \int_{-\infty}^{\infty} h(t) dt . \quad (6.1)$$

Therefore the average received optical signal power, P_{RX} , is

$$P_{RX} = G_0 P_{TX} , \quad (6.2)$$

where P_{TX} is the average transmitted optical signal power. Hence,

$$\text{optical path loss (dB)} = -10 \log_{10} G_0 . \quad (6.3)$$

In this chapter, consideration is limited to the power penalty due to multipath propagation only. Consequently, the channel impulse response is divided by G_0 in order to give unity area. Since the channel $h(t)/G_0$ has the same unity gain as the ideal channel $\delta(t)$, only the effect of multipath dispersion is measured. Thus, in this case, $P_{RX} = P_{TX}$, and for the remainder of this chapter the average optical power will be denoted as P_{avg} .

The RMS delay spread, D_{RMS} , is a parameter which is commonly used to quantify the time dispersive properties of multipath channels, and is defined as the square root of the second central moment of the magnitude squared of the channel impulse response [36, 143]. The RMS delay spread can be found from the channel impulse response using the following [32]:

$$D_{RMS} = \left[\frac{\int_{-\infty}^{\infty} (t - D_{mean})^2 h^2(t) dt}{\int_{-\infty}^{\infty} h^2(t) dt} \right]^{1/2} , \quad (6.4)$$

where D_{mean} is the mean delay, given by:

$$D_{mean} = \frac{\int_{-\infty}^{\infty} th^2(t) dt}{\int_{-\infty}^{\infty} h^2(t) dt}. \quad (6.5)$$

Practical channel measurements by Kahn *et. al.* [32] have shown that both nondirected LOS and diffuse configurations have channel RMS delay spreads which typically range from 1 to 12 ns, with diffuse links generally being slightly larger. As one may expect, shadowing is more detrimental to nondirected LOS channels, increasing delay spreads to typically between 7 and 13 ns, whilst on diffuse channels, the increase in delay spread due to shadowing is relatively modest. Using these channel measurements to analyse the performance of OOK, with and without equalization, the authors discovered a systematic relationship between multipath power penalty and normalized delay spread, D_T , which is a dimensionless parameter defined as the channel RMS delay spread (6.4) divided by the bit duration. This relationship implies that a single parameter model is sufficient to calculate ISI power penalties on all four types of nondirected channel. Using channel measurements from [32, 36], Carruthers and Kahn used this relationship to develop the ceiling bounce model [62, 63], which is given by:

$$h(t, a) = \frac{6a^6}{(t+a)^7} u(t), \quad (6.6)$$

where $u(t)$ is the unit step function and a is related to the RMS delay spread by:

$$D_{RMS}(h(t, a)) = \frac{a}{12} \sqrt{\frac{13}{11}}. \quad (6.7)$$

The authors used the model to predict ISI power penalties for OOK and PPM, with and without equalization, and compared the results with those calculated using impulse responses obtained from practical channel measurements. For both unequalized and equalized operation, the model was found to predict multipath power requirements on nondirected LOS and diffuse channels,

with and without shadowing, with a high degree of accuracy. In this chapter, the multipath channel is modelled using the ceiling bounce model (6.6), normalized such that $G_0 = 1$.

6.3 Unequalized Performance of Various Modulation Techniques

6.3.1 OOK

A block diagram of the unequalized OOK system under consideration is shown in Fig. 6.1.

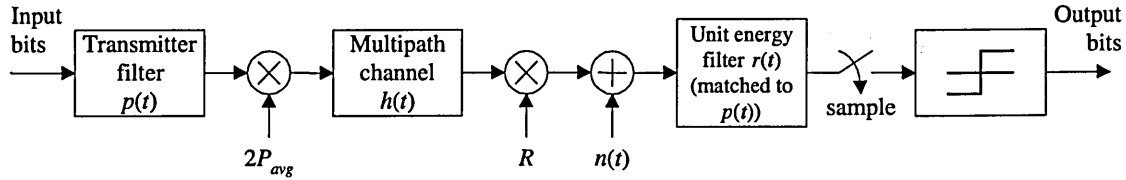


Fig. 6.1: Block diagram of the unequalized OOK system

The input bits, assumed to be IID and uniform on $\{0, 1\}$, are passed to a transmitter filter, which has a unit amplitude rectangular impulse response $p(t)$, with a duration of one bit, T_b . The pulses are then scaled by the peak transmitted optical signal power, $2P_{avg}$, where P_{avg} is the average transmitted optical signal power, before being passed through the multipath channel, $h(t)$. The received optical signal power is converted into a photocurrent by multiplying it with the photodetector responsivity R . AWGN $n(t)$, with a double-sided PSD of $N_0/2$, is then added. The detected signal is passed through a unit energy filter, with an impulse response $r(t)$, which is matched to $p(t)$. Note that this filter is optimum only when there is no multipath dispersion. The output of the matched filter is sampled at the bit rate, and the samples are passed to a threshold detector, which assigns a one or zero to each bit depending on whether the sampled signal is above or below the threshold level, thus generating an estimate of the transmitted bit sequence.

The average BER may be calculated using the method proposed in [71], which is described as follows. Let c_k denote the discrete-time impulse response of the cascaded system:

$$c_k = p(t) \otimes h(t) \otimes r(t) \Big|_{t=kT_b} . \quad (6.8)$$

Unless the channel is nondispersive, c_k contains a zero tap, a single precursor tap and possibly multiple postcursor taps. The magnitude of the zero tap is larger than the magnitudes of the other taps. On a non dispersive channel, the optimum sampling point, i.e. that which minimises the probability of error, occurs at the end of each bit period. However, on dispersive channels, the optimum sampling point changes as the severity of ISI changes. In order to isolate the power penalty due to ISI, two assumptions are made. Firstly perfect timing recovery is assumed. This is achieved by shifting the time origin so as to maximise the zero tap, c_0 [71]. Secondly, optimal decision threshold is assumed. For OOK, basic symmetry arguments can be used to deduce that the optimum threshold level lies midway between expected one and zero levels, regardless of the severity of ISI [71].

Suppose that c_k contains m taps. Let \mathbf{a}_i be an m -bit sequence and a_i be the value of the penultimate bit in that sequence, where $a_i \in \{0,1\}$. Let y_i denote the receiver filter output corresponding to the penultimate bit, which, in the absence of noise, is given by:

$$y_i = 2RP_{avg} \mathbf{a}_i \otimes c_k \Big|_{k=m} . \quad (6.9)$$

Thus, the probability of error for the penultimate bit in \mathbf{a}_i is given by:

$$\epsilon_i = \begin{cases} Q\left(\frac{y_i - \alpha_{opt}}{\sqrt{N_0/2}}\right) & \text{if } a_i = 1 \\ Q\left(\frac{\alpha_{opt} - y_i}{\sqrt{N_0/2}}\right) & \text{if } a_i = 0 \end{cases}, \quad (6.10)$$

where α_{opt} is the optimum threshold level, set to the midway value of $RP_{avg} \sqrt{T_b}$. The average probability of bit error is then found by averaging over all possible m -bit sequences:

$$P_{e,bit,OOK} = \frac{1}{2^m} \sum_{i=1}^{2^m} \epsilon_i. \quad (6.11)$$

The reason why the penultimate bit in each sequence is considered can be explained with the aid of Fig. 6.2. Suppose that c_k contains a zero tap, a precursor tap and 3 post cursor taps. If a sequence is transmitted which contains a single pulse in bit position 1, assuming that the peak output of c_k occurs in bit position 1 at the receiver, the post cursor ISI resulting from this one affects bit positions 2, 3 and 4, and the precursor ISI affects bit position 0, as illustrated by case 1 of Fig. 6.2. Considering the probability of error for bit position 4, any pulse transmitted before bit position 1 has no effect on bit position 4, as illustrated by case 2. At the other extreme, the precursor ISI from a pulse transmitted in bit position 5 affects bit position 4, as illustrated by case 3, but pulses transmitted in positions 6 onwards have no effect on bit position 4, as illustrated by case 4. Therefore, only bits in positions 1 to 5 result in ISI which affects bit position 4. Therefore it is only necessary to consider every combination of bits 1 to 5 in order to calculate the average BER for bit position 4.

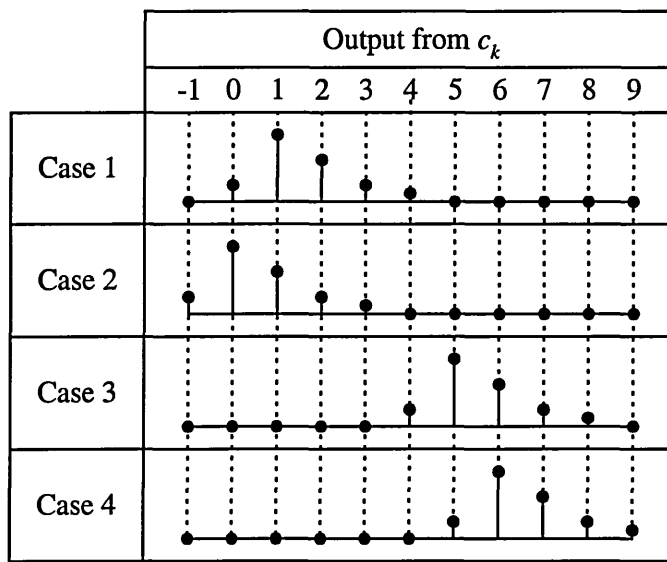


Fig. 6.2: Response of c_k to a single one in various bit positions

For a given packet length of D bits, the average probability of bit error given in (6.11) may be converted into a corresponding PER using (5.9).

For each value of D_T in the range 10^{-3} to 0.5, the RMS delay spread is found by multiplying D_T by the bit duration, T_b . Note that the actual bit duration used is irrelevant in this analysis, since the RMS delay spread is normalized to it. The parameter a is then determined using (6.7), and from this, the channel impulse response is calculated using (6.6). The discrete-time impulse response of the cascaded system is then determined, with the sampling instants chosen so as to maximise c_0 . The average transmitted optical signal power is then varied until the target PER of 10^{-6} is achieved. Fig. 6.3 shows a plot of average optical power requirement versus normalized delay spread for unequalized OOK.

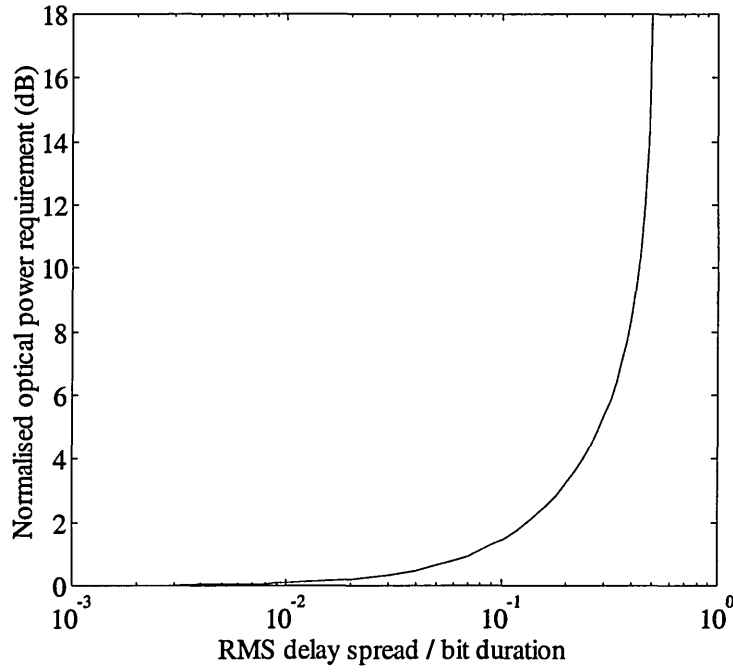
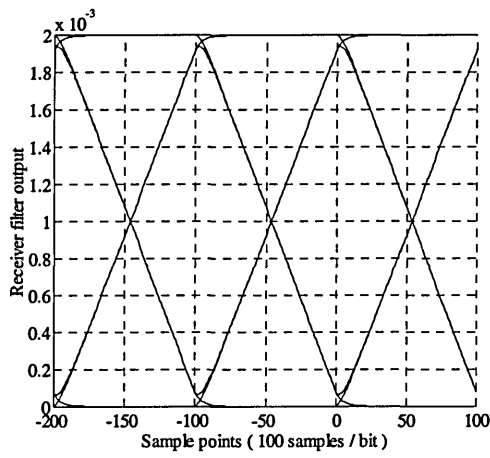


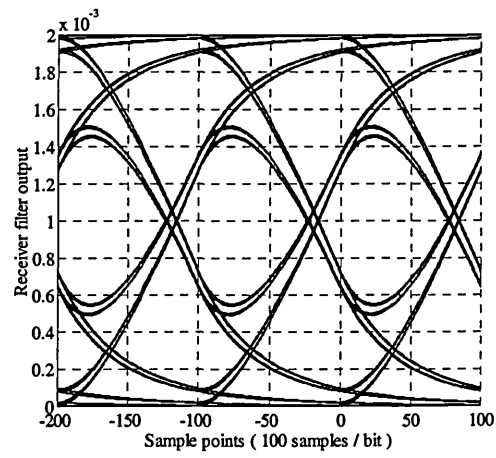
Fig. 6.3: Normalized average optical power requirement vs. normalized delay spread for OOK

From Fig. 6.3, it may be observed that the unequalized power requirement of OOK increases approximately exponentially as D_T increases. A 3 dB average optical power penalty is incurred when the normalized delay spread is 0.2, and beyond ~ 0.52 the error rate becomes irreducible, i.e. the target PER cannot be achieved simply by increasing the transmit power.

Using the continuous-time cascaded impulse response, Fig. 6.4 shows simulated eye diagrams at the output of the receiver filter for D_T of 0.02 and 0.2. For both plots, $P_{avg} = 1$ W and $R_b = 1$ Mbit/s. The zero point on the x-axis corresponds to the optimum sampling point in the absence of ISI. From Fig. 6.4, the shift in optimum sampling point as the severity of ISI changes is clearly observed, as is the optimum threshold level, which remains at the midway value of 1×10^{-3} regardless of D_T .



(a)



(b)

Fig. 6.4: Simulated eye diagrams at the receiver filter output for: (a) $D_T = 0.02$, and (b) $D_T = 0.2$

6.3.2 PPM

A block diagram of the unequalized PPM system, including both threshold detection and MAP detection, is shown in Fig. 6.5.

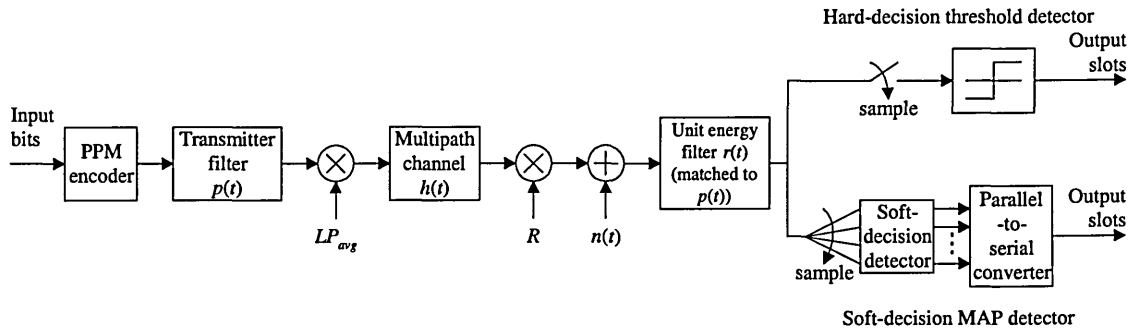


Fig. 6.5: Block diagram of the unequalized PPM system

The PPM encoder maps each block of $\log_2 L$ input bits to one of L possible symbols. The symbols are passed to a transmitter filter, which has a unit-amplitude rectangular impulse response $p(t)$, with a duration of one slot T_s , as given in (3.11). The output of the transmitter filter is scaled by the peak transmitted optical signal power, LP_{avg} , and passed through the multipath channel $h(t)$. The received optical signal power is converted into a photocurrent by

multiplying it with the photodetector responsivity R . AWGN $n(t)$ is added to the detected signal, which is then passed to a unit energy filter with an impulse response $r(t)$, which is matched to $p(t)$. The filtered signal is then sampled at the slot rate. For the threshold detection based receiver, a one or zero is assigned to each slot depending on whether the sampled signal is above or below the threshold level. For the MAP detection based receiver, each block of L samples is passed to a block decoder, which assigns a one to the slot which contains the largest sample and zeros to the remaining slots.

PPM(TH) may be analysed using the same method outlined for OOK in section 6.3.1. The discrete-time equivalent impulse response, c_k , is given by (6.8) with the sampling times replaced by $t = kT_s$, where T_s is given in (3.11). Again, the optimum sampling point is selected by maximising the zero tap c_0 . Assuming c_k has m taps, all possible m -slot PPM sequences are generated, and their corresponding occurrence probabilities are calculated. Note that, since the slots are not i.i.d., different m -slot sequences may have different occurrence probabilities, and when $m > 2$, the total number of valid sequences is always less than 2^m . For any given m -slot PPM sequence, denoted as \mathbf{b}_i , let b_i be the value of the penultimate slot in that sequence, where $b_i \in \{0, 1\}$. Let y_i denote the output of the receiver filter corresponding to the penultimate slot, which, in the absence of noise, is given by [107]:

$$y_i = LRP_{avg} \mathbf{b}_i \otimes c_k \big|_{k=m} . \quad (6.12)$$

Thus, the probability of slot error for the $(m-1)^{\text{th}}$ slot of sequence \mathbf{b}_i is given by:

$$\epsilon_i = \begin{cases} Q\left(\frac{y_i - \alpha_{opt}}{\sqrt{N_0/2}}\right) & \text{if } b_i = 1 \\ Q\left(\frac{\alpha_{opt} - y_i}{\sqrt{N_0/2}}\right) & \text{if } b_i = 0 \end{cases} . \quad (6.13)$$

Since slots containing a one are less likely than empty slots, the optimum threshold level does not simply lie midway between expected one and zero values, as it does for OOK. It is a complicated function of the signal and noise powers, the discrete-time impulse response c_k and the order L , and is determined iteratively in the analysis.

The average probability of slot error is found by multiplying the probability of slot error for the $(m-1)^{\text{th}}$ slot of a given m -slot sequence by the probability of occurrence for that particular sequence, and summing over all possible sequences. Therefore,

$$P_{e,slot,PPM(TH)} = \sum_{\text{all } i} P(\mathbf{b}_i) \epsilon_i . \quad (6.14)$$

For a given packet length of D bits, the average probability of slot error may be converted into a corresponding PER using (5.11).

For each value of D_T in the range 10^{-3} to 0.4, the optical power requirement was calculated, using the optimum sampling point and threshold level, for various orders of PPM(TH), as shown in Fig. 6.6. For comparison, the average optical power requirement for OOK is also shown in the figure.

In order to keep simulation run times manageable, the method used for OOK and PPM(TH) is not practical for $m > 20$. In order to evaluate PPM(MAP), whole symbols must be considered, making the method impractical for higher values of L . Therefore, a slightly different approach is taken. Rather than generating every possible PPM sequence containing m slots, one long sequence containing n symbols, is analysed, where $n \gg m$. Whilst this method does not give absolute results, accuracy and computation time can be traded off to give meaningful results. By trial and error, $n = 10^4$ was found to give a good compromise.

Let \mathbf{b} denote a sequence containing n symbols. When the sequence is passed through the system, the sampled output of the receiver filter is given by [107]:

$$y_j = LRP_{avg} \mathbf{b} \otimes c_k \Big|_{k=k \dots k+(nL-1)}, \quad (6.15)$$

Assuming that the one occurs in slot q of each symbol, the average probability of symbol error is given as [107]:

$$P_{e, \text{sym}, \text{PPM (MAP)}} = \frac{1}{n} \sum_{i=1}^n \sum_{\substack{p=1 \\ p \neq q}}^L Q \left(\frac{y_{(i-1)L+q} - y_{(i-1)L+p}}{\sqrt{N_0}} \right). \quad (6.16)$$

For a given packet length of D bits, the average probability of symbol error may then be converted into a corresponding PER using (5.13).

For each value of D_T in the range 10^{-3} to 0.4, the average optical power requirement was calculated, using the optimum sampling point, for various orders of PPM(MAP), as shown in Fig. 6.6. For comparison, the average optical power requirement for OOK is also shown in the figure.

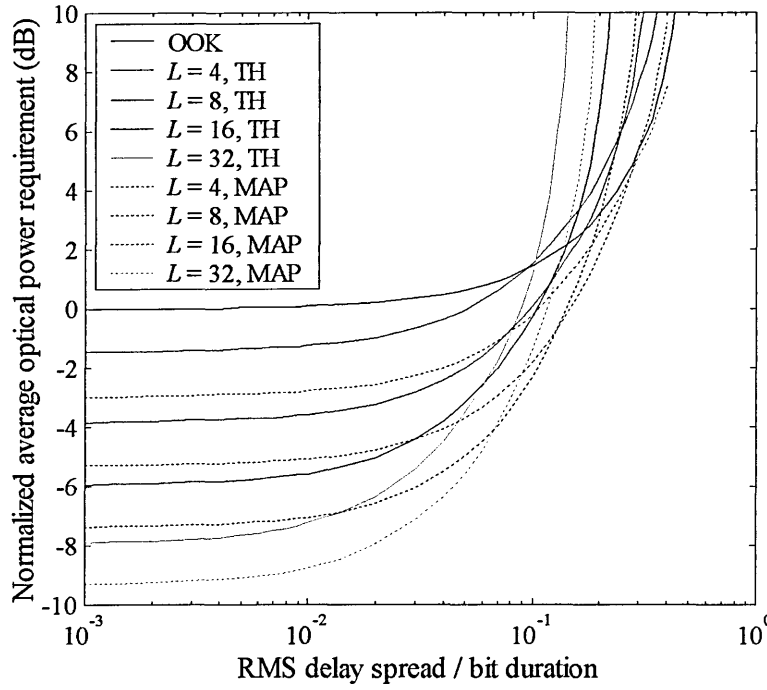


Fig. 6.6: Normalized average optical power requirement versus normalized delay spread
for OOK, PPM(TH) and PPM(MAP)

For both methods of detection, as D_T increases, the power requirements of higher order PPM increase more rapidly than those of lower order systems. This is due to the lower slot duration, which means that a greater number of slots are affected by the ISI. As an example, for normalized delay spreads above ~ 0.11 , the ISI is severe enough such that $L = 4$ actually offers a lower average optical power requirement than $L = 32$ for both PPM(TH) and PPM(MAP). For any given order and D_T , PPM(MAP) has a lower power requirement than PPM(TH). On an ideal channel this difference is ~ 1.5 dB [17], but on multipath channels the difference is found to increase as D_T increases. This is best illustrated by plotting the ISI power penalty versus D_T for various orders of PPM(TH) and PPM(MAP), as shown in Fig. 6.7.

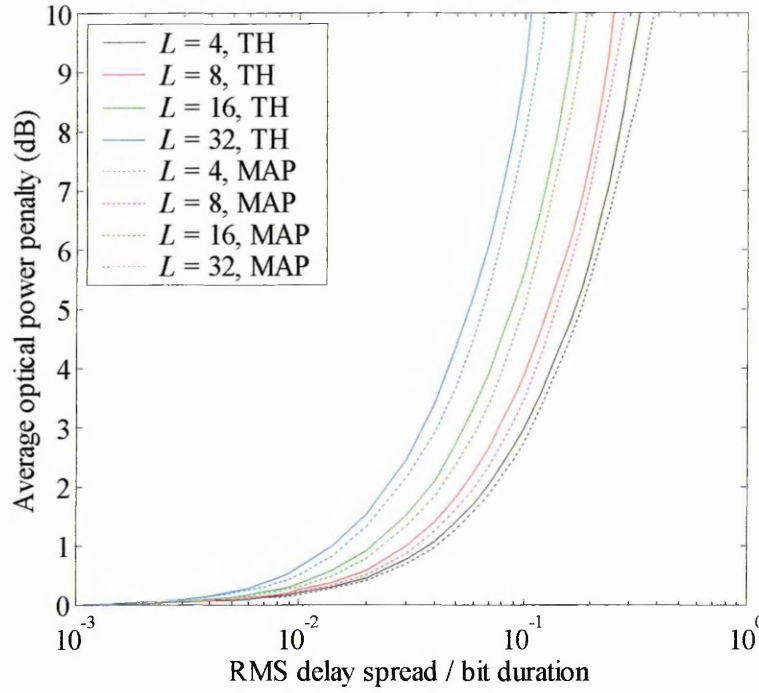


Fig. 6.7: Average optical power penalty versus normalized delay spread for OOK, PPM(TH) and PPM(MAP)

It is evident from Fig. 6.7 that, for any given value of D_T , MAP detection offers a lower ISI power penalty than TH detection, and the difference between the two techniques is found to increase slowly as D_T increases. As a result, for any given L , the difference in average optical power requirement between the two schemes also increases slowly as D_T increases.

Despite the improved power efficiency of PPM(MAP), from Fig. 6.6 it is evident that OOK outperforms 16-PPM(MAP) and 32-PPM(MAP) for D_T beyond ~ 0.2 , and offers a similar average optical power requirement to 4-PPM(MAP) and 8-PPM(MAP) at $D_T \sim 0.3$. Furthermore, compared with PPM(TH), OOK offers a lower average optical power requirement than any of the orders considered for normalised delay spreads above ~ 0.17 .

6.3.3 DPIM

In this section, the unequalized performance of DPIM is analysed, without a guard band present.

A block diagram of the unequalized DPIM(NGB) system under consideration is shown in Fig.

6.8.

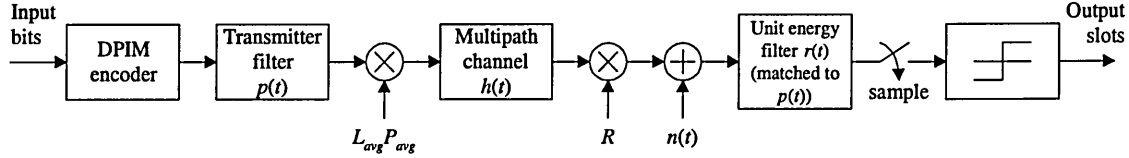


Fig. 6.8: Block diagram of the unequalized DPIM(NGB) system

The encoder maps each block of $\log_2 L$ input bits to one of L possible DPIM(NGB) symbols. The symbols are passed to a transmitter filter, which has a unit-amplitude rectangular impulse response $p(t)$, with a duration of one slot T_s , as given in (4.1). The pulses are scaled by the peak transmitted optical signal power, $L_{avg} P_{avg}$, and passed through the multipath channel $h(t)$. The received optical signal power is converted into a photocurrent by multiplying it with the photodetector responsivity R . AWGN $n(t)$ is added to the detected signal, which is then passed to a unit energy filter with an impulse response $r(t)$, which is matched to $p(t)$. The filter output is sampled at the slot rate, and a threshold detector then assigns a one or zero to each slot depending on whether the sampled signal is above or below the threshold level.

The method used in the analysis of OOK and PPM(TH) may also be used to determine the performance of DPIM(NGB). The discrete-time equivalent impulse response, c_k , is given by (6.8) with the sampling times replaced by $t = kT_s$, where T_s is given in (4.1). Again, the optimum sampling point is selected, such that c_0 is maximised. Using the same notation as used for PPM(TH) in section 6.3.2, let \mathbf{b}_i be an m -slot DPIM(NGB) sequence and b_i be the value of the penultimate slot in that sequence, where $b_i \in \{0, 1\}$. Let y_i denote the output of the receiver filter corresponding to the penultimate slot, which, in the absence of noise, is given by:

$$y_i = L_{avg} RP_{avg} \mathbf{b}_i \otimes c_k \big|_{k=m} . \quad (6.17)$$

As with PPM(TH), the optimum threshold level for DPIM(NGB) is dependent on a number of factors, one of which is the severity of the ISI. Again, the optimum threshold level used in the analysis is determined iteratively. The probability of slot error for the $(m-1)^{\text{th}}$ slot of sequence \mathbf{b}_i is given by (6.13). Again, as for PPM(TH), the average probability of slot error for DPIM(NGB) is then found by multiplying the probability of slot error for the $(m-1)^{\text{th}}$ slot of a given m -slot sequence by the probability of occurrence for that particular sequence, and summing over all possible sequences. Thus,

$$P_{e,slot,DPIM(NGB)} = \sum_{\text{all } i} P(\mathbf{b}_i) \epsilon_i . \quad (6.18)$$

Note that unlike PPM, there are 2^m possible m -slot sequences for all m , though the occurrence probabilities are different since the slots are not i.i.d. For a given packet length of D bits, the average probability of slot error for DPIM(NGB) may be converted into a corresponding PER using (4.11), with the substitution $L_{avg} = (L + 1)/2$.

For each value of D_T in the range 10^{-3} to 0.4, the average optical power requirements were calculated, using the optimum sampling point and threshold level, for various orders of DPIM(NGB), as shown in Fig. 6.9. For comparison, the average optical power requirement for OOK is also shown in the figure.

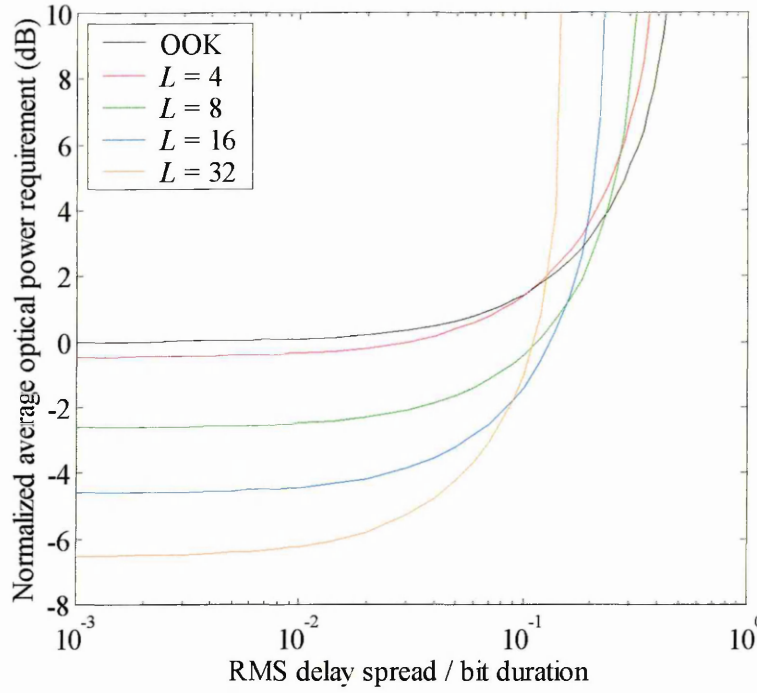


Fig. 6.9: Normalized average optical power requirement versus normalized delay spread
for DPIM(NGB)

In the absence of multipath dispersion or when the normalized delay spread is small, PPM(TH) has a lower average optical power requirement than DPIM(NGB) for any given order. This is due to the lower average duty cycle of PPM(TH), which results in increased power efficiency. However, due to its lower bandwidth requirement, DPIM(NGB) has a lower ISI power penalty than PPM(TH). Consequently, as D_T increases, the average optical power requirement curves for the two schemes intersect, and beyond the point of intersection, DPIM(NGB) offers the lower power requirement of the two schemes. As an example, at $D_T = 10^{-3}$, PPM(TH) has average optical power requirements which are lower than DPIM(NGB) by 1 dB and 1.3 dB for $L = 4$ and $L = 16$, respectively. However, when $D_T = 0.2$, it is DPIM(NGB) which outperforms PPM(TH) by ~ 0.8 dB and ~ 2.6 dB for $L = 4$ and $L = 16$, respectively. Both PPM(TH) and DPIM(NGB) have irreducible error rates which occur at very similar values of D_T . In contrast, for a given order, PPM(MAP) always achieves a lower power requirement than DPIM(NGB). Compared with OOK, all orders of DPIM(NGB) considered offer a lower average optical power requirement for D_T below ~ 0.1 . However, beyond ~ 0.22 it is OOK which yields the lowest power requirement.

If the x- and y- axes of Fig. 6.9 are changed to represent the ratio of RMS delay spread to slot duration and optical power penalty due to ISI, respectively, it can be observed that the relationship between these two quantities is almost the same for all orders of DPIM(NGB), as shown in Fig. 6.10. The same phenomenon has also been observed for PPM [102] and DPPM [120, 121].

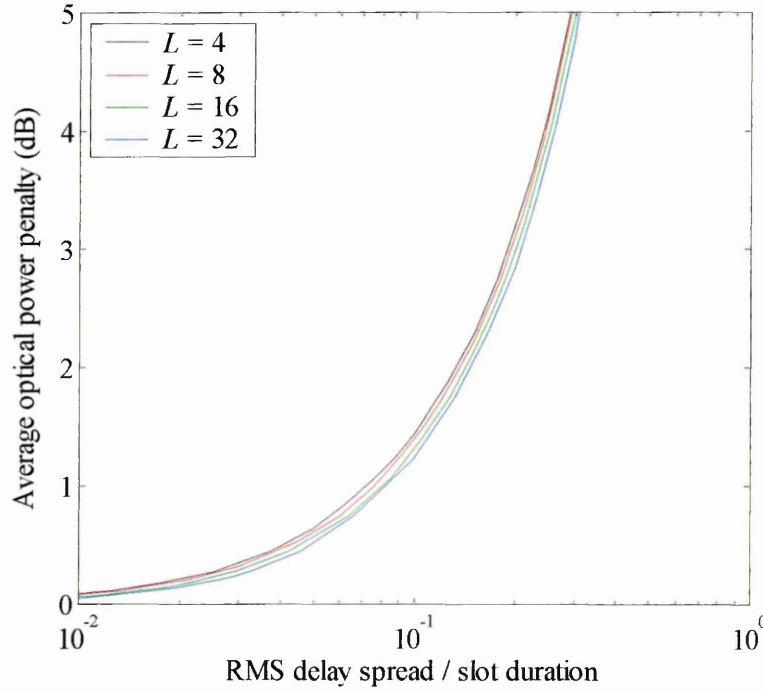


Fig. 6.10: Average optical power penalty versus RMS delay spread normalized to slot duration for DPIM(NGB)

In addition to the optimum threshold level, α_{opt} , two suboptimal levels are also considered. The first threshold level, α_1 , is given by:

$$\alpha_1 = \frac{L_{avg} RP_{avg}}{2} \sum_{\text{all } k} c_k, \quad (6.19)$$

and is essentially half the total photocurrent received when an isolated pulse is transmitted. The second suboptimal threshold level considered, α_2 , is given by:

$$\alpha_2 = \frac{L_{avg} RP_{avg}}{2} c_0, \quad (6.20)$$

and is equal to half the peak photocurrent received when an isolated pulse is transmitted.

Fig. 6.11 shows the normalized average optical power requirement versus normalized delay spread for $L = 4$ and $L = 32$ using all three threshold levels. The first suboptimum threshold level, α_1 , is found to give a performance close to that of the optimum level, particularly for lower orders. In contrast, α_2 results in a significant performance degradation, and leads to irreducible error rates being incurred at much lower normalized delay spreads. As an example, for $D_T = 0.1$, using α_2 results in a ~ 1.4 dB average optical power penalty compared with the other two threshold levels for $L = 4$. For $L = 32$, the error rate is irreducible when α_2 is used, whilst the other two threshold levels yield finite power penalties.

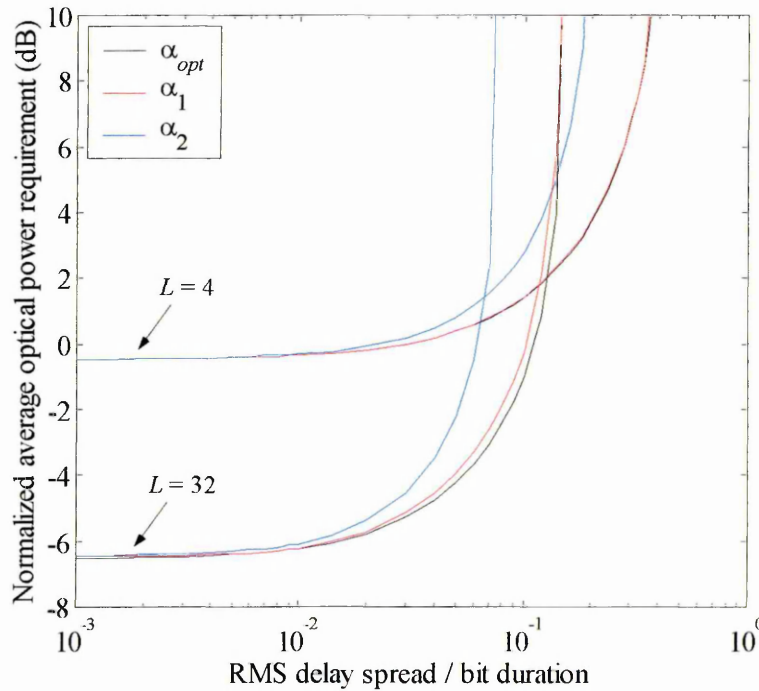


Fig. 6.11: Normalized average optical power requirement versus normalized delay spread for DPIM(NGB) with $L = 4$ and $L = 32$ using various threshold levels

6.4 DPIM With a Guard Band

Intuitively, when a DPIM slot sequence is passed through a multipath channel, the postcursor ISI is most severe in the slots immediately following a pulse. Using this fact, the unique symbol structure of DPIM may be exploited to provide a simple method of improving error performance in the presence of ISI. This method involves placing a guard band, which consists of one or more guard slots, in each symbol immediately following the pulse. Upon detection of a pulse, the following slot(s) contained within the guard band are automatically assigned as zeros, regardless of whether or not the sampled output of the receiver filter is above or below the threshold level. Thus, the postcursor ISI present in these slot(s) has no effect on system performance, provided that the pulse initiating the symbol is correctly detected. The mapping of source data to transmitted symbols for 4-DPIM(NGB), 4-DPIM(1GS) and 4-DPIM with a guard band consisting of 2 guard slots, denoted as 4-DPIM(2GS), is shown in Fig. 6.12. The shaded areas in the figure represent the guard slots.









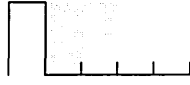
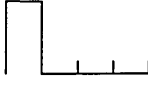
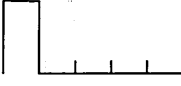
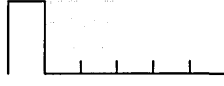
Source Data	4-DPIM Symbols		
	NGB	1GS	2GS
00			
01			
10			
11			

Fig. 6.12: Mapping of source data to transmitted symbols for 4-DPIM(NGB), 4-DPIM(1GS) and 4-DPIM(2GS)

The inclusion of a guard band increases the average number of slots per symbol, and consequently, in order to maintain the same average bit rate, it is necessary to reduce the slot duration. For DPIM(1GS) and DPIM(2GS) the slot duration is given in (4.1), where $L_{avg} = (L+3)/2$ and $(L+5)/2$, respectively. On its own, a reduction in slot duration would result in increased optical power requirements, since the ISI would affect a greater number of slots. Therefore, in order for the guard band to achieve a net reduction in optical power requirement, the reduction in power due to the presence of the guard band must outweigh the increase in power due to the reduced slot duration.

For DPIM(1GS), the probability of error for any given slot is dependent not only on the sampled signal value corresponding to that particular slot, but also on the sampled value of the previous slot. Thus, when evaluating DPIM(1GS), if c_k has m taps, it is necessary to generate sequences of length $(m+1)$, and evaluate the probability of slot error for the m^{th} slot, using sample values for the m^{th} and $(m-1)^{\text{th}}$ time slots. Note that by including a guard band, for a sequence length of $(m+1)$ slots, not all the 2^{m+1} possible DPIM(NGB) sequences are actually valid, since the guard band excludes all sequences which contain adjacent pulses. The guard band does, however, increase the maximum run length of consecutive zeros.

In order to explain the function of the guard band, the following notation is used. Let b_m and b_{m-1} represent the values of the m^{th} and $(m-1)^{\text{th}}$ slots in a DPIM(1GS) sequence, respectively, where $b_m, b_{m-1} \in \{0,1\}$. Let \hat{b}_m and \hat{b}_{m-1} represent the estimate of b_m and b_{m-1} , respectively, after passing through the multipath channel. Since the probability of slot error for the m^{th} slot in a sequence is affected by the detection of the $(m-1)^{\text{th}}$ slot, there are 4 possible detection scenarios, as outlined below:

- (i) If $b_{m-1} = 1$ and is correctly detected, b_m must be a zero and \hat{b}_m is automatically assigned a zero. Therefore, there is no chance of an error in slot m .

- (ii) If $b_{m-1} = 1$ but is falsely detected as a zero, b_m must be a zero but \hat{b}_m is not automatically assigned a zero. Therefore, an error will occur if $\hat{b}_m = 1$.
- (iii) If $b_{m-1} = 0$ and is correctly detected, b_m could be either a one or zero, and the $(m-1)^{\text{th}}$ slot has no effect on the probability of error in slot m .
- (iv) If $b_{m-1} = 0$ but is falsely detected as a one, \hat{b}_m is automatically assigned a zero, but an error will occur if $b_m = 1$.

The probability of slot error for DPIM(1GS) cannot easily be expressed in a concise form. Consequently, pseudo code is used. In conjunction with the above notation, let y_m and y_{m-1} be the sampled output of the receiver filter corresponding to the m^{th} and $(m-1)^{\text{th}}$ slots, and α_{opt} be the optimum threshold level. For any given $(m+1)$ -slot DPIM(1GS) sequence, the probability of slot error in the m^{th} slot may be calculated as follows:

```

if  $b_{m-1} = 1$  &  $\hat{b}_{m-1} = 1$            {  $b_m = 0$  and  $\hat{b}_m$  is automatically set to 0 }
     $\epsilon_m = 0$ 

elseif  $b_{m-1} = 1$  &  $\hat{b}_{m-1} = 0$        {  $b_m = 0$  but  $\hat{b}_m$  is not automatically set to 0 }
     $\epsilon_m = Q((\alpha_{opt} - y_m) / \sqrt{N_0/2})$ 

elseif  $b_{m-1} = 0$  &  $\hat{b}_{m-1} = 0$        {  $b_m$  could be 1 or 0 }
    if  $b_m = 1$ 
         $\epsilon_m = Q((y_m - \alpha_{opt}) / \sqrt{N_0/2})$ 
    else
         $\epsilon_m = Q((\alpha_{opt} - y_m) / \sqrt{N_0/2})$ 
    end

elseif  $b_{m-1} = 0$  &  $\hat{b}_{m-1} = 1$        {  $\hat{b}_m$  is automatically set to 0, but  $b_m$  could be 1 }

```

```

    if  $b_m = 1$ 
         $\varepsilon_m = 1$ 
    else
         $\varepsilon_m = 0$ 
    end
end

```

As before, in order to calculate the average probability of slot error, the above pseudo code is used to calculate the probability of slot error for the m^{th} slot in every possible $(m+1)$ slot sequence. These probabilities are then multiplied by their corresponding occurrence probabilities and the results are summed. The average probability of slot error may then be converted into a corresponding PER using (4.11), with the substitution $L_{\text{avg}} = (L+3)/2$.

As a simple extension to this technique, the duration of the guard band may be increased such that it consists of two slots. In this case, if c_k has m taps, it is necessary to generate slot sequences of length $(m+2)$, and evaluate the probability of slot error for the $(m+1)^{\text{th}}$ slot, using sample values for the $(m+1)^{\text{th}}$, m^{th} and $(m-1)^{\text{th}}$ time slots. Let b_{m+1} represent the value of the $(m+1)^{\text{th}}$ slot in a DPIM(1GS) sequence, and let \hat{b}_{m+1} represent the estimate of b_{m+1} after passing through the multipath channel. With two guard slots, the number of possible detection scenarios increases, as outlined below:

- (i) If $b_{m-1} = 1$ and is correctly detected, b_{m+1} must be a zero and \hat{b}_{m+1} is automatically assigned a zero. Therefore, there is no chance of an error in slot $(m+1)$.
- (ii) If $b_{m-1} = 1$ but is falsely detected as a zero, b_{m+1} must be a zero but \hat{b}_{m+1} is not automatically assigned a zero. If \hat{b}_m is falsely assigned as a one, then \hat{b}_{m+1} will automatically be assigned a zero and no error will occur. If \hat{b}_m is correctly detected as a zero, then an error will occur if $\hat{b}_{m+1} = 1$.

- (iii) If $b_{m-1} = 0$ and is correctly detected, the probability of error is calculated in the same way as the DPIM(1GS) method.
- (iv) If $b_{m-1} = 0$ and is falsely detected as a one, \hat{b}_{m+1} is automatically assigned a zero, but an error will occur if $b_{m+1} = 1$.

Let y_{m+1} be the sampled output of the receiver filter corresponding to the $(m+1)^{\text{th}}$ slot. Again, using pseudo code, for any given $(m+2)$ -slot DPIM(2GS) sequence, the probability of slot error in the $(m+1)^{\text{th}}$ slot may be calculated as follows:

```

If  $b_{m-1} = 1$  &  $\hat{b}_{m-1} = 1$       {  $b_{m+1} = 0$  and  $\hat{b}_{m+1}$  is automatically set to 0 }
     $\epsilon_{m+1} = 0$ 

elseif  $b_{m-1} = 1$  &  $\hat{b}_{m-1} = 0$     {  $b_{m+1} = 0$  but  $\hat{b}_{m+1}$  is not automatically set to 0 }
    if  $\hat{b}_m = 1$ 
         $\epsilon_{m+1} = 0$ 
    else
         $\epsilon_{m+1} = Q((\alpha_{opt} - y_{m+1}) / \sqrt{N_0/2})$ 
    end

elseif  $b_{m-1} = 0$  &  $\hat{b}_{m-1} = 0$     {  $b_{m+1}$  could be 1 or 0 }
    if  $b_m = 1$  &  $\hat{b}_m = 1$       {  $b_{m+1} = 0$  and  $\hat{b}_{m+1}$  is automatically set to 0 }
         $\epsilon_{m+1} = 0$ 
    elseif  $b_m = 1$  &  $\hat{b}_m = 0$     {  $b_{m+1} = 0$  but  $\hat{b}_{m+1}$  is not automatically set to 0 }
         $\epsilon_{m+1} = Q((\alpha_{opt} - y_{m+1}) / \sqrt{N_0/2})$ 
    elseif  $b_m = 0$  &  $\hat{b}_m = 0$     {  $b_{m+1}$  could be 1 or 0 }
        if  $b_{m+1} = 1$ 
             $\epsilon_{m+1} = Q((y_{m+1} - \alpha_{opt}) / \sqrt{N_0/2})$ 
        else

```

```

                                 $\epsilon_{m+1} = Q((\alpha_{opt} - y_{m+1})/\sqrt{N_0/2})$ 
                                end
elseif  $b_m = 0$  &  $\hat{b}_m = 1$  {  $\hat{b}_{m+1}$  is automatically set to 0, but  $b_{m+1}$  could be 1 }

                                if  $b_{m+1} = 1$ 
                                     $\epsilon_{m+1} = 1$ 
                                else
                                     $\epsilon_{m+1} = 0$ 
                                end

                                end

elseif  $b_{m-1} = 0$  &  $\hat{b}_{m-1} = 1$  {  $\hat{b}_{m+1}$  is automatically set to 0, but  $b_{m+1}$  could be 1 }

                                if  $b_{m+1} = 1$ 
                                     $\epsilon_{m+1} = 1$ 
                                else
                                     $\epsilon_{m+1} = 0$ 
                                end

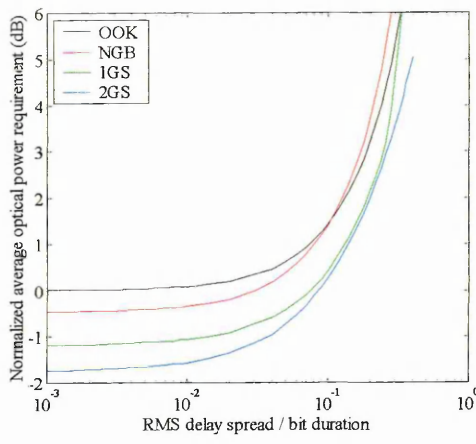
                                end

end

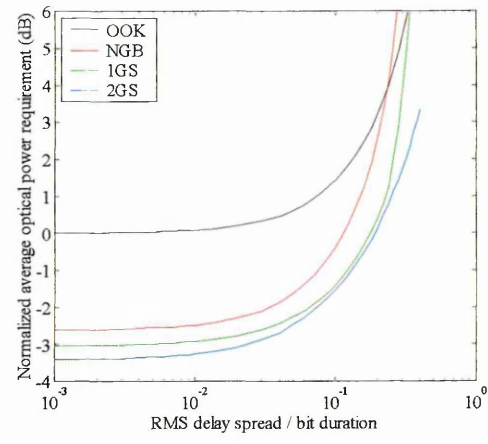
```

Again, the average probability of slot error is found by multiplying each error probability by its corresponding probability of occurrence and then summing the results. This may then be converted into a PER using (4.11), with the substitution $L_{avg} = (L+5)/2$.

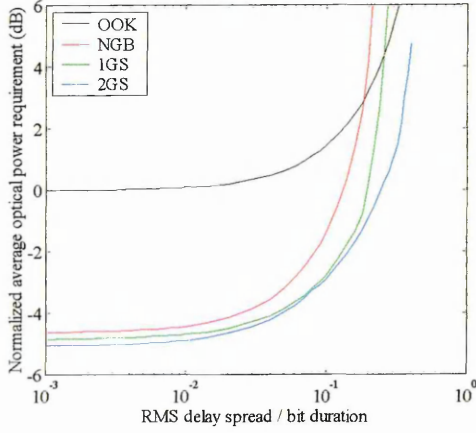
For each value of D_T in the range 10^{-3} to 0.4, the average optical power requirement was calculated, using the optimum sampling point and threshold level, for various orders of DPIM(1GS) and DPIM(2GS). These normalized average optical power requirements are plotted in Fig. 6.13, along with those of DPIM(NGB). For comparison, the average optical power requirement for OOK is also shown in the figure.



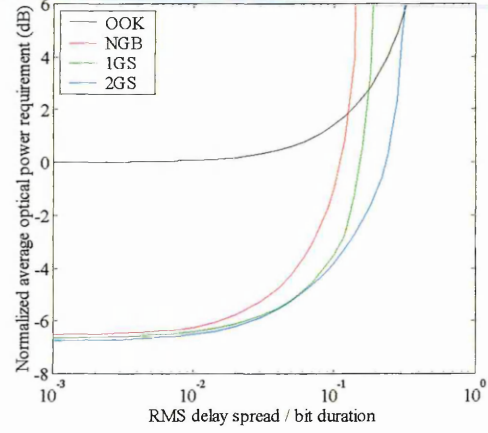
(a)



(b)



(c)



(d)

Fig. 6.13: Normalized average optical power requirement versus normalized delay spread for DPIM(NGB), DPIM(1GS) and DPIM(2GS) with: (a) $L = 4$, (b) $L = 8$, (c) $L = 16$, and (d) $L = 32$

At low values of D_T , adding a guard band reduces the average duty cycle of the transmitted signal and hence, gives a reduction in the average optical power requirement relative to the NGB case. This effect is more pronounced at lower orders, where the average duty cycle is reduced by a greater percentage. As an example, for $D_T = 1 \times 10^{-3}$ and $L = 4$, the reductions are ~ 0.7 dB for 1GS and ~ 1.25 dB for 2GS, whilst for $L = 16$, the reductions are ~ 0.25 dB and ~ 0.45 dB for 1GS and 2GS, respectively. As D_T increases, the difference between the NGB and 1GS curves increases, thus highlighting the effectiveness of adding a single guard slot. Again taking 16-DPIM as an example, at $D_T = 0.1$, the difference between NGB and 1GS has increased to ~ 1.4 dB. At normalized delay spreads where DPIM(NGB) experiences irreducible

error rates, the power requirements are finite for DPIM(1GS). Adding a second guard slot gives a further reduction in power requirements at low values of D_T . Again, this is more pronounced at lower orders. For high normalized delay spreads, the improvement in performance over 1GS is clear, with irreducible error rates occurring at higher values of D_T than they do for 1GS. For intermediate normalized delay spreads however, adding a second guard slot results in only a marginal reduction in power requirement. As an example, for $L = 16$ and $D_T = 0.1$, 2GS yields a mere ~ 0.1 dB reduction relative to 1GS. The reason for this can be explained with the aid of Fig. 6.14, which shows the average optical power penalty due to ISI versus normalized delay spread.

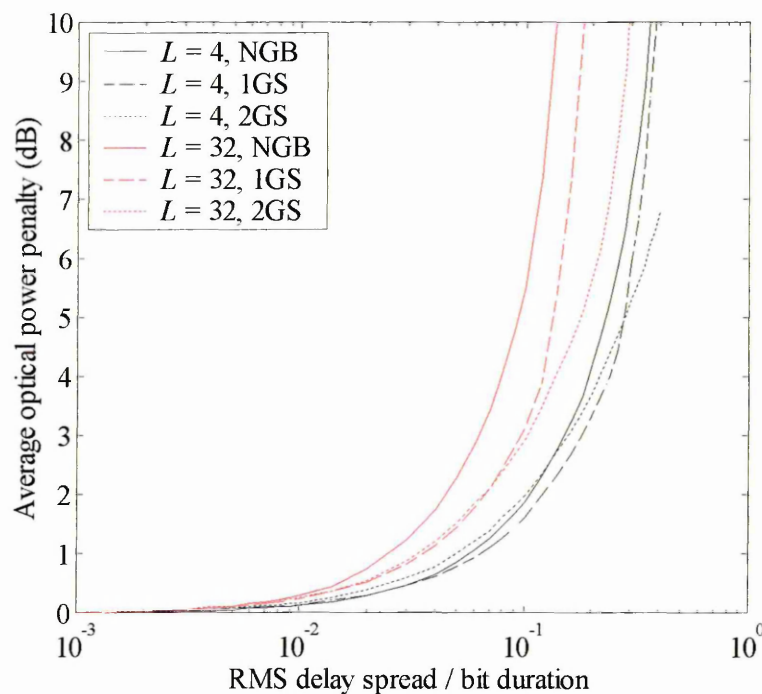


Fig. 6.14: Average optical power penalty versus normalized delay spread for DPIM(NGB), DPIM(1GS) and DPIM(2GS) with $L = 4$ and $L = 32$

From Fig. 6.14 it may be observed that at intermediate values of D_T , typically $0.01 - 0.1$, 2GS results in a marginally higher average optical power penalty than 1GS. This means that the benefit of adding a second guard slot is outweighed by the reduction in slot duration required to accommodate it. Therefore, within these regions, the power requirements of 2GS converge with those of 1GS.

Even when a guard band is used, OOK still yields a lower average optical power requirement than DPIM at high values of D_T . The inclusion of the guard band simply increases the value at which the crossover takes place. For example, with reference to Fig. 6.13(d), OOK offers a lower average optical power requirement than 32-DPIM(NGB) for $D_T > \sim 0.13$, whilst this crossover does not take place until $D_T = \sim 0.18$ for 32-DPIM(1GS), and $D_T = \sim 0.31$ for 32-DPIM(2GS).

6.5 DPIM With Equalization

As discussed in chapter 4, since symbol boundaries are not known prior to detection, practical implementation of maximum likelihood sequence detection for DPIM is unfeasible. Therefore, in this section, suboptimal decision feedback equalization is considered. The DFE, first proposed by Austin [144], is a nonlinear receiver structure which offers a good compromise between performance and implementation complexity [18]. DFEs have attracted considerable interest for use in indoor wireless infrared links [10, 32, 105, 106, 108-110, 112, 113, 120, 121], and a number of experimental systems using DFEs have been reported [35, 36, 41]. As previously discussed in chapter 3, the two most popular criteria which a DFE can use to optimize its filter coefficients are ZF and MSE. Belfiore [104] showed that whilst the performance of MSE-DFEs is generally superior to that of ZF-DFEs, at high signal-to-noise ratios their performance is virtually identical. Using measured indoor infrared channels, Audeh *et. al.* [110] compared the performance of PPM using both ZF-DFEs and MSE-DFEs, and found their performance to be identical. Since the analysis of ZF-DFEs is more straightforward, the majority of the research carried out has focussed on this type of DFE. Therefore, for continuity, the ZF-DFE is considered exclusively in this analysis.

The DFE consists of a feedforward filter, a detector and a feedback filter. Price [145] showed that the optimum feedforward filter in a ZF-DFE is the WMF, first proposed by Forney [100]. In the context of the ZF-DFE, the WMF plays an important role of equalizing the precursor ISI, which is defined as the interference from future data symbols [18]. Therefore the remaining ISI is postcursor, meaning that it is due to past data symbols. By feeding back the detected estimate of these past data symbols, the ISI they introduce on future symbols may be cancelled. This task is performed by the feedback filter, which is sometimes referred to as the postcursor equalizer.

A block diagram of the DPIM(NGB) system using a slot-rate DFE is shown in Fig. 6.15(a). The DPIM(NGB) slot sequence, \mathbf{b}_k , is passed through a transmitter filter, which has a unit-amplitude rectangular impulse response $p(t)$, with a duration of T_s . The pulses are scaled by the peak transmitted optical power, $L_{avg}P_{avg}$, and passed through a multipath channel with an impulse response $h(t)$. The received optical signal power is converted into a photocurrent by multiplying it with the photodetector responsivity R . AWGN $n(t)$, with a double-sided PSD of $N_0/2$, is added to the detected signal. A whitened-matched filter is then used, which consists of a receiver filter which is matched to the received pulse shape, followed by a slot-rate sampler and a noise whitening filter.

The impulse response of the receiver filter is given by:

$$r(t) = p(-t) \otimes h(-t). \quad (6.21)$$

The noise whitening filter is calculated as follows. The discrete-time impulse response of the cascaded transmitter filter, channel and receiver filter is given by:

$$c_k = p(t) \otimes h(t) \otimes r(t) \Big|_{t=kT_s}. \quad (6.22)$$

Since the receiver filter has an impulse response which is a time reversed version of the received pulse shape, if the optimum sampling point is selected by maximising the zero tap c_0 , then c_k will have an equal number of precursor and postcursor taps. Assuming that c_k has a total of $(2m+1)$ taps, following [99], let $C(z)$ denote the two-sided z transform of c_k , i.e.,

$$C(z) = \sum_{k=-m}^m c_k z^{-k} . \quad (6.23)$$

The $2m$ roots of $C(z)$ have the symmetry that if ρ is a root, then $1/\rho^*$ is also a root. Note that the asterisk denotes complex conjugate. Therefore, $C(z)$ can be factored and expressed as:

$$C(z) = W(z)W^*(1/Z^*), \quad (6.24)$$

where $W(z)$ has m roots $\rho_1, \rho_2, \dots, \rho_m$ and $W^*(1/z^*)$ has m roots $1/\rho_1^*, 1/\rho_2^*, \dots, 1/\rho_m^*$. If all the roots of $W^*(1/z^*)$ are inside the unit circle, i.e. the filter is minimum phase, $1/W^*(1/z^*)$ represents a physically realisable, stable, recursive discrete-time noise whitening filter. The whitening filter whitens the noise which is coloured by the receiver filter $r(t)$. Let w_k denote the tap coefficients of $1/W^*(1/z^*)$. The transmitter filter, channel and WMF may be expressed as a discrete-time impulse response, given by:

$$g_k = L_{avg} RP_{avg} \cdot c_k \otimes w_k , \quad (6.25)$$

which includes the scaling for the peak transmitted optical power and the conversion from received optical power to photocurrent. The discrete-time output of the whitening filter is passed to a threshold detector, which assigns a one or a zero to each slot. The output of the threshold detector $\hat{\mathbf{b}}_k$ is the estimate of the transmitted slot sequence \mathbf{b}_k , and forms the input to a feedback filter with an impulse response $g_k - g_0\delta_k$, which represents the strictly causal portion of g_k . The block diagram of Fig. 6.15(a) may be simplified to an equivalent discrete-time block

diagram, as illustrated in Fig. 6.15(b), where the noise samples n_k are IID with zero mean and a variance of $N_0/2$.

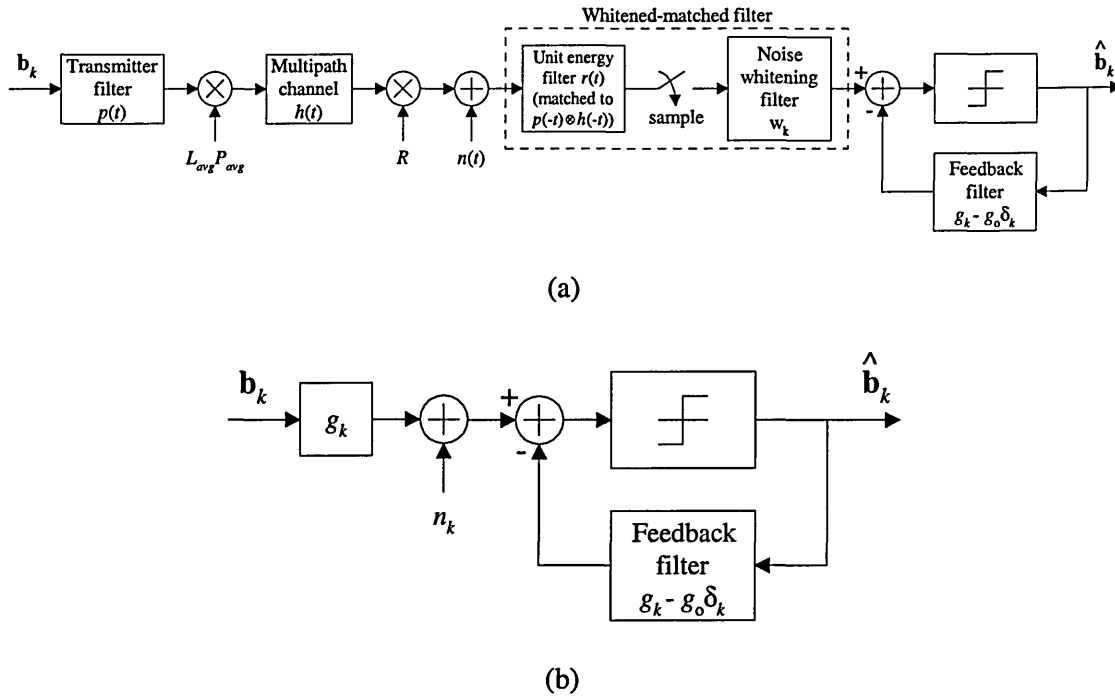


Fig. 6.15: (a) Block diagram of DPIM system with DFE, and (b) Equivalent discrete-time block diagram of DPIM system with DFE

Assuming that all detected slots are correct, and the filters have an infinite number of taps which are optimally adjusted in accordance with the ZF criterion, the probability of slot error using a ZF-DFE with the threshold level set midway between expected one and zero levels is given by [120, 121]:

$$P_{e,slot,ZF-DFE} = Q\left(\frac{g_0}{2\sqrt{N_0/2}}\right). \quad (6.26)$$

Using (6.26), and converting $P_{e,slot,ZF-DFE}$ into an average PER using (4.11), with the substitution $L_{avg} = (L + 1)/2$, the average optical power requirement for DPIM(NGB) using a slot-rate ZF-DFE was calculated for various orders and normalized delay spreads, as plotted in Fig. 6.16.

Also shown in the figure, for comparison, are the average optical power requirements for unequalized DPIM(NGB).

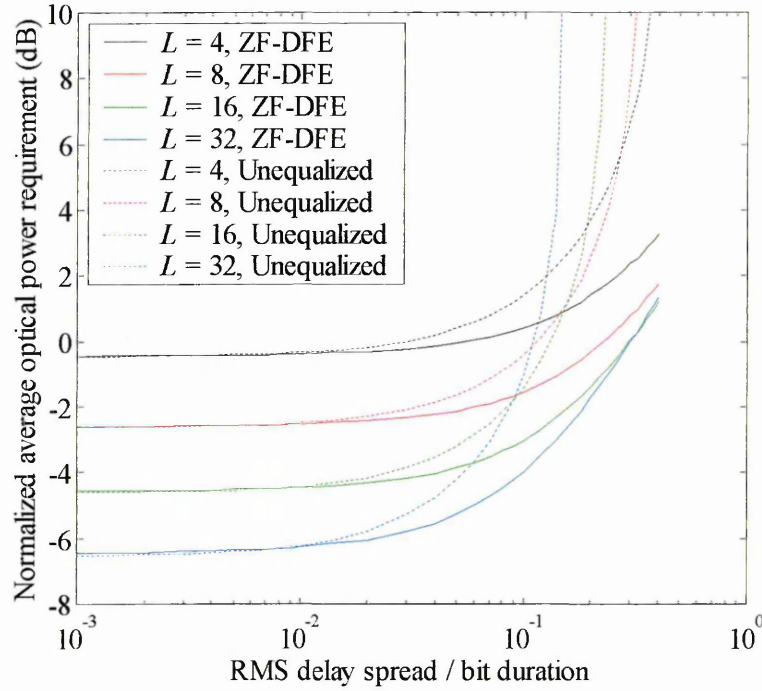


Fig. 6.16: Normalized average optical power requirement versus normalized delay spread for DPIM(NGB) with a ZF-DFE

At low normalized delay spreads, typically below 0.01, the ZF-DFE gives no improvement in performance. However, as expected, the effectiveness of the equalizer in reducing the average optical power requirement becomes apparent as D_T increases. For example, when $D_T = 0.1$, the ZF-DFE yields power penalty reductions of ~ 1 dB - ~ 3 dB, for the orders considered. Furthermore, at normalized delay spreads which result in irreducible error rates for the unequalized system, using a ZF-DFE results in finite power requirements at these values.

In order to compare the effectiveness of the guard band technique, as discussed in the previous section, with the ZF-DFE, optical power requirements for both are plotted in Fig. 6.17 for $L = 4$ and $L = 32$.

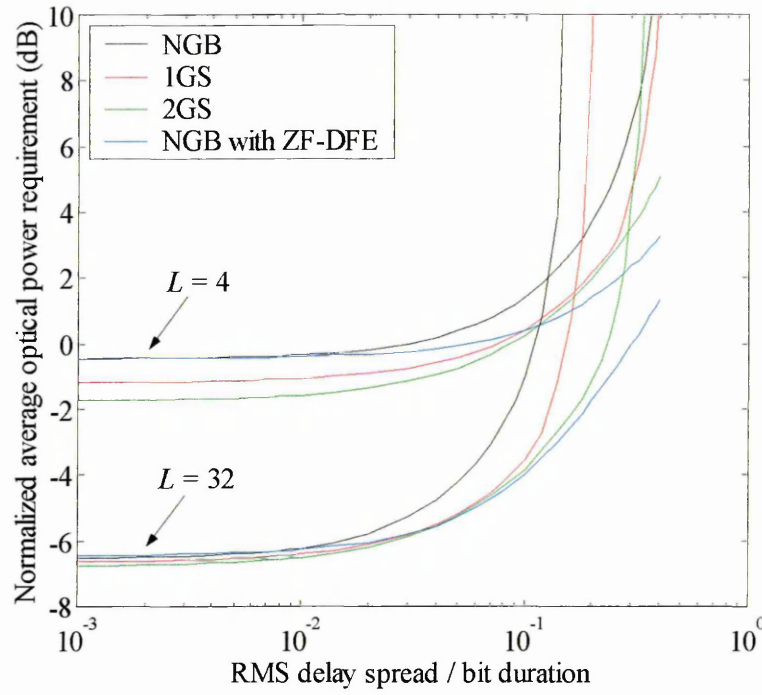


Fig. 6.17: Normalized average optical power requirement versus normalized delay spread for DPIM(NGB), DPIM(1GS), DPIM(2GS) and DPIM(NGB) with a ZF-DFE for $L = 4$ and $L = 32$

At low normalized delay spreads, the power requirements of DPIM(NGB) using a ZF-DFE are virtually identical to those without equalization, and consequently, DPIM with a guard band outperforms the equalized scheme. However, for any given normalized delay spread, the ISI power penalty for DPIM(NGB) using a ZF-DFE is lower than it is for unequalized DPIM(NGB), DPIM(1GS) and DPIM(2GS). Consequently, as D_T increases, the power requirement curves for DPIM(NGB) using a ZF-DFE intersect with those of DPIM(1GS) and DPIM(2GS). Beyond the final points of intersection, DPIM(NGB) using a ZF-DFE offers the lowest average optical power requirements of the schemes considered. However, significant improvements in performance are not achieved until D_T is high, typically above 0.3, and on channels where the ISI is not too severe, the guard band technique incurs only a small power penalty compared with the ZF-DFE. For example, with $L = 32$ and $D_T = 0.16$, DPIM(NGB) has an irreducible error rate, whilst DPIM(1GS) results in an optical power requirement which is ~ 3.2 dB higher than that of DPIM(NGB) using a ZF-DFE. By using DPIM(2GS), this power penalty reduces to a mere ~ 0.4 dB compared with DPIM(NGB) using a ZF-DFE.

The analysis carried out in this section make the assumptions that the channel impulse response is known *a priori*, and the filters used in the ZF-DFE have an infinite number of taps with the tap weights perfectly adjusted. In practise, neither of these are true, and an adaptive ZF-DFE with a finite number of taps will give a performance below that of the optimum ZF-DFE used in this section. Furthermore, if the threshold detector makes an incorrect decision, the ISI correction is flawed for future decisions. This phenomenon is known as error propagation, and tends to result in bursts of errors. This effect has not been considered in this analysis. Nevertheless, the primary objective of the ZF-DFE analysis is to provide some reference by which to access the effectiveness of the guard band technique. In this respect, the analysis carried out is adequate, and any further investigation is beyond the scope of this thesis.

6.6 Summary

In the absence of multipath dispersion, the power efficiency of DPIM and PPM can be improved by increasing the order. However, increasing the order also increases the bandwidth requirement, which on multipath channels results in a greater ISI power penalty. When D_T is sufficiently large, the reduction in average optical power requirement due to the reduced duty cycle is outweighed by the increased ISI power penalty, and it becomes more efficient to switch to a lower order. Therefore, for unequalized DPIM and PPM, the most power efficient order on any given channel is a function of the normalized delay spread. As an example, when the ISI is negligible, i.e. $D_T = 10^{-3}$, 16-DPIM(NGB) has an average optical power requirement which is ~ 4.2 dB lower than that of 4-DPIM(NGB). However, when $D_T = 0.2$, it is 4-DPIM(NGB) which outperforms 16-DPIM(NGB) by ~ 0.5 dB.

Although OOK has the lowest power efficiency of the schemes considered in the absence of ISI, it also has the lowest bandwidth requirement, and consequently the lowest ISI power penalty for unequalized operation on multipath channels. Therefore, when the normalized delay spread is sufficiently large, OOK gives the lowest average optical power requirement of any unequalized

scheme considered, with the exception of 4-PPM(MAP), which gives very similar results at high values of D_T . Due to its more sophisticated detection technique, PPM(MAP) always outperforms PPM(TH), and the margin of improvement is found to increase as D_T increases. For a given order, DPIM(NGB) has a lower bandwidth requirement than PPM, and consequently has a lower ISI power penalty than PPM(TH). However, at low normalized delay spreads, PPM(TH) is more power efficient due to its reduced duty cycle. Consequently, the average optical power requirements of the two schemes intersect at a certain value of D_T , and above this value DPIM(NGB) offers the lower average optical power requirement, though both schemes do give irreducible error rates at very similar values of D_T . To cite the example given previously in section 6.3.3, at $D_T = 10^{-3}$, 16-PPM(TH) has a ~ 1.3 dB lower average optical power requirement than 16-DPIM(NGB). However, when $D_T = 0.2$, it is 16-DPIM(NGB) which outperforms 16-PPM(TH) by ~ 2.6 dB. Compared with PPM(MAP), DPIM(NGB) gives lower ISI power penalties for low to medium normalized delay spreads, but is always inferior to PPM(MAP) in terms of average optical power requirement.

By introducing a guard band, the performance of DPIM in the presence of ISI can be improved considerably. In order to achieve a net reduction in average optical power requirement, the reduction in power due to the effectiveness of the guard band in mitigating postcursor ISI must outweigh the increase in power due to the increased bandwidth required to accommodate the guard band. On channels where the ISI is nominal, the presence of a guard band gives a reduction in average optical power requirement due to the reduced average duty cycle of the transmitted signal. As the severity of ISI increases, the difference in performance between DPIM with and without a guard band increases, thus highlighting the effectiveness of the guard band technique. Considering 16-DPIM as an example, when $D_T = 10^{-3}$, adding a single guard slot reduces the average optical power requirement by ~ 0.2 dB. When $D_T = 0.2$, the difference between 16-DPIM(NGB) and 16-DPIM(1GS) has increased to ~ 4.1 dB. Furthermore, normalized delay spreads which result in irreducible error rates without a guard band give finite power requirements when a guard band is used. At intermediate values of D_T , typically $0.01 \leq D_T \leq 0.1$, the reduction in power requirement offered by adding a second guard slot is

minimal. However, increasing the length of the guard band from one to two slots becomes worthwhile at high values of D_T . The performance of DPIM(NGB) using a ZF-DFE was found to be significantly better than that of DPIM(1GS) and DPIM(2GS) only on channels which suffer from severe ISI, i.e. typically for $D_T \geq 0.2$. On the majority of channels, the guard band technique is sufficient to achieve reliable operation over a useful range of delay spreads, especially considering the reduced cost and complexity associated with implementing a guard band compared with an adaptive DFE.

Chapter 7

System Implementation

7.1 Introduction

To augment the theoretical and simulated performance of DPIM, a low bit rate prototype diffuse link was designed and constructed. Based on 16-DPIM(1GS), the link has a slot frequency of 6 MHz, thereby achieving an average bit rate of ~2.5 Mbit/s. In this chapter, results of error performance measurements carried out on the link under a variety of ambient light conditions are presented. For reference, the design of the prototype link is described in detail in appendix B. The remainder of this chapter is organised as follows. A brief outline of the experimental system is given in section 7.2, and the setup of the link is described in section 7.3. Results of error performance measurements carried out on the prototype link are presented in section 7.4, and finally, a summary of the chapter is given in section 7.5.

7.2 System Overview

A block diagram of the experimental system is shown in Fig. 7.1

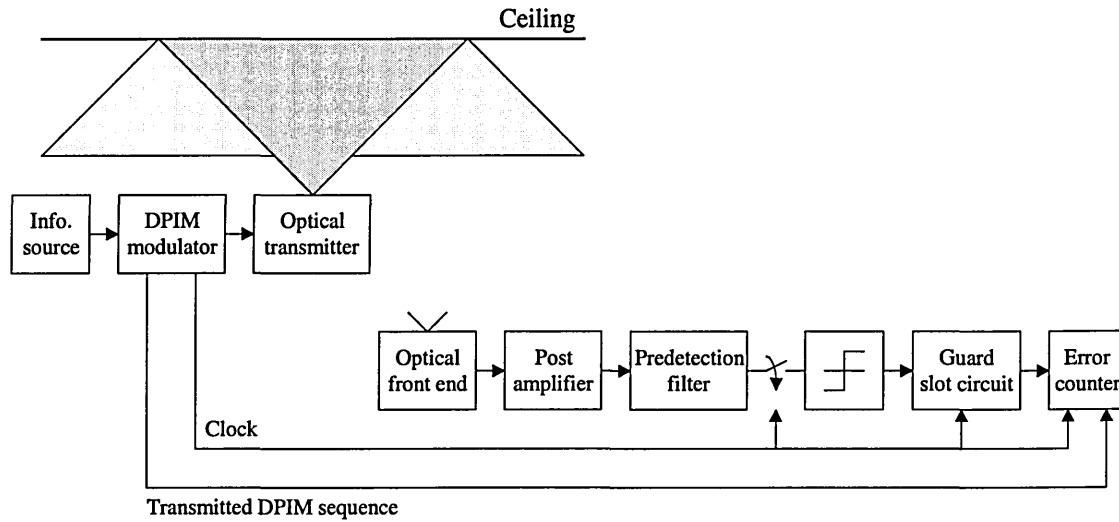


Fig. 7.1: System block diagram

The transmitter is comprised of an information source, a DPIM modulator and an optical transmitter. The DPIM modulator encodes data from the information source into 16-DPIM(1GS) symbols. The circuitry required to perform this task is synthesized on a field programmable gate array (FPGA) device, the code for which is included in appendix B. The slot sequence emerging from the DPIM modulator is passed to an optical transmitter which consists of an array of 12 infrared LEDs, each of which can be enabled or disabled separately such that the optical transmit power can be varied. The LEDs have a centre wavelength of 875 nm, a viewing angle of 30°, and are operated such that the specified radiant optical power for each LED is 38 mW. With all 12 LEDs on, the peak optical power of the array is 456 mW, which for 16-DPIM(1GS), corresponds to an average optical transmit power of 48 mW. Note that all 12 LEDs are aligned vertically, pointing at the ceiling of the room.

At the receiver, photodetection is carried out by an array of 5 silicon PIN photodiodes connected in parallel. The photodiodes have a spectral range of 400 - 1100 nm, a half angle of 60°, and an

active area of 7 mm^2 , giving a total active area of 35 mm^2 for the detector array. The optical front end also contains a second detector array, identical to the first, which is used to measure the received photocurrent due to both the transmitted signal and the ambient light sources. At a wavelength centred on 875 nm , the photodiodes have a specified responsivity R of 0.6 A/W . Knowing this, the measured average photocurrent I_B may be converted into an average received irradiance H_{avg} with units dBm/cm^2 using:

$$H_{avg} = 10 \log_{10} \left(\frac{I_B \cdot \frac{100}{35} \cdot \frac{1}{R}}{1 \times 10^{-3}} \right). \quad (7.1)$$

The photocurrent generated by the first photodiode array is amplified by a transimpedance preamplifier, which is then followed by an additional gain stage. A two stage post amplifier is then used to further increase the gain, resulting in an overall transimpedance of $\sim 12 \text{ M}\Omega$. The AC coupling within the post amplifier forms a high-pass filter, and was initially tuned to give a cut-on frequency of $\sim 50 \text{ kHz}$. As discussed in section 7.4.1, this choice of cut-on frequency is sufficient to reject interference resulting from fluorescent lamps driven by low-frequency ballasts, whilst introducing only a negligible amount of baseline wander.

The amplified signal is then passed to a predetection filter, the fundamental purpose of which is to increase the likelihood of successfully detecting pulses in the presence of noise. A 4th order Bessel low pass filter with a cut-off frequency of 3.6 MHz was used which, from the analysis carried out in appendix B, was found to give a performance close to that of a matched filter. A threshold detector is then used to compare the output of the predetection filter with a threshold voltage, and assign a logic one or zero to each slot depending on whether the signal is above or below the threshold voltage at the sampling instant. The sampling points are derived from the transmitter clock, thereby eliminating the effect of timing jitter from the results obtained.

The output of the threshold detector is passed to a guard slot circuit, the purpose of which is to automatically assign a zero to any slot which immediately follows a pulse. The regenerated DPIM slot sequence is then compared with the transmitted sequence, and the number of slots in which the two signals differ are counted.

7.3 Link Setup

The experimental link was set up in a laboratory with dimensions 6.85 m x 6.64 m x 2.9 m, with large windows on two walls facing north and west. The position of the transmitter and receiver within the room, which was fixed throughout all the measurements, is shown in Fig. 7.2. The horizontal distance between the transmitter and receiver was 2 m. Both the transmitter and receiver were situated on benches, pointing vertically upwards towards the ceiling, i.e. a diffuse configuration.

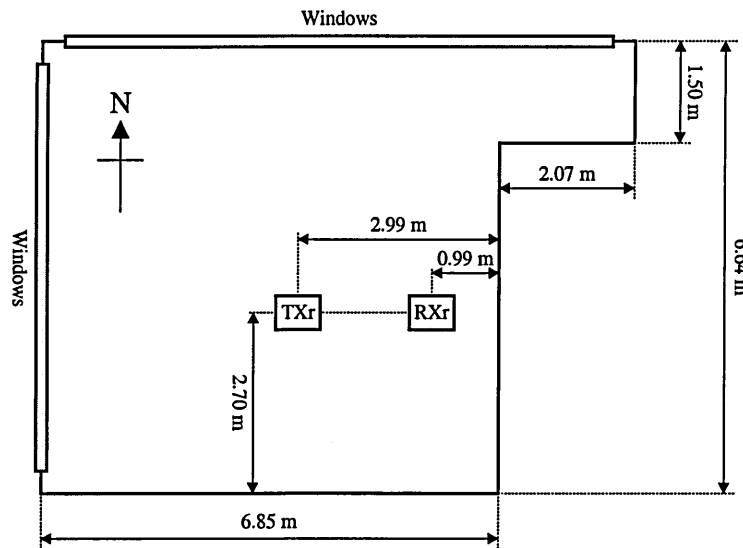


Fig. 7.2: Position of transmitter and receiver

In order to measure the effect of various ambient light sources on link performance, the light sources described and measured in chapter 2 were used. The positioning of these sources is shown in Fig. 7.3. The laboratory is illuminated by 18 x 36 W ceiling mounted low-frequency

fluorescent lamps, which generate an average background photocurrent of $17.9\ \mu\text{A}$ at the receiver location indicated in Fig. 7.2, when no optical filter is used. Consequently, the position of the fluorescent lamp (FL) indicated in Fig. 7.3 was chosen such that a similar photocurrent was obtained from a single lamp, thus making the results valid for a typical indoor environment. Note that the fluorescent lamp was positioned such that the centre of the tube was on the transmitter-receiver axis. The position of the incandescent bulb (B) was chosen to simulate a desk lamp.

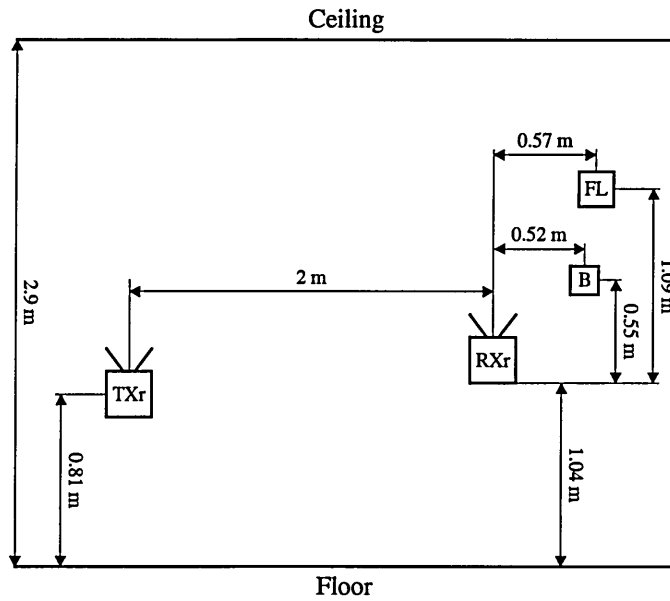


Fig. 7.3: Position of artificial ambient light sources

The average background photocurrent I_B generated by these artificial ambient light sources, with and without the RG780 optical filter, are listed in Table 7.1, along with daylight measurements.

Source	I_B (μA) (without optical filter)	I_B (μA) (with optical filter)	Reduction (%)
Incandescent bulb	114	75	34.2
LF fluorescent lamp	17.9	1.3	92.7
HF fluorescent lamp	18.6	1.1	94.1
Natural daylight	40 - 50	12 - 15	70

Table 7.1: Average background photocurrent from various ambient light sources

The performance of the experimental link was measured in terms of the slot error rate (SER), since using the PER would slow down the measurement process significantly. Measurements were taken under a variety of ambient light conditions, both with and without optical filtering. The optical transmit power was varied by switching on/off the 12 individual LED drivers. This allowed the average received irradiance, due to the transmitted signal, to be varied between -39.7 and -50.2 dBm/cm². Note that, without optical filtering, the ambient light sources result in an average background irradiance which is 29 - 37 dB higher than the maximum average received signal irradiance. For each measurement taken, the threshold level was manually adjusted to minimize the SER.

7.4 Performance of Experimental Link

7.4.1 Receiver not optimized for high-frequency fluorescent lamp

For low-frequency electronic ballasts, the detected electrical spectrum contains harmonics which do not extend beyond a few tens of kHz. Consequently, a HPF cut-on frequency of 50 kHz is sufficient to filter out the majority of this interference signal. Note that for a bit rate of ~2.5 Mbit/s, this corresponds to a normalized cut-on frequency f_c/R_b of ~0.02, which from Fig. 5.18, should introduce virtually no baseline wander power penalty. To achieve this cut-on frequency, the capacitors C_1 and C_2 in the post amplifier of Fig. B.7 were set to 2.2 nF, giving a cut-on frequency of ~48 kHz. For each of the ambient light sources listed in Table 7.1, the SER performance was measured both with and without the optical filter. Plots of SER versus average received irradiance in the presence of natural and artificial ambient light sources are shown in Figs. 7.4 and 7.5, respectively.

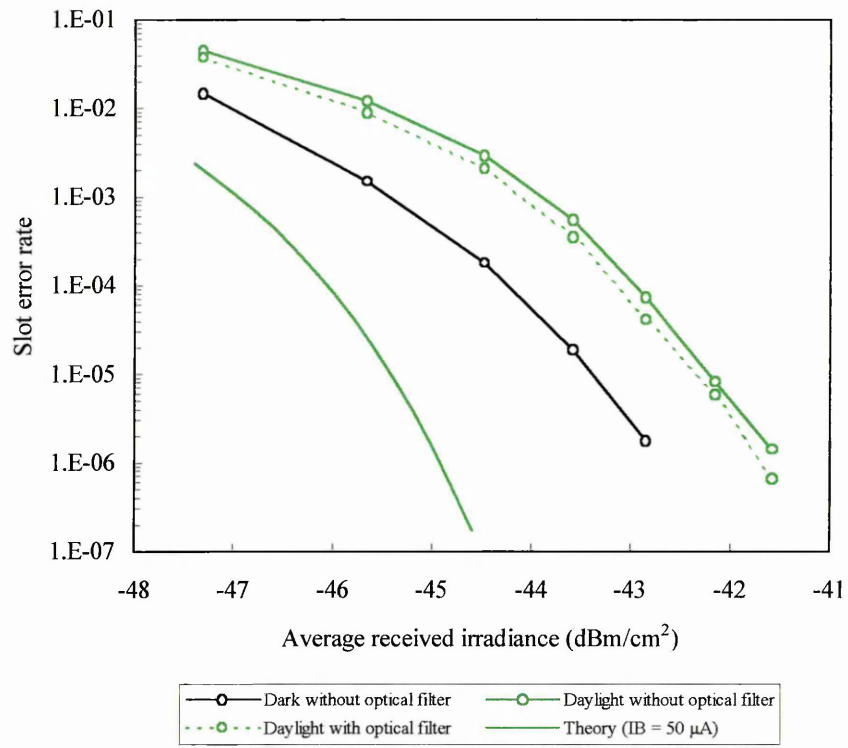


Fig. 7.4: SER versus average received irradiance in the presence of natural light
with $f_c \approx 48$ kHz

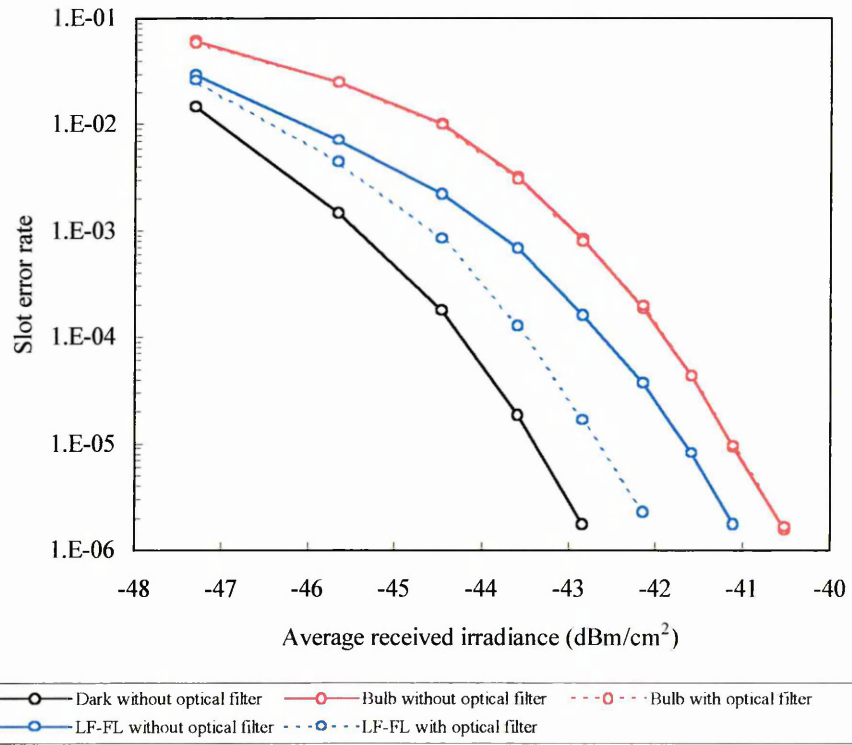


Fig. 7.5: SER versus average received irradiance in the presence of various artificial ambient
light sources with $f_c \approx 48$ kHz

With reference to Fig. 7.4, for the link to achieve an average SER of 10^{-5} when operating in darkness, an average received irradiance of -43.4 dBm/cm^2 is required. When operating in daylight, an average optical power penalty of 1.2 dB is incurred due to the shot noise resulting from the 40 - 50 μA background photocurrent. Whilst the optical filter reduces the background photocurrent by 70% (see Table 7.1), it only results in a modest 0.2 dB reduction in average optical power penalty. Figure 7.4 also shows the theoretical SER for an ideal system, limited only by shot noise resulting from an average background photocurrent of 50 μA . The average optical power requirement of this ideal system is 3.2 dB less than the value obtained for the experimental link when operating in daylight with no optical filter. Some of this difference is due to the bandwidth limitations of the transmitter and receiver, and the use of a suboptimum predetection filter. Additionally, the theoretical performance assumes that all other noise sources are negligible when compared with shot noise, which may not be the case in practice, particularly when considering receiver noise.

In the chosen receiver location, the incandescent bulb generates a background photocurrent which is more than twice that generated in daylight conditions. Consequently, an increased amount of shot noise is generated which, with reference to Fig. 7.5, results in a 2.3 dB average optical power penalty compared with the darkness case. Whilst optical filtering does reduce the background photocurrent by 34% (see Table 7.1), the error performance of the link using the optical filter is almost identical to that achieved without it. It is worth noting that along with attenuating the background photocurrent, the optical filter also attenuates the signal photocurrent slightly. This attenuation has been measured to be $\sim 1.4 \text{ dB}$. Figure 7.6 shows eye diagrams of the signal at the predetection filter output for two ambient light cases, these being darkness and incandescent bulb with no optical filter. For both eye diagrams, all 12 LEDs were switched on, thus producing an average optical transmit power of 48 mW. The closing of the eye due to the shot noise generated by the incandescent bulb is clearly observed from the figure.

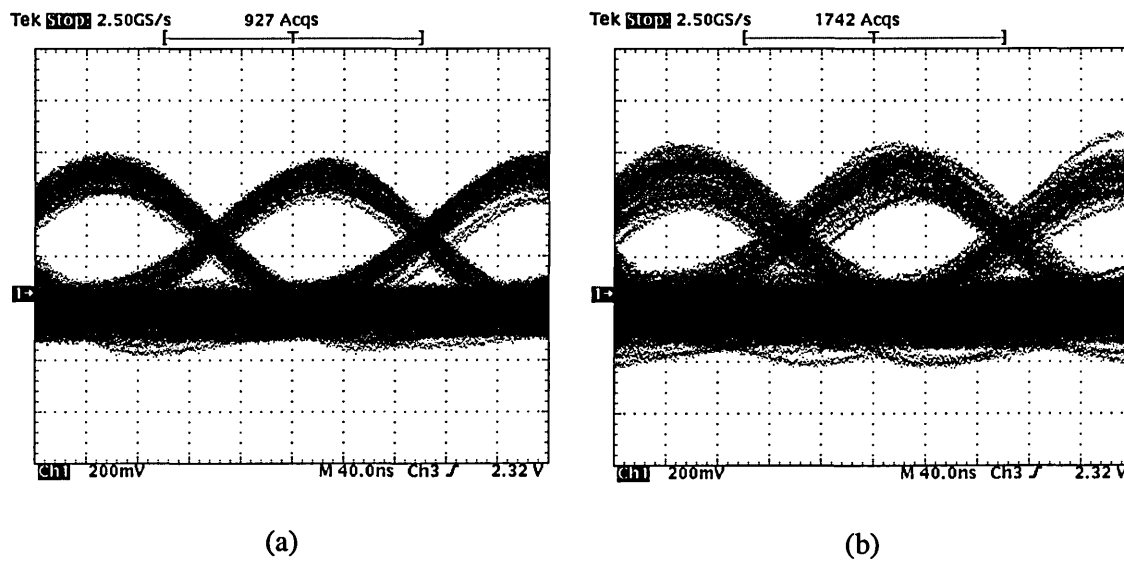


Fig. 7.6: Eye diagram at predetection filter output for two ambient light cases:

(a) darkness, and (b) incandescent bulb without optical filter

With reference to Fig. 7.5, in the absence of optical filtering, the low-frequency fluorescent lamp introduces an average optical power penalty of 1.7 dB compared with the performance in darkness. This is actually higher than the daylight power penalty, even though the background photocurrent generated is less than half that of daylight. This finding implies that not all of the interference signal has been filtered, and consequently, some of the power penalty is down to the actual interference signal, as well as the shot noise generated by the average background photocurrent. Optical filtering was found to reduce the power penalty by 1 dB. In section 2.6.2 of chapter 2, the optical filter was found to reduce the interference signal amplitude by 86 %. Consequently, some of the 1 dB reduction is due to the optical filter attenuating the interference signal, as well as reducing the average background photocurrent. The link was also operated in the presence of ambient light generated by the high-frequency fluorescent lamp. With a HPF cut-on frequency of ~ 48 kHz, even with all 12 LEDs on, it was not possible to achieve a SER below 0.05, with or without the optical filter.

7.4.2 Receiver optimized for high-frequency fluorescent lamp

Fluorescent lamps driven by high-frequency electronic ballasts have a detected electrical spectrum which may contain harmonics extending into the MHz region [15, 16]. Consequently, when operating in the presence of such an ambient light source, it is necessary to increase the HPF cut-on frequency significantly in order to attenuate the interference signal generated by the lamp. If a suitably high cut-on frequency is not employed, then the received signal is superimposed on the periodic interference signal, which has a catastrophic affect on link performance. To illustrate this, using the high-frequency fluorescent lamp as the source of ambient light, Fig. 7.7 shows the transmitted DPIM signal and the corresponding predetection filter output, for a HPF cut-on frequency of ~ 100 kHz (C_1 and C_2 of Fig. B.7 set to 1 nF).

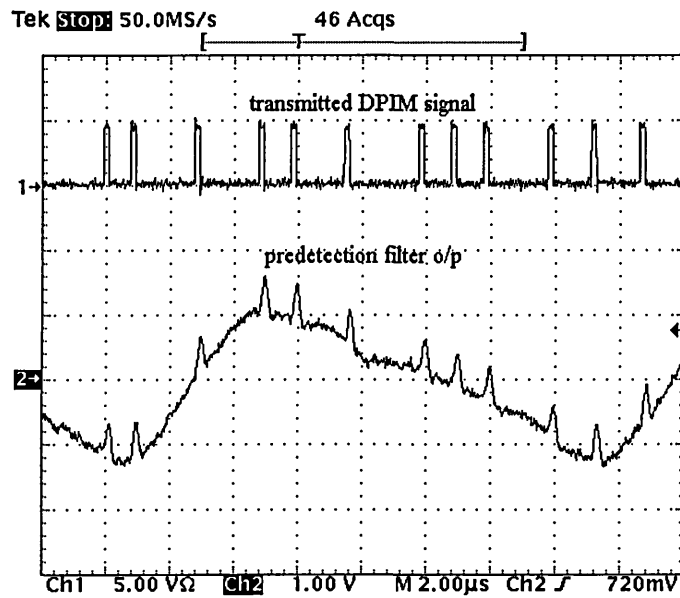


Fig. 7.7: Transmitted and received signal with $f_c = 100$ kHz

As discussed in detail in chapter 5, whilst increasing the HPF cut-on frequency is successful in attenuating the interference signal, it also introduces baseline wander, which has a power penalty associated with it. Therefore, for optimum link performance, it is necessary to determine the optimum cut-on frequency which minimizes the overall power penalty resulting from these two effects.

Using the method described in section 5.5.3, the optimum HPF cut-on frequency was determined using simulation. In the fluorescent light model described in section 5.2, the constants A_1 and A_2 , which relate the interference amplitude to the average background photocurrent, were multiplied by a factor of 3.6. This value makes the ratio of average received irradiance to interference amplitude identical to the actual fluorescent lamp used in practise, without optical filtering. Note that the switching frequency used in the model was left at 37.5 kHz, whilst the actual switching frequency of the lamp was 35 kHz. The results of the simulation are shown in Fig. 7.8. Note that the simulated results are based on a predetection filter with a rectangular impulse response, and assume no bandwidth limitations are imposed by the transmitter or receiver. In Fig. 7.8, the average optical power requirement is normalized to the power required in the absence of electrical high-pass filtering.

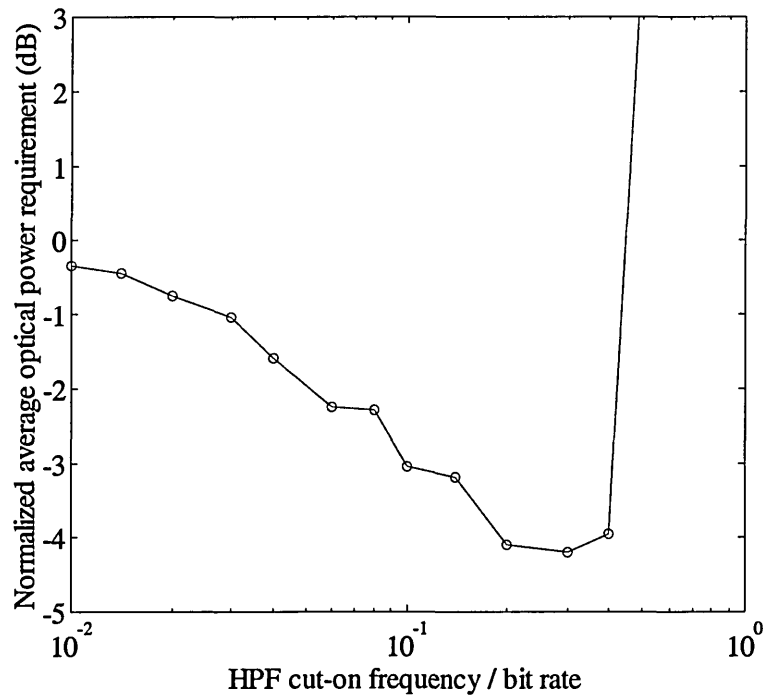


Fig. 7.8: Normalized average optical power requirement versus
normalized HPF cut-on frequency (simulated)

From Fig. 7.8, it is evident that the average optical power requirement is at a minimum when the normalized HPF cut-on frequency is 0.3. For a bit rate of ~ 2.5 Mbit/s, this corresponds to an actual cut-on frequency of ~ 750 kHz.

In order to validate this finding, the optimum HPF cut-on frequency was also determined experimentally. With all 12 LEDs switched on, using the high-frequency fluorescent lamp without optical filtering at the receiver, nine values for C_1 and C_2 were tested between 2.2 nF and 56 pF. For each value the sampling point and threshold level were adjusted to optimize link performance. Results of this are shown in Fig. 7.9.

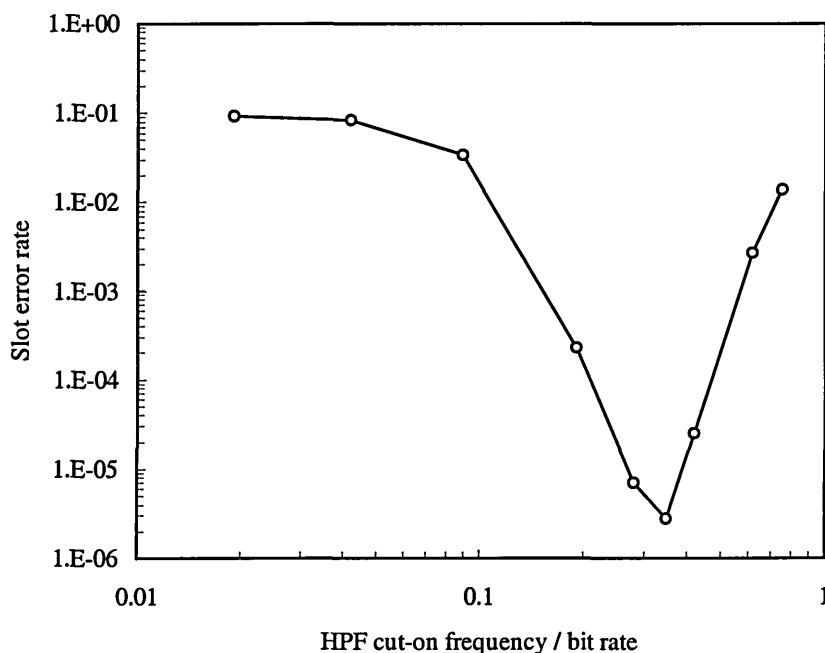


Fig. 7.9: SER versus normalized HPF cut-on frequency (measured)

Of the cut-on frequencies tested, the lowest SER was obtained using a normalized HPF cut-on frequency of 0.35, which corresponds to an actual cut-on frequency of 884 kHz. This was achieved using a capacitance of 120 pF for C_1 and C_2 , and is in good agreement with the optimum cut-on frequency predicted by simulation. Using this optimized cut-on frequency, link performance was again measured in the presence of natural and artificial sources of ambient light, both with and without optical filtering, as shown in Figs. 7.10 and 7.11, respectively.

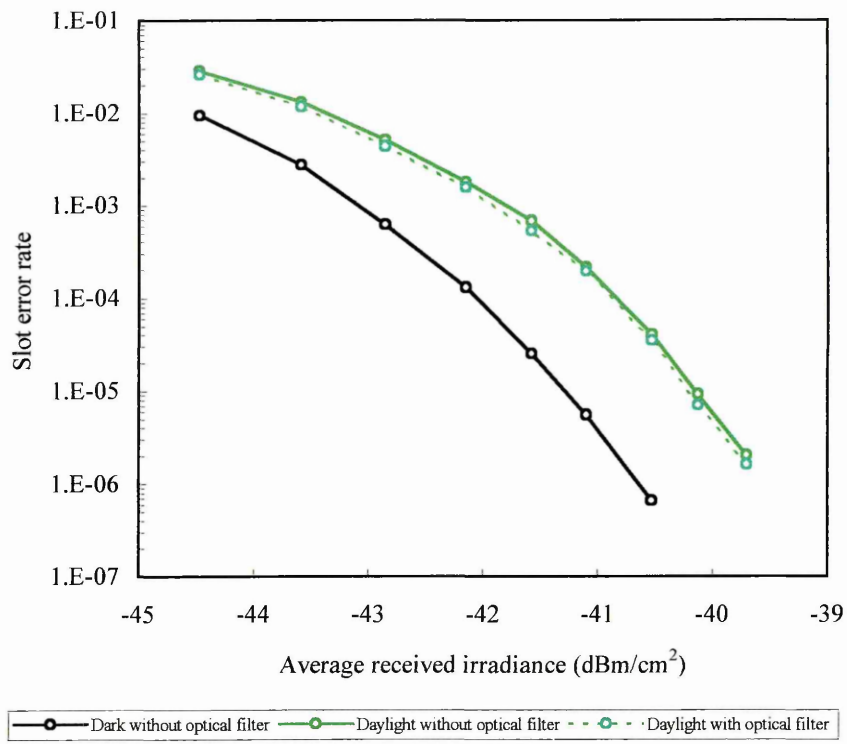


Fig. 7.10: SER versus average received irradiance in the presence of natural light
with $f_c \approx 884$ kHz

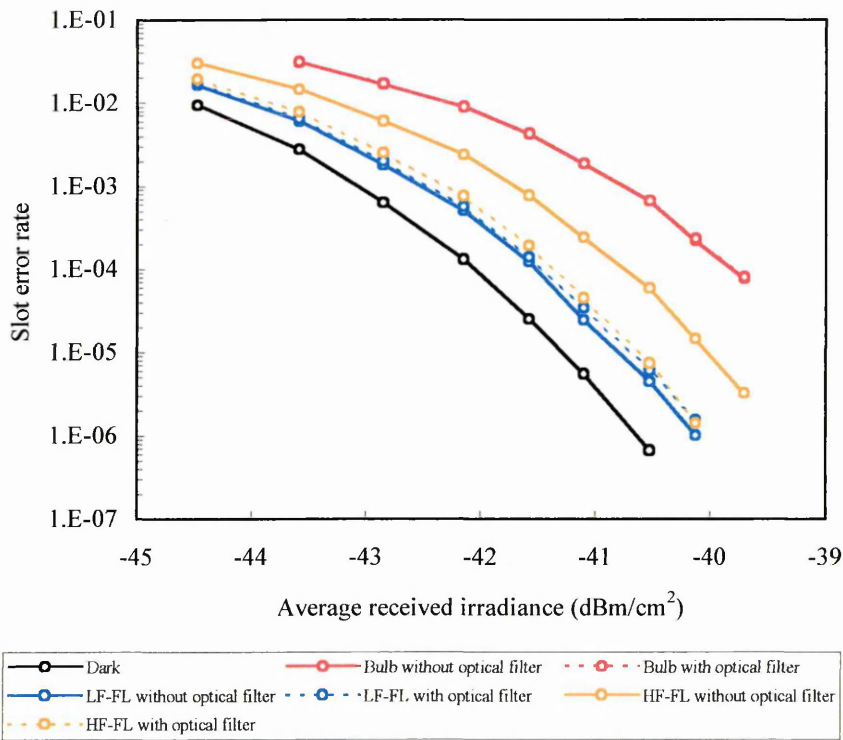


Fig. 7.11: SER versus average received irradiance in the presence of various artificial ambient
light sources with $f_c \approx 884$ kHz

With reference to Fig. 7.10, the link requires an average received irradiance of -41.3 dBm/cm^2 when operating in darkness, which is 2.1 dB more than that required using the previous cut-on frequency of $\sim 48 \text{ kHz}$. This value is significantly less than the $\sim 7.5 \text{ dB}$ optical power penalty predicted by Fig. 5.18. However, note that the theoretical analysis in section 5.4.3 assumes no bandwidth limitations are imposed on the transmitter or receiver, assumes the use of a first-order RC HPF, and uses a rectangular impulse response filter. Daylight operation results in an optical power penalty of 1.2 dB, which is reduced by 0.1 dB when optical filtering is employed. These power penalties are very similar to those obtained for daylight operation in the previous section.

With reference to Fig. 7.11, in the presence of ambient light generated by the incandescent bulb, the link cannot achieve a SER of 10^{-5} with all 12 LEDs switched on. Approximating from Fig. 7.11, the required irradiance is $\sim -39 \text{ dBm}$, corresponding to a 2.3 dB optical power penalty, which is identical to the power penalty obtained with a cut-on frequency of $\sim 48 \text{ kHz}$. Again, the optical filter was found to have virtually no effect on link performance. Figure 7.12 shows eye diagrams of the signal at the predetection filter output for two ambient light cases, these being darkness and incandescent bulb with no optical filter. All 12 LEDs were switched on. Compared with the previous eye diagrams, the effect increasing the HPF cut-on frequency is clear. The peak filter output is reduced, and the eye diagram now contains a significant portion below DC. The closing of the eye as a result of the shot noise generated by the incandescent bulb is again clearly observable from the figure.

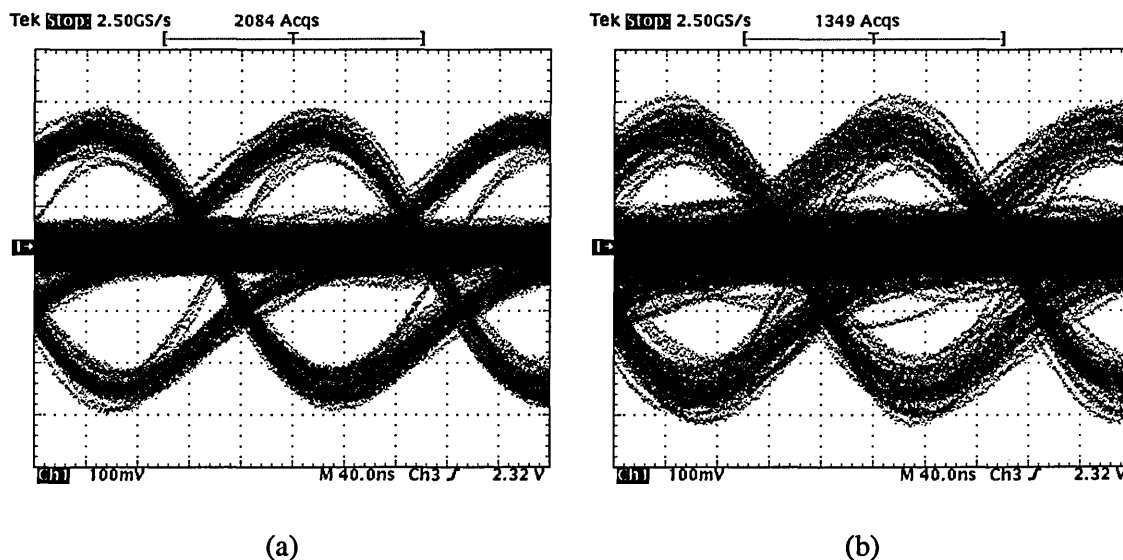


Fig. 7.12: Eye diagram at predetection filter output for two ambient light cases:

(a) darkness, and (b) incandescent bulb without optical filter

With reference to Fig. 7.11, the low-frequency fluorescent lamp was found to introduce an average optical power penalty of 0.5 dB. Interestingly, rather than being improved, the performance of the link is actually degraded by a further 0.1 dB when optical filtering is used. This implies that the effect of reducing the shot noise, due to the reduced background photocurrent, is outweighed by the ~ 1.4 dB reduction in the photocurrent generated by the signal. For the high-frequency fluorescent lamp, in contrast to the previous section where the SER could not be reduced below 0.05 with the optical transmit power available, using a HPF cut-on frequency of 884 kHz results in a modest 1.3 dB average optical power penalty. This power penalty is 0.8 dB higher than that of the low-frequency fluorescent lamp, which gives a similar background photocurrent, thus implying that the HPF cut-on frequency is not sufficient to attenuate all the interference signal, and consequently, some of the power penalty is due to the remaining interference signal, as well as the shot noise. Optical filtering was found to reduce the average optical power penalty by 0.6 dB, resulting in a power penalty which is just 0.1 dB above that of the low-frequency fluorescent lamp, when optical filtering is used.

7.5 Summary

In this chapter, the performance of an experimental 2.5 Mbit/s diffuse infrared link using 16-DPIM(1GS) has been examined under a variety of ambient light conditions. A HPF cut-on frequency of 48 kHz, which corresponds to a normalized delay spread of ~ 0.02 , was found to be sufficient to reject the interference signal from all the artificial ambient light sources with the exception of the high-frequency fluorescent lamp. Using this cut-on frequency, an average received irradiance of -43.4 dBm/cm^2 is required to achieve a SER of 10^{-5} when operating in darkness, and average optical power penalties in the range 1.2 – 2.3 dB are incurred when operating in the presence of daylight, an incandescent bulb or a low-frequency fluorescent lamp. Optical filtering was found to give a 1 dB reduction in the average optical power penalty for the low-frequency fluorescent lamp, but gave just a 0.2 dB reduction when operating in daylight, and no reduction for the incandescent bulb. For the high-frequency fluorescent lamp, which has a switching frequency of 35 kHz, the 48 kHz cut-on frequency is not sufficient to significantly attenuate the interference signal. As a result, the SER could not be reduced below 0.05 with the optical transmit power available.

In order to determine the optimum HPF cut-on frequency when operating in the presence of the high-frequency fluorescent lamp, the optical transmit power was fixed and the SER measured for various cut-on frequencies. Of the nine values measured, a cut-on frequency of 884 kHz was found to give the lowest SER, which corresponds to a normalised cut-on frequency of 0.35. When operating in darkness, using such a high cut-on frequency results in a 2.1 dB increase in the average optical power requirement compared with using a cut-on frequency 48kHz. However, when operating in the presence of the high-frequency fluorescent lamp, this cut-on frequency yields a modest power penalty of 1.3 dB, which is reduced by a further 0.6 dB when optical filtering is used. With a HPF cut-on frequency of 884 kHz, it is ambient light sources which generate the highest background photocurrent that result in the greatest performance degradation. For the particular receiver location used in the measurements, the incandescent bulb gave the largest average optical power penalty of 2.3 dB. However, in a different receiver

location, for example close to a window, daylight may well provide the greatest source of degradation. Consequently, even when optimized electrical high-pass filtering is used, it is imperative to take account of the maximum background irradiance due to ambient light sources when evaluating link power budgets.

Chapter 8

Conclusions

The primary objective of the work presented in this thesis was to evaluate DPIM as a candidate modulation technique for indoor optical wireless communication systems. In order to carry out this task, it is first necessary to fully understand the characteristics of the channel on which the scheme is required to operate, and also be well versed in the fundamentals of indoor optical wireless systems. From the review carried out in chapter 2, it is clear that the indoor infrared channel is unique, combining the Gaussian noise characteristics of conventional wire based channels with the IM/DD constraints of fibre-optic systems. The review also revealed that channel properties are largely dependent on the choice of link configuration, each of which pose different problems in terms of system design. Of these configurations, the diffuse link topology is the most challenging since it must contend with interference from artificial sources of ambient light and multipath propagation.

When evaluating modulation techniques for use in indoor optical wireless communication systems, the important criteria are power efficiency, bandwidth efficiency, complexity, resistance to ambient light interference, and resistance to multipath dispersion. Of the numerous

schemes which have already been proposed for use in indoor infrared links, OOK and PPM are by far the most widely adopted techniques, to date. From the review of modulation techniques presented in chapter 3, it may be concluded that the primary advantages of OOK are its simplicity and bandwidth efficiency. Compared with OOK, PPM yields an improvement in power efficiency at the expense of an increased bandwidth requirement and greater complexity. PPM offers a choice of two detection methods, the more sophisticated of which is virtually immune to the effects of ambient light interference at high data rates. However, on multipath channels, unequalized PPM is found to suffer a larger ISI power penalty than unequalized OOK, due to its increased bandwidth requirement. For both schemes, their performance in the presence of multipath dispersion can be improved using MLSD, suboptimal equalization and/or some form of coding scheme, though this obviously results in increased system complexity.

The proposed scheme, DPIM, is an anisochronous modulation technique in which data is represented by the interval between adjacent pulses. Since each symbol is initiated with a pulse, symbol synchronisation is not required, thereby resulting in a simpler receiver structure compared with PPM. Although variable in length, DPIM symbols contain, on average, fewer slots than PPM symbols for any given L . Consequently, DPIM requires a lower slot rate to achieve the same average data rate as PPM, thereby making it a more bandwidth efficient modulation technique. On the down side, the fact that DPIM symbols contain, on average, fewer slots than PPM symbols also means that DPIM has a lower peak-to-mean power ratio compared with PPM, resulting in an increased average optical power requirement. However, by encoding an additional bit per symbol, it was found that DPIM can achieve a lower average power requirement compared with PPM(TH), whilst still achieving a lower bandwidth requirement. As an example, 32-DPIM(NGB) requires approximately 0.6 dB less average optical power than 16-PPM(TH), and uses 17.5 % less bandwidth.

One of the unusual characteristics of DPIM is the fact that, since it does not have a predetermined symbol structure, errors are not confined to the symbols in which they originate. A single slot error has the potential to affect every remaining bit in the packet, and

consequently, comparing the error performance of DPIM with other schemes in terms of the BER is meaningless. For this reason, the PER was used as the measure of error performance throughout this thesis. Another consequence of the lack of symbol structure in DPIM is the fact that MLSD is unfeasible due to the computational overheads required to implement it. Consequently, hard-decision decoding using a threshold detector is the most likely receiver implementation. The performance of hard-decision decoding is largely dependent on the choice of threshold level. One of the outcomes of the theoretical analysis carried out in chapter 4 is that, in terms of performance on nondistorting AWGN channels, there is very little improvement to be gained by using the optimum threshold level as oppose to the midway value. For an average PER of 10^{-6} , the maximum average optical power penalty incurred when using a midway threshold level as oppose to the optimum value is a mere ~ 0.08 dB, for the DPIM schemes and orders considered.

In the vast majority of cases, indoor infrared links are required to operate in environments containing intense ambient light, emanating from both natural and artificial sources. There are numerous factors which determine the extent to which these sources affect link performance. Examples of these include the number, type and position of the sources relative to the receiver, the type of link configuration used, the receiver FOV, the location of windows, and weather conditions. Due to the existence of such a large number of factors, the analysis presented in chapter 5 was based on a typical indoor environment containing natural daylight and light from a fluorescent lamp driven by a high frequency electronic ballast. This artificial source of ambient light has been identified as potentially the most degrading, since the periodic interference signal generated can contain harmonics which extend into the MHz region. Similar to findings reported for OOK and PPM(TH), in the presence of fluorescent light interference, both DPIM(NGB) and DPIM(1GS) were found to have optical power requirements which are almost independent of the bit rate. Relative to the power requirements without interference, the power penalty is seen to fall as the bit rate increases. Taking 16-DPIM(NGB) as an example, for the scenario considered in chapter 5, the fluorescent light interference resulted in significant

average optical power penalties of 15.1, 10.3 and 6.0 dB, for bit rates of 1, 10 and 100 Mbit/s, respectively.

One of the simplest techniques for mitigating the interference from artificial sources of ambient light is electrical high-pass filtering. However, electrical high-pass filtering introduces a form of intersymbol interference known as baseline wander, which is more severe for baseband schemes which contain a significant amount of power located at DC and low frequencies. From the spectral analysis of DPIM carried out in chapter 4, it was observed that DPIM has a non-zero DC component, unlike PPM. Whilst this DC component is significantly smaller than that of OOK, it does suggest that DPIM is more susceptible to the effects of baseline wander compared with PPM, a prediction which is supported by the analysis carried out in chapter 5. For OOK, baseline wander was found to introduce a 3 dB average optical power penalty when the HPF cut-on frequency is a mere $\sim 1\%$ of the bit rate. In contrast, 16-PPM(TH) and 16-PPM(MAP) do not incur 3 dB power penalties until the normalized cut-on frequency reaches ~ 0.3 . For 16-DPIM(NGB), the normalized 3 dB cut-on frequency was found to be ~ 0.05 , which is almost an order of magnitude lower than that of PPM. Whilst the addition of a guard slot appeared to make little difference to the PSD of DPIM, it does make the scheme more resistant to baseline wander. The reason for this is that in the presence of baseline wander, the probability of error for DPIM(NGB) is dominated by the occurrence of consecutive ones, which are not permitted when a guard band is used. Consequently, the normalized HPF cut-on frequency can be increased to ~ 0.1 before 16-DPIM(1GS) incurs a 3 dB power penalty due to baseline wander.

When using electrical high-pass filtering to mitigate the effects of fluorescent light interference, a trade off exists between the amount of attenuation of the interference signal and the severity of the baseline wander introduced by the HPF. Consequently, an optimum HPF cut-on frequency exists which minimises the overall power penalty due to these two factors. At a data rate of 100 Mbit/s, electrical high-pass filtering was found to be very effective for both DPIM and PPM, virtually eliminating the power penalty due to fluorescent light interference. However, this was not found to be the case at lower data rates. At 1 Mbit/s, the schemes cannot support a

high enough cut-on frequency for electrical high-pass filtering to be very effective. Consequently, virtually no reduction in the average optical power requirement is given for DPIM(NGB), and only modest reductions of 0.5 - 5.5 dB are achieved for DPIM(1GS) when electrical high-pass filtering is used. In comparison, power penalties for PPM(TH) are approximately halved when electrical high-pass filtering is used. At 10 Mbit/s, electrical high-pass filtering yields power penalty reductions for both DPIM schemes which range between 3.2 – 8.8 dB depending on L and the scheme considered. Furthermore, since the addition of a guard slot makes the scheme more resistant to baseline wander, electrical high-pass filtering was found to be slightly more effective for DPIM(1GS) compared with DPIM(NGB). However, for PPM operating at 10 Mbit/s, electrical high-pass filtering was again found to be more effective, reducing power penalties to a mere ~1 dB when threshold detection is used, and virtually eliminating them when MAP detection is employed. Thus, although electrical high-pass filtering was found to be more effective for DPIM compared with OOK, compared with PPM it is less effective at low to medium data rates. Consequently, in environments containing significant high-frequency fluorescent light interference, electrical high-pass filtering, on its own, is not sufficient for DPIM to offer a similar level of performance to PPM at low to medium data rates.

In both diffuse and nondirected LOS link configurations, the transmitted optical signal may undergo multiple reflections from the walls, ceiling, floor and objects within the room, before arriving at the photodetector. This multipath propagation gives rise to ISI, which starts to become significant for bit rates above 10 Mbit/s. Due to its improved bandwidth efficiency, DPIM(NGB) was found to have a lower unequalized ISI power penalty compared with PPM(TH), for any given L and normalized delay spread. As an example, for a normalized delay spread of 0.1, 16-DPIM(NGB) suffers a ~3.2 dB average optical power penalty, whereas 16-PPM(TH) and 16-PPM(MAP) suffer power penalties of ~5.6 dB and ~5.1 dB, respectively. In contrast, the more bandwidth efficient OOK is found to have an unequalized average optical power penalty of just ~1.4 dB for the same normalized delay spread. Consequently, the average optical power requirements of OOK and DPIM(NGB) get closer to those of PPM as the severity of the ISI increases and/or the bit rate increases. As a result, there comes a point where, in the

absence of equalization, DPIM(NGB) offers a lower overall power requirement than PPM(TH) for a given value of L . In contrast, the more sophisticated PPM(MAP) always yields a lower power requirement than DPIM(NGB), for any given L .

Intuitively, postcursor ISI is most severe in the slots immediately following a pulse. By adding a guard band to each DPIM symbol, these slots are effectively ignored. Thus, if the reduction in power due to the presence of the guard band outweighs the increase in power associated with the expanded bandwidth, then an overall reduction in optical power requirement is achieved. The original analysis presented in chapter 6 quantifies the effectiveness of this technique. For a normalized delay spread of 0.1, 16-DPIM(1GS) was found to offer a 1.4 dB reduction in the average optical power requirement compared with 16-DPIM(NGB). Adding a second guard slot was found to give a further reduction in the optical power requirement for high normalized delay spreads. In order to assess the effectiveness of the guard band technique, analysis has also been presented which considers the use of a ZF-DFE, which represents a more conventional approach to combating the effects of ISI. DPIM using a ZF-DFE was found to give an improvement in performance over DPIM(1GS) and DPIM(2GS) for normalized delay spreads above ~ 0.1 . However, the difference in performance does not become significant until high normalized delay spreads are reached, typically beyond 0.2. Consequently, on the majority of channels, the use of a guard band may be sufficient to achieve reliable operation over a useful range of delay spreads, especially considering the reduced cost and complexity in implementing a guard band compared with an adaptive ZF-DFE.

In order to support the theoretical work carried out in this thesis, a prototype 2.5 Mbit/s diffuse infrared link employing 16-DPIM(1GS) was designed and constructed. Initially, the HPF cut-on frequency was set to ~ 48 kHz, which is sufficient to reject the interference resulting from fluorescent lamps driven by conventional ballasts whilst introducing only a negligible amount of baseline wander. When operating in complete darkness, the receiver required an average irradiance of -43.4 dBm/cm² in order to achieve an average SER of 10^{-5} . In daylight conditions, an average optical power penalty of 1.2 dB was incurred due to the shot noise resulting from the

~50 μ A background photocurrent. Similar power penalties of 1.7 dB and 2.3 dB were also incurred when operating in the presence of a low-frequency fluorescent lamp and an incandescent bulb, respectively. When a high-frequency fluorescent lamp was used as the ambient light source, the link was not able to achieve the target SER of 10^{-5} , even when the maximum optical transmit power was used and optical filtering was employed in the receiver. This is due to the fact that a HPF cut-on frequency of ~48 kHz is not sufficient to significantly attenuate the interference signal emitted by this artificial ambient light source.

By keeping the average optical transmit power constant and measuring the SER for various HPF cut-on frequencies, the optimum value when operating in the presence of the high-frequency fluorescent lamp was found to be ~884 kHz, which is in good agreement with the optimum value predicted by simulation. In complete darkness, this cut-on frequency results in an average optical power penalty of 2.1 dB compared with using a cut-on frequency of ~48 kHz. However, by using such a high cut-on frequency, the average optical power penalty due to the high-frequency fluorescent lamp was reduced to a mere 0.7 dB, when optical filtering is used in the receiver. In fact, with a cut-on frequency of ~884 kHz, the incandescent bulb resulted in the greatest optical power penalty, since this source was positioned to simulate a desk lamp and consequently generated by far the highest background photocurrent.

In summary, an investigation has been carried out in order to assess into the suitability of DPIM as a candidate modulation technique for indoor optical wireless communication systems. Having analysed the code properties, considered the performance in the presence of fluorescent light interference and multipath dispersion, and constructed a prototype system, it can be concluded that DPIM is well suited for use in low cost indoor infrared links, where simple threshold detection based receivers are employed.

Chapter 9

Future Work

Whilst the research objectives outlined in section 1.1 have been achieved, there are several areas of work which warrant further investigation.

As discussed in chapter 4, since symbol boundaries are not known prior to detection, the optimal soft-decision decoding of DPIM requires the use of MLSD, which is unfeasible even for relatively short packet lengths. One possible solution to this would be to split packets into a number of shorter length blocks, and encode each block into a DPIM sequence containing a fixed number of slots. This could be achieved, for example, by employing a dual mapping technique as suggested by Shiu and Kahn for DPPM [121], and then appending empty slots to the end of each sequence until the fixed length is reached. Depending on the chosen length, this would greatly reduce the number of possible sequences which need to be considered, and thus make MLSD a more feasible task. However, block lengths would have to be small in order to make this technique practical, and this would inevitably affect the throughput of the scheme.

From the results presented in chapter 5, it is clear that DPIM is more susceptible to baseline wander compared with PPM, a finding which is supported by comparing the PSDs of the two schemes. In order to make DPIM more resistant to baseline wander, some form of line coding could be introduced in order to reduce the low-frequency spectral content of the scheme. This would then permit higher cut-on frequencies to be used, thereby improving the effectiveness of electrical high-pass filtering as a means of mitigating the effect of high-frequency fluorescent light interference. In addition to line coding, the use of error control coding in DPIM is also worthy of consideration.

Whilst the prototype system described in chapter 7 was useful in demonstrating the use of DPIM in an indoor optical wireless link, it only achieved an average bit rate of ~ 2.5 Mbit/s. Furthermore the performance of the practical system did not tie in particularly well with the theoretical performance. This was probably due to the fact that the receiver noise was not negligible in comparison with the shot noise generated by the background radiation. Consequently, the obvious first step for any future work on the practical system would be to improve the sensitivity of the receiver such that it is in better agreement with the theoretical performance. Following this, the bit rate of ~ 2.5 Mbit/s achieved by the prototype link is low by today's standards, and therefore the next step would be to increase this value significantly. By making the bit rate sufficiently high, this would allow error performance measurements to be carried out in the presence of multipath propagation. The effectiveness of adding a guard band could then be evaluated experimentally, and compared with the theoretical predictions.

Appendix A

Derivation of Slot Autocorrelation

Function of DPIM(1GS)

Let a_n be a DPIM(1GS) slot sequence. Assume that, in any given slot n , a_n may take a value of either 0 or 1. Thus,

$$a_n \in \{0, 1\} \text{ for all } n. \quad (\text{A.1})$$

The autocorrelation function of this slot sequence is given by [95]:

$$R_k = \overline{a_n a_{n+k}} = \sum_{i=1}^I (a_n a_{n+k})_i P_i, \quad (\text{A.2})$$

where P_i is the probability of getting the i^{th} $a_n a_{n+k}$ product, and I is the number of possible values for the product.

When $k = 0$, the possible products are $1 \times 1 = 1$ and $0 \times 0 = 0$, and consequently $I = 2$. The probability of getting a product of 1 is $1/L_{avg}$, and the probability of getting a product of 0 is $(L_{avg} - 1)/L_{avg}$. Thus,

$$R_0 = \sum_{i=1}^2 (a_n a_n)_i P_i = 1 \cdot \frac{1}{L_{avg}} + 0 \cdot \frac{(L_{avg} - 1)}{L_{avg}} = L_{avg}^{-1}, \quad (\text{A.3})$$

where, from (4.3), $L_{avg} = (L + 3)/2$.

By including a guard slot in each symbol, it is not possible for pulses to occur in adjacent slots. Thus, when $k = 1$, the probability of getting a product of 1 is 0, and therefore:

$$R_1 = 0. \quad (\text{A.4})$$

When $k = 2$, the probability of getting a product of 1 is simply the probability of a 1 multiplied by the probability that that 1 represents the start of a shortest duration symbol. Thus,

$$R_2 = 1 \cdot L_{avg}^{-1} \cdot L^{-1}. \quad (\text{A.5})$$

Similarly, when $k = 3$, the probability of getting a product of 1 is simply the probability of a 1 multiplied by the probability that that 1 represents the start of a symbol containing a guard slot and one empty slot. Thus,

$$R_3 = 1 \cdot L_{avg}^{-1} \cdot L^{-1}. \quad (\text{A.6})$$

When $k = 4$ and $L = 2$, the only way to obtain a product of 1 is to have a 1 in slot n which represents the start of a shortest duration symbol, which is then followed by another shortest duration symbol, as illustrated in Fig. A.1(a). For $L > 2$, along with the sequence just described for $L = 2$, a product of 1 may also be obtained by having a 1 in slot n which represents the start of a symbol containing a guard slot and two empty slots, as illustrated in Fig. A.1(b).

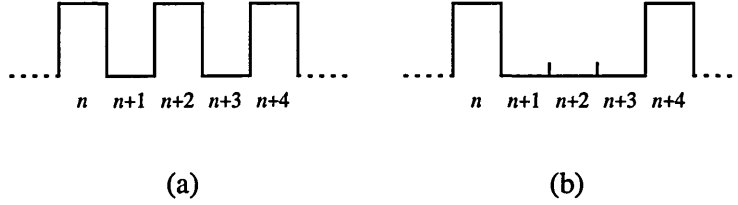


Fig. A.1: Possible DPIM(1GS) slot sequences resulting in a product of 1 when $k = 4$

Thus, for $k = 4$,

$$R_4 = \begin{cases} 1 \cdot L_{avg}^{-1} \cdot L^{-1} \cdot L^{-1} = L_{avg}^{-1} \cdot L^{-2} & \text{for } L = 2 \\ 1 \cdot L_{avg}^{-1} \cdot L^{-1} \cdot L^{-1} + 1 \cdot L_{avg}^{-1} \cdot L^{-1} = L_{avg}^{-1} (L^{-2} + L^{-1}) & \text{for } L > 2 \end{cases}. \quad (\text{A.7})$$

By continuing this process to obtain further values of R_k for various values of L , it may be observed that, in the limit $2 \leq k \leq L+1$,

$$R_k = R_{k-1} + L^{-1} R_{k-2}. \quad (\text{A.8})$$

This is a second order linear recurrence relationship. In order to derive an expression for R_k in terms of L , first assume a basic solution of $R_k = Am^k$, where m is to be determined. Hence,

$$Am^k = Am^{k-1} + L^{-1} Am^{k-2}. \quad (\text{A.9})$$

Assuming $A \neq 0$ and $m \neq 0$, this may be simplified to,

$$m^2 = m + L^{-1}, \quad (\text{A.10})$$

$$m^2 - m - L^{-1} = 0. \quad (\text{A.11})$$

Therefore,

$$m = \frac{1 \pm \sqrt{1 + 4L^{-1}}}{2}. \quad (\text{A.12})$$

The general solution is therefore,

$$R_k = Am_1^k + Bm_2^k, \quad (\text{A.13})$$

where,

$$m_1 = \frac{1 + \sqrt{1 + 4L^{-1}}}{2} \quad \text{and} \quad m_2 = \frac{1 - \sqrt{1 + 4L^{-1}}}{2}. \quad (\text{A.14})$$

Now, $R_0 = L_{avg}^{-1}$ and $R_1 = 0$. Substituting these into (A.13) gives:

$$\begin{aligned} L_{avg}^{-1} &= A + B \\ 0 &= Am_1 + Bm_2 \end{aligned} \quad (\text{A.15})$$

Solving for A and B gives:

$$A = \frac{-L_{avg}^{-1}m_2}{\sqrt{1 + 4L^{-1}}} \quad \text{and} \quad B = \frac{L_{avg}^{-1}m_1}{\sqrt{1 + 4L^{-1}}}. \quad (\text{A.16})$$

Therefore,

$$R_k = \frac{L_{avg}^{-1}}{\sqrt{1+4L^{-1}}} \left(-m_2 m_1^k + m_1 m_2^k \right), \quad (\text{A.17})$$

$$R_k = \frac{L_{avg}^{-1}(-m_1 m_2)}{\sqrt{1+4L^{-1}}} \left(m_1^{k-1} - m_2^{k-1} \right). \quad (\text{A.18})$$

Since $m_1 m_2 = -L^{-1}$, this gives:

$$R_k = \frac{L_{avg}^{-1} L^{-1}}{\sqrt{1+4L^{-1}}} \left(m_1^{k-1} - m_2^{k-1} \right). \quad (\text{A.19})$$

Thus, substituting for m_1 and m_2 , which are defined in (A.14), the full expression for R_k is:

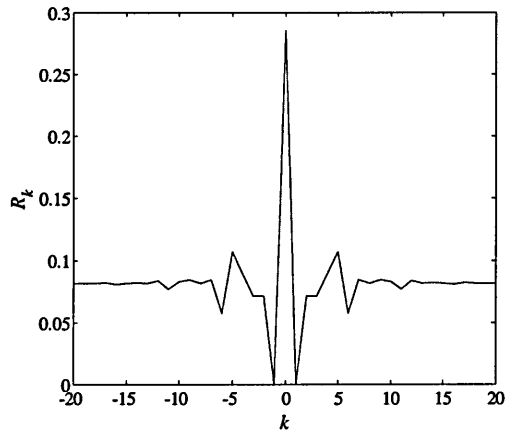
$$R_k = \left(\frac{L_{avg}^{-1} L^{-1}}{\sqrt{1+4L^{-1}}} \right) \left[\left(\frac{1+\sqrt{1+4L^{-1}}}{2} \right)^{k-1} - \left(\frac{1-\sqrt{1+4L^{-1}}}{2} \right)^{k-1} \right] \text{ for } 2 \leq k \leq L+1. \quad (\text{A.20})$$

By calculating further values of R_k for $k > L+1$, for various values of L , it may be observed that

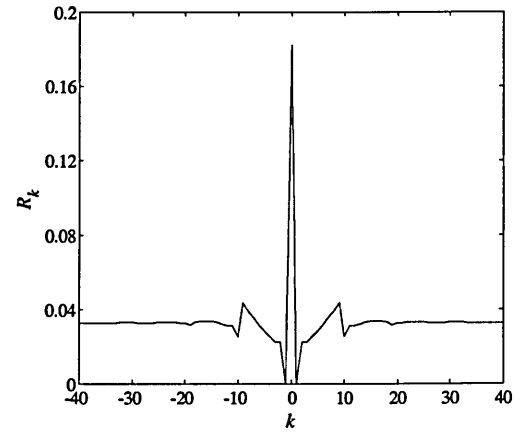
R_k is given by the following summation:

$$R_k = \frac{1}{L} \sum_{i=1}^L R_{k-1-i} \quad \text{for } k > L+1. \quad (\text{A.21})$$

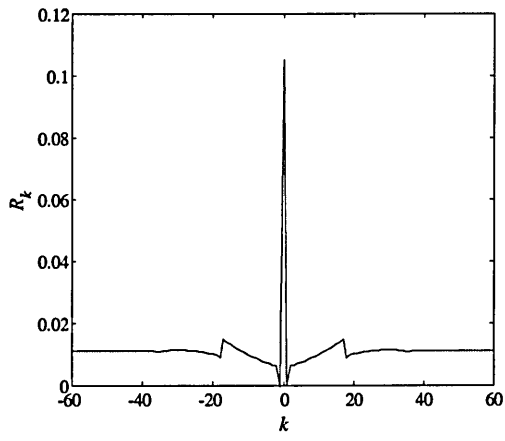
For reference, the ACF of DPIM(1GS) is plotted in Fig. A.2, for various values of L . Note that all four plots were generated using $a_n \in \{0, 1\}$.



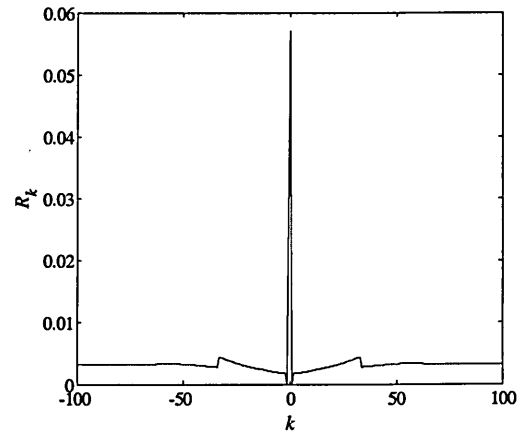
(a)



(b)



(c)



(d)

Fig. A.2: ACF of DPIM(1GS) for: (a) $L = 4$, (b) $L = 8$, (c) $L = 16$, and (d) $L = 32$

Appendix B

Details of Experimental System

In this appendix, each individual module of the transmitter and receiver is described in detail.

B.1 Transmitter

The transmitter is shown in the block diagram of Fig. B.1, and consists of a PC, a field programmable gate array (FPGA) development board and an optical transmitter.

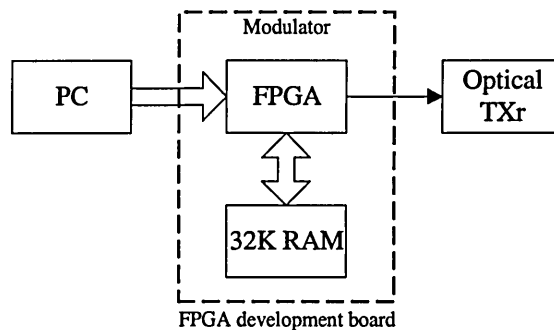


Fig. B.1: Transmitter block diagram

The FPGA development board comprises of a Xilinx XC4005B FPGA and a 32K RAM, and interfaces to the PC through the parallel port. By downloading a bitstream file from the PC, the FPGA is configured to act as the DPIM modulator, and the 32K RAM is used to store the random data which is transmitted. Using an FPGA for this application is convenient in the sense that it allows various system parameters such as slot frequency, number of bits per symbol and size of guard band to be changed simply by reconfiguring the device. The optical transmitter uses the DPIM signal from the modulator to drive the optical source, which in this prototype 74link is an array of infrared light emitting diodes (LEDs).

B.1.1 Modulator

Generating a DPIM signal to pass to the optical transmitter is a two stage process. Firstly, the FPGA is configured as an interface between the parallel port on the PC and the 32K RAM. Random data is generated by the PC, which is then loaded into the memory on the development board. Secondly, with the random data stored, the FPGA is then reconfigured to act as a DPIM modulator, using the data stored in the memory for transmission.

In order to download data to the 32K RAM, the FPGA is configured using a module entitled 'wr_mem', which is loosely based on an example given in [146]. A block diagram of the module is shown in Fig. B.2, and the code which defines the module, written in ABEL hardware description language (HDL), is listed in section B.3.

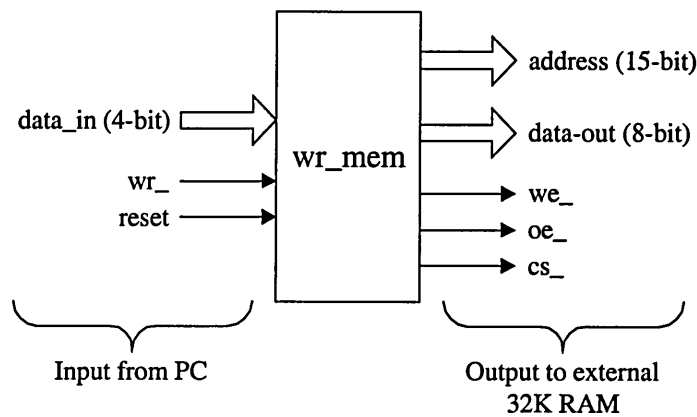


Fig. B.2: Block diagram of 'wr_mem' module

The 32K RAM is organised as 32768 x 8. Each of the 32K bytes is used to store one 4-bit symbol. The module uses a 15-bit write pointer to store the address of the next memory location to be written to, and is initially set to zero using the reset input. A random value between 0 and 15 is generated by the PC and passed to data_in through the parallel port. The value of data_in appears on the first 4-bits of data-out. The upper 4-bits are not used and are arbitrarily set to zero. When the active-low write input (wr_) is taken low, write enable (we_) goes low and the value on data_out is loaded into the addressed memory location. When wr_ returns high, we_ goes high and the write pointer is incremented, ready for the next write operation. Another random value is then output by the PC and so on until the RAM is full. During this writing process, the memory is enabled by tying chip select (cs_) low, and the output drivers are disabled by tying output enable (oe_) high. The C code used to generate the random data and download it to the memory is also listed, for reference, in section B.3.

Once the random data has been stored in the 32K RAM, the FPGA is then reconfigured to act as a DPIM modulator. Note that this process does not require the power supply to be switched off and hence, the data stored in the RAM is not lost. The DPIM modulator was defined using a combination of schematic capture and ABEL HDL. A module entitled 'rd_mem' was defined to interface the modulator with the 32K RAM. A block diagram of this module is shown in Fig. B.3, and the ABEL HDL code for the module is listed in section B.3.

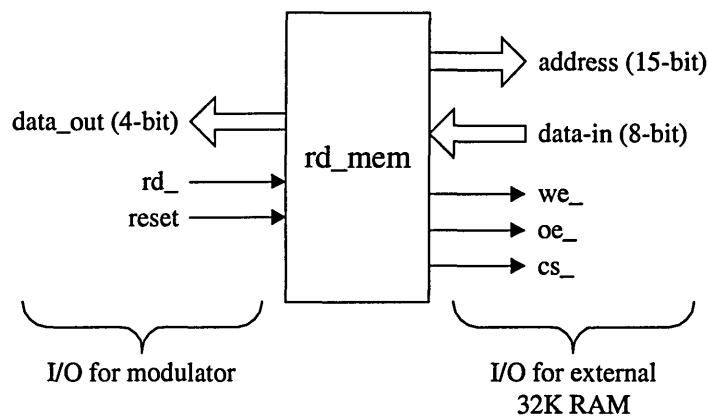
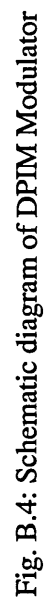
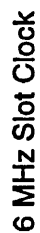


Fig. B.3: Block diagram of 'rd_mem' module

Similar to the `wr_mem` module, a 15-bit read pointer stores the address of the next memory location to be read, and is initially set to zero using the reset input. The read input (`rd_`) is used to read data from the RAM. Taking `rd_` low causes `oe_` to go low, and the contents of the first memory location are output on `data_in`. Since $L = 16$, only the first 4 bits are passed to `data_out`. When `wr_` returns high, `oe_` goes high, and the read pointer is incremented on the rising edge, ready to read the contents of the next memory location, and so on. Again, `cs_` is tied low to enable the memory, and writing is disabled by tying `we_` high.

A schematic diagram of the DPIM modulator is shown in Fig. B.4. The operation of the modulator is described as follows. With the read pointer reset, the first 4 bits of data are loaded into the 4-bit register, and the 4-bit counter is reset. The counter, which is incremented at the slot rate, then begins to count. When the counter reaches the same value as that held in the register, the output of the 4-bit comparator goes high. This output is inverted and used to read the next 4 bits of data from the memory. The output is also connected to a pair of D-type flop flips, which generate a pulse which is delayed by one clock cycle relative to the comparator output, and ensure that the pulse only remains high for one clock cycle. Note that it is this delay which adds a single guard slot to each DPIM symbol. The output of the first flip flop, which represents the DPIM encoded data, is used to load the next 4 bits of data into the register and reset the counter, and the whole process then starts again for the next symbol. When the final memory location has been read, the read pointer then starts again at zero. A divide by two

32K RAM Interface



counter is used to derive the 6 MHz slot clock from the 12 MHz clock present on the FPGA development board.

B.1.2 Optical transmitter

The output of the DPIM modulator is connected to an optical transmitter, the circuit diagram for which is shown in Fig. B.5. The DPIM input drives 4 AND gates, with the other inputs tied to +5V. The output of one of the gates, TX DPIM, is used by the error detector during link performance measurements. The remaining 3 outputs each connect to four more AND gates, again with the other inputs tied to +5V. Each of the 12 outputs are connected to a separate LED driver circuit. The infrared LEDs used (Hewlett Packard HDSL-4220) have a centre wavelength of 875 nm and a viewing angle of 30°. Each LED is driven by a ZTX313 high-speed switching transistor. A 100 pF speedup capacitor is connected in parallel with the base driving resistor to improve transition speed. The 34 Ω resistance in series with each LED was chosen such that, when switched on, the forward current through the LED is ~100 mA, giving a specified radiant optical power of 38 mW. Each of the 12 LED drivers may be enabled or disabled using a separate switch. These switches are used to vary the optical transmit power during error performance measurements.

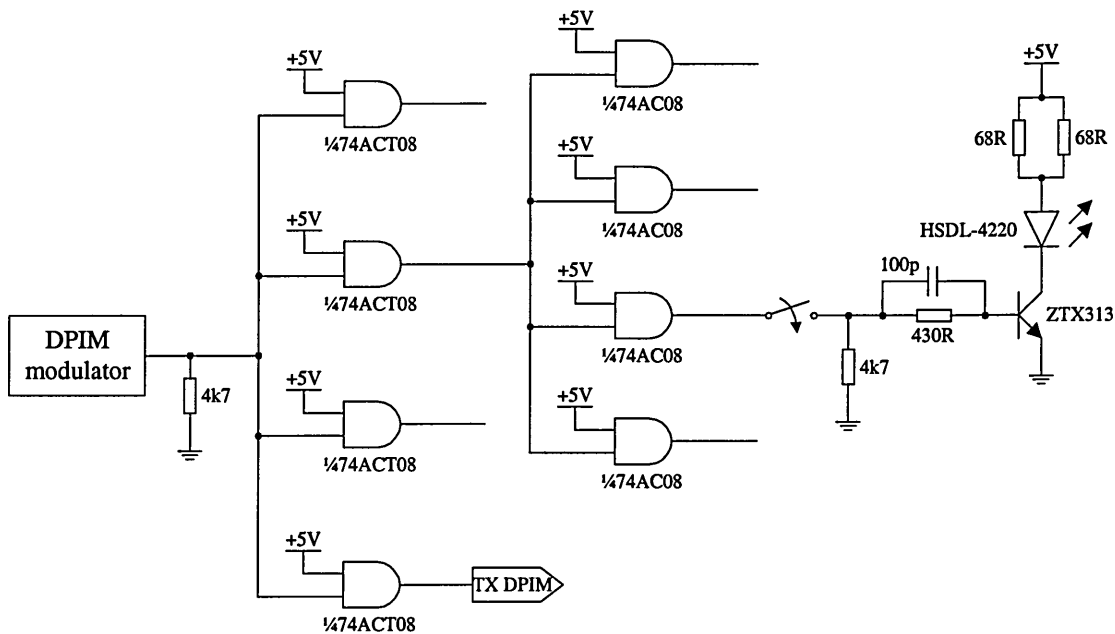


Fig. B.5: Optical transmitter

B.2 Receiver

A block diagram of the receiver is shown in Fig. B.6.

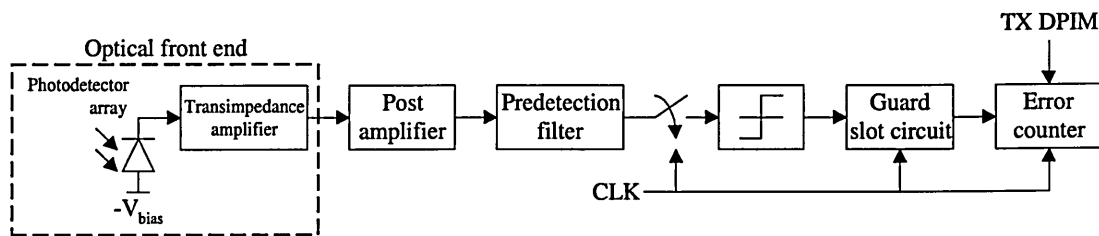


Fig. B.6: Receiver block diagram

B.2.1 Optical front end

The optical front end consists of an array of 5 silicon PIN photodiodes (Infineon BPW34) connected in parallel, and a two-stage transimpedance amplifier, as shown in Fig. B.7. The

photodiodes have a spectral range of 400 - 1100 nm, a half angle of 60°, and an active area of 7 mm², giving a total active area of 35 mm² for the detector array. The photodiodes are operated with a 5V reverse bias, resulting in a total capacitance of ~110 pF for the detector array. The transimpedance amplifier is constructed using a Burr-Brown OPA686 operational amplifier, which is well suited to such an application due to its low noise and high 1.6 GHz gain bandwidth product (GBP) [147]. The output of the transimpedance stage is connected to a second OPA686, which is used in a non-inverting amplifier configuration to provide additional gain.

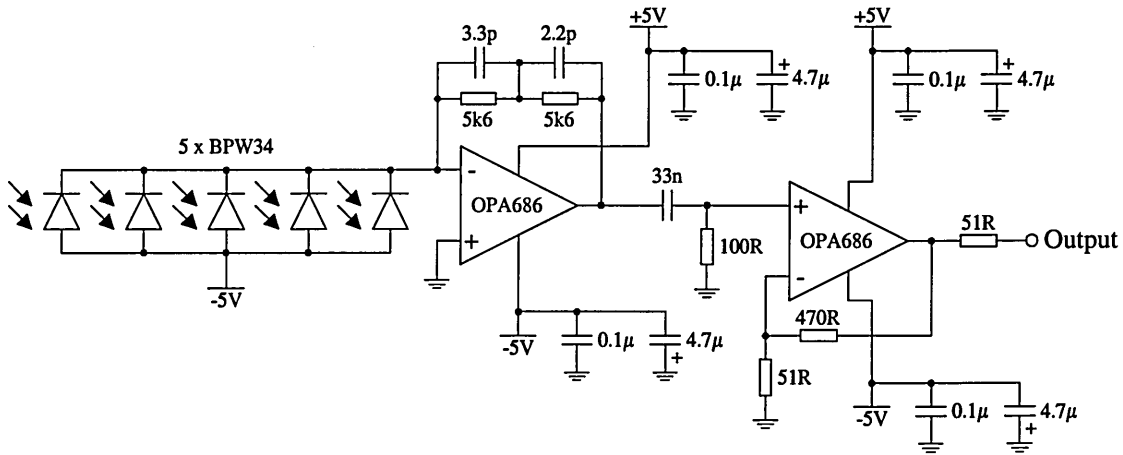


Fig. B.7: Optical front end

The key to broadband transimpedance design is to set the compensation capacitance across the feedback resistor to achieve a flat, or bandlimited, frequency response [148]. The important parameters required to achieve this are the source capacitance, C_S , the desired transimpedance gain, R_F , and the GBP of the operational amplifier. The source capacitance is the sum of the diode capacitance, with the reverse bias voltage applied, and the common-mode and differential-mode input capacitance of the OPA686. From [147], in order to achieve a maximally flat 2nd order Butterworth frequency response, the feedback pole should be set to:

$$f_{pole} = \sqrt{\frac{GBP}{4\pi R_F C_S}}. \quad (B.1)$$

With a source capacitance of 113 pF and a target transimpedance of 11.2 k Ω , a feedback pole set to 10.0 MHz is required. From this, the required feedback capacitance is determined using:

$$C_F = \frac{1}{2\pi R_F f_{pole}}. \quad (\text{B.2})$$

For the values chosen, a total feedback capacitance of 1.42 pF is required. This is achieved using the feedback network shown in Fig. B.6. Typical surface mount resistors have a parasitic capacitance of 0.2 pF [147], which in conjunction with the 3.3 pF and 2.2 pF capacitors, results in a total feedback capacitance of ~1.42 pF. The approximate 3 dB bandwidth of the transimpedance amplifier is given by [147]:

$$f_{-3dB} = \sqrt{\frac{GBP}{2\pi R_F C_S}}. \quad (\text{B.3})$$

For the values chosen, the theoretical bandwidth is approximately 14 MHz, which is sufficient to accommodate a slot frequency of 6 MHz.

The gain of the non-inverting amplifier stage is set to ~20 dB, resulting in a total transimpedance of ~114 k Ω for the front-end. The AC coupling between the two stages is tuned to achieve a cut-on frequency of ~50 kHz. As discussed later, this choice of cut-on frequency is sufficient to reject interference resulting from fluorescent lamps driven by low-frequency ballasts, whilst introducing only a negligible amount of baseline wander.

The optical front end also contains a second detector array, again consisting of 5 BPW34 detectors connected in parallel, which is situated physically close to the first array. With the same 5 V reverse bias applied, this second array is connected to a picoammeter, and is used to measure the received photocurrent, due to both the transmitted signal and the ambient light

sources. The measured photocurrent may be converted into an average received irradiance using (7.1).

B.2.2 Post amplifier

To further amplify the signal emerging from the front end, a post amplifier is used, which comprises of two low noise operational amplifiers (MAX477), as shown in Fig. B.8. Each non-inverting stage has a gain of ~ 20 dB, and in conjunction with the front end, results in a total transimpedance for the receiver of ~ 12 M Ω .

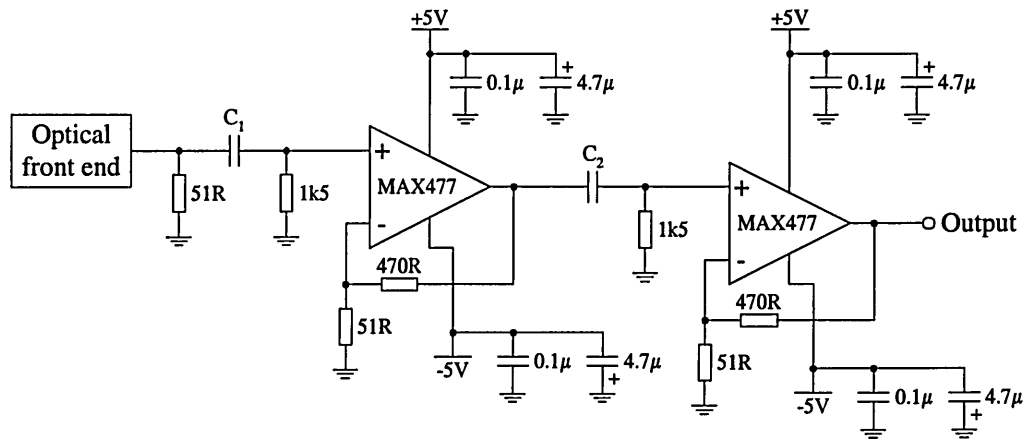


Fig. B.8: Post amplifier

The AC coupling between the optical front end and the first stage of the post amplifier may be tuned by adjusting C_1 . Similarly, the coupling between the first and second stages of the post amplifier may be tuned by adjusting C_2 . For a target cut-on frequency of 50 kHz, as used in the optical front end, a capacitance of 2.2 nF is used for C_1 and C_2 . However, for operating in the presence of interference produced by electronic ballast driven fluorescent lamps, a significantly higher cut-on frequency is required. Determining the optimum value of this cut-on frequency is one of the topics discussed in section 7.4.

B.2.3 Predetection filter

The fundamental purpose of the predetection filter is to increase the likelihood of successfully detecting pulses in the presence of noise. Maintaining fidelity of pulse shape is not a priority [96]. The optimum predetection filter is the matched filter, which maximises the output signal to noise ratio at the sampling instant. Matched filters may be implemented using either analogue or digital circuit techniques [149]. For a given application the best choice is dependent on a number of factors such as implementation complexity, programmability requirement, operating speed and precision. One example of an analogue implementation is the reset integrator, which is a common choice if the received signal consists of rectangular pulses [150].

An alternative, though suboptimum, approach to predetection filtering is to use a traditional analogue low-pass filter. By carefully selecting the bandwidth and shape of the filter characteristic to optimize the peak SNR, the performance of a matched filter can be closely approximated [96]. Due to their superior transient characteristics, i.e. no ringing in the impulse and step responses, Bessel filters are a common choice for suboptimum predetection filters. For the experimental link, a 4th order Bessel filter was chosen, which has a normalized transfer function given by [151, 152]:

$$H(s) = \frac{105}{s^4 + 10s^3 + 45s^2 + 105s + 105} \quad (\text{B.4})$$

In order to determine the optimum cut-off frequency, which maximises the peak output signal to noise ratio, first consider the general case for any linear filter. If a signal with Fourier transform $S(\omega)$ is corrupted by AWGN with zero mean and double-sided PSD $N_0/2$, after passing through a filter with transfer function of $H(\omega)$, the SNR at sampling time t_0 is given by [153]:

$$SNR_{out} = \frac{\left| \int_{-\infty}^{\infty} S(\omega) H(\omega) e^{j\omega t_0} d\omega \right|^2}{\frac{N_0}{2} \int_{-\infty}^{\infty} |H(\omega)|^2 d\omega}. \quad (B.5)$$

The numerator represents the instantaneous signal power at the output of the filter at time t_0 , and the denominator represents the average noise power at the filter output. The optimum $H(\omega)$, which maximises SNR_{out} , is the matched filter, which can be found from (B.6) by applying Schwarz's inequality [153]. It can be shown that when a matched filter is used, the maximum SNR at the output of the filter is given by [153]:

$$SNR_{max} = \frac{2E}{N_0}, \quad (B.6)$$

where E is the energy of the input signal, given by:

$$E = \int_{-\infty}^{\infty} |S(\omega)|^2 d\omega. \quad (B.7)$$

For the 4th order Bessel filter, $H(\omega)$ is found from (B.5) using the substitution:

$$H(\omega) = H(s) \Big|_{s=j\omega}. \quad (B.8)$$

The transfer function given in (B.5) is normalized to have unit delay at $\omega = 0$, rather than a 3 dB attenuation at $\omega = 1$, which is standard for other analogue filter designs. Consequently, in order to generate a transfer function with a 3 dB cut-off frequency of $f_{c,off}$, s must be scaled by a factor of $2.111/2\pi f_{c,off}$. The value 2.111 is the angular frequency at which the normalized 4th order Bessel filter has an attenuation of 3 dB. Considering two different pulse shapes, these being

rectangular and raised cosine with 100% excess bandwidth, (B.6) was used to calculate the peak output SNR for a 4th order Bessel filter with a range of cut-off frequencies, as shown in Fig. B.9. On the horizontal axis, $f_{c,off}$ is normalized to $1/T$, where T is the pulse duration. On the vertical axis, SNR_{out} is plotted relative to SNR_{max} , given in (B.7), which is assumed to be 0 dB.

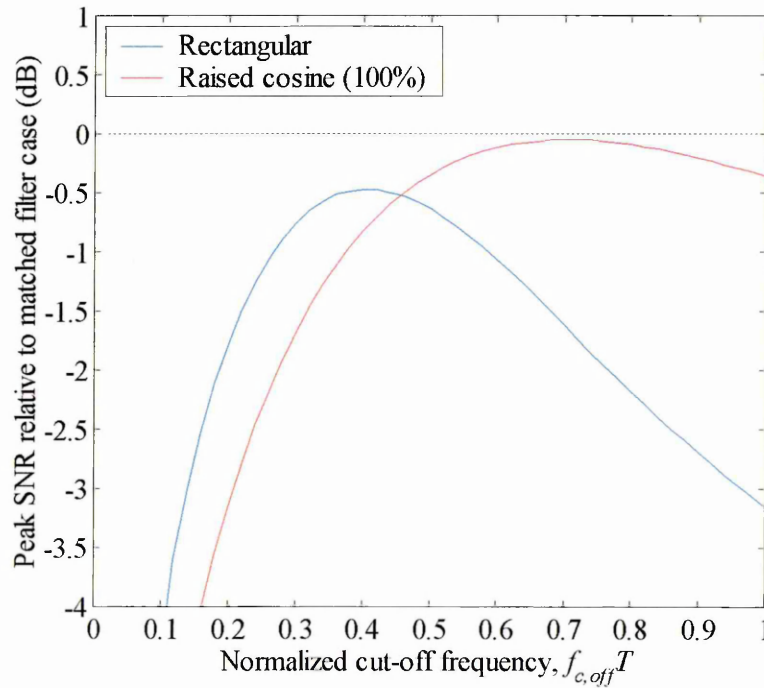


Fig. B.9: Peak SNR of 4th order Bessel low-pass filter (relative to matched filter case) versus normalized cut-off frequency for two different pulse shapes

When the received signal consists of rectangular shaped pulses, the optimum cut-off frequency for the 4th order Bessel filter is $0.4/T$, which results in an output SNR which is ~ 0.47 dB less than that obtained using a matched filter. In the case of raised cosine pulses, the optimum cut-off frequency is $0.7/T$, and results in a SNR which is just ~ 0.05 dB below the matched filter case. The smaller SNR penalty is due to the fact that the impulse response of the Bessel filter is a much closer match to the shape of a raised cosine pulse than it is to a rectangular pulse. Note that this analysis represents an isolated pulse case, and does not take into consideration the ISI which the filter may introduce. Consequently, the cut-off frequency which maximizes the SNR for a single pulse is not necessarily the optimum value in terms of minimizing the average

probability of error. Nevertheless, the above analysis is still a worthwhile exercise to determine approximate values for the optimum cut-off frequency.

For the experimental link, the received pulse shape is somewhere between rectangular and 100 % raised cosine, and consequently, a cut-off frequency of $0.6/T$ was chosen. For a slot frequency of 6 MHz, i.e. a pulse duration of 167 ns, this corresponds to a cut-off frequency of 3.6 MHz. The circuit diagram for a passive 4th order Bessel low-pass filter is shown in Fig. B.10 [154]:

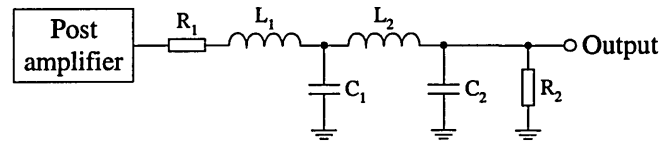


Fig. B.10: 4th order Bessel low-pass filter

From [154], the normalized component values for this filter are given in Table B.1.

R_1	L_1	C_1	L_2	C_2	R_2
1.0000	0.2334	0.6725	1.0815	2.2404	1.0000

Table B.1: Normalized component values for 4th order Bessel low-pass filter

Note that in this case, the term normalized means having an attenuation of 3 dB at $\omega = 1$. In order to achieve a specified cut-off frequency of 3.6 MHz, the reactive elements are divided by a frequency scaling factor (FSF), which is given by:

$$FSF = \frac{\text{desired cut - off frequency (rad/s)}}{1 \text{ (rad/s)}} = \frac{2\pi 3.6 \times 10^6}{1} = 22.62 \times 10^6. \quad (\text{B.9})$$

To obtain practical component values, an impedance scaling factor may then be used. Any linear network maintains its transfer function if all resistor and inductor values are multiplied by

the impedance scaling factor, and all capacitor values are divided by the same factor [154].

Using an impedance scaling factor of 1000, the calculated component values, along with their nearest preferred values (NPV), are given in Table B.2.

	R_1	L_1	C_1	L_2	C_2	R_2
Calculated	1 k Ω	10.32 μ H	29.73 pF	47.81 μ H	99.05 pF	1 k Ω
NPV	1 k Ω	10 μ H	33 pF	47 μ H	100 pF	1 k Ω

Table B.2: Calculated and nearest preferred component values for $f_{c,off} = 3.6$ MHz

B.2.4 Threshold detector

The threshold detector compares the output of the predetection filter with a threshold voltage, and assigns a logic one or zero to each slot depending on whether the amplitude is above or below the threshold voltage at the sampling instant. The circuit is based around a MAX903 high-speed voltage comparator, as shown in Fig. B.11, with separate analogue and digital power supplies. The threshold voltage is connected to the inverting input, and can be manually adjusted between 0 and 480 mV using the 1 k Ω trimmer.

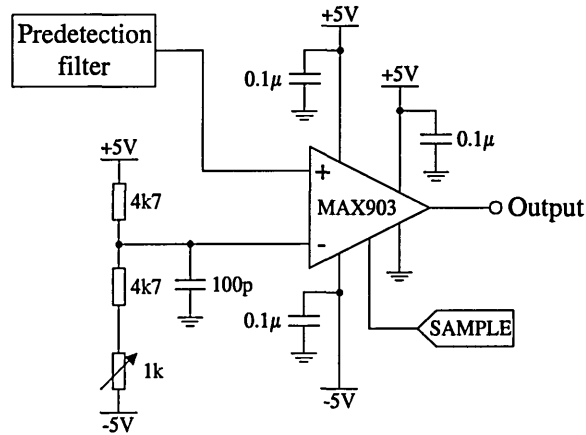


Fig. B.11: Threshold detector

The instant at which the two levels are compared is controlled by a sampling pulse applied to the latch input. The pulse must remain high for a minimum of 10 ns in order to perform the comparison. On the falling edge of the pulse, the comparator output is latched until the next sampling pulse. The sampling pulse is derived from the transmitter clock, using the circuit shown in Fig. B.14. In order to ensure that sampling takes place at the correct instant, the transmitter clock is passed through a tapped delay line having 10 taps with a tap-to-tap delay of 10 ns. Depending on the high-pass filter cut-on frequency of the post amplifier, the appropriate tap is chosen such that the sampling point coincides with the maximum amplitude of the pulses emerging from the predetection filter, i.e. where the eye diagram is at its most open. Sampling pulses with a duration of ~12 ns are generated on the rising edge of the clock using 3 low speed inverters (74LS04) and an AND gate, as shown in Fig. B.14. The operation of the threshold detector is shown in Fig. B.12.

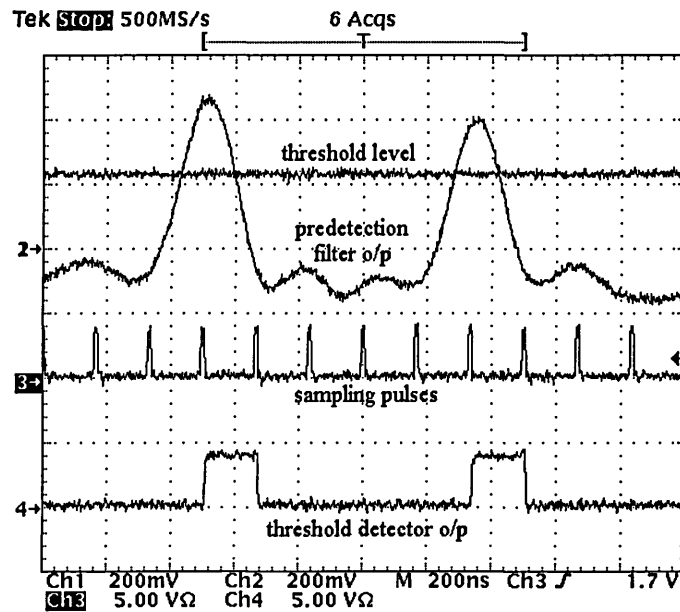


Fig. B.12: Threshold detector operation

B.2.5 Guard slot circuit

In the prototype link, a guard band consisting of one slot is employed. When the output of the threshold detector goes high to indicate the detection of a pulse, the purpose of the guard slot circuit is to automatically assign a zero to the following slot, regardless of the threshold detector output. The circuit used to achieve this function uses two D-type flip flops with asynchronous clear, as shown in Fig. B.13.

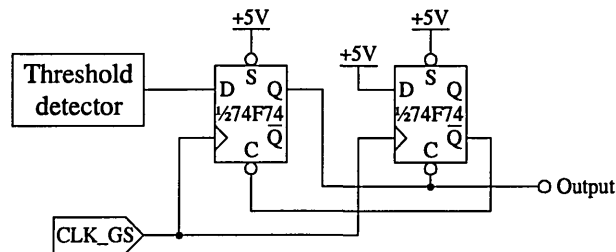


Fig. B.13: Guard slot circuit

The operation of the circuit is as follows. Upon reception of a pulse, the output goes high on the rising edge of the clock. After one clock cycle, \overline{Q} of the second flip flop goes low which then clears both flip flops. The clock signal (CLK_GS) is derived from the transmitter clock using the circuit shown in Fig. B.14.

B.2.6 Error counter

The error counter compares the transmitted DPIM signal with the regenerated signal on a slot-by-slot basis, and counts the number of slots where the two signals differ. In order to avoid a significant amount of noise being introduced into the receiver circuit when the transmitted DPIM signal (TX DPIM) and the clock (CLK) from the transmitter are connected, it is necessary to separate the transmitter and receiver grounds using an optoisolator, as shown in Fig. B.14.

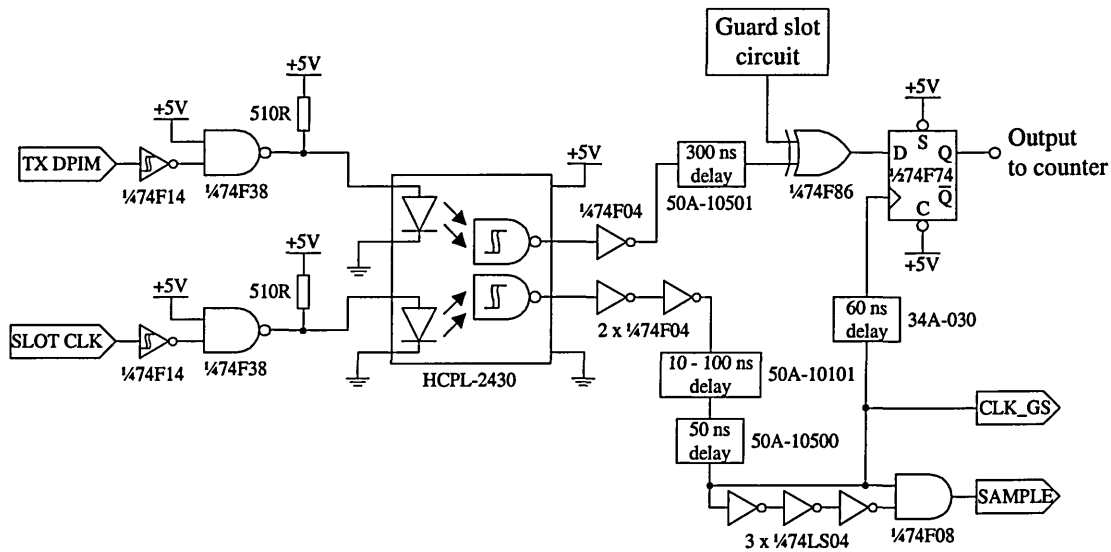


Fig. B.14: Error counter

Figure B.14 also shows how the sampling pulses (SAMPLE) used in the threshold detector are generated, along with the clock signal used by the guard slot circuit (CLK_GS). In order to compensate for the delay associated with the receiver circuitry, it is necessary to delay the transmitted signal by 300 ns. The transmitted and regenerated DPIM signals are compared using an XOR gate. A D-type flop-flop is then used to latch the output of the XOR gate, which is clocked in the centre of each slot period. The operation of this is shown in Fig. B.15.

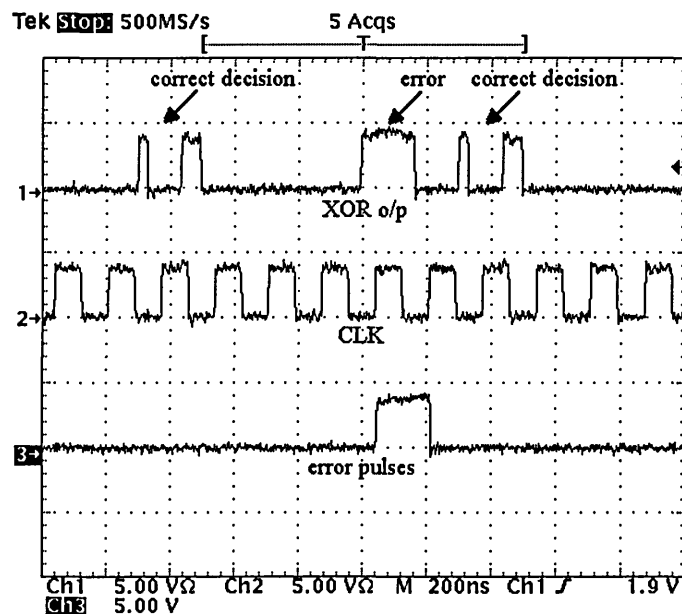


Fig. B.15: Error counter operation

B.3 ABEL HDL and C Source Code

B.3.1 ABEL HDL for 'wr_mem' module

```
MODULE wr_mem

TITLE 'WRITE DATA TO 32K RAM'

DECLARATIONS

"----- inputs to user interface -----

reset                PIN;  "reset counter
wr_                  PIN;  "active-low write to memory
data_in3..data_in0   PIN;  "4-bit data input bus

"----- outputs to external 32K RAM -----

cs_                  PIN ISTYPE 'COM';  "active-low chip select
oe_                  PIN ISTYPE 'COM';  "active-low output enable
we_                  PIN ISTYPE 'COM';  "active-low write enable
address14..address0  PIN ISTYPE 'COM';  "15-bit RAM address bus
data_out7..data_out0 PIN ISTYPE 'COM';  "8-bit data output bus

"----- internal nodes -----

wrptr14..wrptr0      NODE ISTYPE 'REG';  "15-bit write pointer

"----- shorthand for signal vectors -----

data_in = [data_in3..data_in0];
address = [address14..address0];
wrptr = [wrptr14..wrptr0];

EQUATIONS

"----- write pointer logic -----

wrptr := wrptr+1;      "increment pointer when a transition occurs
wrptr.CLK = wr_;       "pointer clocked by rising edge of wr_
wrptr.ACLR = reset;    "pointer cleared by reset

"----- interface to external RAM -----

cs_ = 0;  "set chip select low to enable external RAM
oe_ = 1;  "set output enable high to disable output from RAM
we_ = wr_;

address = wrptr;

[data_out3..data_out0] = data_in;
[data_out7..data_out4] = 0;  "set upper 4 data bits to 0

END wr_mem
```

B.3.2 C source code used to fill RAM with random data

```
#include <stdio.h>
#include <dos.h>
#include <time.h>
#include <stdlib.h>

void main ()
{

int value, val_out, hold;
long int loop;
randomize();
hold=1;

/* write pointer reset to zero */

outportb(0x378,1);
delay(hold);
outportb(0x378,0);
delay(hold);
outportb(0x378,1);

for (loop=0;loop<32768;loop++)
{
    value=rand() % 16; /* generate random integers in range 0 - 15 */
    val_out=4*value; /* multiply by 4 since output is on bits 2 - 5 */
    outportb(0x378,val_out+1);
    delay(hold);
    outportb(0x378,val_out+3);
    delay(hold);
    outportb(0x378,val_out+1);
}
}
```

B.3.3 ABEL HDL for 'rd_mem' module

```
MODULE rd_mem

TITLE 'READ DATA FROM 32K RAM'

DECLARATIONS

"----- i/o pins to modulator -----

reset                PIN; "reset counter
rd_                  PIN; "active-low read from memory
data_out3..data_out0 PIN; "4-bit data output bus

"----- i/o pins to external 32K RAM -----

cs_                  PIN ISTYPE 'COM'; "active-low chip select
oe_                  PIN ISTYPE 'COM'; "active-low output enable
we_                  PIN ISTYPE 'COM'; "active-low write enable
address14..address0  PIN ISTYPE 'COM'; "15-bit RAM address bus
data_in7..data_in0   PIN ISTYPE 'COM'; "8-bit data input bus

"----- internal nodes -----

rdptr14..rdptr0      NODE ISTYPE 'REG'; "15-bit read pointer

"----- shorthand for signal vectors -----

data_out = [data_out3..data_out0];
address = [address14..address0];
rdptr = [rdptr14..rdptr0];

EQUATIONS

"----- read pointer logic -----

rdptr := rdptr+1;    "increment pointer when clocked by rd_
rdptr.CLK = rd_;     "pointer clocked by rising edge of rd_
rdptr.ACLR = reset;  "pointer cleared by reset

"----- interface to external 32K RAM -----

cs_ = 0;    "set chip select low to enable external RAM
we_ = 1;    "set write enable high to disable writing to RAM
oe_ = rd_;  "the first 4 bits of the addressed memory location
            "appear on data output bus when when oe_=0

address = rdptr;

data_out = [data_in3..data_in0];

END rd_mem
```

References

- [1] F. Halsall, *Data Communications, Computer Networks and Open Systems*, Fourth Edition. Addison-Wesley, 1996.
- [2] IEEE Standard 802.11-1997, Institute of Electrical and Electronics Engineers, 18 November 1997.
- [3] IEEE Standard 802.11b-1999, Institute of Electrical and Electronics Engineers, 20 January 2000.
- [4] L. Chinitz, "HomeRF technical overview," HomeRF Technical Committee, 9 May 2001, http://www.homerf.org/data/events/past/pubseminar_0501/tech_overview.pdf.
- [5] IEEE Standard 802.11a-1999, Institute of Electrical and Electronics Engineers.
- [6] M. Johnsson, "HiperLAN/2 - the broadband radio transmission technology operating in the 5 GHz frequency band," HiperLAN/2 Global Forum, 1999.
- [7] Bluetooth Specification, Version 1.1, 22 February 2001.
- [8] F. R. Gfeller, H. R. Muller and P. Vettiger, "Infrared communication for in-house applications," in *Proceedings of IEEE Conference on Computer Communication*, Washington DC, U.S.A., 5-8 September 1978, pp. 132-138.
- [9] F. R. Gfeller and U. H. Bapst, "Wireless in-house data communication via diffuse infrared radiation," *Proceedings of the IEEE*, vol. 67, no. 11, pp. 1474-1486, November 1979.
- [10] J. R. Barry, *Wireless Infrared Communications*. Kluwer Academic, 1994.
- [11] Serial Infrared Physical Layer Specification, Version 1.4, Infrared Data Association, 30th May 2001.
- [12] J. M. Kahn and J. R. Barry, "Wireless infrared communications," *Proceedings of the IEEE*, vol. 85, no. 2, pp. 265-298, February 1997.
- [13] J. Bellon, M. J. N. Sibley, D. R. Wisely and S. D. Greaves, "Hub architecture for infrared wireless networks in office environments," *IEE Proceedings - Optoelectronics*, vol. 146, no. 2, pp. 78-82, April 1999.
- [14] V. Jungnickel, T. Haustein, A. Forck and C. von Helmolt, "155Mbit/s wireless transmission with imaging infrared receiver," *Electronics Letters*, vol. 37, no. 5, pp. 314-315, March 2001.
- [15] A. J. C. Moreira, R. T. Valadas and A. M. de Oliveira Duarte, "Performance of infrared transmission systems under ambient light interference," *IEE Proceedings - Optoelectronics*, vol. 143, no. 6, pp. 339-346, December 1996.
- [16] R. Narasimhan, M. D. Audeh and J. M. Kahn, "Effect of electronic-ballast fluorescent lighting on wireless infrared links," *IEE Proceedings - Optoelectronics*, vol. 143, no. 6, pp. 347-354, December 1996.

- [17] A. J. C. Moreira, A. M. R. Tavares, R. T. Valadas and A. M. de Oliveira Duarte, "Modulation methods for wireless infrared transmission systems: performance under ambient light noise and interference," in *Proceedings of SPIE Conference on Wireless Data Transmission*, Philadelphia, U.S.A., 23-25 October 1995, vol. 2601, pp. 226-237.
- [18] E. A. Lee and D. G. Messerschmitt, *Digital Communication*, Second Edition. Kluwer Academic, 1994.
- [19] A. M. Street, P. N. Stavrinou, D. C. O'Brien and D. J. Edwards, "Indoor optical wireless systems – a review," *Optical and Quantum Electronics*, vol. 29, pp. 349-378, 1997.
- [20] P. P. Smyth, P. L. Eardley, K. T. Dalton, D. R. Wisely, P. McKee and D. Wood, "Optical wireless: a prognosis," in *Proceedings of SPIE Conference on Wireless Data Transmission*, Philadelphia, U.S.A., 23-25 October 1995, vol. 2601, pp. 212-225.
- [21] C. S. Yen and R. D. Crawford, "The use of directed optical beams in wireless computer communications," in *Proceedings of IEEE Global Communications Conference*, New Orleans, U.S.A., 2-5 December 1985, pp. 1181-1184.
- [22] T. S. Chu and M. J. Gans, "High speed infrared local wireless communication," *IEEE Communications Magazine*, vol. 25, no. 8, pp. 4-10, August 1987.
- [23] L. B. Ribeiro, "Point-to-point optical wireless network for factory communications," in *Proceedings of International Symposium on Industrial Electronics*, vol. 1, pt. 1, Guimaraes, Portugal, 7-11 July 1997, pp. 103-105.
- [24] J. I. Matsuda, T. Nyu, T. Saito and S. Yamazaki, "125 Mbps IR wireless link for IEEE 1394 multimedia home network," in *Proceedings of European Conference on Optical Communication*, Madrid, Spain, 20-24 September 1998, pp. 343-344.
- [25] P. P. Smyth, M. McCullagh, D. Wisely, D. Wood, S. Ritchie, P. Eardley and S. Cassidy, "Optical wireless local area networks - enabling technologies," *BT Technology Journal*, vol. 11, no. 2, pp. 56-64, April 1993.
- [26] M. J. McCullagh, D. R. Wisely, P. L. Eardley and P. P. Smyth, "A 50 Mbit/s optical wireless LAN link using novel optical and electronic enabling technologies," in *International Zurich Seminar on Digital Communications*, Zurich, Switzerland, 1994, pp. 298-309.
- [27] M. J. McCullagh and D. R. Wisely, "155 Mbit/s optical wireless link using a bootstrapped silicon APD receiver," *Electronics Letters*, vol. 30, no. 5, March 1994.
- [28] P. Nicholls, S. D. Greaves and R. T. Unwin, "Optical wireless telepoint," in *Proceedings of IEE Colloquium on Optical Free Space Communication Links*, London, U.K., 19 February 1996, pp. 4/1-4/6.
- [29] D. J. T. Heatley, I. B. Cockburn, F. T. Lyne, A. K. Williamson, K. J. Fisher, I. Neild and N. Haque, "Concept 2010 – BT's new generation dealing desk," *BT Technology Journal*, vol. 14, no. 4, October 1997.
- [30] D. J. T. Heatley and I. Neild, "Optical wireless - the promise and the reality," in *Proceedings of IEE Colloquium on Optical Wireless Communications*, London, U.K., 22 June 1999, pp. 1/1-1/6.
- [31] JVC VIPSLAN-10, JVC Professional Products (UK) Ltd., London.

- [32] J. M. Kahn, W. J. Krause and J. B. Carruthers, "Experimental characterization of non-directed indoor infrared channels," *IEEE Transactions on Communications*, vol. 43, no. 2/3/4, pp. 1613-1623, February/March/April 1995.
- [33] T. H. Tsaor, K. C. Chen, C. Lien, M. T. Shih and C. P. J. Tzeng, "A nondirective infrared transceiver for indoor high speed wireless data communication," *IEEE Transactions on Consumer Electronics*, vol. 40, no. 1, pp. 20-27, February 1994.
- [34] J. R. Barry and J. M. Kahn, "Design of non-directed infrared links for high-speed wireless networks," in *Proceedings of the 7th Annual Meeting of the IEEE Lasers and Electro-Optic Society*, Boston, U.S.A., 31 October – 3 November 1994.
- [35] G. W. Marsh and J. M. Kahn, "50-Mb/s diffuse infrared free-space link using on-off keying with decision feedback equalisation," *IEEE Photonics Technology Letters*, vol. 6, no. 10, pp. 1268-1270, October 1994.
- [36] G. W. Marsh and J. M. Kahn, "Performance evaluation of experimental 50-Mb/s diffuse infrared wireless link using on-off keying with decision-feedback equalisation," *IEEE Transactions on Communications*, vol. 44, no. 11, pp. 1496-1504, November 1996.
- [37] D. Roviras, M. Lescure, R. Bensalah and T. Bosch, "Wireless infrared factory network for hand-held terminals," *European Transactions on Telecommunications*, vol. 6, no. 2, pp. 207-217, March/April 1995.
- [38] A. M. R. Tavares, A. J. C. Moreira, C. R. A. T. Lomba, L. M. V. Moreira, R. J. M. T. Valadas and A. M. de Oliveira Duarte, "Experimental results of a 1Mbps IR transceiver for indoor wireless local area networks," in *5th International Conference on Advances in Communication and Control*, Crete, Greece, 26-30 June 1995, pp. 717-727.
- [39] R. Valadas, A. Moreira, C. Oliveira, L. Moreira, C. Lomba, A. Tavares and A. M. de Oliveira Duarte, "Experimental results of a pulse position modulation infrared transceiver," in *Proceedings of the 7th IEEE International Symposium on Personal, Indoor and Mobile Radio Communications*, Taipei, Taiwan, 15-18 October 1996, pp. 252-256.
- [40] P. Nicholls, R. T. Unwin and K. T. Dalton, "A 10 MB/s optical wireless ethernet – practical results," in *Proceedings of SPIE Conference on Wireless Data Transmission*, Philadelphia, U.S.A., 23-25 October 1995, vol. 2601, pp. 294-304.
- [41] D. C. Lee and J. M. Kahn, "Experimental 25-Mb/s wireless infrared link using 4-PPM with scalar decision-feedback equalization," in *Proceedings of IEEE International Conference on Communications*, Atlanta, U.S.A., 7-11 June 1998, pp. 26-30.
- [42] Spectrix Wireless Network, Technical Overview, Spectrix Corporation, 30 November 2000, <http://www.spectrixcorp.com/techoverview.pdf>.
- [43] G. Yun and M. Kavehrad, "Spot diffusing and fly-eye receivers for indoor infrared wireless communications," in *Proceedings of the 1992 IEEE Conference on Selected Topics in Wireless Communications*, Vancouver, Canada, 25-26 June 1992, pp. 286-292.
- [44] J. M. Kahn, P. Djahani, A. G. Weisbin, K. T. Beh, A. P. Tang and R. You, "Imaging diversity receivers for high-speed infrared wireless communication," *IEEE Communications Magazine*, vol. 36, no. 12, pp. 88-94, December 1998.

- [45] R. T. Valadas and A. M. de Oliveira Duarte, "Sectorized receivers for indoor wireless optical communication systems," in *Proceedings of the 5th IEEE International Symposium on Personal, Indoor and Mobile Radio Communications*, The Hague, Netherlands, 21-23 September 1994, pp. 1090-1095.
- [46] C. R. A. T. Lomba, R. T. Valadas and A. M. de Oliveira Duarte, "Sectorized receivers to combat the multipath dispersion of the indoor optical channel," in *Proceedings of the 6th IEEE International Symposium on Personal, Indoor and Mobile Radio Communications*, Toronto, Canada, 27-29 September 1995, pp. 321-325.
- [47] A. M. R. Tavares, R. J. M. T. Valadas and A. M. de Oliveira Duarte, "Performance of an optical sectorized receiver for indoor wireless communication systems in presence of artificial and natural noise sources," in *Proceedings of SPIE Conference on Wireless Data Transmission*, Philadelphia, U.S.A., 23-25 October 1995, vol. 2601, pp. 264-273.
- [48] R.T. Valadas, A.R. Tavares and A.M. de Oliveira Duarte, "Angle diversity to combat the ambient noise in indoor optical wireless communication systems," *International Journal of Wireless Information Networks*, vol. 4, no. 4, pp. 275-288, 1997.
- [49] K. L. Sterckx, J. M. H. Elmirghani and R. A. Cryan, "Pyramidal fly-eye detection antenna for optical wireless systems," in *Proceedings of IEE Colloquium on Optical Wireless Communications*, London, U.K., 22 June 1999, pp. 5/1-5/6.
- [50] K. L. Sterckx, J. M. H. Elmirghani and R. A. Cryan, "Sensitivity assessment of a three-segment pyramidal fly-eye detector in a semidisperse optical wireless communication link," *IEE Proceedings - Optoelectronics*, vol. 147, no. 4, pp. 286-294, August 2000.
- [51] K. L. Sterckx, J. M. H. Elmirghani and R. A. Cryan, "Three-segment pyramidal fly-eye detection antenna for optical wireless communication systems under the constraint of ambient noise introduced by highly directive spotlights," *International Journal of Communication Systems*, vol. 13, no. 7 & 8, pp. 577-588, November-December 2000.
- [52] A. P. Tang, J. M. Kahn and K. P. Ho, "Wireless infrared communication links using multi-beam transmitters and imaging receivers," in *Proceedings of IEEE International Conference on Communications*, Dallas, U.S.A., 23-27 June 1996, pp. 180-186.
- [53] S. Jivkova and M. Kavehrad, "Indoor wireless infrared local access, multi-spot diffusing with computer generated holographic beam-splitters," in *Proceedings of IEEE International Conference on Communications*, Vancouver, Canada, 6-10 June 1999, vol. 1, pp. 604-608.
- [54] J. B. Carruthers and J. M. Kahn, "Angle diversity for nondirected wireless infrared communication," *IEEE Transactions on Communications*, vol. 48, no. 6, pp. 960-969, June 2000.
- [55] S. Jivkova and M. Kavehrad, "Multispot diffusing configuration for wireless infrared access," *IEEE Transactions on Communications*, vol. 48, no. 6, pp. 970-978, June 2000.
- [56] P. Djahani and J.M. Kahn, "Analysis of infrared wireless links employing multi-beam transmitters and imaging diversity receivers," *IEEE Transactions on Communications*, vol. 48, no. 12, pp. 2077-2088, December 2000.
- [57] D. R. Wisely, "A 1Gbit/s optical wireless tracked architecture for ATM delivery," in *Proceedings of IEE Colloquium on Optical Free Space Communication Links*, London, U.K., 19 February 1996, pp. 14/1-14/7.

- [58] A. M. Street, K. Samaras, D. C. O'Brien and D. J. Edwards, "High speed wireless IR-LANs using spatial addressing," in *Proceedings of the 8th IEEE International Symposium on Personal, Indoor and Mobile Radio Communications*, Helsinki, Finland, 1-4 September 1997, pp. 969-973.
- [59] E. B. Zyambo, D. C. O'Brien, G. E. Faulkner and D. J. Edwards, "Design of a high speed wireless LAN at long wavelengths," in *Proceedings of SPIE Conference on Optical Wireless Communications III*, Boston, U.S.A., 7 November 2000, vol. 4214, pp. 115-124.
- [60] F. Parand, G. E. Faulkner, D. C. O'Brien and D. J. Edwards, "A cellular optical wireless system demonstrator," in *Proceedings of IEE Colloquium on Optical Wireless Communications*, London, U.K., 22 June 1999, pp. 12/1-12/6.
- [61] D. Wisely and I. Neild, "A 100Mbit/s tracked optical wireless telepoint," in *Proceedings of the 8th IEEE International Symposium on Personal, Indoor and Mobile Radio Communications*, Helsinki, Finland, 1-4 September 1997, pp. 964-968.
- [62] J. B. Carruthers and J. M. Kahn, "Modeling of nondirected wireless infrared channels," in *Proceedings of IEEE International Conference on Communications*, Dallas, U.S.A., 23-27 June 1996, vol. 2, pp. 1227-1231.
- [63] J. B. Carruthers and J. M. Kahn, "Modeling of nondirected wireless infrared channels," *IEEE Transactions on Communications*, vol. 45, no. 10, pp. 1260-1268, October 1997.
- [64] C. R. A. T. Lomba, R. T. Valadas and A. M. de Oliveira Duarte, "Propagation losses and impulse response of the indoor optical channel: a simulation package," Document IEEE P802.11-93/78, IEEE, May 1993.
- [65] C. R. A. T. Lomba, R. T. Valadas and A. M. de Oliveira Duarte, "Radiation pattern specification for the baseband IR PHY," Document IEEE P802.11-94/173, IEEE, August 1994.
- [66] M. R. Pakravan and M. Kavehrad, "Design considerations for broadband indoor infrared wireless communication systems," *International Journal of Wireless Information Networks*, vol. 2, no. 4, pp. 223-238, October 1995.
- [67] J. J. G. Fernandes, P. A. Watson and J. C. Neves, "Wireless LANs: physical properties of infrared systems vs. MMW systems," *IEEE Communications Magazine*, vol. 32, no. 8, pp. 68-73, August 1994.
- [68] G. N. Bakalidis, E. Glavas, Ph. Tsalides, "Optical power distribution in wireless infrared LANs," *IEE Proceedings - Communications*, vol. 143, no. 2, pp. 93-97, April 1996.
- [69] H. Yang and C. Lu, "Infrared wireless LAN using multiple optical sources," *IEE Proceedings - Optoelectronics*, vol. 147, no. 4, pp. 301-307, August 2000.
- [70] J. R. Barry, J. M. Kahn, E. A. Lee, and D. G. Messerschmitt, "Simulation of multipath impulse response for indoor diffuse optical channels," in *Proceedings of IEEE Workshop on Wireless Local Area Networks*, Worcester, U.S.A., May 1991, pp. 81-87.
- [71] J. R. Barry, J. M. Kahn, W. J. Krause, E. A. Lee, and D. G. Messerschmitt, "Simulation of multipath impulse response for indoor wireless optical channels," *IEEE Journal on Selected Areas in Communications*, vol. 11, no. 3, pp. 367-379, April 1993.

- [72] M. Abtahi and H. Hashemi, "Simulation of indoor propagation channel at infrared frequencies in furnished office environments," in *Proceedings of the 6th IEEE International Symposium on Personal, Indoor and Mobile Radio Communications*, Toronto, Canada, 27-29 September 1995, vol. 1, pp. 306-310.
- [73] C. R. Lomba, R. T. Valadas and A. M. de Oliveira Duarte, "Efficient simulation of the impulse response of the indoor wireless optical channel," *International Journal of Communication Systems*, vol. 13, no. 7 & 8, pp. 537-550, November-December 2000.
- [74] F. J. Lopez-Hernandez, R. Perez-Jimenez and A. Santamaria, "Monte Carlo calculation of impulse response on diffuse IR wireless indoor channels," *Electronics Letters*, vol. 34, no. 12, June 1998.
- [75] F. J. Lopez-Hernandez, R. Perez-Jimenez and A. Santamaria, "Modified Monte Carlo scheme for high-efficiency simulation of the impulse response on diffuse IR wireless indoor channels," *Electronics Letters*, vol. 34, no. 19, September 1998.
- [76] H. Hashemi, G. Yun, M. Kavehrad, F. Behbahani and P. A. Galko, "Indoor propagation measurements at infrared frequencies for wireless local area networks applications," *IEEE Transactions on Vehicular Technology*, vol. 43, no. 3, pp. 562-576, August 1994.
- [77] IEC 60825-1, Edition 1.2, International Electrotechnical Commission, August 2001.
- [78] BS EN 60825-1 : 1994 Standard, British Standards Institution, Issue 3, June 1997.
- [79] Hewlett-Packard, "Compliance of infrared communication products to IEC 825-1 and CENELEC EN 60825-1," Application Note 1118, 1997.
- [80] P. McKee, D. Wood, J. Towers and P. Smyth, "Applications of computer generated, free-space diffractive optics from interconnections and packaging to optical wireless antennas," in *Proceedings of 4th International Conference on Holographic Systems, Components and Applications*, Neuchatel, Switzerland, 13-15 September 1993, IEE Conference Publication no. 379, pp. 260-264.
- [81] P. L. Eardley, D. R. Wisely, D. Wood and P. McKee, "Holograms for optical wireless LANs," *IEE Proceedings - Optoelectronics*, vol. 143, no. 6, pp. 365-369, December 1996.
- [82] V. Pohl, V. Jungnickel, R. Hentges and C. von Helmolt, "Integrating sphere diffuser for wireless infrared communication," in *Proceedings of IEE Colloquium on Optical Wireless Communications*, London, U.K., 22 June 1999, pp. 4/1-4/6.
- [83] V. Pohl, V. Jungnickel and C. von Helmolt, "Integrating sphere diffuser for wireless infrared communication," *IEE Proceedings - Optoelectronics*, vol. 147, no. 4, pp. 281-285, August 2000.
- [84] A. J. C. Moreira, R. T. Valadas and A. M. De Oliveira Duarte, "Characterisation and modelling of artificial light interference in optical wireless communication systems," in *Proceedings of the 6th IEEE International Symposium on Personal, Indoor and Mobile Radio Communications*, Toronto, Canada, 27-29 September 1995, pp. 326-331.
- [85] A. J. C. Moreira, R. T. Valadas and A. M. de Oliveira Duarte, "Optical interference produced by artificial light," *Wireless Networks*, vol. 3, no. 2, pp. 131-140, 1997.
- [86] A. C. Boucouvalas, "Indoor ambient light noise and its effect on wireless optical links," *IEE Proceedings - Optoelectronics*, vol. 143, no. 6, pp. 334-338, December 1996.

- [87] A. J. C. Moreira, R. T. Valadas and A. M. de Oliveira Duarte, "Reducing the effects of artificial light interference in wireless infrared transmission systems," in *Proceedings of IEE Colloquium on Optical Free Space Communication Links*, London, U.K., 19 February 1996, pp. 5/1-5/10.
- [88] R. Narasimhan, M. D. Audeh and J. M. Kahn, "Effect of electronic-ballast fluorescent lighting on wireless infrared links," in *Proceedings of IEEE International Conference on Communications*, Dallas, U.S.A., 23-27 June 1996, pp. 1213-1219.
- [89] K. Samaras, A. M. Street, D. C. O'Brien and D. J. Edwards, "Error rate evaluation of wireless infrared links," in *Proceedings of IEEE International Conference on Communications*, Atlanta, U.S.A., 7-11 June 1998, vol. 2, pp. 826-831.
- [90] A. M. R. Tavares, R. J. M. T. Valadas and A. M. de Oliveira Duarte, "Performance of wireless infrared transmission systems considering both ambient light interference and inter-symbol interference due to multipath dispersion," in *Proceedings of SPIE Conference on Optical Wireless Communications*, Boston, U.S.A., 5 November 1998, vol. 3532, pp. 82-93.
- [91] K. K. Wong, T. O'Farrell and M. Kiatweerasakul, "Infrared wireless communication using spread spectrum techniques," *IEE Proceedings - Optoelectronics*, vol. 147, no. 4, pp. 308-314, August 2000.
- [92] K. K. Wong, T. O'Farrell and M. Kiatweerasakul, "The performance of optical wireless OOK, 2-PPM and spread spectrum under the effects of multipath dispersion and artificial light interference," *International Journal of Communication Systems*, vol. 13, no. 7 & 8, pp. 551-576, November-December 2000.
- [93] A. B. Carlson, *Communication Systems*, Second Edition. McGraw-Hill, 1975.
- [94] F. G. Stremler, *Introduction to Communication Systems*, Second Edition. Addison-Wesley, 1982.
- [95] L. W. Couch II, *Digital and Analog Communication Systems*, Fifth Edition. Prentice-Hall, 1997.
- [96] M. Schwartz, *Information Transmission, Modulation, and Noise*, Fourth Edition. McGraw-Hill, 1990.
- [97] J. B. Carruthers and J. M. Kahn, "Multiple-subcarrier modulation for nondirected wireless infrared communication," *IEEE Journal on Selected Areas in Communications*, vol. 14, no. 3, pp. 538-546, April 1996.
- [98] F. M. Davidson and X. Sun, "Slot clock recovery in optical PPM communication systems with avalanche photodiode photodetectors," *IEEE Transactions on Communications*, vol. 37, no. 11, pp. 1164-1171, November 1989.
- [99] J. G. Proakis, *Digital Communications*, Third Edition. McGraw-Hill, 1995.
- [100] G. D. Forney, "Maximum-likelihood sequence estimation of digital sequences in the presence of intersymbol interference," *IEEE Transactions on Information Theory*, vol. IT-18, no. 3, pp. 363-378, May 1972.
- [101] A. J. Viterbi, "Error bounds for convolutional codes and an asymptotically optimum decoding algorithm," *IEEE Transactions on Information Theory*, vol. IT-13, no. 2, pp. 260-269, April 1967.

- [102] M. D. Audeh, J. M. Kahn and J. R. Barry, "Performance of PPM with maximum-likelihood sequence detection on measured non-directed indoor infrared channels," in *Proceedings of IEEE International Conference on Communications*, Seattle, U.S.A., 18-22 June 1995, vol. 2, pp. 1177-1181.
- [103] M. D. Audeh, J. M. Kahn and J. R. Barry, "Performance of pulse-position modulation on measured non-directed indoor infrared channels," *IEEE Transactions on Communications*, vol. 44, no. 6, pp. 654-659, June 1996.
- [104] C. A. Belfiore, "Decision feedback equalization," *Proceedings of the IEEE*, vol. 67, no. 8, pp. 1143-1156, August 1979.
- [105] M. D. Audeh and J. M. Kahn, "Performance simulation of baseband OOK modulation for wireless infrared LANs at 100 Mb/s," in *Proceedings of IEEE Conference on Selected Topics in Wireless Communications*, Canada, June 1992, pp. 271-274.
- [106] M. D. Audeh and J. M. Kahn, "Performance evaluation of baseband OOK for wireless indoor infrared LAN's operating at 100 Mb/s," *IEEE Transactions on Communications*, vol. 43, no. 6, pp. 2085-2094, June 1995.
- [107] M. D. Audeh and J. M. Kahn, "Performance evaluation of L -pulse-position modulation on non-directed indoor infrared channels," in *Proceedings of IEEE International Conference on Communications*, New Orleans, U.S.A., 1-5 May 1994, vol. 2, pp. 660-664.
- [108] J. R. Barry, "Sequence detection and equalization for pulse-position modulation," in *Proceedings of IEEE International Conference on Communications*, New Orleans, U.S.A., 1-5 May 1994, pp. 1561-1565.
- [109] J. R. Barry, "Equalization for wireless optics communications over multipath channels," in *Proceedings of 9th Meeting of Optical Engineering in Israel*, Tel Aviv, Israel, October 1994, SPIE vol. 2426, pp. 596-607.
- [110] M. D. Audeh, J. M. Kahn and J. R. Barry, "Decision-feedback equalization of pulse-position modulation on measured nondirected indoor infrared channels," *IEEE Transactions on Communications*, vol. 47, no. 4, pp. 500-503, April 1999.
- [111] D. C. Lee, J. M. Kahn and M. D. Audeh, "Trellis-coded pulse-position modulation for indoor wireless infrared communications," *IEEE Transactions on Communications*, vol. 45, no. 9, pp. 1080-1087, September 1997.
- [112] D. C. Lee and J. M. Kahn, "Coding and equalization for PPM on wireless infrared channels," in *Proceedings of IEEE Global Communications Conference*, Sydney, Australia, 8-12 November 1998, vol. 1, pp. 201-206.
- [113] D. C. Lee and J. M. Kahn, "Coding and equalization for PPM on wireless infrared channels," *IEEE Transactions on Communications*, vol. 47, no. 2, pp. 255-260, February 1999.
- [114] H. Sugiyama and K. Nosu, "MPPM: A method for improving the band-utilization efficiency in optical PPM," *Journal of Lightwave Technology*, vol. 7, no. 3, pp. 465-472, March 1989.
- [115] J. M. Budinger, M. Vanderaar, P. Wagner and S. Bibyk, "Combinatorial pulse position modulation for power-efficient free-space laser communications," in *Proceedings of SPIE Conference on Free Space Laser Communication Technologies*, Los Angeles, U.S.A., 20-21 January 1993, vol. 1866, no. 5, pp. 214-225.

- [116] H. Park and J. R. Barry, "Modulation analysis for wireless infrared communications," in *Proceedings of IEEE International Conference on Communications*, Seattle, U.S.A., 18-22 June 1995, vol. 2, pp. 1182-1186.
- [117] H. Park and J. R. Barry, "Performance analysis and channel capacity for multiple-pulse position modulation on multipath channels," in *Proceedings of the 7th IEEE International Symposium on Personal, Indoor and Mobile Radio Communications*, Taipei, Taiwan, 15-18 October 1996, vol. 1, pp. 247-251.
- [118] H. Park and J. R. Barry, "Performance of multiple pulse position modulation on multipath channels," *IEE Proceedings - Optoelectronics*, vol. 143, no. 6, pp. 360-364, December 1996.
- [119] H. Park and J. R. Barry, "Trellis-coded multiple-pulse position modulation for wireless infrared communications," in *Proceedings of IEEE Global Communications Conference*, Sydney, Australia, 8-12 November 1998, vol. 1, pp. 225-230.
- [120] D. Shiu and J. M. Kahn, "Differential pulse position modulation for power-efficient wireless infrared communication," in *Proceedings of IEEE Global Communications Conference*, Sydney, Australia, 8-12 November 1998, vol. 1, pp. 219-224.
- [121] D. Shiu and J. M. Kahn, "Differential pulse-position modulation for power-efficient optical communication," *IEEE Transactions on Communications*, vol. 47, no. 8, pp. 1201-1210, August 1999.
- [122] Y. Ueno, Y. Ohgushi and T. Yasugi, "An optical fiber communication system using pulse-interval modulation," in *IEE First European Conference on Optical Fibre Communication*, September 1975, pp. 156-158.
- [123] Y. Ueno and T. Yasugi, "Optical fiber communication systems using pulse-interval modulation," *NEC Research and Development Journal*, no. 48, pp. 45-51, January 1978.
- [124] A. Okazaki, "Pulse-interval modulation applicable to narrowband transmission," *IEEE Transactions on Cable Television*, vol. CATV-3, no. 4, pp. 155-164, October 1978.
- [125] A. Okazaki, "Still picture transmission by pulse-interval modulation," *IEEE Transactions on Cable Television*, vol. CATV-4, no. 1, pp. 17-22, January 1979.
- [126] Z. Ghassemlooy, E. D. Kaluarachchi, R. U. Reyher and A. J. Simmonds, "A new modulation technique based on digital pulse interval modulation for optical fibre communication," *Microwave and Optical Technology Letters*, vol. 10, no. 1, pp. 1-4, September 1995.
- [127] B. Wilson, Z. Ghassemlooy and E. D. Kaluarachchi, "Digital pulse interval modulation for fiber transmission," in *Proceedings of SPIE Conference on All-Optical Communication Systems: Architecture, Control and Network Issues*, Philadelphia, U.S.A., 25-26 October 1995, vol. 2614, pp. 53-59.
- [128] E. D. Kaluarachchi, Z. F. Ghassemlooy and B. Wilson, "Digital pulse interval modulation for transmission over optical fiber with direct detection," in *Proceedings of SPIE Conference on All-Optical Communication Systems: Architecture, Control, and Network Issues II*, Boston, U.S.A., 18-22 November 1996, vol. 2919, pp. 98-105.
- [129] E. D. Kaluarachchi, "Digital pulse interval modulation for optical communication systems," Ph.D. Thesis, Sheffield Hallam University, Sheffield, U.K., 1997.

- [130] E. D. Kaluarachchi, Z. Ghassemlooy and B. Wilson, "Digital pulse interval modulation for optical fibre transmission," in *Proceedings of 1st International Symposium on Communication Systems and Digital Signal Processing*, Sheffield, U.K., 6-8 April 1998, vol. 2, pp. 589-594.
- [131] E. D. Kaluarachchi, Z. Ghassemlooy and B. Wilson, "Digital pulse interval modulation (DPIM) for free space optical links," in *Proceedings of IEE Colloquium on Optical Free Space Communication Links*, London, U.K., 19 February 1996, pp. 3/1-3/5.
- [132] J. D. Gibson, *Principles of Digital and Analog Communications*, Second Edition. Macmillan, 1993.
- [133] A. R. Hayes, Z. Ghassemlooy, N. L. Seed and R. McLaughlin, "Baseline wander effects on systems employing digital pulse interval modulation," *IEE Proceedings - Optoelectronics*, vol. 147, no. 4, pp. 295-300, August 2000.
- [134] IEEE Standard 802.3, 2000 Edition, Institute of Electrical and Electronics Engineers, 16 October 2000.
- [135] S. B. Alexander, *Optical Communication Receiver Design*. SPIE Optical Engineering Press, 1997.
- [136] G. James, *Modern Engineering Mathematics*, Second Edition. Addison-Wesley, 1996.
- [137] K. Samaras, A. M. Street, D. C. O'Brien and D. J. Edwards, "Methods for evaluating error rates in infrared wireless links," *Electronics Letters*, vol. 33, no. 20, pp. 1720-1721, September 1997.
- [138] *Digital Telecommunications*, Block 6, Coding and Modulation. Open University Press, 1990.
- [139] S. Karni, *Applied Circuit Analysis*. John Wiley & Sons, 1988.
- [140] A. M. Street, K. Samaras, D. C. O'Brien and D. J. Edwards, "Closed form expressions for baseline wander effects in wireless IR applications," *Electronics Letters*, vol. 33, no. 12, pp. 1060-1062, June 1997.
- [141] A. R. Hayes, Z. Ghassemlooy and N. L. Seed, "The effect of baseline wander on the performance of digital pulse interval modulation," in *Proceedings of IEE Colloquium on Optical Wireless Communications*, London, U.K., 22 June 1999, pp. 13/1-13/5.
- [142] J. M. Kahn, J. R. Barry, M. D. Audeh, J. B. Carruthers, W. J. Krause and G. W. Marsh, "Non-directed infrared links for high-capacity wireless LANs," *IEEE Personal Communications Magazine*, vol. 1, no. 2, pp. 12-25, Second Quarter 1994.
- [143] T. S. Rappaport, *Wireless Communications*. Prentice-Hall, 1996.
- [144] M. E. Austin, "Decision-feedback equalisation for digital communication over dispersive channels," M.I.T. Lincoln Laboratory, Lexington, U.S.A., Technical Report 437, August 1967.
- [145] R. Price, "Nonlinearly feedback-equalised PAM vs. capacity for noisy filter channels," in *Proceedings of IEEE International Conference on Communications*, Philadelphia, U.S.A., June 1972, pp. 22/12-22/17.
- [146] D. Van den Bout, *The Practical Xilinx Designer Lab Book*. Prentice-Hall, 1998.

- [147] Burr-Brown, OPA686 Data Sheet, 1997.
- [148] Burr-Brown, OPA655 Data Sheet, 1994.
- [149] M. D. Hahm, E. G. Friedman and E. L. Titlebaum, "A comparison of analog and digital circuit implementations of low power matched filters for use in portable wireless communication terminals," *IEEE Transactions on Circuits and Systems II: Analog and Digital Signal Processing*, vol. 44, no. 6, pp. 498-506, June 1997.
- [150] B. Waggener, *Pulse Code Modulation Techniques*. Van Nostrand Reinhold, 1995.
- [151] C. B. Rorabaugh, *Digital Filter Designer's Handbook*. McGraw-Hill, 1993.
- [152] M. E. Van Valkenburg, *Analog Filter Design*. Holt, Rinehart and Winston, 1982.
- [153] B. Sklar, *Digital Communications*. Prentice-Hall, 1988.
- [154] A. B. Williams, *Electronic Filter Design Handbook*. McGraw-Hill, 1981.